# Theoretical Modeling of Heat and Mass Transfer Processes in Phase Change and Electrochemical Energy Storage Systems

by

MOHAMMAD PARHIZI

DISSERTATION

Submitted in partial fulfillment of the requirements

For the degree of Doctor of Philosophy at

The University of Texas at Arlington

August, 2020

Arlington, Texas

Supervising Committee:

Dr. Ankur Jain (Committee Chairperson)

Dr. Miguel Amaya

Dr. Judy Jeevarajan

Dr. Ratan Kumar

Dr. Hyejin Moon

# ACKNOWLEDGEMENTS

I would like to express my sincere gratitude and appreciation to my supervisor, Professor Ankur Jain for believing in me and giving me the opportunity to start my research in his lab – Microscale Thermophysics Laboratory – where I have developed a keen interest in heat transfer and energy storage and conversion systems. I am sincerely grateful for his constant support and guidance throughout my PhD. He has been always supportive and his passion for research has been always inspiring.

I would like to thank my dissertation committee for their time, guidance, and support. Their valuable suggestions helped me to improve the quality of my dissertation.

I would like to thank my family who provided me invaluable emotional and financial support throughout this journey. Without their sacrifice, my success would have not been possible. I am forever grateful to have an understanding, supportive and encouraging family. Special thanks to my wife, Nazanin, for being caring, understanding and an amazing supporter. She has been always there whenever needed. Without her, I would not be able to accomplish my goals.

I would also like to thank everyone at Microscale Thermophysics Laboratory for providing productive suggestions and helping me at various stages of research.

Special thanks to MAE department at the University of Texas at Arlington for all their support. I would also like to thank National Science Foundation for their financial support for my research and Summer internship.

I would like to sincerely thank Dr. Judy Jeevarajan for her invaluable help and support in my NSF internship grant application. I would also like to thank her for being a great mentor during

my internship. I would like to thank Carlos Lopez and Saad Azam for their help and support during my internship.

July 30, 2020.

# ABSTRACT

## Theoretical Modeling of Heat and Mass Transfer Processes in Phase Change and Electrochemical Energy Storage Systems

Mohammad Parhizi, Ph.D.

The University of Texas at Arlington, 2020

Supervising Professor: Dr. Ankur Jain

Theoretical understanding of heat and mass transfer processes in energy storage and conversion devices is of much interest for a wide variety of engineering applications. Two commonly used mechanisms for energy storage are electrochemical energy storage, such as in Li-ion cells, and phase change based energy storage, such as in phase change materials (PCM). Previous studies show that heat and mass transfer in both PCMs and Li-ion cells are critical processes affecting the performance and safety of these systems. This dissertation investigates several theoretical aspects of heat and mass transfer in these energy storage systems, with the goal of improving performance and safety.

In the first part, this dissertation presents a solution for a one-dimensional phase change problem with any arbitrary time-dependent heat flux boundary condition using the perturbation method. The solution presented here is shown to offer key advantages both in accuracy and stability over past papers. The theoretical result is then used for understanding the nature of phase change propagation heat transfer for a wide variety of applications. The model is used to investigate phase change heat transfer including a pre-melted or pre-solidified length between the region of interest and a time-dependent temperature boundary condition. Such a scenario can occur in multiple engineering applications when the heating or cooling process is intermittent in time.

Furthermore, the perturbation-based model is used to provide a theoretical understanding of how thermal conductivity and other thermophysical properties affect rate of energy stored (W) and energy storage density (J/m$^3$) as two critical performance parameters of a system. Finally, the method is used to study phase change cooling of Lithium-ion cells.

In the second part, this dissertation presents a heat transfer model to determine the core temperature of a Li-ion cell during thermal runaway using surface temperature and chemical kinetics data. The model presented here provides key insight into the internal state of Li-ion cells during thermal runaway. Later, mathematical modeling of species diffusion in Li-ion cell is carried out for improving performance and efficiency of electrochemical energy storage  in Li-ion cells. Green's functions approach is used to solve the solution phase and solid-phase diffusion limitations in composite electrodes operating under a time-dependent flux boundary condition. The mathematical models presented in this work are validated by comparison with past studies and numerical simulations. The Green's-function based model is then used to present an analytical Single Particle Model (SPM) based model to predict the terminal voltage and consequently estimate the state of charge (SoC) of Li-ion cells operating under realistic time-dependent current profiles. The mathematical model presented here is compared against numerical simulations and past experimental data for different operating conditions.

It is expected that the theoretical models developed in this dissertation will help in designing and improving the performance of electrochemical and phase change energy storage systems.

# Table of Contents

# Chapter 1

## 1-1. Introduction

Theoretical understanding of heat and mass transfer processes in energy storage and conversion systems is critical to improve the performance and safety of these systems. Two commonly used mechanisms for energy storage are phase change based energy storage, such as in phase change materials (PCMs) and electrochemical energy storage, such as in Lithium-ion cells. A broad introduction to each of these systems is presented next and a more detailed introduction is given in the beginning of each chapter.

Phase change materials are used in a wide variety of engineering applications such as thermal management, energy storage, etc. Typical PCMs can be broadly divided into two categories – organic PCMs which are usually paraffin based and inorganic PCMs such as salt hydrates that offer large latent heat [1]. Operation of engineering systems comprising of PCMs always involves phase change heat transfer. The large latent heat of phase change relative to the magnitude of typical sensible heat is utilized commonly for designing effective thermal management [2] or energy storage techniques [3]. In both cases, energy is absorbed from a source of heat into a PCM that undergoes phase change from solid to liquid. As an example, latent heat storage has been widely investigated for storing energy harnessed from renewable sources [4], and forms a critical part of the infrastructure needed to address the intermittent nature of these sources and ultimately make renewable energy feasible. Compared to other competing mechanisms for energy storage, such as sensible heat [5], thermochemical [6], electrochemical [7], etc., phase change energy storage offers several advantages such as large rates of energy transfer, large energy storage density, etc. [4].

Thermophysical properties such as thermal conductivity ($k$), heat capacity ($C_p$) and latent heat ($L$) of the PCM play a key role in determining the performance of phase change energy storage. PCMs are typically chosen for their large values of latent heat, these materials also have low thermal conductivity, in the range of 0.1-2.5 W/mK [8]. Due to this low thermal conductivity, as the phase change process proceeds, thermal impedance offered by the melted liquid slows down the rate of further melting. This self-limiting nature of phase change energy storage has been recognized to be an important limitation of phase change based energy storage [9], and the energy storage system is often designed to counter these effects, for example by providing fins into the PCM to increase surface area [10], or by enhancing PCM thermal conductivity by introducing nano/micro-particles [11].

The average rate of energy transferred and stored into the PCM over a certain time period is an important performance parameter for both thermal management and energy storage applications. Further, from a systems perspective, the density of energy stored is also an important parameter in order to ensure compactness of energy storage. High energy storage density can be a critical performance parameter when the space available for energy storage is limited and minimizing system weight is important. These considerations often arise in automotive, aerospace and military applications as well as compact consumer electronic devices. While the total energy stored is determined largely by the integral of heat flux at the PCM-source interface over time, the energy storage density additionally involves the volume of PCM melted over the time period.

While most experimental papers have focused on improving thermal conductivity, which clearly improves the rate of heat transfer from the source into the PCM, one must recognize that an increased thermal conductivity also increases the rate of melting. This is expected to increase the total volume of PCM required, and therefore, may negatively impact energy storage density. Unlike extensive experimental work, a key gap in the literature pertains to the modeling and analysis of such effects. There is a lack in the literature of analytical models that connect these two key performance parameters – total energy stored and energy storage density – with underlying thermal properties of the PCM. Further, such an analytical model may also play a key role in materials selection. For example, given two candidate phase change materials that differ from each other in the values of both $k$ and $C_p$, an analytical model may help determine which material is expected to have better performance in terms of total energy stored and energy storage density. In some cases, either one of total energy stored and energy storage density may be more critical than the other, and therefore, the choice of the ideal PCM depends on system-level considerations, which is not possible to account for using analytical models available in the literature. Moreover, such theoretical models which describe heat transfer during phase change can be used to investigate multiple engineering problems such as thermal energy storage, heat exchangers, additive manufacturing, welding and casting of metals, crystal growth and thermal management systems.

In theoretical analysis of such problems, the interest is often in predicting the propagation of the phase change front as well as temperature distribution in the newly formed phase. The analysis of phase change problems is considerably complicated due to their non-linear nature – exact solutions exist only for a few idealized cases. The simplest model for phase change based energy storage is the case of heat transfer from a constant temperature wall into a PCM. This is indeed the well-known Stefan problem [12,13], for which progression of the melting front is known to be proportional to $\sqrt{\alpha t}$ where $\alpha$ is the thermal diffusivity of the PCM. For this problem, equations are also available for temperature distribution in the melted material, and therefore, the rate of heat transfer into the PCM [12]. However, similar models are lacking for more complicated cases, such as in cylindrical coordinates, or for a heat-generating source surrounded by a PCM, for which, analysis using a time-dependent temperature boundary condition is more realistic than a constant temperature one. These limitations in the literature have made it difficult to optimize phase change based energy storage in practical engineering applications that cannot be reasonably modeled by the simplest, constant-temperature Stefan problem, or that are cylindrical or spherical in nature. Phase change heat transfer problems are, in general, non-linear in nature, making such theoretical analysis challenging.

Operation of electrochemical energy storage devices such as Li-ion cells on the other hand, involves reaction kinetics, mass, charge and thermal transport phenomena [13,14]. Mathematical modeling of Li-ion cells is therefore, necessary to fully understand the underlying processes towards design and optimization of electrochemical energy conversion and storage systems [15,16].

Extensive research has been reported towards development of theoretical models to predict electrochemical and thermal transport in Li-ion cells subject to different operating conditions [17,18]. These electrochemical models solve the underlying charge, mass and thermal transport equations, as well as reaction kinetics [17-20]. Two most extensively-used electrochemical models are the Pseudo-2D model (P2D) and Single Particle Model (SPM) [17]. P2D model was constructed based on the porous electrode theory introduced by Newman [18] and the concentrated solution theory [19]. It solves the species and charge transport in both solution and solid phases [17,20]. P2D model is generally coupled and non-linear, resulting in a large number of equations and significant computational time. Thus, Single Particle Model (SPM) was developed to reduce the complexity associated with P2D model. In SPM, concentration gradients in the solution phase are neglected, leading to dominance of solid phase diffusion in the porous electrode, which can be represented by a single, one-dimensional particle [14,21,22]. At low discharge rates and for thin electrodes this may be a reasonable assumption [23-24]. However, at larger discharge rates or for thick electrodes for example energy cells, when concentration gradient in the solution phase cannot be neglected, the governing equations become coupled and simplification is needed in order to derive an analytical solution. Towards this, Doyle et al. [25] assumed a specific form for the reaction rate distribution in the porous electrode, leading to uncoupling of the governing equations. Based on this approach, analytical solutions have been derived using the Separation of Variables (SOV) method for three limiting cases – solid phase, solution phase and Ohmically-dominated cell [25]. The governing equations in the solid phase were defined based on Fick's law and the material balance in the solution phase was defined using the concentrated solution theory [25].

Mathematical models summarized above often result in a set of coupled equations that are often non-linear. As a result, exact solutions for these mathematical models exist only for a few limited cases. For example, diffusion equation for a solid solution cathodes initially at zero concentration has been solved using Laplace transformation approach [26]. Separation of Variables (SOV) technique has been used to solve a similar model for discharging of a Li-ion cell for different limiting cases [25]. Analytical solution for 1-D transient diffusion in a thin film, spherical electrode particle and composite electrode under constant galvanostatic discharge boundary condition and zero initial concentration has been developed using an extended separation of variables method [27,28]. Laplace transformation technique has been used to solve material balance equation in both solid and solution phases with non-zero initial concentration [29].

While most of the past analytical models focus on constant galvanostatic discharge conditions, there is a relative lack of work on time-dependent flux boundary conditions. In some cases, time-dependent boundary conditions are also important since the applied current density may be time-dependent. Therefore, mathematical models which can account for arbitrary time-dependent boundary condisions, generation or consumption and arbitrary space-dependent initial condisions are of much interests. Such models can be used to estimate the state of charge of cells which is necessary for an accurate estimation of the state of the cell, and to ensure safety and efficient performance by avoiding overcharge or overdischarge. Thus, determining the concentration field in the electrodes particle is a key step for SPM-based SoC estimation. Analytical solutions for the diffusion equation governing the concentration field are available only for galvanostatic (constant current) operating conditions where the applied current density is constant. Even though step-wise changes in current can, in principle, be addressed by successively solving the concentration field in each galvanostatic time period, doing so is very difficult for rapidly changing current profiles encountered in vehicle drive cycles, or when the current changes smoothly over time, such as in alternating current (AC) systems. Previous studies have implemented a variety of numerical procedures and algorithms to predict the voltage and consequently SoC under dynamic discharge current conditions. However, an analytical solution for determining the SoC during time-varying charge/discharge conditions is very desirable since it may offer the capability of rapid, in-line SoC estimation that integrates well with other BMS functions.

This dissertation first presents an approximate analytical solution for a one-dimensional phase change problem with any arbitrary time-dependent heat flux boundary condition using the perturbation method. The solution presented here is shown to offer key advantages both in accuracy and stability over past papers. Later, the theoretical result is used for understanding the nature of phase change propagation heat transfer for a wide variety of applications. For example, perturbation method is used to investigate phase change heat transfer including a pre-melted or pre-solidified length between the region of interest and a time-dependent temperature boundary condition. Such a scenario can occur in multiple engineering applications when the heating or cooling process is intermittent in time. Furthermore, the perturbation-based model is used to provide a theoretical understanding of how thermal conductivity and other thermophysical properties affect rate of energy stored (W) and energy storage density (J/m$^3$) as two critical performance parameters of a system. Finally, the method is used develop a theoretical model for PCM-based thermal management of Li-ion battery packs.

In the second part of this dissertation, mathematical modeling of species diffusion in Li-ion cell is discussed for improving performance and efficiency of electrochemical energy storage in Li-ion cells. Green’s functions approach is used to solve the solution phase and solid-phase diffusion limitations in composite electrodes operating under a time-dependent flux boundary condition. The mathematical models presented in this work are validated by comparison with past studies and numerical simulations. The Greens-function based model is then used to present an analytical SPM-based model to predict the terminal voltage and consequently estimate the state of charge (SoC) of Li-ion cells operating under realistic time-dependent current profiles. The mathematical model presented here is compared against numerical simulations and past experimental data for different operating conditions.

## 1.1 References

[1] B. Zalba, Marín José Ma, L.F. Cabeza, H. Mehling, Review on thermal energy storage with phase change: materials, heat transfer analysis and applications, Applied Thermal Engineering. 23 (2003) 251–283. doi:10.1016/s1359-4311(02)00192-8.

[2] Z. Ling, Z. Zhang, G. Shi, X. Fang, L. Wang, X. Gao, et al., Review on thermal management systems using phase change materials for electronic components, Li-ion batteries and photovoltaic modules, Renewable and Sustainable Energy Reviews. 31 (2014) 427–438. doi:10.1016/j.rser.2013.12.017

[3] A. Sharma, V. Tyagi, C. Chen, D. Buddhi, Review on thermal energy storage with phase change materials and applications, Renewable and Sustainable Energy Reviews. 13 (2009) 318–345. doi:10.1016/j.rser.2007.10.005.

[4] M.M. Farid, A.M. Khudhair, S.A.K. Razack, S. Al-Hallaj, A review on phase change energy storage: materials and applications, Energy Conversion and Management. 45 (2004) 1597–1615. doi:10.1016/j.enconman.2003.09.015.

[5] S. Hasnain, Review on sustainable thermal energy storage technologies, Part I: heat storage materials and techniques, Energy Conversion and Management. 39 (1998) 1127–1138. doi:10.1016/s0196-8904(98)00025-9.

[6] J. Cot-Gores, A. Castell, L.F. Cabeza, Thermochemical energy storage and conversion: A-state-of-the-art review of the experimental research under practical conditions, Renewable and Sustainable Energy Reviews. 16 (2012) 5207–5224. doi:10.1016/j.rser.2012.04.007.

[7] K. Shah, N. Balsara, S. Banerjee, et al., State-of-the-art and future research needs for multiscale analysis of Li-ion cells, ASME J. Electrochem. Energy Conversion & Storage 14 (2017) 020801:1-17. doi: 10.1115/1.4036456

[8] F. Agyenim, N. Hewitt, P. Eames, M. Smyth, A review of materials, heat transfer and phase change problem formulation for latent heat thermal energy storage systems (LHTESS), Renewable and Sustainable Energy Reviews. 14 (2010) 615–628. doi:10.1016/j.rser.2009.10.015.

[9] L. Fan, J. Khodadadi, Thermal conductivity enhancement of phase change materials for thermal energy storage: A review, Renewable and Sustainable Energy Reviews. 15 (2011) 24–46. doi:10.1016/j.rser.2010.08.007.

[10] A. Mostafavi, M. Parhizi, A. Jain, Theoretical modeling and optimization of fin-based enhancement of heat transfer into a phase change material, International Journal of Heat and Mass Transfer. (2019) in review.

[11] L. Liu, D. Su, Y. Tang, G. Fang, Thermal conductivity enhancement of phase change materials for thermal energy storage: A review, Renewable and Sustainable Energy Reviews. 62 (2016) 305–317. doi:10.1016/j.rser.2016.04.057.

[12] D. W. Hahn, and M. N. Özişik, 2012, “Heat Conduction.” Third ed., John Wiley & Sons, Hoboken, New Jersey.

[13] K. Shah, N. Balsara, S. Banerjee, M. Chintapalli, A.P. Cocco, W.K.S. Chiu, et al., State of the Art and Future Research Needs for Multiscale Analysis of Li-Ion Cells, Journal of Electrochemical Energy Conversion and Storage. 14 (2017). doi:10.1115/1.4036456.

[14] B. Diouf, R. Pode, Potential of lithium-ion batteries in renewable energy, Renewable Energy. 76 (2015) 375–380. doi:10.1016/j.renene.2014.11.058.

[15] J. Zhang, J. Lee, A review on prognostics and health monitoring of Li-ion battery, Journal of Power Sources. 196 (2011) 6007–6014. doi:10.1016/j.jpowsour.2011.03.101.

[16] M.L. Sushko, K.M. Rosso, J.-G.(J. Zhang, J. Liu, Multiscale Simulations of Li Ion Conductivity in Solid Electrolyte, The Journal of Physical Chemistry Letters. 2 (2011) 2352–2356. doi:10.1021/jz201032w.

[17] A. Jokar, B. Rajabloo, M. Désilets, M. Lacroix, Review of simplified Pseudo-two-Dimensional models of lithium-ion batteries, Journal of Power Sources. 327 (2016) 44–55. doi:10.1016/j.jpowsour.2016.07.036.

[18] J. Newman, K.E. Thomas-Alyea. Electrochemical systems. John Wiley & Sons, 2012.

[19] T. F. Fuller, J. A. Newman, Concentrated solution theory model of transport in solid–polymer–electrolyte fuel cells. Electrochem. Soc. Proc. (1989). Ser, 89-14.

[20] M. Doyle, Modeling of Galvanostatic Charge and Discharge of the Lithium/Polymer/Insertion Cell, Journal of The Electrochemical Society. 140 (1993) 1526. doi:10.1149/1.2221597.

[21] G. Ning, B.N. Popov, Cycle Life Modeling of Lithium-Ion Batteries, Journal of The Electrochemical Society. 151 (2004). doi:10.1149/1.1787631.

[22] S. Santhanagopalan, Q. Guo, P. Ramadass, R.E. White, Review of models for predicting the cycling performance of lithium ion batteries, Journal of Power Sources. 156 (2006) 620–628. doi:10.1016/j.jpowsour.2005.05.070.

[23] V. Ramadesigan, V. Boovaragavan, V.R. Subramanian, Efficient Reformulation of Solid-Phase Diffusion in Physics-Based Lithium-ion Battery Models, ECS Transactions. (2009). doi:10.1149/1.3115314.

[24] S.K. Rahimian, S. Rayman, R.E. White, Extension of physics-based single particle model for higher charge–discharge rates, Journal of Power Sources. 224 (2013) 180–194. doi:10.1016/j.jpowsour.2012.09.084.

[25] M. Doyle, J. Newman, Analysis of capacity–rate data for lithium batteries using simplified models of the discharge process, Journal of Applied Electrochemistry 27, 846–856 (1997). https://doi.org/10.1023/A:1018481030499

[26] S. Atlung, K. West, T. Jacobsen, Dynamic aspects of solid solution cathodes for electrochemical power sources, Journal of The Electrochemical Society 126, no. 8 (1979): 1311.

[27] V. R. Subramanian, R. E. White, New separation of variables method for composite electrodes with galvanostatic boundary conditions, Journal of power sources 96, no. 2 (2001): 385-395.

[28] B. Suthar and V. R. Subramanian, Lithium intercalation in core-shell materials–theoretical analysis, Journal of the Electrochemical Society 161, no. 5 (2014): A682

[29] S. H. Ali, A. Hussin, and A. Arof, Short-and long-time solutions for material balance equation in lithium-ion batteries by Laplace transform, Journal of power sources 112, no. 2 (2002): 435-442.

# Chapter 2

# Solution of the Phase Change Stefan Problem with Time-Dependent Heat Flux using Perturbation Method

**Published as**: Parhizi, M., & Jain, A. (2019). Solution of the Phase Change Stefan Problem With Time-Dependent Heat Flux Using Perturbation Method. *Journal of Heat Transfer, 141*(2).

## 2-1. Introduction

A fundamental understanding of heat transfer processes during phase change is critical for optimizing multiple engineering applications where melting and solidification occurs, such as metal casting, thermal management, process manufacturing, etc. [1, 2]. Heat transfer in an engineering system involving phase change requires the modeling of heat absorption or release at the phase change front, the location of which usually changes with time [3]. In general, such problems are non-linear in nature, although engineering approximations are often made in order to linearize and solve these problems [1-4]. The Stefan number, defined as $Ste = \frac{C_p(T_{ref}-T_m)}{L}$, which represents the ratio of sensible heat to latent heat, is a key non-dimensional parameter in such problems. The simplest phase change problem involves a one-dimensional, semi-infinite solid, initially at the melting temperature, $T_m$, being heated up or cooled down by a constant temperature, $T_0$ imposed at its end. This problem, often referred to as the Stefan problem has a standard solution, which shows that the location of the phase change front, $Y(\tau)$ is proportional to $\sqrt{\alpha\tau}$ where $\alpha$ is the thermal diffusivity [5]. Several variants of this problem have been addressed in past work, including a heat flux boundary condition [6-11], convective flow within the melted liquid [12,13], time-dependent temperature boundary condition [14-16], convective boundary condition [8], phase change over a temperature range [17], etc. Only the simplest of these phase change problems admits an exact solution – in most other cases, one must resort to approximate analytical methods that often result in series solutions.

A number of approximate solution methods are available for solving phase change problems [2, 18]. For example, the perturbation method has been used to solve the problem with a time-dependent boundary condition [14,15] as well as a problem with a constant heat flux boundary condition [8]. This method involves expressing the temperature distribution as a series solution involving powers of the Stefan number, and solving for each term individually. Solving for only the first few terms of the expansion provides a reasonably accurate solution, particularly for small values of *Ste*. Integral methods apply the heat balance integral to phase change problems, similar to the momentum integral in boundary layer theory [19], and have been used for solving phase change problems with time-dependent temperature boundary conditions. Quasi-stationary and quasi-steady methods have also been used [3]. These methods are particularly applicable if the solid-liquid interface location moves slowly and the transient term in the energy equation can be neglected. While much of the work in this direction addresses cases with temperature boundary condition, relatively lesser work exists on analysis of heat flux boundary condition. This problem has been solved for the specific cases of constant heat flux using the integral method [6] and by approximating the form of the temperature distribution [7]. A series solution has been derived for the specific case of a sinusoidal boundary condition [8]. Solution for the problem with time-dependent heat flux has been derived using a series solution [11] as well as expansion of the temperature distribution as a function of the error integral family [9]. A few highly mathematical treatments of such problems also exist, including proofs for existence and uniqueness of solutions for non-linear Stefan problems [20,21], although these results are difficult to apply for engineering problems.

This work presents a theoretical analysis of the problem of one-dimensional phase change involving a time-dependent heat flux boundary condition using a perturbation method. Time-dependent heat flux may be encountered when, for example, a heat-generating body such as a Li-ion cell undergoing high rate discharge is being cooled by a phase change material. In this case, heat flux entering the phase change material may change with time due to time-dependent heat generation and transient thermal conduction within the Li-ion cell [22]. In this work, this problem is solved by expanding the temperature distribution in a power series involving the Stefan number and solving for the first three terms of the power series. Comparison of the theoretical results with past papers is presented. For a specific case of constant heat flux, results from this work are shown to be close to results from past papers that utilized other methods. The present work is shown to be able to accurately predict the time evolution of the phase change front at large times while several past models are found to diverge. Results are found to be in good agreement with finite-element simulation results, while providing significant advantage in terms of computational time. The analytical method is used for analyzing the dependence of the solution on key thermal parameters. This technical note contributes towards an improved theoretical understanding of a heat transfer problem that is commonly encountered in multiple engineering applications.

## 2-2. Mathematical Modeling

Consider a one-dimensional, semi-infinite body initially at its phase change temperature $T_m$. Figure 1 shows this schematically for the specific case of solid-to-liquid phase change, although the reverse process of liquid-to-solid phase change can also be analyzed using the results derived in this section. Heat flux at the $X$=0 end is a known function of time, $q(\tau)$. Heat enters or leaves the body with time, resulting in phase change and propagation of the phase change front with time. A key quantity of interest in such a problem is the location of the solid-liquid interface as a function of time, $Y(\tau)$. In addition, temperature distribution within the newly formed phase, $T(X,\tau)$ is also of interest. Convection in the liquid phase is neglected.

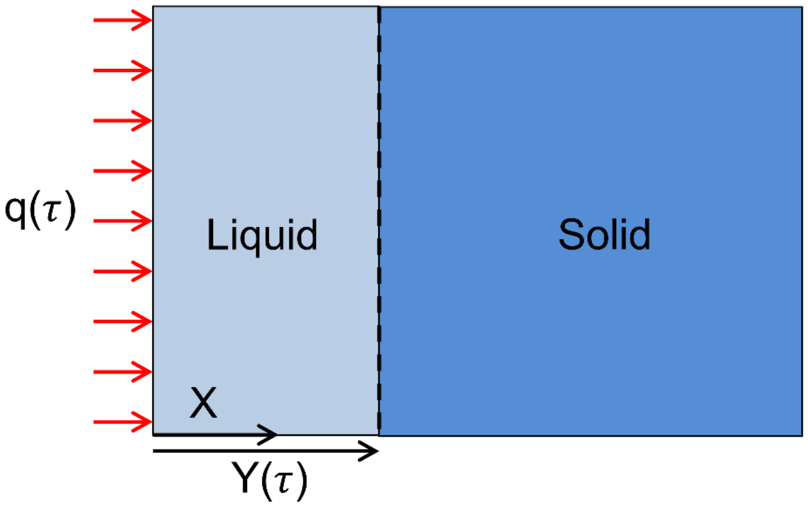

Figure 1. Schematic of the one-dimensional phase change problem with time-dependent heat flux. The schematic shows solid-to-liquid phase change, but the opposite process can also be analyzed in the same framework.

Following the non-dimensionalisation summarized in the Nomenclature section, the temperature field must satisfy the following governing energy conservation equation:

$$\frac{\partial^2 \theta}{\partial x^2} = \frac{\partial \theta}{\partial t} \tag{1}$$

where $x>0$ and $t>0$.

$\theta(x,t)$ is subject to the following boundary condition

$$-\frac{\partial \theta}{\partial x} = g(t) \qquad \text{at } x=0 \tag{2}$$

where $g(t)$ is the non-dimensional heat flux.

Temperature continuity and energy conservation at the solid-liquid interface requires that

$$\theta = 0 \qquad \text{at } x=y(t) \tag{3}$$

and

$$-Ste\left[\frac{\partial\theta}{\partial x}\right]_{x=y(t)}=\frac{dy}{dt} \qquad \text{at } x=y(t) \qquad (4)$$

In order to determine the unknown phase change front *y(t)* and the temperature distribution following phase change *θ(x,t)*, equation (1) is transformed in order to replace *t* with *y* as an independent variable. By doing so, equation (1) results in

$$\frac{\partial^2\theta}{\partial x^2}=-Ste\frac{\partial\theta}{\partial y}\left[\frac{\partial\theta}{\partial x}\right]_{x=y} \qquad (5)$$

The boundary condition at *x*=0 is re-written in terms of *y* as follows

$$-\frac{\partial\theta}{\partial x}=g(t)=G(y) \qquad \text{at } x=0 \qquad (6)$$

In order to solve this problem for time-varying heat flux *g(t)*, the temperature distribution *θ(x,y)* is written in the form of a series involving the first three powers of *Ste*, similar to past papers that utilized this approach for a time-dependent temperature boundary condition [14,15]

$$\theta(x,y)=\theta_0(x,y)+Ste\times\theta_1(x,y)+Ste^2\times\theta_2(x,y) \qquad (7)$$

By substituting equation (7) into (5), governing equations and associated boundary conditions for the temperature components $\theta_0(x,y)$, $\theta_1(x,y)$ and $\theta_2(x,y)$ can be derived. These ordinary differential equations can be easily solved to result in the following solution

$$\theta_0(x,y)=-G(y)(x-y) \qquad (8)$$

$$\theta_1(x,y)=G(y)\left[-G'(y)\left(\frac{x^3-y^3}{6}\right)+\left(G(y)+G'(y)y\right)\left(\frac{x^2-y^2}{2}\right)\right] \qquad (9)$$

$$\theta_2(x,y) = \frac{A}{20}\left(x^5 - y^5\right) + \frac{B}{12}\left(x^4 - y^4\right) + \frac{C}{6}\left(x^3 - y^3\right) + \frac{D}{2}\left(x^2 - y^2\right) \tag{10}$$

where

$$A = -\frac{1}{6}G(y)\left(G'^2(y) + G''(y)G(y)\right) \tag{11}$$

$$B = \frac{1}{2}G(y)\left(y\left(G'^2(y) + G''(y)G(y)\right) + 3G(y)G'(y)\right) \tag{12}$$

$$C = G(y)G'(y)\left[\, y\left(yG'(y) + G(y)\right) - G'(y)\frac{y^2}{2}\right] \tag{13}$$

$$D = \begin{bmatrix} -G(y)\left(yG'(y) + G(y)\right)\left(\, y\left(yG'(y) + G(y)\right) - G'(y)\dfrac{y^2}{2}\right) + \\ G(y)\left(-2G(y)G'(y)y^2 - yG^2(y) - \dfrac{1}{3}y^3\left(G'^2(y) + G''(y)G(y)\right)\right) \end{bmatrix} \tag{14}$$

Note that the forcing function *G(y)* is assumed to be appropriately differentiable.

The location of the phase change front, *y(t)* in equations (8)-(14) is unknown. In order to solve for *y(t)*, energy balance at the interface is utilized. Substituting equations (7)-(14) in equation (4) results in

$$\frac{dy}{dt} = -Ste\begin{bmatrix} -G(y) + Ste \times G(y)\left(\left(yG'(y) + G(y)\right)y - G'(y)\dfrac{y^2}{2}\right) + \\ Ste^2\left(\dfrac{A}{4}y^4 + \dfrac{B}{3}y^3 + \dfrac{C}{2}y^2 + Dy\right) \end{bmatrix} \tag{15}$$

Finally, as is the case in perturbation analysis [14,15], derivatives of G are neglected, the following non-linear ordinary differential equation is obtained for *y(t)*

$$y' + Ste^2 G^2(y) y - 2 Ste^3 G^3(y) y^2 = (Ste) G(y) \tag{16}$$

For cases with relatively simple expression for the heat flux, this equation can be directly solved. In general, a solution for *y(t)* can be derived by neglecting the $Ste^3$ term, which may be reasonable since *Ste*<<1. In such a case, the general solution for *y(t)* is found to be

$$y(t) = \left( \int Ste \times g(t^*) \exp\left( \int Ste^2 g^2(t^{**}) dt^{**} \right) dt^* + C \right) \left( \exp\left( - \int Ste^2 g^2(t^*) dt^* \right) \right) \tag{17}$$

Where *C* is a constant which is determined using the initial condition of *y(0)*=0. The temperature distribution *θ(x,y)* can be determined by substituting *y(t)* from equation (17) into equations (7) through (14).

This completes the derivation of solution of the problem with time-dependent heat flux using perturbation method. Due to approximations made during the derivation, this solution is valid only for small values of *Ste*, which is usually appropriate for materials of engineering interest due to the relatively large value of the enthalpy of phase change compared to heat capacity. Further, note that since the derivation above involves derivatives of the forcing function *G(y)*, the approach utilized here may not be appropriate in the case of a heat flux profile that is not appropriately differentiable.

Comparison of these results with past work, particularly for the specific case of constant heat flux is analyzed next.

## 2-3. Results and discussion

In order to compare with results from past work [9, 10, 19], it is instructive to examine the solution of equation (16) when the heat flux is constant, for which, solutions based on other methods are available. There are two distinct approaches for simplifying the general treatment in section 2 and deriving the solution for the phase change front when $g(t)=g_0$.

Firstly, for constant heat flux, equation (16) can be shown to have an exact solution, given by

$$y(t)=\frac{\sqrt{7}\tan\left(\frac{1}{2}\sqrt{7}\gamma^2 t-\tan^{-1}\left(\sqrt{7}\right)\right)+1}{4\gamma} \tag{18}$$

where

$$\gamma = Ste\times g_0 \tag{19}$$

Alternately, the integral in equation (17) can be computed for the case of constant heat flux to result in the following solution

$$y(t)=\gamma t-\frac{1}{2}\gamma^3 t^2+\frac{1}{6}\gamma^5 t^3-\frac{1}{24}\gamma^7 t^4+\frac{1}{120}\gamma^9 t^5-\frac{1}{720}\gamma^{11} t^6 \ldots \tag{20}$$

While equation (18) represents the general solution for the constant heat flux case, equation (20) is based on neglecting higher order terms in equation (16). Note that the solution in equation (18) is not valid for large *t* where the tan function may diverge which is the case for the past work as well. On the other hand, equation (20) does not have such a restriction and converges uniformly even at large times.

Equation (20) offers a good physical insight into the solution. The first term in equation (20) represents the rate of heat absorption at the phase change interface, and further terms represent the effect of thermal diffusivity in the newly formed phase. In many engineering cases, where latent heat dominates over sensible heat, heat absorption in the newly formed phase can be neglected, and only the first term of this equation may be sufficient.

It is instructive to compare the solutions derived here, equations (18) and (20) with results from past papers that have presented solutions for the constant heat flux case. Specifically, the solution for the phase change front has been derived by Tao [9], Goodman [19] and Carslaw & Jaegar [10] as follows

$$y(t) = \gamma t - \frac{1}{2}\gamma^3 t^2 + \frac{5}{6}\gamma^5 t^3 - \frac{17}{18}\gamma^7 t^4 + \frac{827}{120}\gamma^9 t^5 \ldots \qquad (21)\ [9]$$

$$y(t) = \gamma t - \frac{1}{2}\gamma^3 t^2 + \frac{5}{6}\gamma^5 t^3 - \frac{17}{18}\gamma^7 t^4 + \frac{795}{120}\gamma^9 t^5 \ldots \qquad (22)\ [19]$$

$$y(t) = \gamma t - \frac{1}{2}\gamma^3 t^2 + \frac{5}{6}\gamma^5 t^3 \ldots \qquad (23)\ [10]$$

While equation (21) was derived by Tao by expressing temperature in terms of polynomial functions of error integrals [9], equation (22) was derived by Goodman using the heat balance integral method [19]. Equation (23) was derived by Carslaw & Jaegar by writing *y(t)* as a power series [10].

It can be seen that the expression for the phase change front derived in this work for the specific case of constant heat flux by neglecting the $Ste^3$ term, equation (20) is close to results from several papers that solved the same problem using other techniques. The first two terms are identical, with a departure occurring in the third term. Figure 2(a) plots *y(t)* as a function of *t* derived in this work (equations (18) and (20)) and compares with past papers [9,10,19] as well as numerical computation based on finite element method (FEM) for a non-dimensional, constant heat flux $g_0$=5000. In this case, the enthalpy method is used in the finite-element simulations for solving for computing temperature distribution in the phase change material, which is defined as a binary mixture of liquid and solid. Results obtained from FEM simulation are validated separately against the analytical solution of the well-known Stefan problem with constant temperature boundary condition. Mesh independence is also ensured. Very good agreement with past papers is seen up to a non-dimensional time of around $2.5\times10^{-4}$. As time increases, solutions from past studies lose accuracy beyond around $t$=$2.5\times10^{-4}$, while the present result continues to agree well with finite element simulations. Figure 2(b) investigates this further by plotting the phase change front $Y(\tau)$ over a much larger time range, up to $\tau$=4000 for different values of thermal diffusivity. This plot is shown in dimensional form since plotting in non-dimensional form would not be appropriate as thermal diffusivity influences both $t$ and $y(t)$. It is clearly seen that previous models diverge and fail to accurately predict $Y(\tau)$ at large times, beyond around $\tau$=1500 s for $\alpha=1.10\times10^{-7}$ m$^2$/s. While the convergence of past models can be improved by including many more terms [3], derivation of further terms for these models is very cumbersome and impractical [3,9]. While equation (18) may also diverge at large times due to the presence of the tan function, equation (20) in the present work clearly converges even at large times, even with a few number of terms. Computation of terms further than those showed in equation (20) is also simpler than past work.

It has been shown [3] that the result from Tao [9], shown in equation (21) is valid only when the non-dimensional parameter $\beta = \frac{q^2}{\rho^2 \alpha L^2}\tau$ is less than 0.4. This explains why the solution by Tao [3], equation (21), diverges at large times. This also explains divergence at even smaller times when computed for larger value of $\alpha$, as shown in Figure 2(b). On the other hand, the present solution, equation (20) does not suffer from such divergence problems, and continues to predict the interface location even at large times. This represents a key advantage of the present model compared to past work.

Note that in Figure (2), the value of the reference length for non-dimensionalization is taken to be $b$=1 m. Further, the value of Stefan number is 0.008 based on $T_{ref}$-$T_m$=1 K and thermal properties of commercial paraffin wax.

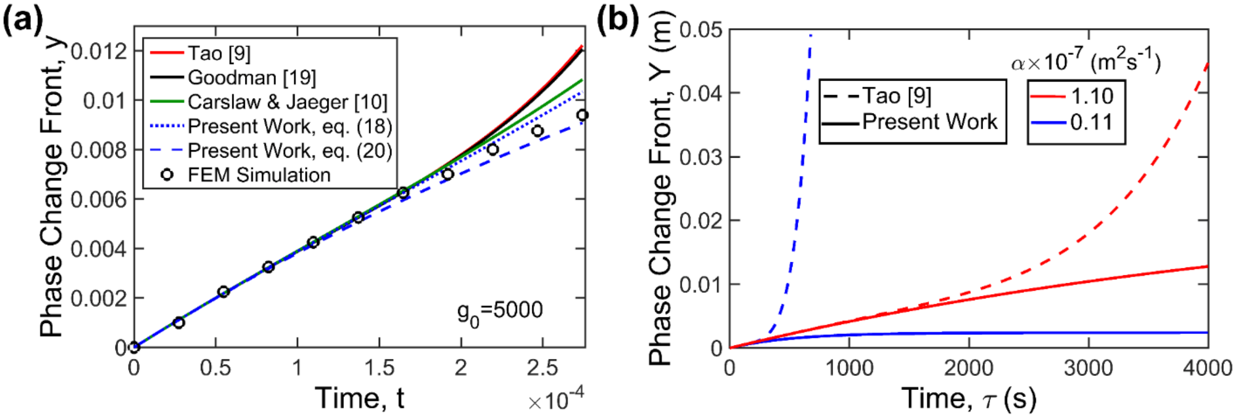

Figure 2. Comparison of the present analytical result with past results for the special case of constant heat flux: (a) Plot of non-dimensional phase change front location, y(t) as a function of non-dimensional time, t for the present work and three past results

For further validation of the theoretical results, the phase change front *y(t)* is plotted in Figure 3(a) as a function of time based on equation (17) assuming a linear heat flux profile $g(t) = A + Bt$. While the value of *A* is held constant at 5000, a number of cases with different values of *B* are considered in order to investigate the effect of the slope of *g(t)*. The values of *b* and *Ste* are the same as in Figure 2. Results from FEM computations are also plotted in Figure 3(a) for comparison. Further, Figure 3(b) plots the temperature distribution in the newly formed phase at different times for a specific input heat flux, with $A=5000$ and $B=-4.56\times 10^{7}$. Figure 3(a) shows very good agreement between the analytical solution and FEM-based computations for each heat flux considered. As the value of *B* increases, the nature of *y(t)* curves changes from concave to convex, which is along expected lines, since an increase in the value of *B* results in more heat flux into the medium, and therefore, a greater rate of propagation of the phase change front. There is also very good agreement in the temperature distribution at multiple times, as shown in Figure 3(b). Note that the analytical solution is significantly faster than finite element simulation since the solution is obtained as a closed form equation, and does not require time-intensive discretization and solution of a large system of equations.

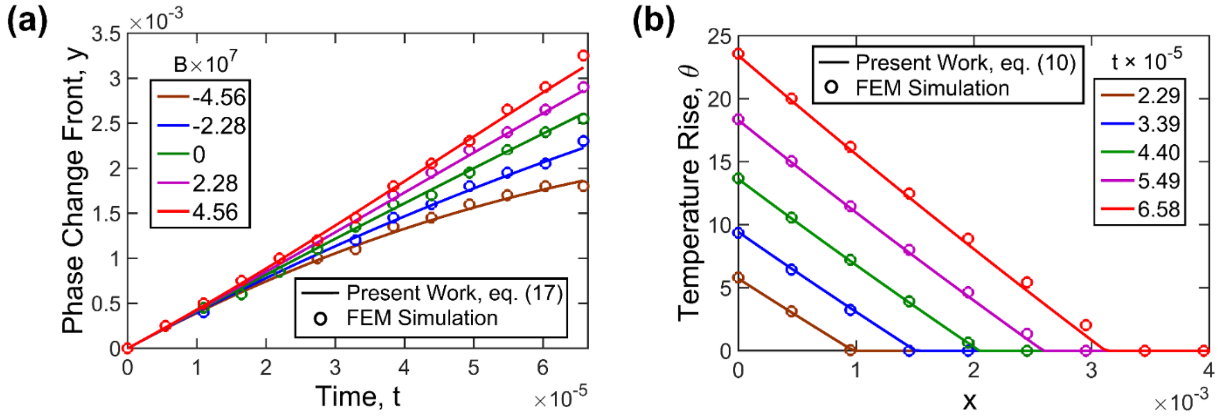

Figure 3. Validation of the present work with finite element simulation for linear, time-varying heat flux: (a) Phase change front $y(t)$ as a function of t for linear heat flux $g(t) = A + Bt$. The value of $A$ is taken to be 5000 and values of $B$ are shown in the legend. (b) Temperature distribution as a function of $x$ for the specific case of $B$=4.56×$10^7$. Both plots show very good agreement between the analytical model and finite element simulation.

Periodic heat flux boundary conditions are of interest in a variety of applications. Figure 4(a) presents computed profiles of the solid-liquid interface as a function of time for periodic heat flux, $g(t) = A(1 + Cos(\varepsilon t))$, where $\varepsilon = \frac{\omega b^2}{\alpha}$ is the non-dimensional frequency. The values of $b$ and *Ste* are the same as in Figure 2, and $A$=5000. Figure 4(a) shows that the theoretical model presented in this work is able to capture the time evolution of the phase change front for different frequencies. The number of oscillations within the time period considered decreases as frequency decreases, as expected.

It is of interest to examine the dependence of the solution on the value of thermal diffusivity, which is a key thermophysical property that governs phase change propagation. Figure 4(b) plots phase change front as a function of time for multiple values of thermal diffusivity $\alpha$. Figure 4(b) considers up to ±50% variation in thermal diffusivity from the baseline value of $1.1\times10^{-7}$ $m^2/s$, which is the typical value of thermal diffusivity of paraffin wax used for multiple phase change heat transfer applications. This plot indicates that an increase in thermal diffusivity results in a slight increase in *y(t)*. This happens because of more rapid heat transfer through the newly formed phase at a higher value of thermal diffusivity, and vice versa. Unlike the case of constant temperature boundary condition, where the phase change front location is known to be proportional to $\sqrt{\alpha\tau}$ [3,4], a similar explicit relationship is not available for heat flux boundary conditions.

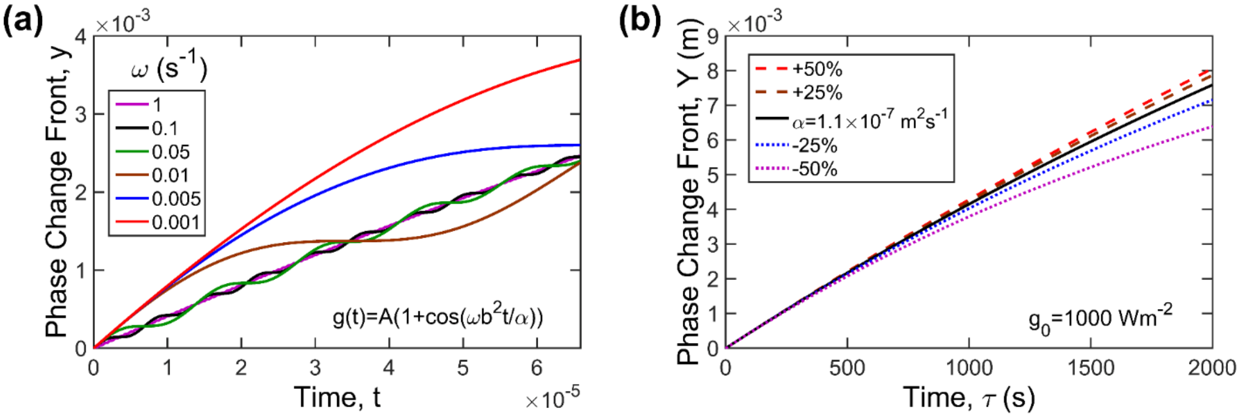

Figure 4. (a) Plot of phase change front $y(t)$ as a function of time for periodic heat flux $g(t) = A(1 + cos(\varepsilon t))$ for multiple values of the non-dimensional frequency, $\varepsilon$. (b) Plot of the variation in phase change front propagation for different values of thermal diffusivity for constant heat flux case.

Time-varying heat flux in a phase change problem can be encountered in applications where a phase change material cools down a heat-generating body in which the heat generation itself is a function of time. For example, phase change cooling of Li-ion cells has been of much recent research attention [22, 23]. Since heat generation in Li-ion cells changes with time as the electrical load changes [24], therefore, heat flux into the phase change material is also likely to change with time. For such applications, the present model offers a theoretical framework for thermal analysis and optimization. While the perturbation method used here does not apply for very short times, such information is usually not important for engineering analysis.

Extension of the treatment discussed here to problems in cylindrical and spherical coordinate systems, which may also have practical applications, is reasonably straightforward, following the same approach as equations (7)-(17) to account for the time-dependent heat flux.

## 2-4. Conclusions

This work presents a solution for the phase change heat transfer problem with time-dependent heat flux boundary condition using the perturbation method. The solution is shown to converge at large times, where solutions from past papers are known to diverge. This represents a significant improvement in our theoretical understanding of phase change heat transfer. The theoretical results presented here may be relevant to multiple engineering applications such as cooling of Li-ion cells. Results derived here are used to understand the effect of linear and periodic heat flux boundary conditions, which may arise in such applications. These results can be easily extended to cylindrical and spherical coordinate systems.

## 2-5. Nomenclature

| | |
|---|---|
| $b$ | reference length scale (m) |
| $C_p$ | specific heat capacity (J/kgK) |
| $L$ | latent heat of fusion (J/kg) |
| $g$ | non-dimensional heat flux, $g=qb/k(T_{ref}-T_m)$ |
| $k$ | thermal conductivity (W/mK) |
| $q$ | heat flux (W/m$^2$) |
| $Ste$ | Stefan number, $Ste=Cp(T_{ref}-T_m)/L$ |
| $t$ | non-dimensional time, $t= \alpha\tau/b^2$ |
| $T$ | temperature (K) |
| $T_m$ | phase change temperature (K) |
| $T_{ref}$ | reference temperature (K) |
| $x$ | non-dimensional lengthscale, $x=X/b$ |
| $y$ | non-dimensional location of phase change front, $y=Y/b$ |
| $X$ | lengthscale (m) |
| $Y$ | location of phase change front (m) |
| $\theta$ | non-dimensional temperature, $\theta=(T-T_m)/(T_{ref}-T_m)$ |
| $\alpha$ | thermal diffusivity (m$^2$/s) |
| $\varepsilon$ | non-dimensional frequency, $\varepsilon= \omega b^2/\alpha$ |
| $\omega$ | frequency (1/s) |
| $\tau$ | time (s) |

## 2-6. References

[1] Viskanta, R., 1988, “Heat Transfer During Melting and Solidification of Metals,” ASME J. Heat Transfer, 110(4b), p. 1205.

[2] Fukusako, S., and Seki, N., 1987, “Fundamental Aspects of Analytical and Numerical Methods on Freezing and Melting Heat-Transfer Problems,” Annual Review of Heat Transfer, 1(1), pp. 351–402.

[3] Cheng, K.C. and Seki, N. eds., 1991. “Freezing and Melting Heat Transfer in Engineering: Selected Topics on Ice-Water Systems and Welding and Casting Processes,” CRC Press.

[4] Stefan, J., 1891, “Uber die Theorie des Eisbildung, Insbesonder uber die Eisbildung im Polarmere,” Ann. Phys. u Chem., Neue Folge, Bd. 42, Ht, 2, pp. 269-286.

[5] Hahn, D. W., and Özişik, M. N., 2012, “Heat Conduction.” Third ed., John Wiley & Sons, Hoboken, New Jersey.

[6] Ruehr, O. G., 2002, “Analytical-Numerical Treatment of the One-Phase Stefan Problem with Constant Applied Heat Flux,” Integral Methods in Science and Engineering, pp. 215–220.

[7] Cho, S. H., and Sunderland, J. E., 1981, “Approximate Temperature Distribution for Phase Change of a Semi-Infinite Body,” Journal of Heat Transfer, 103(2), pp. 401.

[8] Gutman, L. N., 1986, “On the Problem of Heat Transfer in Phase-Change Materials for Small Stefan Numbers,” International Journal of Heat and Mass Transfer, 29(6), pp. 921–926.

[9] Tao, L. N., 1979, “On Free Boundary Problems with Arbitrary Initial and Flux Conditions,” Zeitschrift für angewandte Mathematik und Physik ZAMP, 30(3), pp. 416–426.

[10] Carslaw, H. S. and Jaeger, J. C., 1986, “Conduction of Heat in Solids,” Oxford Science Publications, ISBN: 978-0198533689.

[11] Evans, G.W., Isaacson, E. and MacDonald, J.K.L., 1950. Stefan-Like Problems. Quarterly of Applied Mathematics, 8(3), pp.312-319.

[12] Szekely, J., and Stanek, V., 1970, “Natural Convection Transients and Their Effects on Unconditional Solidification,” Metallurgical Transactions, 1(1), pp. 2243–2251.

[13] Cole, G. S., and Winegard, W. C., 1962, “Thermal Convection Ahead of a Solid-Liquid Interface,” Canadian Metallurgical Quarterly, 1(1), pp. 29–31.

[14] Lock, G., Gunderson, J., Quon, D., and Donnelly, J., 1969, “A Study of One-Dimensional Ice Formation with Particular Reference to Periodic Growth and Decay,” International Journal of Heat and Mass Transfer, 12(11), pp. 1343–1352.

[15] Caldwell, J., and Kwan, Y., 2003, “On the Perturbation Method for the Stefan Problem with Time-Dependent Boundary Conditions,” International Journal of Heat and Mass Transfer, 46(8), pp. 1497–1501.

[16] Tao, L. N., 1978, “The Stefan Problem with Arbitrary Initial and Boundary Conditions,” Quarterly of Applied Mathematics, 36(3), pp. 223–233.

[17] Tien, R. T., 1965, “Freezing of Semi-Infinite Slab with Time Dependent Surface Temperature — an Extension of Neumann′s Solution,” Transf. AIME, 233, 1887–1891.

[18] Mori, A., and Araki, K., 1976, “Methods for Analysis of the Moving Boundary-Surface Problem,” Journal of Mathematical Analysis and Applications, 16(2), pp. 734–744.

[19] Goodman, T. R., 1958, “The Heat Balance Integral and its Application to Problems Involving Change of Phase,” Journal of Mathematical Analysis and Applications, 80(2), pp. 335–342.

[20] Cannon, J., and Primicerio, M., 1971, “Remarks on the One-Phase Stefan Problem for the Heat Equation with the Flux Prescribed on the Fixed Boundary,” Journal of Mathematical Analysis and Applications, 35(2), pp. 361–373.

[21] Kyner, W., 1959, “An Existence and Uniqueness Theorem for a Nonlinear Stefan Problem,” Indiana University Mathematics Journal, 8(4), pp. 483–498.

[22] Shah, K., Vishwakarma, V., and Jain, A., 2016, “Measurement of Multiscale Thermal Transport Phenomena in Li-Ion Cells: A Review,” Journal of Electrochemical Energy Conversion and Storage, 13(3), p. 030801.

[23] Ling, Z., Zhang, Z., Shi, G., Fang, X., Wang, L., Gao, X., Fang, Y., Xu, T., Wang, S., and Liu, X., 2014, “Review on Thermal Management Systems Using Phase Change Materials for Electronic Components, Li-ion Batteries and Photovoltaic Modules,” Renewable and Sustainable Energy Reviews, 31, pp. 427–438.

[24] Anthony, D., Wong, D., Wetz, D., and Jain, A., 2017, “Non-Invasive Measurement of Internal Temperature of a Cylindrical Li-Ion Cell During High-Rate Discharge,” International Journal of Heat and Mass Transfer, 111, pp. 223–231.

# Chapter 3

# The Impact of Thermal Properties on Performance of Phase Change Based Energy Storage Systems

**Published as**: Parhizi, M., & Jain, A. (2019). The impact of thermal properties on performance of phase change based energy storage systems. *Applied Thermal Engineering*, *162*, 114154.

## 3-1. Introduction

Solid-liquid phase change occurs in a number of engineering applications such as thermal management, energy storage, etc. The large latent heat of phase change relative to the magnitude of typical sensible heat is utilized commonly for designing effective thermal management [1] or energy storage techniques [2]. In both cases, energy is absorbed from a source of heat into a phase change material (PCM) that undergoes phase change from solid to liquid. As an example, latent heat storage has been widely investigated for storing energy harnessed from renewable sources [3], and forms a critical part of the infrastructure needed to address the intermittent nature of these sources and ultimately make renewable energy feasible. Compared to other competing mechanisms for energy storage, such as sensible heat [4], thermochemical [5], electrochemical [6], etc., phase change energy storage offers several advantages such as large rates of energy transfer, large energy storage density, etc. [3].

As the phase change process proceeds, thermal impedance offered by the melted liquid slows down the rate of further melting. This self-limiting nature of phase change energy storage has been recognized to be an important limitation of phase change based energy storage [7], and the energy storage system is often designed to counter these effects, for example by providing fins into the PCM to increase surface area [8,], or by enhancing PCM thermal conductivity by introducing nano/micro-particles [9].

Typical PCMs can be divided into two categories – organic PCMs which are usually paraffin based and inorganic PCMs such as salt hydrates that offer large latent heat [10]. Clearly, thermophysical properties such as thermal conductivity ($k$), heat capacity ($C_p$) and latent heat ($L$) of the PCM play a key role in determining the performance of phase change energy storage. While

PCMs are typically chosen for their large values of latent heat, these materials also have low thermal conductivity, in the range of 0.1-2.5 W/mK [11]. Significant research has been reported on enhancing thermal conductivity of PCMs. A variety of techniques such as dispersing particles with high thermal conductivity such as graphite and nickel particles [12], adding carbon fibers [13], using expanded graphite and carbon fibers [14], adding high thermal conductivity promoters [7] and using graphite matrix [15] have been used for PCM thermal conductivity enhancement. Graphite matrix insertion has been shown to increase PCM thermal conductivity to up to 17 $Wm^{-1}K^{-1}$ [16]. Multiple microscale mechanisms have been proposed to explain such enhancement, including Brownian motion which enables the particles to move through the fluid, nano-particles clustering and liquid layering around solid particles [17].

The average rate of energy transferred and stored into the PCM over a certain time period is an important performance parameter for both thermal management and energy storage applications. Further, from a systems perspective, the density of energy stored is also an important parameter in order to ensure compactness of energy storage. High energy storage density can be a critical performance parameter when the space available for energy storage is limited and minimizing system weight is important. These considerations often arise in automotive, aerospace and military applications as well as compact consumer electronic devices. While the total energy stored is determined largely by the integral of heat flux at the PCM-source interface over time, the energy storage density additionally involves the volume of PCM melted over the time period.

While most experimental papers have focused on improving thermal conductivity, which clearly improves the rate of heat transfer from the source into the PCM, one must recognize that an increased thermal conductivity also increases the rate of melting. This is expected to increase the total volume of PCM required, and therefore, may negatively impact energy storage density. Unlike extensive experimental work, a key gap in the literature pertains to the modeling and analysis of such effects. There is a lack in the literature of analytical models that connect these two key performance parameters – total energy stored and energy storage density – with underlying thermal properties of the PCM. Further, such an analytical model may also play a key role in materials selection. For example, given two candidate phase change materials that differ from each other in the values of both $k$ and $C_p$, an analytical model may help determine which material is expected to have better performance in terms of total energy stored and energy storage density. In some cases, either one of total energy stored and energy storage density may be more critical than the other, and therefore, the choice of the ideal PCM depends on system-level considerations, which is not possible to account for using analytical models available in the literature.

The simplest model for phase change based energy storage is the case of heat transfer from a constant temperature wall into a PCM. This is indeed the well-known Stefan problem [18,19], for which progression of the melting front is known to be proportional to $\sqrt{\alpha t}$ where $\alpha$ is the thermal diffusivity of the PCM. For this problem, equations are also available for temperature distribution in the melted material, and therefore, the rate of heat transfer into the PCM [18]. However, similar models are lacking for more complicated cases, such as in cylindrical coordinates, or for a heat-generating source surrounded by a PCM, for which, analysis using a time-dependent temperature boundary condition is more realistic than a constant temperature one. These limitations in the literature have made it difficult to optimize phase change based energy storage in practical engineering applications that cannot be reasonably modeled by the simplest, constant-temperature Stefan problem, or that are cylindrical or spherical in nature. Phase change heat transfer problems are, in general, non-linear in nature, making such theoretical analysis challenging.

This work presents analytical modeling of performance parameters for phase change energy storage in a variety of scenarios. The key novelty of this work is that the models presented here help understand the impact of thermal properties such as thermal conductivity and heat capacity on the rate of energy storage and energy storage density, which is largely missing in the past literature. Simplified cases such as heat transfer from a constant temperature wall in Cartesian, cylindrical systems are analyzed first. Perturbation method is used to derive expressions for the average rate of energy storage and energy storage density for cases where an analytical solution is not readily available. Theoretical models are extended to account for more realistic scenarios involving time-dependent temperature boundary conditions, which can represent a heat source with internal heat generation next to the PCM. Results indicate that while the rate of energy storage increases with increasing PCM thermal conductivity in a Cartesian phase change system, the energy storage density remains unchanged. Further, in cylindrical system, an increase in thermal conductivity may actually result in a reduction in energy storage density. By developing a theoretical understanding of the effect of PCM thermal properties on the performance of energy storage, this work addresses a key gap in literature. Results derived here help place ongoing experimental research on thermal conductivity enhancement in perspective, and contribute towards the optimization of practical energy storage systems.

## 3-2. Theoretical Model

This section derives expressions for the two key performance parameters of phase change energy storage – average rate of energy storage and energy storage density – in Cartesian and cylindrical coordinate systems. Section 2.1 analyzes a simplified model that assumes constant wall temperature, whereas Section 2.2 analyzes cases of internal heat generation in the heat source, modeled by an unsteady temperature boundary condition.

### 3-2-1. Energy storage from a constant temperature wall

The thermal interaction between the heat source and PCM can, in the most simplified form, be described as heat transfer from a constant temperature wall. The phase change energy storage system could be designed either in Cartesian or cylindrical geometries. In this sub-section, expressions for average rate of energy stored and energy storage density are derived for this simplified case.

#### 3-2-1-1. Cartesian wall

Figure 1(a) shows a schematic of a Cartesian, one-dimensional phase change energy storage system, where a PCM, initially at its melting temperature $T_m$ absorbs heat from an infinite wall maintained at a constant temperature $T_w$.

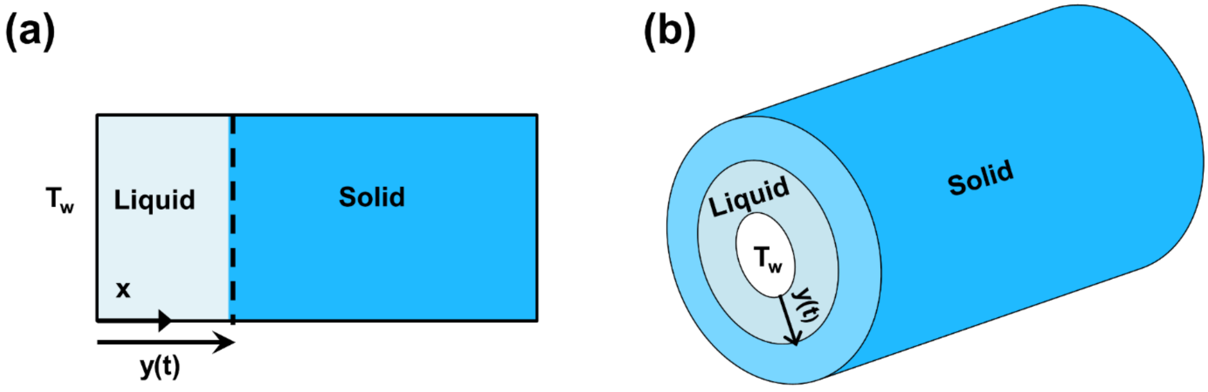

Figure 1. Schematic of the (a) Cartesian and (b) cylindrical phase change problems consider here.

Assuming no fluid flow in the newly formed phase due to forced or natural convection, this is the classical Stefan problem, for which well-known solutions are available [18,19]. The phase change front *y(t)* is given by

$$y(t) = 2\lambda\sqrt{\alpha t} \tag{1}$$

where $\alpha$ is the thermal diffusivity and $\lambda$ is the root of the transcendental equation

$$\lambda erf\ (\lambda)e^{\lambda^2} = \frac{C_p(T_w - T_m)}{L\sqrt{\pi}} \tag{2}$$

Temperature distribution in the newly formed liquid phase is given by [18]

$$T(x,t) = (T_m - T_w)\frac{erf\left(\frac{x}{2\sqrt{\alpha t}}\right)}{\mathrm{erf}(\lambda)} + T_w \tag{3}$$

from where, the average rate of energy absorbed by the PCM up to a given time *t* can be found to be

$$\dot{Q}_{avg}(t) = \frac{1}{t}\int_0^t -kA\left(\frac{\partial T}{\partial x}\right)_{x=0} d\tau = \frac{-2kA(T_m - T_w)}{\sqrt{\pi\alpha}erf(\lambda)\sqrt{t}} \tag{4}$$

Finally, the energy storage density can be found by dividing the total energy absorbed by the volume of PCM melted.

$$Q'''(t) = \frac{\dot{Q}_{avg}(t) \times t}{y(t) \times A} = \rho L e^{\lambda^2} \tag{5}$$

Both $\dot{Q}_{avg}(t)$ and $y(t)$ have the same square root dependence on $k$, which, therefore, cancels out in the expression of the energy storage density. The final expression of the energy storage density is only a function of density, latent heat and specific heat capacity through $\lambda$. It is assumed in the analysis above that the PCM size is not fixed, but rather can be chosen in advance, based on the knowledge of how much PCM is expected to melt in a given time duration. As a result, the use of $y(t)$ – which is a function of thermal properties – in calculating the volume of PCM melted is appropriate.

Note that in most practical phase change problems, the extent of natural convection is not strong enough to produce significant convective heat transfer due to the relatively small temperature difference and consequently small value of the Rayleigh number. This, together with the considerable complications in the coupled analysis of heat transfer and natural convection justifies neglecting natural convection in the present work.

#### 3-2-1-2. Cylindrical wall

Consider an infinite bed of PCM absorbing heat from the outer surface of a cylinder of radius $R$ maintained at temperature $T_w$, as shown in Figure 1(b). Similar to section 2.1.1, the PCM is initially at its melting temperature $T_m$. Unlike the Cartesian Stefan problem discussed in section 2.1.1, this problem in the cylindrical coordinate system does not have an exact solution. A technique based on perturbation method has been presented for solving this problem, based on an assumption of a small Stefan number [20,21].

The governing energy equation in cylindrical coordinate system is given by

$$\frac{1}{r}\frac{\partial}{\partial}\left(r\frac{\partial T}{\partial r}\right)=\frac{1}{\alpha}\frac{\partial T}{\partial t} \tag{6}$$

and the boundary conditions are

$$T=T_w \qquad \text{at } r=R \tag{7}$$

$$T=T_m \qquad \text{at } r=y(t) \tag{8}$$

$$-k\left(\frac{\partial T}{\partial r}\right)_{r=y(t)}=\rho L\frac{dy}{\partial t} \qquad \text{at } r=y(t) \tag{9}$$

Based on perturbation technique discussed in past papers [20,21], *t* is replaced by phase change front, *y(t)* in the governing equation and boundary conditions. Temperature distribution is expressed in the form of a series involving powers of the Stefan number, $Ste=\frac{C_p(T_w-T_m)}{L}$. By substituting temperature distribution back in the governing equation and using boundary conditions, similar to the treatment in [20], the phase change front, *y(t)* is found using an inverse function

$$\begin{aligned} t = \frac{R^2}{\alpha} \Bigg[ & \frac{(2(\bar{y}(t))^2 \log \bar{y}(t) + 1)}{4} + \frac{Ste}{4 \log \bar{y}(t)} ((\bar{y}(t))^2 \log \bar{y}(t) + \log \bar{y}(t) - (\bar{y}(t))^2 + 1) \\ & + \frac{Ste^2}{128(\bar{y}(t))^2 \log \bar{y}(t)} \Big( \bar{y}^4 (8 (\log \bar{y}(t))^3 - 20 (\log \bar{y}(t))^2 + 21 \log \bar{y}(t) \\ & - 8) - 16\big(\bar{y}(t)\big)^2 (\log \bar{y}(t) - 1) - 5 \log \bar{y}(t) - 8 \Big) \Bigg] \end{aligned} \tag{10}$$

where $\bar{y} = \frac{y}{R}$ . Note that equation (10) corrects a minor error in the final result of similar treatment presented in [20]. Temperature distribution in the newly formed liquid is given by

$$T(r,t) = (\theta_0 + Ste \cdot \theta_1 + Ste^2 \cdot \theta_2)(T_w - T_m) + T_m \tag{11}$$

where

$$\theta_0 = 1 - \frac{\log \bar{r}}{\log \bar{y}(t)} \tag{12}$$

$$\theta_1 = \frac{(\bar{r}^2 \log \bar{r} - (\bar{y}(t))^2 \log \bar{r} - \bar{r}^2 + 1)}{4(\bar{y}(t))^2 (\log \bar{y}(t))^3} + \frac{\log \bar{r}((\bar{y}(t))^2 - 1)}{4(\bar{y}(t))^2 (\log \bar{y}(t))^4} \tag{13}$$

$$
\begin{aligned}
\theta_2 = {} & \frac{1}{64(\bar{y}(t))^4(\log \bar{y}(t))^4}\,(8\bar{r}^2(\bar{y}(t))^2 \\
& - 2\bar{r}^4 \log \bar{r} + 10(\bar{y}(t))^4 \log \bar{r} - 8\bar{r}^2 + 3\bar{r}^4 - 8(\bar{y}(t))^2 - 8\bar{r}^2(\bar{y}(t))^2 \log \bar{r} + 5) \\
& + \frac{1}{128(\bar{y}(t))^4(\log \bar{y}(t))^5}\,(16\bar{r}^2 \log \bar{r} - 40\bar{r}^2(\bar{y}(t))^2 \\
& - 10 \log \bar{r} - 6\bar{r}^4 \log \bar{r} + 16\bar{r}^2 \log \bar{r} \\
& - 56(\bar{y}(t))^4 \log \bar{r} - 40\bar{r}^2 + 9\bar{r}^4 + 40(\bar{y}(t))^2 + 40\bar{r}^2(\bar{y}(t))^2 \log \bar{r} + 31) \\
& + \frac{1}{128(\bar{y}(t))^4(\log \bar{y}(t))^6}\big(((\bar{y}(t))^2 - 1)(31 \log \bar{r}) \\
& - 40\bar{r}^2 \log \bar{r} + 71(\bar{y}(t))^2 \log \bar{r} + 40\bar{r}^2 - 40\big) - \frac{(5 \log \bar{r}((\bar{y}(t))^2 - 1)^2)}{16(\bar{y}(t))^4(\log \bar{y}(t))^7}
\end{aligned}
\tag{14}
$$

where $\bar{r} = \frac{r}{R}$ . As a result, the average rate of energy absorbed by the PCM up to a specific time *t* can be determined as follows

$$
\begin{aligned}
\dot{Q}_{avg}(t) = {} & \frac{1}{t}\int_0^t -k(2\pi Rh)\left(\frac{\partial T}{\partial x}\right)_{r=R} d\tau \\
& = \frac{1}{t}\int_0^t \Bigg[ -k(2\pi Rh)(T_w \\
& - T_m)\Bigg(\Bigg(\frac{(10(\bar{y}(t))^4 + 8(\bar{y}(t))^2 - 6)}{64(\bar{y}(t))^4(\log \bar{y}(t))^4} - \frac{(5(\bar{y}(t))^2 - 1)^2}{16(\bar{y}(t))^4(\log \bar{y}(t))^7} \\
& - \frac{(56(\bar{y}(t))^4 + 24(\bar{y}(t))^2 + 44)}{128\bar{y}^4(\log \bar{y}(t))^5} + \frac{((\bar{y}(t))^2 - 1)(71(\bar{y}(t))^2 + 71)}{128(\bar{y}(t))^4(\log \bar{y}(t))^6}\Bigg) Ste^2 \\
& + \left(\frac{((\bar{y}(t))^2 - 1)}{4(\bar{y}(t))^2(\log \bar{y}(t))^4} - \frac{((\bar{y}(t))^2 + 1)}{4(\bar{y}(t))^2(\log \bar{y}(t))^3}\right) Ste - \frac{1}{\log \bar{y}(t)}\Bigg)\frac{1}{R}\Bigg] d\tau
\end{aligned}
\tag{15}
$$

Therefore, the energy storage density can be found by dividing total energy stored in PCM from equation (15) by the volume of the melted PCM.

$$Q'''(t) = \frac{\dot{Q}_{avg}(t) \times t}{\pi((y(t))^2 - R^2)h} \tag{16}$$

For any given time *t*, the phase change front *y(t)* may be obtained from equation (10), following which, equation (16) provides the energy storage density.

Note that, in the cylindrical coordinate system, the volume of PCM melted appearing in the denominator of equation (16) is a function of $y^2$ and not *y,* as was the case in the Cartesian coordinate system. This, along with the complicated expression for $Q_{total}(t)$ indicates that the lack of dependence of $Q'''$ on *k* seen for the Cartesian system may not exist for the cylindrical phase change process.

### 3-2-2. Energy storage from a heat-generating source: time-dependent temperature boundary condition

The constant wall temperature boundary condition analyzed in section 2.1, while easily amenable to theoretical analysis, simplifies the heat generation process in the source that makes energy available for the phase change material to absorb. For example, internal heat generation in the source may occur due to a chemical reaction, or due to volumetric heat absorption from an external source of radiation. Modeling the heat transfer process within the source makes this a considerably more complicated, coupled heat transfer problem. In order to analyze this system without making it mathematically intractable, the effect of the heat-generating source is modeled with a time-dependent temperature boundary condition at the source-PCM interface. This is a reasonable assumption since the interface temperature is expected to rise with time due to heat generation and thermal conduction within the source. This model is considered in this section for the Cartesian and cylindrical coordinate systems.

### 3-2-2-1. Cartesian heat source

This problem is similar to the one analyzed in section 2.1.1 and shown schematically in Figure 1(a), where wall temperature is now time-dependent, $T_w(t)$. In this case, the heat transfer problem in the PCM is a Stefan problem with time-dependent temperature boundary condition, for which, a perturbation method based approach is used [20]. Given a time-dependent temperature distribution $T_w(t)$, the heat absorbed as a function of time is given by

$$\begin{aligned}
\dot{Q}_{avg}(t) &= \frac{1}{t}\int_0^t -kA\left(\frac{\partial T}{\partial x}\right)_{x=0} d\tau \qquad (17)\\
&= \frac{1}{t}\int_0^\tau -kA\left(T_m - T_{ref}\right)\Bigg(-\frac{f(t)}{y(t)} - Ste\,\frac{f(t)\left(f(t) + 2\frac{f'(t)}{y'(t)}y(t)\right)}{6y(t)}\\
&\quad + \frac{(Ste)^2}{360y(t)}\Bigg(f(t)\Bigg(40\left(\frac{f'(t)}{y'(t)}\right)^2(\bar{y}(t))^2 + 85f(t)\frac{f'(t)}{y'(t)}y(t)\\
&\quad + 19f^2(t) + 8\frac{f''(t)}{(\bar{y}(t))^2}f(t)y^2(t)\Bigg)\Bigg)\Bigg) d\tau
\end{aligned}$$

where

$$f(t) = \frac{T_w(t) - T_m}{T_m - T_{ref}} \tag{18}$$

whereas the phase change propagation front is given by

$$y(t) = \left[2(Ste)\alpha \int_0^t f(\tau)\left(1 - \frac{Ste}{3} f(\tau) + \frac{7Ste^2}{45} f(\tau)^2\right) d\tau\right]^{\frac{1}{2}} \tag{19}$$

Note that expressions for *y(t)* and *T(x,t)* are taken from [20]. Further, since the wall temperature is not constant any more, the Stefan number cannot be defined using the wall temperature. Instead, $Ste = \frac{C_p(T_{ref} - T_m)}{L}$, where $T_{ref}$ is a reference temperature. Using equations (17) and (19), the energy storage density is given by

$$Q'''(t) = \frac{\dot{Q}_{avg}(t) \times t}{y(t) \times A} \tag{20}$$

#### 3-2-2-2. Cylindrical heat source

Figure 2(b) shows a schematic of a phase change energy storage system in cylindrical coordinate system, in which the wall temperature is now considered to be a function of time $T_w(t)$. Similar to the Cartesian problem, perturbation method is used to solve this time-dependent boundary condition problem. Following the substitution of *t* with *y(t)* in the governing equations and separation of terms based on the power of *Ste*, temperature distribution in the PCM is given by

$$T(r,t) = (\theta_0 + Ste \cdot \theta_1 + Ste^2 \cdot \theta_2)(T_w - T_m) - T_m \tag{21}$$

where

$$\theta_0 = -f(t)\left(\frac{\log \bar{r} - \log \bar{y}(t)}{\log \bar{y}(t)}\right) \tag{22}$$

$$\begin{aligned}
\theta_1 = \left(\frac{-f(t)}{4(\bar{y}(t))^2(\log \bar{y}(t))^4}\right)\Bigg( & f(t)\log \bar{r} \\
& - f(t)\log \bar{y}(t) + \frac{f'(t)\bar{y}(t)(\log \bar{y}(t))^2}{\bar{y}'(t)} + \frac{f'(t)\bar{y}(t)(\log \bar{y}(t))^3}{\bar{y}'(t)} \\
& + \bar{r}^2 f(t)\log \bar{y}(t) - \big(\bar{y}(t)\big)^2 f(t)\log \bar{r} - \frac{f'(t)\bar{y}(t)\bar{r}^2(\log \bar{y}(t))^2}{\bar{y}'(t)} \\
& - \frac{f'(t)\bar{y}(t)\bar{r}^2(\log \bar{y}(t))^3}{\bar{y}'(t)} - \frac{f'(t)\bar{y}(t)\log \bar{r}\,(\log \bar{y}(t))^2}{\bar{y}'(t)} \\
& + \frac{f'(t)\big(\bar{y}(t)\big)^3 \log \bar{r}\log \bar{y}(t)}{\bar{y}'(t)} - f(t)\bar{r}^2\log \bar{r}\log \bar{y}(t) \\
& + f(t)\bar{y}^2\log \bar{r}\log \bar{y}(t) - \frac{f'(t)\bar{y}(t)\log \bar{r}\log \bar{y}(t)}{\bar{y}'(t)} \\
& + \frac{f'(t)\bar{r}^2\bar{y}(t)\log \bar{r}\,(\log \bar{y}(t))^2}{\bar{y}'(t)}\Bigg)
\end{aligned} \tag{23}$$

Due to the long and cumbersome nature of the expression for $\theta_2$, it is being included in Appendix A.

Once the temperature profile is determined, the rate of change of phase change front with time can be found from the boundary condition, equation (9) given by

$$\begin{aligned}\frac{d\bar{y}}{dt} = \frac{(Ste)f(t)}{128(\bar{y}(t))^5(\log\bar{y}(t))^7}\Big(&128(\bar{y}(t))^4(\log\bar{y}(t))^6 \\ &- 32(Ste)f(t)\big(\bar{y}(t)\big)^2(\log\bar{y}(t))^3\,\Big(2\big(\bar{y}(t)\big)^2(\log\bar{y}(t))^2 \\ &- 2\big(\bar{y}(t)\big)^2\log\bar{y} + \big(\bar{y}(t)\big)^2 - 1\Big) \\ &+ (Ste)^2(f(t))^2\,\Big((\bar{y}(t))^4(48(\log\bar{y}(t))^4 - 112(\log\bar{y}(t))^3 \\ &+ 146(\log\bar{y}(t))^2 - 111\log\bar{y}(t) + 40) \\ &- 16\big(\bar{y}(t)\big)^2(2(\log\bar{y}(t))^2 - 5\log\bar{y}(t)) + 10(\log\bar{y}(t))^2 \\ &+ 31\log\bar{y}(t) + 40\Big)\Big)\end{aligned} \tag{24}$$

Due to the considerable complexity of equation (24), analytical integration in order to derive an expression for *y(t)* similar to equation (10) in the case of constant $T_w$ may not be possible. Therefore, phase change front as a function of time is determined in this case by numerical time-stepping based on the time derivative provided by equation (24) and using the initial condition of zero melting at *t*=0. Note that equation (24) has a singularity at *t*=0, which presents a difficulty in initiation of the timestepping approach. In order to address this problem, it is assumed that for a sufficiently small period from *t*=0 to *t*=*t**, change in the imposed wall temperature *f(t)* is negligible. This reduces the problem to the cylindrical phase change with constant wall temperature, which has been discussed in section 2.1.2. Therefore, between *t*=0 and *t*=*t**, the phase change front is given approximately by equation (10). Once *y(t)* is calculated at *t*=*t**, timestepping is carried out for the remaining time period using the derivative provided by equation (24). For ensuring minimal impact of this approximation on accuracy, the value of $t^*$ must be chosen to be small. In this case, $t^*$ is chosen to be 0.01% of the total time of interest.

Once *y(t)* has been determined in this manner, the average rate of energy stored can be found. Due to its cumbersome nature, the expression for $\dot{Q}_{avg}$ for this case is presented in Appendix A.

Based on this, the energy storage density is given by

$$Q'''(t) = \frac{\dot{Q}_{avg}(t) \times t}{\pi((y(t))^2 - R^2)h} \tag{25}$$

This completes the solution that describes the two key performance parameters of phase change based energy storage in the cylindrical coordinate system for the case of time-dependent temperature boundary condition.

## 3-3. Results and discussion

### 3-3-1. Model Validation

While the constant temperature Cartesian problem discussed in Section 2.1.1 has a well-established solution, validation is desirable for the other solutions discussed in the previous section. This is carried out by comparison with results from a variable time-step finite difference method for phase change problems [18], in which, the space domain is discretized into equal intervals $\Delta x$, whereas the time domain is discretized in such a way that during each successive time interval $\Delta t_i$, the phase change front *y(t)* propagates by $\Delta x$ [18]. This results in a set of discretized linear algebraic equations, which are solved using the implicit method.

A phase change material with $k$=0.2 Wm$^{-1}$K$^{-1}$, $C_p$=2250 Jkg$^{-1}$K$^{-1}$, $\rho$=810 kgm$^{-3}$ and $L$=270700 Jkg$^{-1}$ is considered for comparison between the results derived in Section 2 and the numerical method. Figure 2(a) shows a comparison of phase change front, *y(t)* as a function of time determined from equation (10) and the variable time-step method for the cylindrical coordinate system, with $T_w$-$T_m$=50 ºC and $R$=0.01 m. The analytical model is found to be in very good agreement with the numerical solution. Figure 2(b) plots temperature rise as a function of $x$ for the same problem at $t$=1500s, showing similarly good agreement between analytical and numerical solutions.

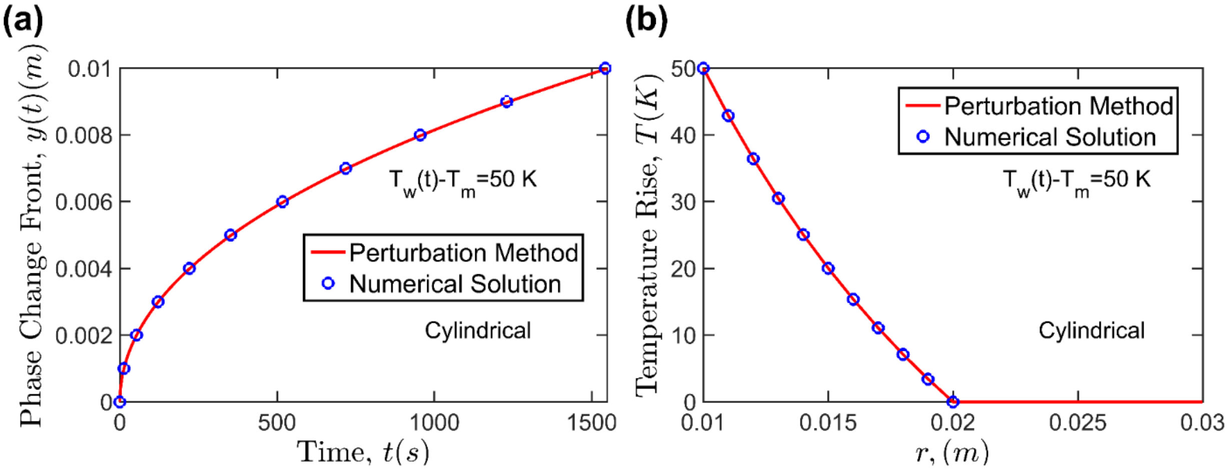

Figure 2. Comparison of the perturbation method based solutions and a finite element simulation for constant temperature boundary condition: (a) Phase change front, *y(t)* as a function of time for a constant temperature boundary condition $T_w$-$T_m$=50 K for the Cartesian problem; (b) Temperature rise as a function of $x$ for the same problem at $t$=1000s.

Figure 3 presents results from similar validation for the analytical models for time-dependent boundary conditions for the two coordinate systems discussed in Section 2.2. Progression of the phase change front is plotted in Figures 3(a) and 3(b) for Cartesian and cylindrical systems, respectively. In each case, wall temperature is assumed to vary as $T_w(t) - T_m = 50 + 0.03t$.

Good agreement between the two is observed, similar to the results for constant temperature boundary conditions. Figures 2 and 3 provide validation of the theoretical models for phase change processes discussed in section 2.

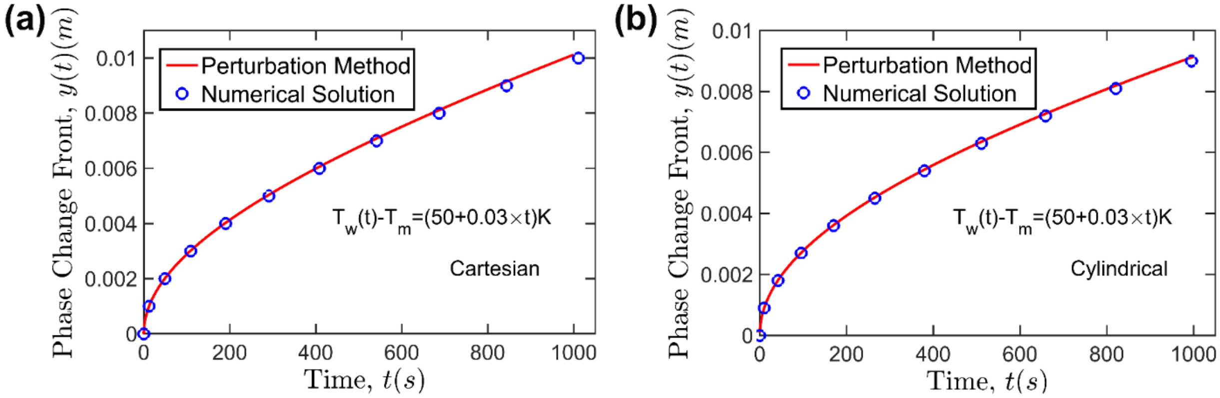

Figure 3. Comparison of the perturbation method based solutions and a finite element simulation for time-varying temperature boundary condition: (a) Phase change front, *y(t)* as a function of time for a time-dependent temperature boundary condition $T_w(t) - T_m = 50 + 0.03t$ for the Cartesian problem; (b) Phase change front, *y(t)* as a function of time for a constant temperature boundary condition $T_w(t) - T_m = 50 + 0.03t$ for the cylindrical problem.

### <u>3-3-2. Effect of *k* on PCM performance parameters</u>

The effect of thermal conductivity, *k* on total energy absorbed by the PCM and energy storage density in a Cartesian body is investigated first. Figures 4(a) and (b) present plots of the average rate of energy stored up to *t*=1000s as a function of thermal conductivity for Cartesian and cylindrical bodies, respectively. $T_w$-$T_m$=50ºC in each case and *R*=0.01m for cylindrical system. Similar plots for the energy storage density at *t*=1000s are presented in Figures 5(a) and (b). Figure 4 shows that the total rate of energy storage increases with increasing *k* for geometry. For the Cartesian system, this originates from the $\sqrt{k}$ dependence of $\dot{Q}_{avg}$, as shown in equation (10). Expressions for the cylindrical system, equations (15), while more complicated, also shown that

$\dot{Q}_{avg}$ increases with $k$. Physically, this occurs because greater $k$ results in greater heat diffusion into the PCM and consequently greater rate of energy stored in the system. As shown in Figure 4, this effect is much stronger in Cartesian bodies due to the larger surface area that heat can be absorbed by the PCM. Therefore, if the amount of heat absorbed is the important variable, cylindrical geometry has better performance than the Cartesian body.

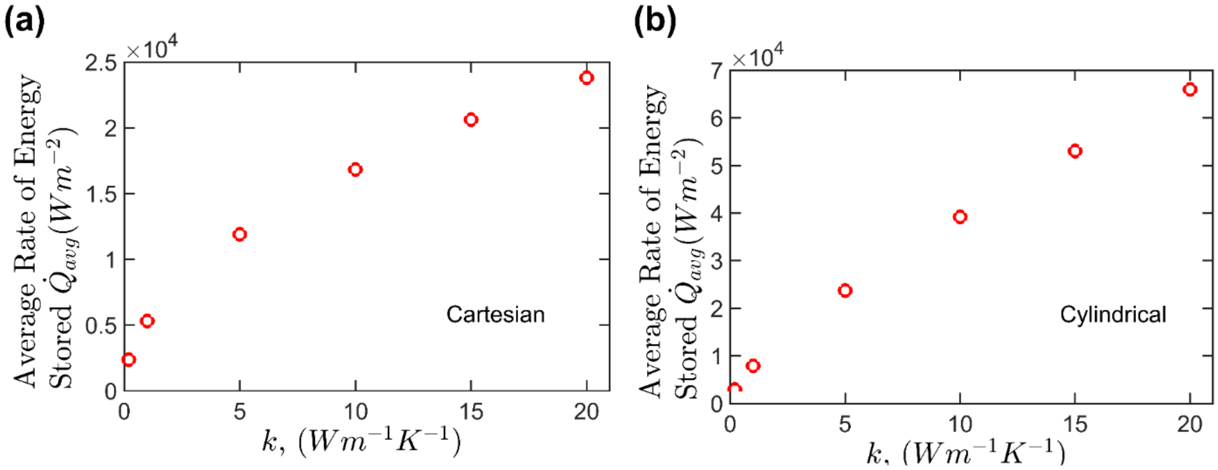

Figure 4. Effect of thermal conductivity, $k$ on average rate of energy stored per unit area of the source-PCM interface in (a) Cartesian and (b) cylindrical systems for a constant temperature boundary condition $T_w$-$T_m$=50 K over a 1000 s time period.

However, as shown in Figure 5, the energy storage density remains constant with increasing $k$ for the Cartesian system, and actually reduces for cylindrical system. This occurs because while increasing PCM thermal conductivity results in greater energy absorbed, it also increases the melted PCM volume. For the Cartesian problem, both $\dot{Q}_{avg}$ and $y$ exhibit a $\sqrt{k}$ dependence, and therefore, these effects exactly cancel each other when determining the energy storage density $Q'''$. On the other hand, for the cylindrical problem, the effect of increased melting rate dominates over the effect of increased rate of energy stored, thereby resulting in a reduction in energy storage density with increasing thermal conductivity. This shows that while increasing thermal conductivity of PCM improves a key performance parameter – rate of energy absorbed – the other key performance parameter, energy storage density remains the same for the Cartesian system and actually decreases for a cylindrical energy storage system.

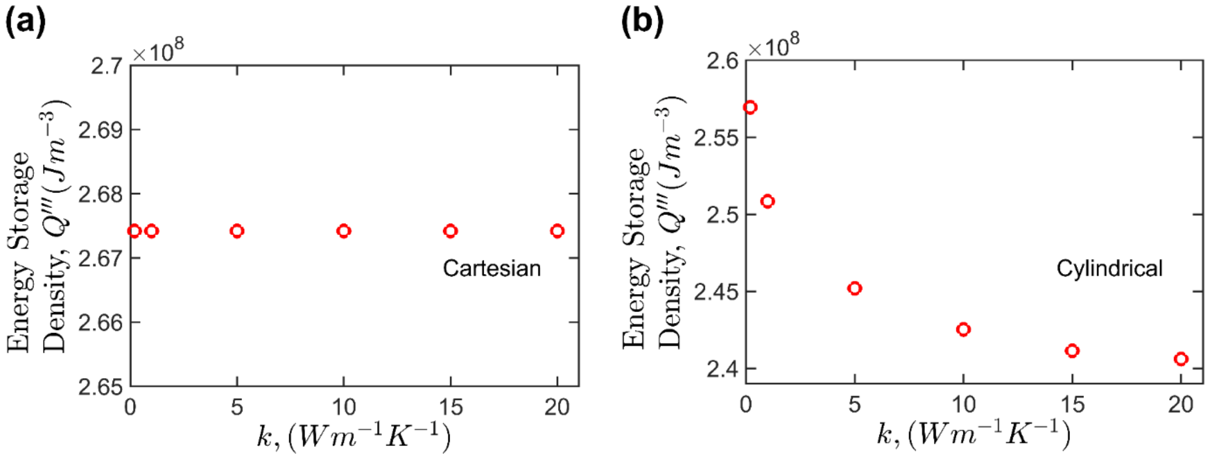

Figure 5. Effect of thermal conductivity, *k* on energy storage density in (a) Cartesian and (b) cylindrical systems for a constant temperature boundary condition $T_w$-$T_m$=50 K over a 1000 s time period.

This trade-off between the rate of energy stored and energy storage density highlighted by Figures 4 and 5 is important to recognize because the relative importance of these two performance parameters differs from one application to the other. In applications where it is important to absorb a large amount of energy very rapidly without regard to storage density, increasing *k* is clearly helpful, regardless of whether the energy storage system is Cartesian or cylindrical. However, when energy storage density is important, for example when energy must be stored compactly, increasing *k* is not likely to be effective, and in fact, may adversely affect energy storage density for cylindrical energy storage. This happens because in the Cartesian system, the volume of PCM melted has a $\sqrt{k}$ dependence due to linear scaling with $y(t)$, as shown in equation (1), whereas in cylindrical system, the dependence is much stronger due to the quadratic dependence of volume of PCM melted on $y(t)$ respectively. Thus, for a Cartesian body, thermal conductivity can be increased in order to increase the rate of heat absorbed without negatively impacting the energy storage density. However, in cylindrical body, such an approach will result in reduced energy storage density. In such a case, optimal system design using the approach presented here may be critical.

For a more comprehensive analysis of how thermal properties affect energy storage performance, colormaps of $\dot{Q}_{avg}$ and $Q'''$ are plotted in Figure 6 for $T_w$-$T_m$=50°C and $t$=1000s for a Cartesian system. Latent heat of the PCM is assumed to be $L$=270700 $\mathrm{Jkg^{-1}}$. Figure 6(a) shows much stronger dependence of $\dot{Q}_{avg}$ on $k$ than on $C_p$, indicating that small changes in $k$ are more likely to affect $\dot{Q}_{avg}$ than changes of similar relative magnitude in $C_p$. However, the impact of these thermal properties on $Q'''$ is quite different, as shown in Figure 6(b). $Q'''$ remains invariant with changes in $k$, whereas it increases with increasing $C_p$. Figure 6 can be used for performance comparison between different candidate PCMs. For example, three candidate PCMs *A*, *B* and *C* are marked on the colorplots in Figure 6(a) and (b) in terms of their thermal properties. PCM *A* has higher $k$ but lower $C_p$ than PCM *B*. PCM *C* lies somewhat in the middle of *A* and *B* in terms of both $k$ and $C_p$. The colorplots in Figures 6(a) and 6(b) show that while *A* is expected to have greater rate of energy stored, its performance in terms of energy storage density is poorer than that of *B*. Further, comparing *A* and *C*, it is seen that due to curvature in the color contours in Figure 6(a), *A* and *C* are expected to result in the same rate of energy stored, while, based on Figure 6(b), *C* is expected to store this energy much more compactly than *A*. The superior performance of *C* is despite its lower thermal conductivity than *A*, and shows that in some conditions, a material may be an attractive PCM despite relatively lower thermal conductivity.

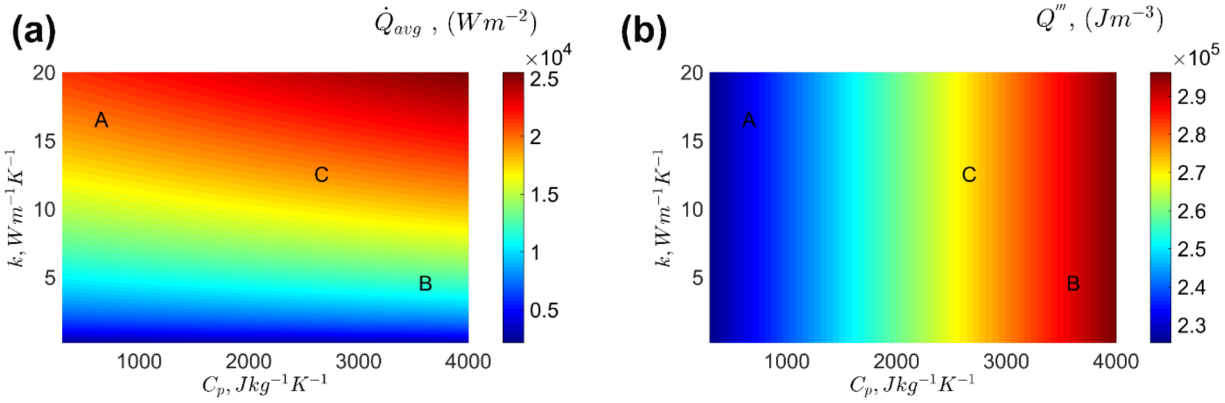

Figure 6. Colorplots of (a) average rate of energy absorbed by the PCM and (b) energy storage density as function of thermal conductivity and heat capacity in a Cartesian system.

Similar colorplots of $\dot{Q}_{avg}$ and $Q'''$ for a cylindrical energy storage system are presented in Figures 7(a) and 7(b) respectively. Similar to the Cartesian case, it is seen that the rate of energy stored increases with *k*. However, the energy storage density actually reduces with increasing *k*. This has several interesting consequences in the choice of thermal properties of candidate PCMs. For example, three candidate PCMs *D*, *E* and *F* are shown in Figures 7(a) and 7(b). It is seen that while *D* has greater rate of energy stored compared to *E* due to greater thermal conductivity, its energy storage density is actually lower. On the other hand, *F*, which has the same *k* as *E* but greater heat capacity, resulting in a high rate of energy stored as well as a high energy storage density.

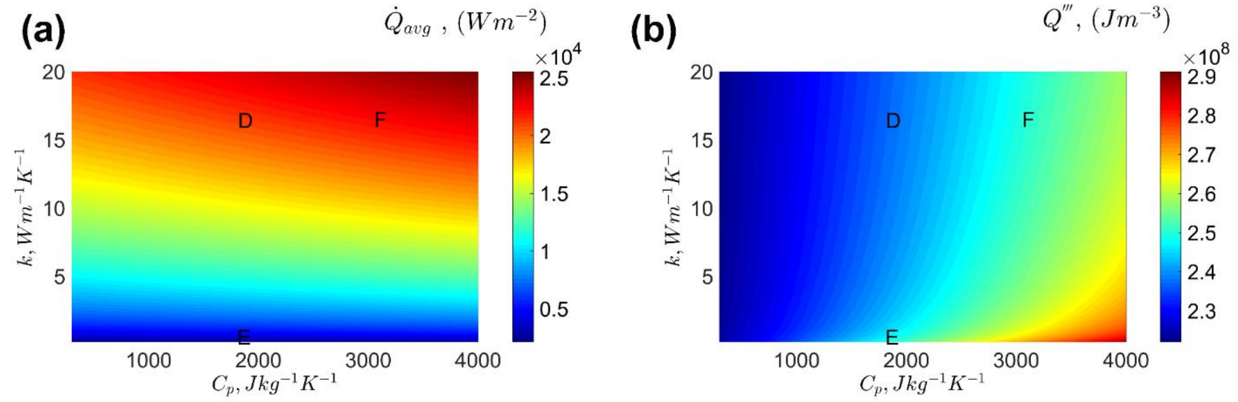

Figure 7. Colorplots of (a) average rate of energy absorbed by the PCM and (b) energy storage density as function of thermal conductivity and heat capacity in a cylindrical system.

These examples illustrate the importance of colorplots such as Figures 6 and 7 in understanding the trade-offs between thermal conductivity and heat capacity in terms of the performance parameters, and in choosing the correct PCM. In general, this choice depends on whether the rate of energy stored or the energy storage density is more critical, as well as on whether the energy storage system is Cartesian or cylindrical in geometry. Results from this section enable engineers to quantify this trade-off and choose the best material corresponding to the goal of their system.

### 3-3-3. Results with time-dependent boundary conditions

The key results discussed in section 3.2 pertain to a constant wall temperature boundary condition. However, for practical scenarios where the hot source generates heat at a certain rate, the temperature at the wall may not be constant and may increase over time. This is also true for scenarios where time-varying heat flux impinges on the wall. In such cases, variation in the wall temperature with time must be accounted for using models presented in Section 2.2. This section discusses results on this practical scenario. A linearly increasing wall temperature $T_w(t) - T_m =$

$50 + 0.03t$ is assumed. Figures 8(a) and 8(b) plot the average rate of energy stored as a function of $k$ for Cartesian and cylindrical energy storage systems respectively. Similar plots for energy storage density are presented in Figures 9(a) and 9(b). For both Cartesian and cylindrical cases, the rate of energy stored increases with $k$, similar to the results for constant wall temperature case discussed in the previous section. The energy storage density remains invariant with $k$ in the Cartesian case, whereas it actually reduces with $k$ for the cylindrical case. This is also similar to the constant wall temperature case. Both $\dot{Q}_{avg}$ and $y(t)$ for the Cartesian case, shown in equations (28) and (30) respectively continue to have a $\sqrt{k}$ dependence, resulting in $Q'''$ remaining independent of $k$, just like the constant $T_w$ case. These relationships for cylindrical case are more difficult to interpret due to the complexity of the equations.

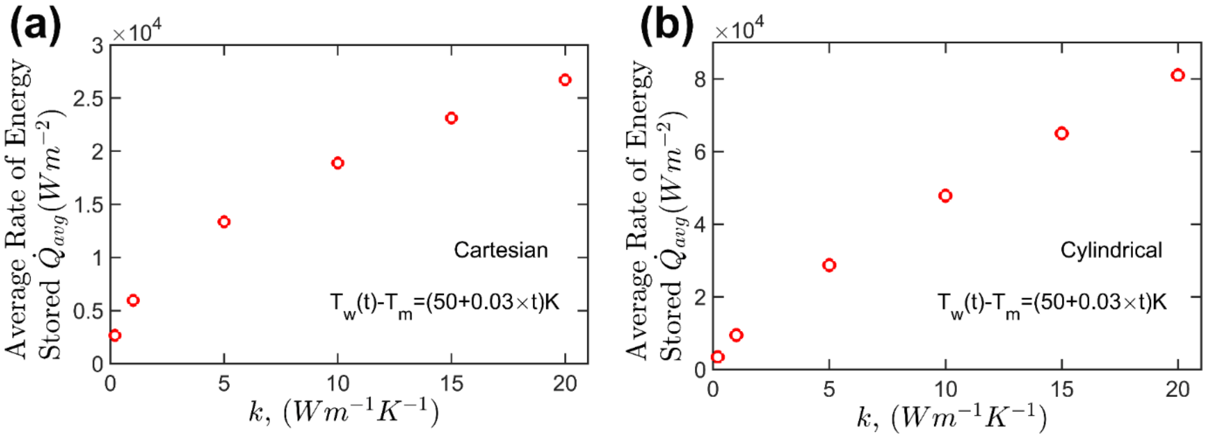

Figure 8. Effect of thermal conductivity, $k$ on average rate of energy stored per unit area of the source-PCM interface in (a) Cartesian and (b) cylindrical coordinate systems for a time-dependent temperature boundary condition $T_w(t) - T_m = 50 + 0.03t$ over a 1000 s time period.

These plots show that the key results discussed for the constant wall temperature case also hold for the more realistic, time-varying wall temperature case. The method presented here is valid for quantifying the effect of improving PCM thermal conductivity on critical performance parameters in practical engineering applications.

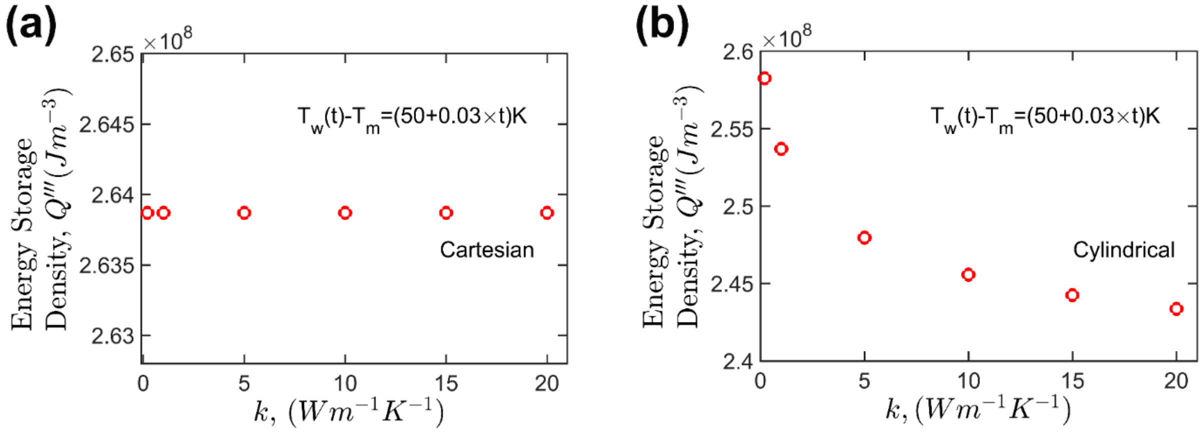

Figure 9. Effect of thermal conductivity, $k$ on energy storage density in (a) Cartesian and (b) Cylindrical coordinate systems for a time-dependent temperature boundary condition $T_w(t) - T_m = 50 + 0.03t$.

In order to further understand the nature of energy storage performance parameters in case of time-dependent boundary conditions, Figure 10(a) and 10(b) plot rate of energy stored and energy storage density as functions of *k*. Plots are presented for both Cartesian and cylindrical energy storage systems for different expressions for $T_w(t)$. Specifically, linearly increasing wall temperature with different values of slopes $T_w(t) - T_m = A + Bt$ is assumed where A=50 and B=0.01, 0.03, 0.05, 0.07 and 0.09 K/s, while *t*=1000s. Figure 10(a) indicates that in both Cartesian and cylindrical coordinates, the rate of energy absorbed increases with *k*, which is consistent with results obtained from Figure 8. Further, the greater the value of slope *B*, the larger is the rate of energy absorbed, which is along expected lines due to greater temperature gradient between the wall and PCM. Figure 10(b) shows that in the Cartesian system, energy storage density is not a function of *k*, similar to previous results, and also increases with increasing value of *B*. Increasing the value of *B* affects increases the rate of heat absorbed as well as the phase change front propagation. The impact on the former is weaker, due to which, the energy storage density increases with increase in *B*. In contrast, energy storage density decreases with increasing k for the cylindrical system, which is consistent with previous results. The energy storage density increases with increasing B, which is explained by the greater impact on the rate of energy stored compared to phase change propagation, similar to the Cartesian result.

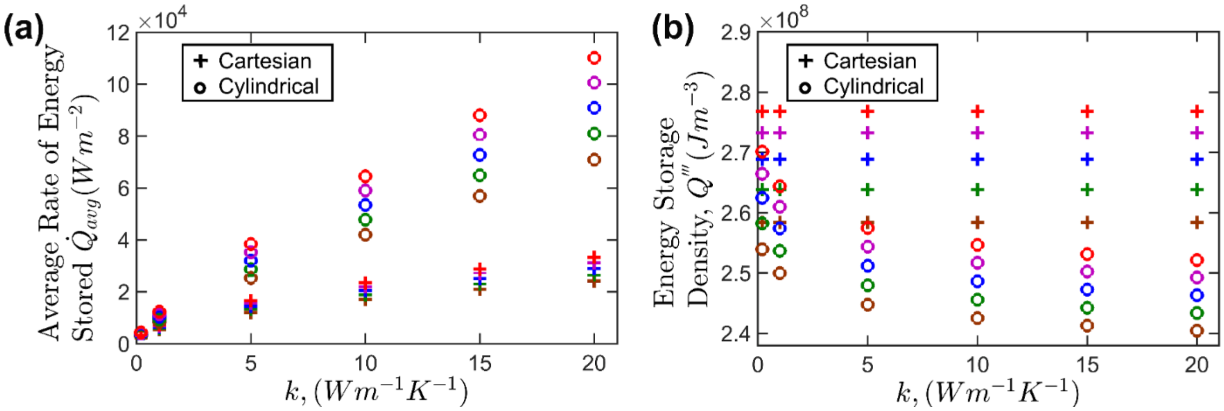

Figure 10. Variation of (a) rate of energy storage and (b) energy storage density with thermal conductivity for various slopes *B* of linearly increasing temperature boundary condition, $T_w(t) - T_m = 50 + Bt$. Red, purple, blue, green and brown colors correspond to B=0.09, 0.07, 0.05, 0.03 and 0.01 $Ks^{-1}$ respectively.

## 3-4. Conclusions

Understanding the impact of thermophysical properties on performance of phase change energy storage systems is very important for the design and optimization of several engineering systems. In the past, several papers have presented strategies for improving thermal conductivity of commonly used PCMs. The present work shows that while improving thermal conductivity is helpful for increasing the rate of energy stored, it is not similarly helpful for improving the energy storage density, which may be an important performance parameter in several applications. Using well-establised theoretical models, the present work helps fully understand the impact of previously reported thermal conductivity enhancement on performance of phase change energy storage systems. Based on the theoretical model, the performance of various PCMs can be compared with each other, and the optimal PCM can be chosen, depending on the relative importance of rate of energy stored and energy storage density, as well the geometry of energy storage system.

## 3-5. Nomenclature

| | |
|---|---|
| $A$ | area (m$^{2}$) |
| $C_p$ | specific heat capacity (Jkg$^{-1}$K$^{-1}$) |
| $f$ | non-dimensional temperature, $f=(T_w(t)-T_m)/(T_m-T_{ref})$ |
| $h$ | height of the cylinder (m) |
| $k$ | thermal conductivity (Wm$^{-1}$K$^{-1}$) |
| $L$ | latent heat of fusion (Jkg$^{-1}$) |
| $\dot{Q}_{avg}$ | average rate of energy absorbed (Wm$^{-2}$) |
| $Q'''$ | energy storage density (Wm$^{-3}$) |
| $r$ | radial coordinate (m) |
| $R$ | radius (m) |
| $Ste$ | Stefan number, $Ste=Cp(\Delta T)/L$ |
| $t$ | time (s) |
| $T$ | temperature (K) |
| $T_m$ | phase change temperature (K) |
| $T_{ref}$ | reference temperature (K) |
| $T_w$ | wall temperature (K) |
| $x$ | Cartesian coordinate (m) |
| $y$ | location of phase change front (m) |
| $\alpha$ | thermal diffusivity (m$^{2}$s$^{-1}$) |
| $\lambda$ | characteristic parameter for phase change front propagation |
| $\rho$ | density (kgm$^{-3}$) |

## 3-6. References

[1] Z. Ling, Z. Zhang, G. Shi, X. Fang, L. Wang, X. Gao, et al., Review on thermal management systems using phase change materials for electronic components, Li-ion batteries and photovoltaic modules, Renewable and Sustainable Energy Reviews. 31 (2014) 427–438. doi:10.1016/j.rser.2013.12.017

[2] A. Sharma, V. Tyagi, C. Chen, D. Buddhi, Review on thermal energy storage with phase change materials and applications, Renewable and Sustainable Energy Reviews. 13 (2009) 318–345. doi:10.1016/j.rser.2007.10.005.

[3] M.M. Farid, A.M. Khudhair, S.A.K. Razack, S. Al-Hallaj, A review on phase change energy storage: materials and applications, Energy Conversion and Management. 45 (2004) 1597–1615. doi:10.1016/j.enconman.2003.09.015.

[4] S. Hasnain, Review on sustainable thermal energy storage technologies, Part I: heat storage materials and techniques, Energy Conversion and Management. 39 (1998) 1127–1138. doi:10.1016/s0196-8904(98)00025-9.

[5] J. Cot-Gores, A. Castell, L.F. Cabeza, Thermochemical energy storage and conversion: A-state-of-the-art review of the experimental research under practical conditions, Renewable and Sustainable Energy Reviews. 16 (2012) 5207–5224. doi:10.1016/j.rser.2012.04.007.

[6] K. Shah, N. Balsara, S. Banerjee, et al., State-of-the-art and future research needs for multiscale analysis of Li-ion cells, ASME J. Electrochem. Energy Conversion & Storage 14 (2017) 020801:1-17. doi: 10.1115/1.4036456

[7] L. Fan, J. Khodadadi, Thermal conductivity enhancement of phase change materials for thermal energy storage: A review, Renewable and Sustainable Energy Reviews. 15 (2011) 24–46. doi:10.1016/j.rser.2010.08.007.

[8] A. Mostafavi, M. Parhizi, A. Jain, Theoretical modeling and optimization of fin-based enhancement of heat transfer into a phase change material, International Journal of Heat and Mass Transfer. (2019) in review.

[9] L. Liu, D. Su, Y. Tang, G. Fang, Thermal conductivity enhancement of phase change materials for thermal energy storage: A review, Renewable and Sustainable Energy Reviews. 62 (2016) 305–317. doi:10.1016/j.rser.2016.04.057.

[10] B. Zalba, Marín José Ma, L.F. Cabeza, H. Mehling, Review on thermal energy storage with phase change: materials, heat transfer analysis and applications, Applied Thermal Engineering. 23 (2003) 251–283. doi:10.1016/s1359-4311(02)00192-8.

[11] F. Agyenim, N. Hewitt, P. Eames, M. Smyth, A review of materials, heat transfer and phase change problem formulation for latent heat thermal energy storage systems (LHTESS), Renewable and Sustainable Energy Reviews. 14 (2010) 615–628. doi:10.1016/j.rser.2009.10.015.

[12] T. Oya, T. Nomura, M. Tsubota, N. Okinaka, T. Akiyama, Thermal conductivity enhancement of erythritol as PCM by using graphite and nickel particles, Applied Thermal Engineering. 61 (2013) 825–828. doi:10.1016/j.applthermaleng.2012.05.033.

[13] J. Fukai, M. Kanou, Y. Kodama, O. Miyatake, Thermal conductivity enhancement of energy storage media using carbon fibers, Energy Conversion and Management. 41 (2000) 1543–1556. doi:10.1016/s0196-8904(99)00166-1.

[14] A. Karaipekli, A. Sarı, K. Kaygusuz, Thermal conductivity improvement of stearic acid using expanded graphite and carbon fiber for energy storage applications, Renewable Energy. 32 (2007) 2201–2210. doi:10.1016/j.renene.2006.11.011.

[15] A. Mills, M. Farid, J. Selman, S. Al-Hallaj, Thermal conductivity enhancement of phase change materials using a graphite matrix, Applied Thermal Engineering. 26 (2006) 1652–1661. doi:10.1016/j.applthermaleng.2005.11.022.

[16] A. Sarı, A. Karaipekli, Preparation, thermal properties and thermal reliability of palmitic acid/expanded graphite composite as form-stable PCM for thermal energy storage, Solar Energy Materials and Solar Cells. 93 (2009) 571–576. doi:10.1016/j.solmat.2008.11.057.

[17] P. Keblinski, S. Phillpot, S. Choi, J. Eastman, Mechanisms of heat flow in suspensions of nano-sized particles (nanofluids), International Journal of Heat and Mass Transfer. 45 (2002) 855–863. doi:10.1016/s0017-9310(01)00175-2.

[18] D. W. Hahn, and M. N. Özişik, 2012, “Heat Conduction.” Third ed., John Wiley & Sons, Hoboken, New Jersey.

[19] J. Stefan, Ueber die Theorie der Eisbildung, insbesondere über die Eisbildung im Polarmeere, Annalen Der Physik. 278 (1891) 269–286. doi:10.1002/andp.18912780206.

[20] J. Caldwell, Y. Kwan, On the perturbation method for the Stefan problem with time-dependent boundary conditions, International Journal of Heat and Mass Transfer. 46 (2003) 1497–1501. doi:10.1016/s0017-9310(02)00415-5.

[21] G. Lock, J. Gunderson, D. Quon, J. Donnelly, A study of one-dimensional ice formation with particular reference to periodic growth and decay, International Journal of Heat and Mass Transfer. 12 (1969) 1343–1352. doi:10.1016/0017-9310(69)90021-0.

# Chapter 4

## Theoretical Modeling of a Phase Change Heat Transfer Problem with a Pre-Melted or Pre-Solidified Region

**Published as**: Parhizi, M., & Jain, A. (2019). Theoretical modeling of a phase change heat transfer problem with a pre-melted or pre-solidified region. *International Journal of Heat and Mass Transfer*, *136*, 635-643.

## 4-1. Introduction

Phase change heat transfer problems involving melting and solidification occur commonly in engineering applications such as thermal energy storage, heat exchangers, additive manufacturing, welding and casting of metals, crystal growth and thermal management systems [1-3]. In theoretical analysis of such problems, the interest is often in predicting the propagation of the phase change front as well as temperature distribution in the newly formed phase. The analysis of phase change problems is considerably complicated due to their non-linear nature – exact solutions exist only for a few idealized cases. The simplest phase change problem is that of a one-dimensional semi-infinite body, originally at its phase change temperature, being heated or cooled with a constant temperature boundary condition at its end [1]. Stefan number $Ste = \frac{C_p(T_m - T_{ref})}{L}$, which represents the ratio of sensible heat storage to latent heat storage is a key non-dimensional parameter in phase change problems. Analytical solution for this problem [4] shows that the location of the solid-liquid interface, *y(t)* is proportional to $\sqrt{\alpha t}$ where $\alpha$ is the thermal diffusivity. This analytical solution was extended later to a problem in which the initial temperature of the body is different from its phase change temperature [1]. Exact solutions exist only for a few other problems. For example, exact solution for one-dimensional solidification of a supercooled liquid has been also derived [5]. An exact solution for solidification of a liquid body around a line heat sink in cylindrical coordinate system has also been presented [6].

Approximate analytical methods or numerical methods have been used extensively for analyzing phase change problems for which an analytical solution does not exist [1,5,7]. Perturbation methods and heat balance integral methods are two commonly used approximate analytical methods for phase change heat transfer problems. In heat balance integral method, the temperature profile is assumed to be a particular function of the spatial coordinate, *x*, similar to the boundary layer theory developed by Karman and Pohlhausen [1]. The governing energy equation is then integrated with respect to *x* and the resulting integral equation is solved to obtain the temperature profile and phase change propagation front as functions of time. This approach has been used for phase change problems with a variety of boundary conditions, including time-dependent temperature boundary condition, constant heat flux and convective boundary conditions [8-12]. In perturbation method, the temperature profile is written as a series involving powers of *Ste*. This expression is then inserted back into the governing equation and the obtained equations are solved through term-by-term comparison and use of energy conservation at the phase change interface. This approach has been used for solving phase change problems subjected to a variety of boundary conditions, including time-dependent temperature boundary condition [13-14], phase change problems in cylindrical [14] and spherical [14] coordinate systems, and time-dependent heat flux [15] boundary conditions In addition to these approaches, the variable eigenvalue method has been also used to solve phase change problems involving time-dependent boundary conditions [1]. Approximate solutions for a number of problems involving convection within the liquid phase have also been presented [16-17].

Most of the past theoretical studies on phase change problems consider cases where the body is initially in one phase exclusively, and the second phase is then gradually formed due to melting or solidification of the original phase. However, there may be some engineering problems where both phases exist at the initial time, such as a melting problem where part of the solid body is already melted at the initial time and is at a certain initial temperature different from that of the solid body itself, as shown schematically in Figure 1(a). This could occur due to discontinuous heating and cooling that causes the phase change process to be intermittent. For example, in phase change thermal management of Li-ion batteries [18-19], heat generated during battery discharge may initiate melting of the phase change material, but because battery discharge may start and stop depending on loading conditions, the melting process may be very intermittent, leading to the existence of a pre-melted region of the phase change material at the start of further phase change. Similarly, the intermittent nature of phase change based solar energy storage may cause a pre-melted region shielding the material that is not yet melted.

In such cases, the nature of heat transfer may be significantly different from classic phase change problems, and this problem may not be solvable within the framework of classical Stefan problems, because the presence of both phases at $t$=0 introduces additional complexity not accounted for by traditional methods. Heat transfer between the phase change front and boundary condition must pass through the pre-melted region, which constitutes a thermal resistance for the flow of heat. Thickness of the pre-melted liquid, its initial temperature distribution and thermal properties are all expected to play a key role in determining the rate at which further melting occurs. Further, depending on the magnitude of the temperature distribution in the pre-melted liquid relative to the temperature boundary condition, heat flow may occur entirely into the solid body, or partly in the reverse direction. Due to these complications in the present problem, solutions available for classical phase change problems may not be applicable for this problem, and other approaches may be needed.

This work develops a theoretical method to solve a one-dimensional melting problem that includes a pre-melted length with an arbitrary initial temperature along with a time-dependent temperature boundary condition. While discussed here in the context of melting, this method can also be used to solve the reverse problem of solidification of a liquid with a pre-solidified length.

A solution method is developed by iteratively solving the thermal conduction problem in the pre-melted length and phase change problem in the remaining body. Specifically, the phase change problem comprises a time-dependent temperature boundary condition, which is solved using a perturbation method. The iterative approach adopted in this work has been used in the past, but only for single phase problems such as heat transfer in three-dimensional integrated circuits 3D ICs [20], thermal management of Li-ion batteries [18, 21] and other conjugate heat transfer problems [22].

The next section presents the theoretical models underlying the iterative method. The effects of various geometrical and thermophysical parameters on the solution are discussed in the subsequent section.

## 4-2. Mathematical Modeling

The heat transfer problem considered here, shown schematically in Figure 1(a), consists of a one-dimensional, semi-infinite solid body initially at its melting temperature. The region $0<x<W$ of the body is already melted, and has an initial temperature distribution $G(x)$. The remainder region is initially a solid at its phase change temperature. A time-dependent temperature boundary condition $T_0(t)$ is applied at the $x=0$ end of the domain. Key heat transfer processes in this problem include thermal conduction from the $x=0$ boundary condition and the pre-melted region into the initially solid region and then into the phase change interface, thermal conduction from the pre-melted region to the boundary at $x=0$ (if the boundary temperature is lower than the temperature in the pre-melted region) and phase change at the liquid-solid interface $y(t)$.

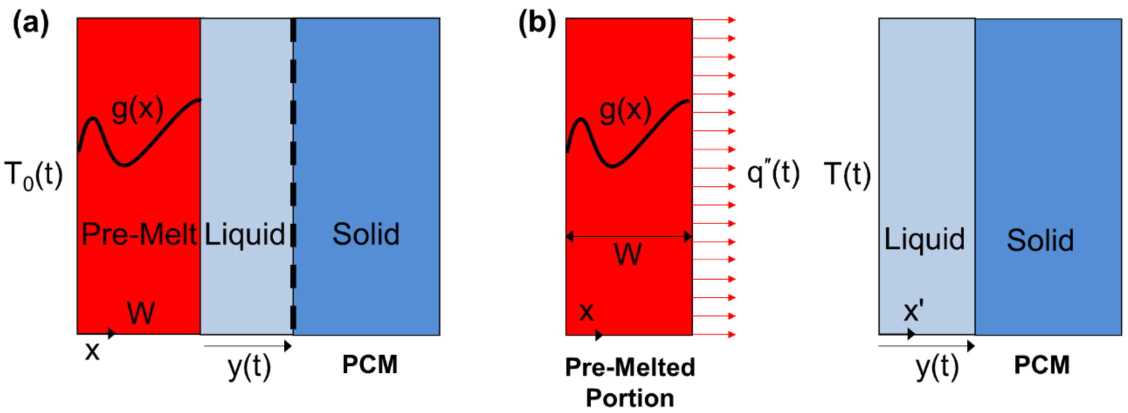

Figure 1. Schematic of the one-dimensional phase change problem with a pre-melted region. (a) Schematic of the overall conjugate problem along with the associated initial and boundary conditions. (b) Schematic of the two sub-problems including the conduction problem and the phase change problem

The nature of these heat transfer processes and relative magnitudes and directions of heat flow in this problem depend on the magnitude of temperature in the pre-melted region, particularly the initial temperature $G(x)$ compared to the magnitude of the time-dependent temperature boundary condition $T_0(t)$. For example, if $T_0(t)$ is always greater than the initial temperature $G(x)$, then heat will always flow from left to right as shown in Figure 1(a), i.e. from the pre-melted region to liquid-solid interface. In a more complicated scenario, if $G(x)$ is greater than $T_0(t)$, then some heat may flow from the pre-melted region to the $x=0$ boundary. Due to the time-dependent nature of $T_0$, these directions of heat flow may also reverse over time. These dynamics make this an interesting problem, with specific interest in understanding the role of various initial and boundary conditions and thermophysical properties in phase change that occurs in this problem.

This problem is solved in an iterative fashion by splitting the domain of interest into two regions – the pre-melt region, $0<x<W$ and the phase change region, $x>W$, and solving for temperature distribution in both regions separately, while ensuring temperature and heat flux continuity at $x=W$. Both heat conduction and phase change occur in the second region ($x>W$), referred to as the phase change sub-problem. Only heat conduction occurs in the pre-melted region ($0<x<W$), referred to as the conduction sub-problem. Figures 1(b) and 1(c) show schematics of these two sub-problems. In order to solve the two sub-problems, an unknown time-dependent heat flux $q''(t)$ leaving the pre-melt region at $x=W$ and entering the phase change region is applied as the boundary condition for the conduction sub-problem at $x=W$. For solving the phase change sub-problem, a time-dependent temperature boundary condition $T_w(t)$ is considered at the interface between the two regions. Since both $q''(t)$ and $T_w(t)$ are unknown, an iterative approach is used wherein time-dependent temperature $T_w(t)$ at $x'=0$ is first guessed and is used to find the temperature profile within the phase change sub-problem. The resulting interfacial heat flux from the solution of the problem is then used as an input into the conduction sub-problem, which in turn provides a value for the temperature profile at $x'=0$ that can be used to improve the initial guess. This iterative process is repeated until the change in temperature from one iteration to another is negligible. The iterative approach explained above is summarized in a flowchart in figure 2. Such an iterative approach has been used in past studies to solve a variety of conjugate steady state and transient problems [18, 20-22].

Analytical solutions for each of the two sub-problems are needed in order to execute the iterative approach. Sub-sections 2.1 and 2.2 below describe these analytical solutions.

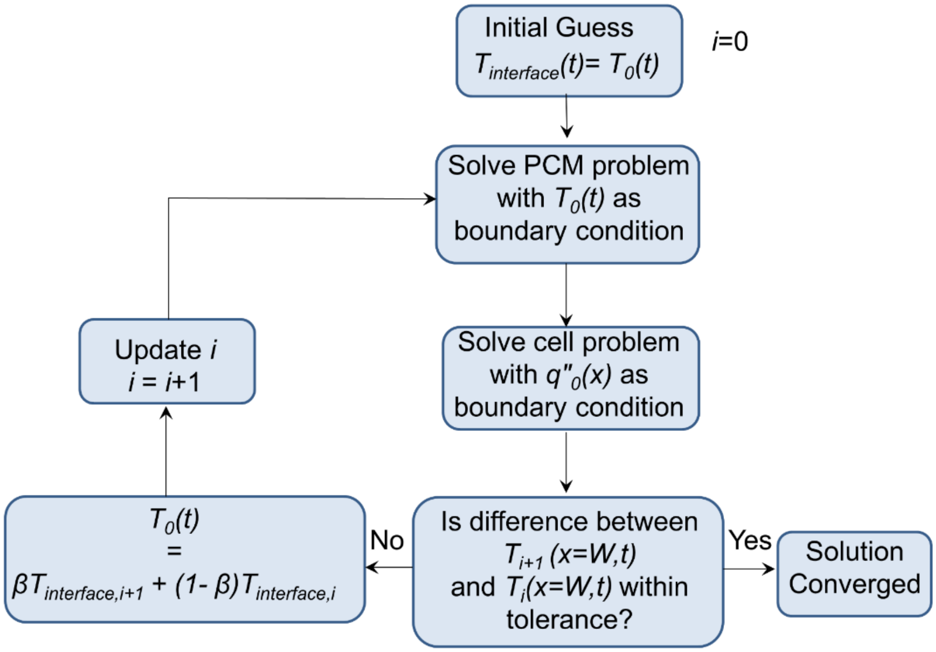

Figure 2. Flowchart of the iterative approach used to solve the overall conjugate problem

### 4-2-1. Solution for the phase change sub-problem

Figure 1(c) shows a schematic of the phase change sub-problem along with the respective boundary condition, in the region $x>W$. For convenience, a new coordinate axis $x'$ shown in Figure 1(c) is used, where $x'=x-W$. Within this region, the entire body is solid at $t=0$, and the phase change front, originates at $x'=0$ and propagates with time. Temperature at $x'=0$ in this problem is taken to be $T_w(t)$. As such, $T_w(t)$ is unknown in advance. The liquid-solid interface position, $y(t)$ is an important parameter of this problem that must be determined from the solution. The phase change problem described above is a generalization of the original Stefan problem, in that the temperature driving the phase change process is time-dependent.

The mathematical description of this sub-problem is as follows: the governing energy conservation equation for the temperature field is

$$\frac{\partial^2 T_1}{\partial x'^2} = \frac{1}{\alpha_l}\frac{\partial T_1}{\partial t} \tag{1}$$

where $\alpha_l$ is the thermal diffusivity of the newly formed liquid. Note that $T_1$ represents temperature rise above the melting temperature $T_m$.

The following time-dependent boundary condition is imposed at one end of the domain.

$$T_1(x', t) = T_w(t) \qquad \text{at } x'=0 \tag{2}$$

Temperature at the solid liquid interface, *y(t)* must equal the melting temperature. Further, energy must be conserved at this interface. These result in the following equations:

$$T_1(x', t) = 0 \qquad \text{at } x'=y(t) \tag{3}$$

and

$$-k_l\left(\frac{\partial T_1}{\partial x'}\right)_{x'=y(t)} = \rho L\frac{dy}{dt} \qquad \text{at } x'=y(t) \tag{4}$$

where $k_l$ and $\rho_l$ are the thermal conductivity and mass density of the liquid, respectively, and *L* is the latent heat. Convection in the newly formed liquid is neglected.

While an exact solution is available for the specific case of constant $T_w$ – the well-known Stefan solution – approximate analytical methods such as integral methods [8] and perturbation methods [14] have been used for solving the more general problem posed in this sub-section. Here, the perturbation technique presented by Caldwell & Kwan [14] is used. The general methodology and final results are briefly outlined below, while complete details may be found in past papers [14].

For solving this problem using the perturbation method, the time variable is first eliminated by replacing *t* with the solid-liquid interface location *y(t)*, which is a monotonic function of time. This is followed by writing the solution of the new governing equation as a series involving powers of *Ste* [14]. Substituting the assumed form of the temperature solution back into the governing equation, applying boundary conditions and a term-by-term comparison results in a set of ordinary differential equations. Temperature profile in the liquid phase is derived by solving these ordinary differential equations. The location of the solid-liquid interface *y(t)* is then determined by utilizing energy conservation at the phase change interface, given by equation (4). This procedure results in the following expression for temperature profile and phase change front *y(t)* [14]

$$T(x,t) = (\theta_0 + Ste \cdot \theta_1 + Ste^2 \cdot \theta_2)(T_{ref}) \tag{5}$$

$$\theta_0 = f(t)\left(1 - \frac{x}{y(t)}\right) \tag{6}$$

$$\theta_1 = \frac{1}{6} f(t) \frac{x}{y(t)}\left(\frac{x}{y(t)} - 1\right)\left[f(t)\left(\frac{x}{y(t)} + 1\right) - \frac{f'(t)}{y'(t)} y(t)\left(\frac{x}{y(t)} - 2\right)\right] \tag{7}$$

$$\begin{aligned}\theta_2 = -\frac{1}{360} f(t) \frac{x}{y(t)}\left(\frac{x}{y(t)} - 1\right)\Bigg[ & f(t)^2\left(\frac{x}{y(t)} + 1\right)\left(9\left(\frac{x}{y(t)}\right)^2 + 19\right) \\ & + 10\left(\frac{f'(t)}{y'(t)}\right)^2 y(t)^2\left(\frac{x}{y(t)} + 4\right) \\ & + 5 f(t) \frac{f'(t)}{y'(t)} y(t)\left(3\left(\frac{x}{y(t)}\right)^2 + 5\frac{x}{y(t)} + 17\right) \\ & + f(t)\frac{f''(t)}{y'(t)^2} y(t)^2\left(\frac{x}{y(t)} - 2\right)\left(3\left(\frac{x}{y(t)}\right)^2 - 6\frac{x}{y(t)} - 4\right)\Bigg]\end{aligned} \tag{8}$$

$$y(t) = \left[2(Ste)\alpha_l \int_0^t f(\tau)\left(1 - \frac{Ste}{3} f(\tau) + \frac{7Ste^2}{45} f(\tau)^2\right) d\tau\right]^{\frac{1}{2}} \tag{9}$$

Where *f(t)* is the non-dimensional time-dependent temperature boundary condition given by [14]

$$f(t) = -\frac{T_w(t)}{T_{ref}} \tag{10}$$

Note that both $T_w$ and $T_{ref}$ represent temperature rise above the melting temperature $T_m$.

Finally, heat flux between the phase change region and the pre-melt region at $x'=0$, which is an input into the second sub-problem, is determined using Fourier's law as follows [18]:

$$q''(t) = -k_l \frac{dT}{dx} = k_l T_{ref} \begin{bmatrix} -\frac{f(t)}{y(t)} - Ste \frac{f(t)\left(f(t)+2\frac{f'(t)}{y'(t)}y(t)\right)}{6y(t)} + \\ Ste^2 \frac{f(t)\left(40\left(\frac{f'(t)}{y'(t)}\right)^2 y^2(t)+85f(t)\frac{f'(t)}{y'(t)}y(t)+19f^2(t)+8\frac{f''(t)}{y'^2(t)}f(t)y^2(t)\right)}{360y(t)} \end{bmatrix} \tag{11}$$

4-2-2. Solution for the conduction sub-problem

Figure 1(b) shows a schematic of the conduction sub-problem along with the associated boundary conditions. The only heat transfer phenomenon of relevance in this region is thermal conduction. Fluid flow and convective heat transfer is neglected.

Initial temperature distribution in the pre-melted region, $G(x)$ is known. In addition, a time-dependent temperature boundary condition $T_0(t)$ is imposed on the boundary at $x=0$. Finally, a time-dependent heat flux leaving the pre-melted region at $x=W$, $q''(t)$ is known based on the solution of temperature distribution in the phase change region. These comprise three non-homogeneities in this thermal conduction problem. The governing energy conservation equation for temperature rise in the pre-melted region relative to melting temperature, $T_2(x,t)$ is

$$\frac{\partial^2 T_2}{\partial x^2} = \frac{1}{\alpha_p}\frac{\partial T_2}{\partial t} \tag{12}$$

where $\alpha_p$ is the thermal diffusivity of the pre-melted region.

The temperature distribution must also satisfy the following initial and boundary conditions:

$$T_2 = G(x) \qquad \text{at } t=0 \tag{13}$$

$$T_2 = T_0(t) \qquad \text{at } x=0 \tag{14}$$

and

$$-k_p \frac{\partial T_2}{\partial x} = q''(t) \qquad \text{at } x=W \tag{15}$$

Equations (12) through (15) can be solved by linearly splitting the problem into three sub-problems *a*, *b* and *c*, each of which account for only one non-homogeneity – initial condition *G(x)*, time-dependent boundary temperature $T_0(t)$ and time-dependent boundary heat flux $q''(t)$, respectively. Solutions for these sub-problems are quite straightforward.

The solution for the initial condition problem, based on the method of separation of variables, [1] is

$$T_{2a}(x,t) = \sum_{n=1}^{\infty} A_n \sin(\lambda_n x) \exp\left(-\alpha_p \lambda_n^2 t\right) \tag{16}$$

where

$$A_n = \frac{1}{N_n} \int_0^W G(x) \sin(\lambda_n x) dx \tag{17}$$

Here, $N_n = \frac{2}{W}$ is the eigenvalue norm, and $\lambda_n = \frac{(2n-1)\pi}{2W}$ , *n*=1,2,3… are the eigenvalues of the problem.

The method of variation of parameters [23-24] is used for solving sub-problems *b* and *c*. The solution for sub-problem *b* is:

$$T_{2b}(x,t) = \sum_{n=1}^{\infty} B_n(t) \sin(\lambda_n x) \tag{18}$$

where the coefficients $B_n$ are given by:

$$B_n(t) = \int_0^t \frac{\lambda_n \alpha_p}{N_n} T_0(t) \exp\left(-\alpha_p \lambda_n^2 (t-\tau)\right) d\tau \tag{19}$$

Similarly, the solution for sub-problem *c* is given by:

$$T_{2c}(x,t) = \sum_{n=1}^{\infty} C_n(t) \sin(\lambda_n x) \tag{20}$$

where the coefficients $C_n$ are given by:

$$C_n(t) = \int_0^t -\frac{\alpha_p}{kN_n} q''(t) \sin(\lambda_n W) \exp\left(-\alpha_p \lambda_n^2 (t-\tau)\right) d\tau \tag{21}$$

Temperature profile within the pre-melted region is then given by

$$T_2(x,t) = T_{2a}(x,t) + T_{2b}(x,t) + T_{2c}(x,t) \quad (22)$$

Based on this solution, temperature at the intersection of the pre-melted and phase change regions is determined by putting $x=W$ in equation (22)

$$T_w(W,t) = \sum_{n=0}^{\infty}\left[A_n \exp\left(-\alpha_p \lambda_n^2 t\right) + B_n(t) + C_n(t)\right]\sin(\lambda_n W) \quad (23)$$

Note that this temperature is an input needed for determining the temperature distribution in the phase change sub-problem, as discussed in section 2.1.

### 4-2-3. Iterative approach

Because the solutions for temperature distributions in the pre-melted and phase change regions are coupled with each other through continuity of temperature and heat flux at their intersecting boundary, the temperature fields in the two regions can be determined in an iterative fashion.

The iterative approach starts with an initial guess of the temperature $T_w(t)$ at the intersecting boundary between the two regions. Based on this, the temperature distribution in the phase change region as well as the location of the phase change front are determined as derived in section 2.1. Solution to this sub-problem provides the heat flux $q''(t)$ at the intersection between the two regions, given by equation (11). In the second step of the iterative approach, this heat flux is used to solve the conduction sub-problem. Based on the solution of this sub-problem, the temperature distribution at the intersection is determined using equation (23), which in turn serves to update $T_w(t)$ that is used for solving the phase change problem. If the difference between the previous and newly computed $T_w(t)$ is within acceptable tolerance, the computation is complete, otherwise, $T_w(t)$ is updated based on the new value and the phase change problem is solved again. Figure 2 shows a schematic of this iterative process. In practice, the old and new values of $T_w(t)$ are blended linearly using a blending factor $\beta$, which is a number between 0 and 1. It is important to note that the blending factor $\beta$ impacts stability and speed of convergence. The larger the value of $\beta$, the larger is the contribution of the newly computed temperature distribution in $T_w(t)$ for the new iteration, and therefore, the faster does the solution converge. However, this may result in instability, and therefore, a reasonably low value of $\beta$ is used throughout to maintain stability.

## 4-3. Results and discussion

### 4-3-1. Validation of the two sub-problems against finite element simulations

Prior to investigating the combined problem, analytical solutions for the separate phase change and thermal conduction sub-problems presented in sections 2.1 and 2.2 are first validated by comparing with finite element method (FEM) simulations.

In order to validate the phase change problem, the same geometry as Figure 1(c) is created and meshed in a finite element solver. Thermal conductivity, heat capacity and latent heat are assumed to be $k_l$=0.2 W/m.K, $C_p$=2250 J/kg.K and $L$=270.7 kJ/kg, corresponding to paraffin wax. The enthalpy method [1] is used in the simulations to account for by defining the phase change material as a binary mixture of liquid and solid, each with its associated properties and a reference enthalpy of fusion. A time-dependent temperature boundary condition given by $T_p(t) = 40 + 0.02t$ is implemented for validating the phase change problem discussed in section 2.1. Figure 3(a) plots the liquid-solid interface location $y(t)$ as a function of time and compares results from the analytical solution given by equation (11) and finite element simulations. This plot shows excellent agreement between the analytical solution and numerical simulations, with less than 1.8% deviation between the two. Similarly, the thermal conduction sub-problem in the pre-melted region is validated by comparison with finite element simulations. A time dependent temperature boundary condition $T_p(t) = 50 + 0.01t$ is applied at $x=0$, while a time-dependent heat flux $q''(t) = 200 + 10t$ leaving the pre-melted region is imposed on the boundary at $x=W$. A linear initial temperature $G(x) = 20 + 3000x$ is considered in the premelt region. Thermal properties of the pre-melted region are taken to be the same as in the phase change problem. Figure 3(b) shows a plot of temperature rise as a function of time at $x=W$ for both analytical model and FEM simulations. Similar to Figure 3(a), results indicate a good agreement between the analytical model and FEM simulations for the thermal conduction problem, with a worst-case deviation of only 1.5% between the two. The analytical model does not require mesh generation, which may result in reduced computational time. This approach also does not involve discretization errors that are possible in numerical simulation and offers the capability of solving such problems without the need for a commercial simulation tool.

Following the validation of the individual sub-problems as described above, the iterative integration of the two is characterized next.

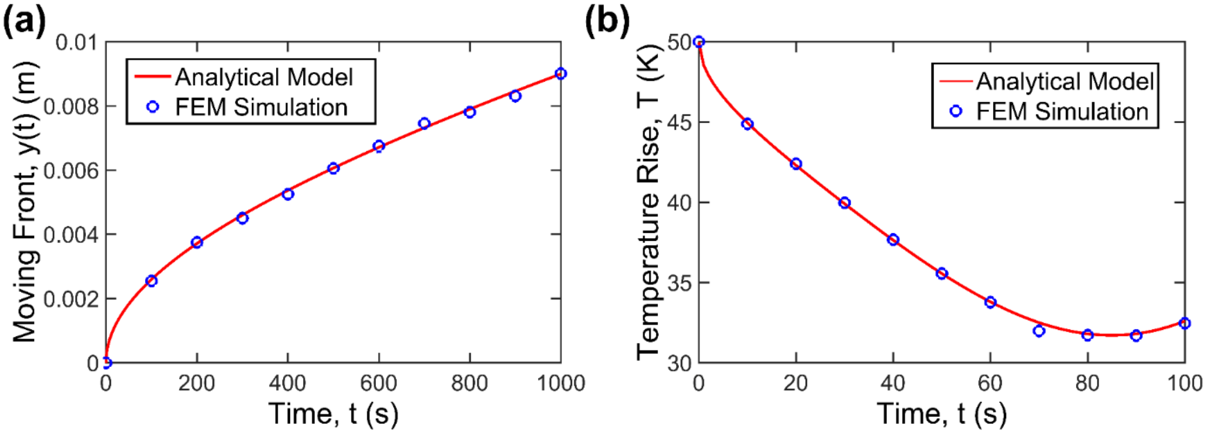

Figure 3. Comparison of the analytical solutions of the two sub-problems with Finite element simulations. (a) Plot of solid-liquid interface location *y(t)* as a function of time; (b) Plot of surface temperature rise at $x=W$ as a function of time for the conduction problem.

## 4-3-2. Validation of the iterative approach

In order to validate the complete problem, a phase change material of the same properties as the previous section is considered. The phase change material is initially at its melting temperature and the initial temperature of the pre-melted region is assumed to be $G(x) = 10 - 1000x$. A time-dependent boundary condition $T_0(t) = 100 + 0.1t$ is applied at *x=0*. This problem is solved using finite-element simulations as well as the iterative approach described in section 2, starting from an initial guess of temperature distribution. Figure 4 plots temperature rise at the intersection between the two regions as a function of time for different number of iterations, including the initial guess, labeled as 0. Figure 4 indicates a rapid change in temperature profile as a function of time for the first few iterations. However, as the number of iterations increases, temperature distribution stabilizes and converges to a single curve. It is seen that after six iterations, the change in temperature curve from one iteration to the next is negligible. This indicates that around six iterations may be sufficient in this case for convergence. In addition, it has been verified that the temperature distribution computed by the iterative approach is largely independent of the initial guess. When the initial guess is much different from the actual temperature distribution, the iterative approach takes a larger number of iterations to converge, but results in the same converged solution irrespective of the initial guess. Note that a blend factor of $\beta=0.1$ is used in this and all further computations in order to avoid instability.

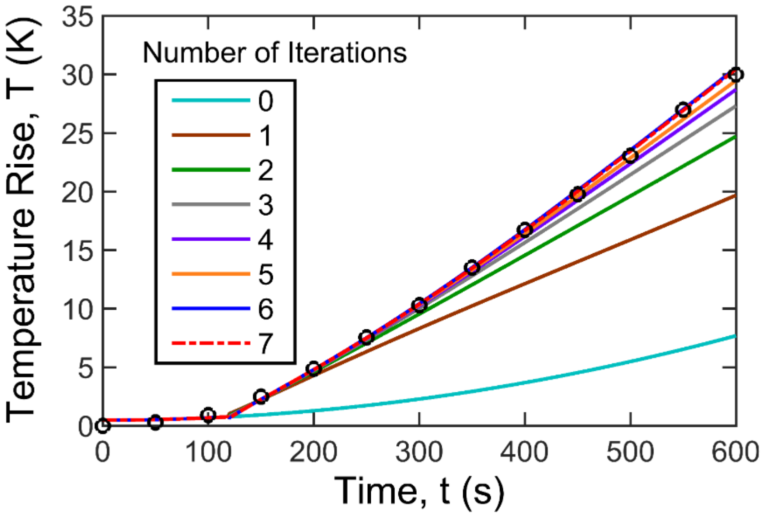

Figure 4. Validation of the iterative approach with finite element simulation for a linear time-dependent temperature $T_0(t)$ and a linear initial temperature distribution in the pre-melted region $G(x)$. Temperature rise at the intersection between the two regions $T_w(t)$ is plotted as a function of time for multiple iterations. Results from the finite element simulation is also plotted.

### 4-3-3. Effects of the initial condition

In this section, effect of the initial condition on the solid-liquid interface location $y(t)$ as well as temperature rise at the intersection between the two regions, $T_w(t)$ is investigated. In order to do so, the iterative approach is implemented for cases with different values of a constant initial condition $G$. The time-dependent temperature boundary condition is chosen to be $T_p(t) = 50 + 0.01t$ up to $t$=1000 s, while values 40, 60 and 80 °C are considered for the initial condition $G$. A heat-generating body such as a Li-ion cell generates heat in a periodic cycle. In this context, the different values of the initial condition $G$ may represent scenarios where the premelted region is initially at different temperatures due to the residual effect of previous cycles of heating. The choice of specific numbers for $G$ here ensure that the initial condition being studied here is not overwhelmed by the time-dependent boundary condition. Thermophysical properties of the pre-melted region and the melting solid are considered to be the same as the previous section. Figure 5(a) plots computed temperature rise at the intersection between the two regions, $T_w(t)$ as a function of time for different values of initial condition $G$. Results show that larger initial temperature results in higher interface temperature at early times. However, this effect of the initial temperature fades away as time increases, and after some time, the three plots are close to each other. At large times, initial thermal energy in the pre-melted region dissipates away, and only the effect of the boundary condition remains. To further confirm this, Figure 5(b) plots the solid liquid interface location $y(t)$ as a function of time for various values of initial condition $G$. It is seen that as initial temperature increases $y(t)$ increases as well due to more heat transfer from the pre-melted region to the melting solid body. For the parameters chosen here, significant impact of $G$ on the phase change propagation occurs in the first few hundred seconds, when the initial temperature is the predominant forcing function. As time passes, there remains only a constant offset between the curves for different values of $G$. In the context of Li-ion cells, the initial period during which significant impact of $G$ is present may be compared with the rest period between successive heat-generating periods to determine if the impact of $G$ dissipates away sufficiently during the rest period.

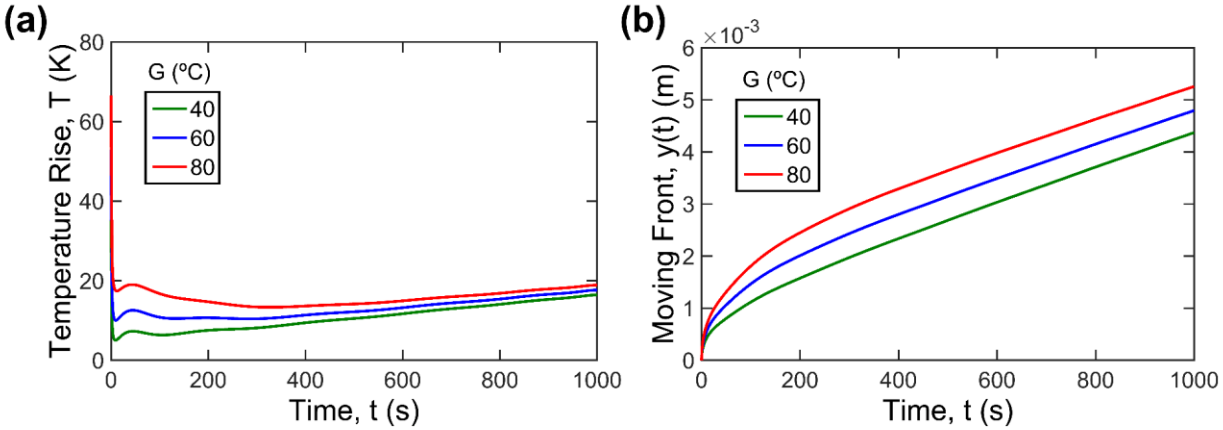

Figure 5. Effect of the initial temperature distribution *G(x)*. (a) Plot of temperature rise at the intersection between the two regions $T_w(t)$ as a function of time for multiple values of constant *G*. (b) Plot of solid-liquid interface location *y(t)* as a function of time for different values of *G*.

### 4-3-4. Effect of length of pre-melted region

Effect of the length of the pre-melted region *W* is investigated next. Four different lengths *W*=1, 5, 10, 15 and 20 mm are considered. A constant temperature boundary condition $T_0$=70 ºC is applied at *x=0* for 1000 s and the initial condition is considered to be *G*=60 ºC, similar to the previous section. All thermophysical properties are also the same as the previous sections. Figure 6(a) plots temperature rise at *x*=*W*, the intersection between the two regions as a function of time for four different values of *W*. Figure 6(b) shows a plot of the location of the solid-liquid interface *y(t)* as a function of time for these cases. These plots show that as the length of the pre-melted region increases, the temperature at *x*=*W* and location of the phase change front both decrease. This is however, not a linear effect – there is significant reduction between *W*=1 mm and *W*=5 mm, but the effect saturates at larger values of *W*. In general, the interface temperature is influenced by both the temperature boundary condition $T_0$ as well as the initial temperature *G(x)*. As *W* increases, the influence of $T_0$ decreases due to increased thermal resistance between the boundary condition and the phase change front. On the contrary, increasing *W* increases the effect of *G(x)* due to greater total initial energy in the pre-melted region. As a result, the net impact of increasing *W* depends on the relative magnitude of these two effects. Similarly, Figure 6(b) plots the solid-liquid interface location *y(t)* as a function of time. Results indicate that as *W* increases, the rate of phase change propagation decreases. This can be explained based on Figure 6(a), which shows larger values of *W* resulting in lower $T_w(t)$, and consequently lesser heat entering the phase change region, which eventually results in slower melting front propagation.

In addition to plots for different values of *W*, Figure 6(b) also plots the phase change propagation for the classical Stefan problem with the same boundary condition, for which, phase change propagation occurs at a rate proportional to $\sqrt{\alpha t}$ [4]. Figure 6(b) shows, as expected, that as the value of *W* gets close to zero, the phase change propagation predicted by the iterative model approaches that predicted by the classical Stefan problem.

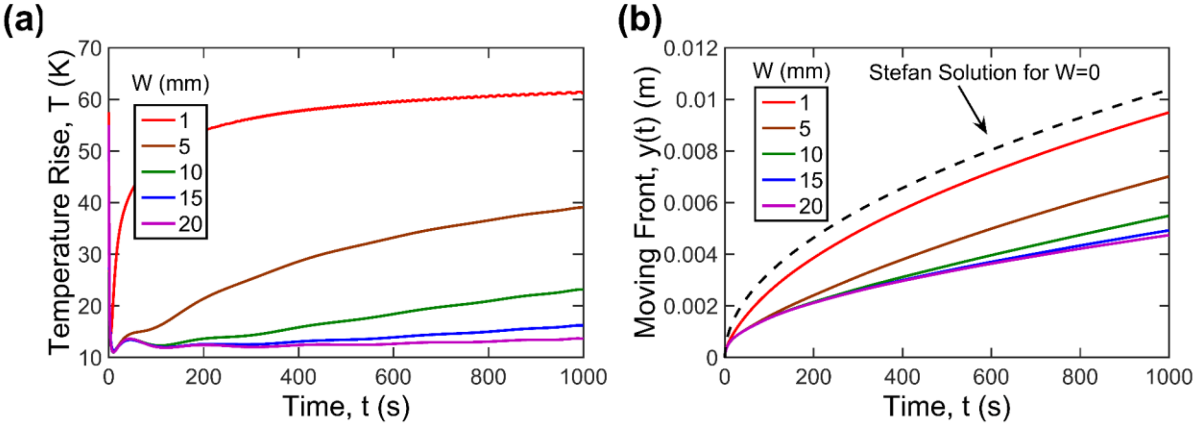

Figure 6. Effect of the pre-melted length *W*. (a) Plot of temperature rise at the intersection between the two regions $T_w(t)$ as a function of time for multiple values of *W*. (b) Plot of solid-liquid interface location *y(t)* as a function of time for different values of *W*. Result for the special case of *W* approaches to zero is also plotted.

### 4-3-5. Effect of pre-melted region thermal diffusivity

In order to investigate the effect of thermal diffusivity of the pre-melted region, $\alpha_p$, on the phase change process, the temperature field is computed using the iterative technique for different values of $\alpha_p$. In each case, a time-dependent temperature boundary condition $T_0 = 50 + 0.02t$ is applied at $x=0$, along with an initial temperature of $G=40$ ºC for the pre-melted region of length $W$=10 mm.

Figures 7(a) and 7(b) plot the temperature rise at the intersection between the two regions, $T_w(t)$ and the location of the phase change front, $y(t)$ respectively as functions of time for different values of $\alpha_p$. These plots show that the thermal diffusivity of the pre-melted region plays a key role in the phase change process. As $\alpha_p$ increases, temperature at $x=W$ goes up due to increased diffusion of thermal energy, both from the $T_0$ boundary condition as well as the initial condition $G$. The increased diffusion also explains the strong dependence of the rate of phase change propagation on thermal diffusivity of the pre-melted region, as shown in Figure 7(b).

While the trends shown in Figures 7(a) and 7(b) may be expected based on an understanding of the governing heat transfer physics, the iterative model makes it possible to quantifiably compute the impact of $\alpha_p$ on the phase change process, as shown in Figures 7(a) and 7(b).

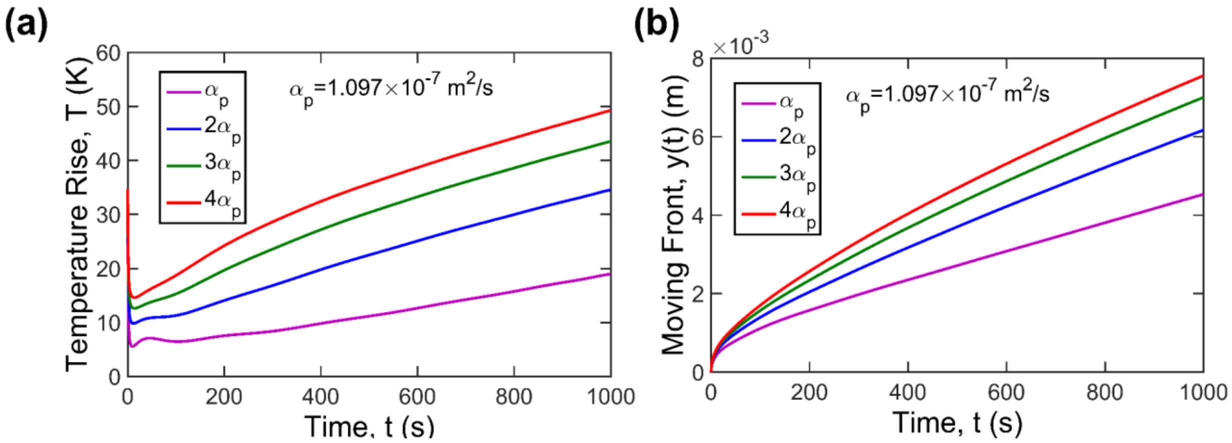

Figure 7. Effect of pre-melted region thermal diffusivity $\alpha_p$. (a) Plot of temperature rise at the intersection between the two regions $T_w(t)$ as a function of time for multiple values of $\alpha_p$. (b) Plot of solid-liquid interface location $y(t)$ as a function of time for different values of $\alpha_p$.

### 4-3-6. Effects of phase change material thermal diffusivity

Effect of thermal diffusivity of the phase change material, $\alpha_l$, on the phase change front location $y(t)$ and temperature rise at the intersection between the two regions is investigated next. In order to do so, different values of PCM thermal diffusivity, $\alpha_l$ are considered while keeping the initial condition, time-dependent boundary condition at $x$=0 and the pre-melted region $W$ the same as in sub-section 3.5. Figure 8(a) plots temperature rise at the intersection between the two regions, $T_w(t)$ as a function of time for different values of $\alpha_l$. In addition, Figure 8(b) plots the location of the phase change front $y(t)$ as a function of time for these cases. Results indicate that as the value of PCM thermal diffusivity increases, the temperature rise at the intersection between the two regions increases as well. This effect stems from an enhanced rate of thermal conduction from the pre-melted region into the phase change region at larger values of the PCM thermal diffusivity. Figure 8(b) also confirms this by showing an increase in the solid-liquid interface location in the phase change region at larger values of the PCM thermal diffusivity.

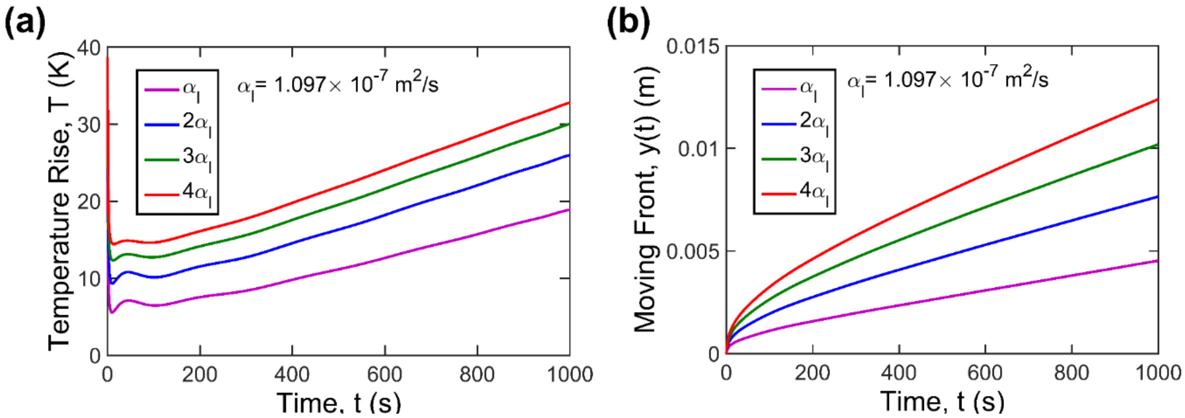

Figure 8. Effect of phase change material thermal diffusivity $\alpha_l$. (a) Plot of temperature rise at the intersection between the two regions $T_w(t)$ as a function of time for multiple values of $\alpha_l$. (b) Plot of solid-liquid interface location $y(t)$ as a function of time for different values of $\alpha_l$.

### 4-3-7. Phase change over multiple heat absorption cycles

In order to demonstrate the capability of the model discussed in this work to address problems of practical relevance, the effect of heat absorption from a hot source over multiple cycles is investigated. Heat absorption processes often occur in a cyclic fashion, which may result in the pre-melted scenario addressed in this work. A phase change material with the same thermal properties as previous sections is considered. Heat absorption occurs over multiple cycles, each of 1000 s duration. Between cycles, it is assumed that the PCM melted in the previous cycles cools back down until it reaches the melting temperature. In the first stage, the phase change material is initially solid at the melting temperature and in direct contact with a heat source maintained at 70 K above the melting temperature. The first stage can be described by a simple Stefan problem. Thermal analysis for subsequent stages is carried out using the analytical model, which, in each case accounts for the effect of the cumulative pre-melted liquid due to all previous heating periods. Figure 9 plots the location of the phase change front *y(t)* as a function of time for all four heating periods. In the first period, *y(t)* is proportional to $\sqrt{t}$ according to the solution of the Stefan problem. In subsequent periods, Figure 9 shows that the rate of growth of *y(t)* becomes slower and slower due to the growing pre-melted region.

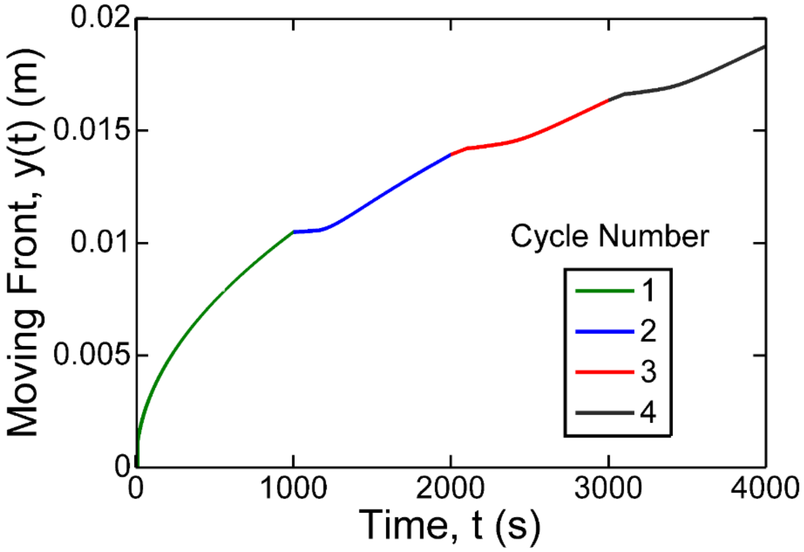

Figure 9. Propagation of phase change front with time during a four-cycle heat absorption process.

## 4-4. Conclusions

This work presents a theoretical solution for heat transfer problems involving phase change in which a pre-melted or pre-solidified region exists initially. Results derived here, based on an iterative approach, highlight the nature of heat transfer in a problem that can be used to model a number of engineering problems. While presented here for the specific case of melting, the solidification problem can also be addressed based on these results. Other complexities, such as convection in the liquid phase may also be accounted for, provided the underlying analytical solutions for the liquid phase are available. This work improves our fundamental understanding of phase change heat transfer, and facilitates analysis of heat transfer in applications related to energy conversion and thermal management.

## 4-5. Nomenclature

| | |
|---|---|
| $C_p$ | specific heat capacity (J/kgK) |
| $L$ | latent heat of fusion (J/kg) |
| $G$ | initial temperature distribution, relative to $T_m$ (K) |
| $f$ | non-dimensional, time-dependent temperature boundary condition, $f=(T_0-T_m)/(T_m-T_{ref})$ |
| $k$ | thermal conductivity (W/mK) |
| $q$ | heat flux (W/m$^2$) |
| $Ste$ | Stefan number, $Ste=C_p(T_{ref}-T_m)/L$ |
| $t$ | time (s) |
| $T$ | temperature, relative to $T_m$ (K) |
| $T_m$ | phase change temperature (K) |
| $T_0$ | time-dependent temperature at the boundary, relative to $T_m$ (K) |
| $T_{ref}$ | reference temperature, relative to $T_m$ (K) |
| $W$ | length of the initially melted/solidified region (m) |
| $x$ | spatial coordinate (m) |
| $y$ | location of phase change front (m) |
| $\alpha$ | thermal diffusivity (m$^2$/s) |
| $\lambda$ | eigenvalues |

Subscripts

| | |
|---|---|
| 1 | phase change region |
| 2 | pre-melt region |
| $\rho$ | mass density (kg/m$^3$) |

## 4-6. References

[1] D.W. Hahn, M.N. Özişik, Heat Conduction, (2012). doi:10.1002/9781118411285.

[2] R. Viskanta, Heat Transfer During Melting and Solidification of Metals, Journal of Heat Transfer. 110 (1988) 1205. doi:10.1115/1.3250621.

[3] N. Seki, S. Fukusako, Fundamental Aspects Of Analytical And Numerical Methods On Freezing And Melting Heat-Transfer Problems, Annual Review of Heat Transfer. 1 (1987) 351–402. doi:10.1615/annualrevheattransfer.v1.90.

[4] J. Stefan, Uber die Theorie des Eisbildung, Insbesonder uber die Eisbildung im Polarmere, Ann. Phys. u Chem., Neue Folge, 42 (1891) pp. 269-286.

[5] V. Alexiades, Mathematical Modeling of Melting and Freezing Processes, Routledge, (2017).

[6] S. Paterson, Propagation of a boundary of fusion, Glasgow Mathematical Journal, 1, (1952) 42-47.

[7] K.C. Cheng, and N. Seki, eds., Freezing and Melting Heat Transfer in Engineering: Selected Topics on Ice-Water Systems and Welding and Casting Processes, CRC Press (1991).

[8] T.R. Goodman, The Heat Balance Integral and its Application to Problems Involving Change of Phase, Journal of Mathematical Analysis and Applications, 80(2), (1958) 335–342.

[9] L.N. Gutman, On the problem of heat transfer in phase-change materials for small Stefan numbers, International Journal of Heat and Mass Transfer. 29 (1986) 921–926. doi:10.1016/0017-9310(86)90187-0.

[10] J. Cannon, M. Primicerio, Remarks on the one-phase Stefan problem for the heat equation with the flux prescribed on the fixed boundary, Journal of Mathematical Analysis and Applications. 35 (1971) 361–373. doi:10.1016/0022-247x(71)90223-x.

[11] T.R. Tien, Freezing of Semi-Infinite Slab with Time Dependent Surface Temperature — an Extension of Neumann′s Solution, Transf. AIME, 233, (1965) 1887–1891.

[12] S.H. Cho, J.E. Sunderland, Approximate Temperature Distribution for Phase Change of a Semi-Infinite Body, Journal of Heat Transfer. 103 (1981) 401. doi:10.1115/1.3244476.

[13] G. Lock, J. Gunderson, D. Quon, J. Donnelly, A study of one-dimensional ice formation with particular reference to periodic growth and decay, International Journal of Heat and Mass Transfer. 12 (1969) 1343–1352. doi:10.1016/0017-9310(69)90021-0.

[14] J. Caldwell, Y. Kwan, On the perturbation method for the Stefan problem with time-dependent boundary conditions, International Journal of Heat and Mass Transfer. 46 (2003) 1497–1501.

[15] M. Parhizi, A. Jain, Solution of the phase change Stefan problem with time-dependent heat flux using perturbation method, Journal of Heat and Mass Transfer, ASME, (2018)

[16] G.S. Cole, W.C. Winegard, Thermal Convection Ahead of a Solid-Liquid Interface, Canadian Metallurgical Quarterly. 1 (1962) 29–31. doi:10.1179/cmq.1962.1.1.29.

[17] J. Szekely, V. Stanek, Natural convection transients and their effects in unidirectional solidification, Metallurgical Transactions. 1 (1970) 2243–2251. doi:10.1007/bf02643441.

[18] M. Parhizi, A. Jain, Analytical Modeling and Optimization of Phase Change Thermal Management of a Li-ion Battery Pack, In Review, Applied Thermal Engineering, (2018).

[19] K. Shah, V. Vishwakarma, A. Jain, Measurement of Multiscale Thermal Transport Phenomena in Li-Ion Cells: A Review, Journal of Electrochemical Energy Conversion and Storage. 13 (2016) 030801. doi:10.1115/1.4034413.

[20] L. Choobineh, A. Jain, Analytical Solution for Steady-State and Transient Temperature Fields in Vertically Stacked 3-D Integrated Circuits, IEEE Transactions on Components, Packaging and Manufacturing Technology. 2 (2012) 2031–2039. doi:10.1109/tcpmt.2012.2213820.

[21] D. Chalise, K. Shah, R. Prasher, A. Jain, Conjugate Heat Transfer Analysis of Thermal Management of a Li-Ion Battery Pack, Journal of Electrochemical Energy Conversion and Storage. 15 (2017) 011008. doi:10.1115/1.4038258.

[22] K. Shah, A. Jain, An Iterative, Analytical Method for Solving Conjugate Heat Transfer Problems, International Journal of Heat and Mass Transfer. 90 (2015) 1232–1240. doi:10.1016/j.ijheatmasstransfer.2015.07.056.

[23] G.E. Myers, Analytical Methods in Conduction Heat Transfer, 2nd Ed, AMCHT Publications, Madison, WI, (1998).

[24] D. Anthony, D. Wong, D. Wetz, A. Jain, Non-invasive measurement of internal temperature of a cylindrical Li-ion cell during high-rate discharge, International Journal of Heat and Mass Transfer. 111 (2017) 223–231. doi:10.1016/j.ijheatmasstransfer.2017.03.095.

# Chapter 5

# Analytical Modeling and Optimization of Phase Change Thermal Management of a Li-ion Battery Pack

**Published as**: Parhizi, M., & Jain, A. (2019). Analytical modeling and optimization of phase change thermal management of a Li-ion battery pack. *Applied Thermal Engineering*, *148*, 229-237.

## 5-1. Introduction

Li-ion cells are used commonly for energy storage and conversion in a variety of applications including electric vehicles, renewable energy storage, consumer electronics, etc. [1-2]. Despite favorable electrochemical characteristics compared to competing technologies, Li-ion cells often suffer from overheating due to excessive heat generation [3,4], which has severely limited the application of this technology. Overheating is undesirable for both safety and performance. For example, current draw from a cell is often throttled in order to limit temperature rise, which reduces cell performance and lowers the power density of the battery pack. Excessive temperature rise in a Li-ion cell may also result in thermal runaway [5-8], which causes severe safety problems due to fire and explosion. Some fundamental reasons behind these severe thermal challenges in a Li-ion cell include poor thermal conductivity within the cell [9-10], non-linear temperature-dependent heat generation [7-8], particularly at high temperatures, and the stacking of cells very close to each other in a battery pack in order to maximize energy storage density [11].

Due to the reasons outlined above, thermal management of a Li-ion battery pack is of utmost importance, particularly for aggressive applications that require large discharge rates. For reference, discharge rate of a cell is often represented by its C-rate [3,4], which is the reciprocal of the time needed for complete discharge in hours. The larger the C-rate, the more aggressive is the discharge process in terms of heat generation rate [3,4]. A number of thermal management approaches have been investigated in the past, and are well summarized in multiple review papers [3,12]. These include cold plate cooling [13,14], single phase convective cooling [15,16], heat pipe cooling [17,18], etc. Innovations in materials within the cell have been pursued in order to improve thermal conduction within the cell. Both water and air have been used as coolants in battery packs [11,16]. A variety of heat pipe configurations including oscillating heat pipes have been implemented, both within a single cell and between cells in a battery pack [17,18]. The thermal effect of Boron Nitride coating on the cell casing has been investigated [19].

In contrast to thermal management approaches outlined above, phase change cooling involving melting and solidification may offer many advantages. A much greater heat removal rate may be achieved through phase change cooling compared to single phase thermal management due to the large latent heat associated with phase change. Due to its promising nature, experimental investigation of phase change cooling of Li-ion cells has been reported in several recent papers [20-24]. Experimental measurements of the performance of phase change materials (PCMs) such as paraffin wax for cooling of Li-ion cells have been carried out, and a significant reduction in cell temperature has been reported [21, 25]. A number of innovative materials and composites, such as metal foams have been investigated for further improving the performance of phase change cooling through thermal conductivity enhancement [20,21,24,25]. Experiments have shown that phase change cooling can prevent propagation of thermal runaway induced by nail penetration to neighboring cells [22]. Despite the various advantages of phase change cooling, however, it may lead to increased system complexity. Particularly, in the context of a Li-ion battery pack, the insertion of phase change material between cells reduces energy storage density. As a result, there is a need for careful co-optimization of PCM cooling with other system-level performance characteristics, for which, theoretical modeling is critical.

In comparison with the extensive literature available on measurements of phase change thermal management in Li-ion cells, there is a lack of theoretical modeling of these processes. Rigorous theoretical modeling is critical not only for fully optimizing the benefits of phase change cooling, but also for balancing trade-offs that exist with other system-level performance parameters such as energy storage density. Some simulation models using commercial finite-element tools are available [21,26], but these do not provide good analytical insight into the fundamental nature of the problem. Rigorous theoretical analysis of this problem is complicated considerably by the non-linear nature of phase change [27], making it difficult to analyze using standard theoretical tools. The coupling between phase change heat transfer with thermal conduction within the cell as well as electrochemical heat generation further complicates this problem. From a heat transfer perspective, this is a conjugate problem [28-30], involving thermal conduction in a heat-generating body and phase change heat transfer in the coolant. While these two modes of heat transfer have been individually analyzed extensively, the conjugate problem has not been paid much attention. For example, while the well-known Stefan problem addresses phase change in an infinite body with a constant temperature boundary condition [27], the presence of thermal conduction in a heat-generating body – the Li-ion cell in this case – makes the problem much more difficult to solve.

A good theoretical understanding of this problem is important for many practical reasons. The inclusion of a phase change material in a battery pack reduces overall energy density, since the phase change material increases pack weight and volume without contributing to electrochemical energy storage. A robust theoretical model can help understand the minimum amount of phase change material needed for a given cell undergoing a specific charge or discharge process, and therefore avoid overdesign of thermal management. A robust theoretical model can also help predict the effect of PCM cooling on internal temperature of the cell, which is critical for cell performance and safety, but is difficult to measure directly. Predictions from a theoretical model can also be used for accurate thermal management design in conditions where experimental data may not be available in advance. A theoretical model also helps understand the parametric dependence of the thermal characteristics of the system on various parameters such as thermal properties of the cell and phase change material, geometry, dimensions, etc.

This work presents a theoretical model for predicting the transient temperature distribution in the cooling of a heat-generating Li-ion cell with a phase change material. The novelty of the theoretical approach in this work lies in solving the energy conservation equations in the two bodies in an iterative fashion to determine the transient temperature fields in both. This approach offers significantly reduced computational time compared to finite element simulations, and provides key insights into the fundamental nature of PCM cooling of Li-ion cells. A key result from this work is that while improving thermal conductivity of the PCM reduces cell surface temperature through greater melting rate, it does not effectively cool the core of the cell, which remains a key shortcoming of PCM cooling. Most of the past experimental work evaluates the effectiveness of PCM cooling based on surface temperature measurement alone, whereas, this work shows that PCM cooling provides only limited benefit to the core temperature. Results show that improving thermal conductivity of the cell is critical for fully benefiting from PCM thermal management. Another key contribution of this work is the analysis of the system-level trade-off between thermal management effectiveness and energy storage density. This work not only develops a good theoretical understanding of heat transfer during phase change thermal management of a Li-ion cell, but also contributes towards understanding key design trade-offs in practical thermal management systems for Li-ion cells.

## 5-2. Mathematical Modeling

Figure 1(a) shows a schematic of the geometry of a battery pack with multiple prismatic Li-ion cells being cooled by a phase change material (PCM) inserted between cells. Assuming uniformly spaced cells in a single direction, symmetry could be used to analyze only one part of the pack, shown in Figure 1(b). Within this region, the relevant heat transfer processes include heat generation inside the cell of half-thickness *W*, thermal conduction within the cell, heat transfer from the cell into the phase change material at the cell-PCM interface, conduction into the PCM and phase change at the liquid-solid interface, located by $x=y(t)$. Thermal contact resistance between the cell and PCM is neglected due to the expected intimate contact between the cell surface and PCM that melts and solidifies repeatedly. Note that the location of the liquid-solid interface, $y(t)$, is a function of time – as more and more heat is absorbed by the PCM, $y(t)$ increases with time.

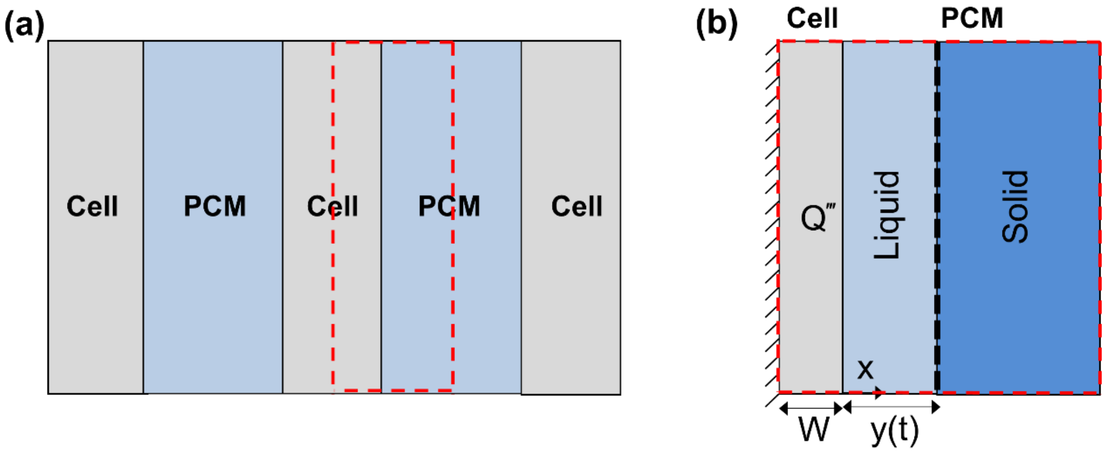

Figure 1. (a) Schematic of a prismatic Li-ion battery pack with phase change cooling; (b) Schematic of the overall conjugate heat transfer problem.

Given the complicated and coupled nature of this conjugate heat transfer problem, a direct solution may not be possible. Instead, this problem is solved by splitting into two sub-problems, which are solved individually while considering continuity of temperature and heat flux at the cell-PCM interface. The two sub-problems are shown schematically in Figure 2. The cell sub-problem involves a certain heat flux $q''(t)$ leaving the cell at the cell-PCM interface, while the PCM sub-problem involves a certain time-dependent temperature $T_0(t)$ at the interface. Both $q''(t)$ and $T_0(t)$ are unknown. However, this problem can be solved in an iterative process, wherein a certain $T_0(t)$ is guessed and used to solve the PCM sub-problem. Based on the solution of this problem, interfacial heat flux is calculated and used to solve the cell problem, which requires the heat flux as an input. The solution of the cell problem is then used to determine the interface temperature $T_0(t)$, which is used to improve the initial guess of the interfacial temperature. The process is then repeated iteratively until there is acceptably small change in $T_0(t)$ from one iteration to the next. Figure 3 shows a flowchart of the iterative method for determining the solution of the conjugate heat transfer problem.

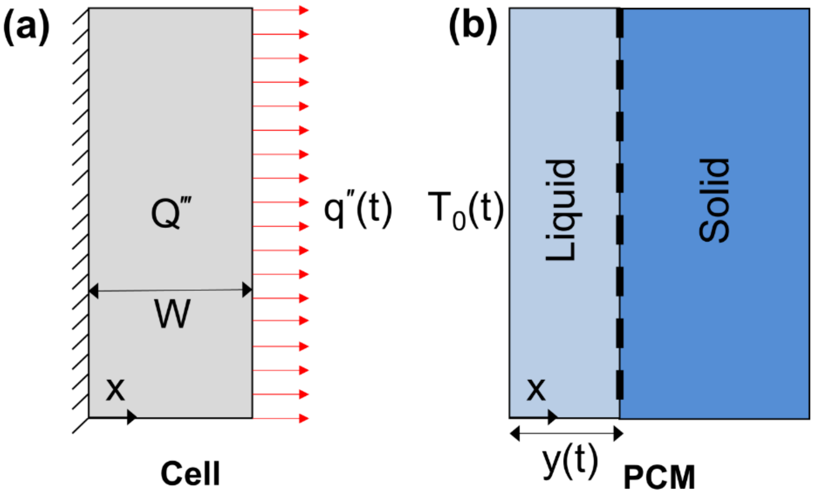

Figure 2. Schematic of the two heat transfer sub-problems: (a) Cell problem; (b) PCM problem.

Such an iterative process has been used for solving a variety of conjugate problems [11,29], including the problem of single phase cooling of cells in a Li-ion battery pack. The novelty of the approach adopted in this work lies in the conjugate analysis of the much more complicated phase change problem. Further, unlike past papers, where only steady state problems were solved

[11,29], this work addresses a more realistic, transient problem, involving increasing cell temperature with time, as well as a phase change front in the PCM that advances with time.

The iterative approach described above requires analytical solutions for the cell and PCM sub-problems, given the interfacial heat flux and temperature respectively as functions of time. These solutions are derived in the next two sub-sections.

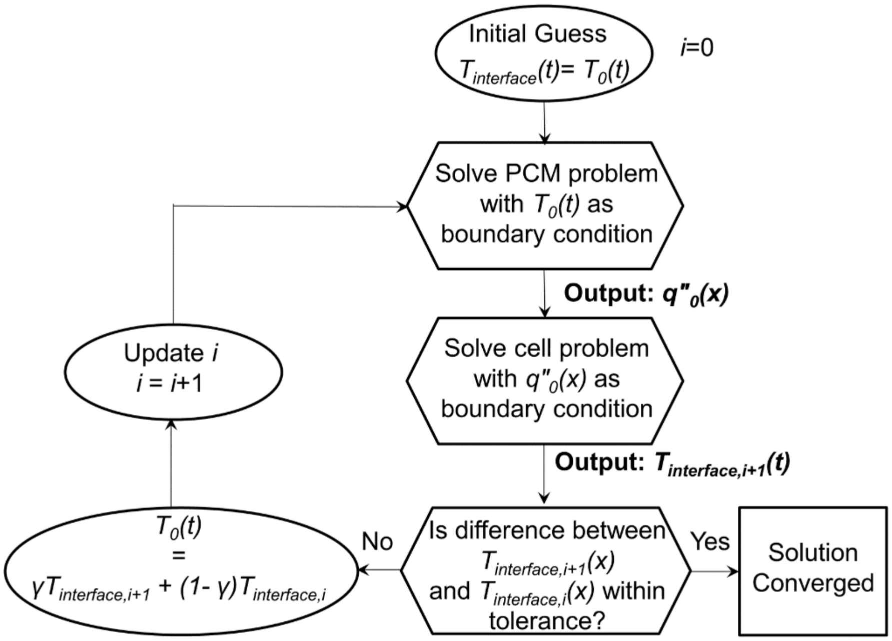

Figure 3. Flowchart of the iterative process for determining the solution of the conjugate heat transfer problem.

### 5-2-1. Solution for the PCM sub-problem

The PCM sub-problem involves a one-dimensional phase change material of thermal conductivity $k$, specific heat capacity $C_p$, latent heat $L$ and mass density $\rho$ being heated up by an imposed temperature $T_0(t)$ at the boundary $x$=0, as shown in Figure 2(b). Due to this temperature boundary condition, the PCM slowly melts, starting at $x$=0. The liquid-solid interface, located at $x=y(t)$ progresses towards the right as time passes, and more and more liquid is formed due to phase change. This is a generalization of the well-known Stefan problem, in which a constant temperature boundary condition is imposed, as opposed to a time dependent $T_0(t)$ considered here. The governing energy conservation equation for $T_p(x,t)$, the temperature field in the melted PCM is

$$\frac{\partial^2 T_p}{\partial x^2} = \frac{\rho C_p}{k}\frac{\partial T_p}{\partial t} \qquad 0 \le x \le y(t) \tag{1}$$

along with the following boundary condition

$$T_p(x,t) = T_0(t) \qquad \text{at } x=0 \tag{2}$$

where $T_0(t)$ is the imposed time-dependent temperature boundary condition on the face of the PCM.

In addition, energy conservation and continuity of temperature at liquid-solid front requires that

$$T_p(x,t) = T_m \qquad \text{at } x=y(t) \tag{3}$$

and

$$-k\left(\frac{\partial T_p}{\partial x}\right)_{x=y(t)} = \rho L\frac{dy(t)}{dt} \qquad \text{at } x=y(t) \tag{4}$$

where $T_m$ is the PCM melting temperature. Equations (1) through (4) represent a non-linear phase change problem, which is further complicated by the time-dependence in the boundary condition at $x=0$. While a direct analytical solution for this general problem is likely not possible, several approximate analytical methods have been presented in the literature for solving similar problems, including integral methods [31], perturbation methods [30], etc. In this case, the perturbation method [30] is used. Briefly, the solution is assumed to be a power series expansion based on the

Stefan number, $Ste = \frac{C_p(T_m - T_{ref})}{L}$ where $T_{ref}$ is a reference temperature [27,30]. The problem is transformed in order to change one of the dependent variables from time to the interface location *y(t)*. The power series form of the temperature solution is inserted into the governing equation and simplified using boundary conditions. Through a term-by-term comparison, a solution for the temperature profile in the liquid is derived in terms of the interface location. Finally, the location of the phase change front itself is determined by using the principle of energy conservation at the phase change front [30], given by equation (4). The interface heat flux is then determined by differentiating the liquid temperature distribution as follows:

$$q''_{PCM}(t) = -k\left(T_m - T_{ref}\right)\left[\begin{array}{l} -\dfrac{f(t)}{y(t)} - Ste\dfrac{f(t)\left(f(t) + 2\dfrac{f'(t)}{y'(t)}y(t)\right)}{6y(t)} + \\ Ste^2\dfrac{f(t)\left(40\left(\dfrac{f'(t)}{y'(t)}\right)^2 y^2(t) + 85f(t)\dfrac{f'(t)}{y'(t)}y(t) + 19f^2(t) + 8\dfrac{f''(t)}{y'^2(t)}f(t)y^2(t)\right)}{360y(t)} \end{array}\right] \tag{5}$$

where *f(t)* is the non-dimensional time-dependent boundary temperature given by [30]

$$f(t) = \frac{T_0(t) - T_m}{T_m - T_{ref}} \tag{6}$$

and the liquid-solid interface location, *y(t)* is given by [30]

$$y(t) = \left[2\alpha(Ste)\int_0^t f(\tau)\left(1 - \frac{Ste}{3}f(\tau) + \frac{7Ste^2}{45}f(\tau)^2\right)d\tau\right]^{1/2} \tag{7}$$

where $\alpha$ is the PCM thermal diffusivity. The interfacial heat flux determined in this manner from equation (5) can be used to solve the cell sub-problem as described below.

5-2-2. Solution for the cell sub-problem

The cell sub-problem involves a one-dimensional body of thickness *H,* thermal conductivity $k_c$ and thermal diffusivity $\alpha_c$ generating heat at a volumetric rate of $Q'''$, as shown in Figure 2(a). There is zero heat flux at $x$=0 due to symmetry, whereas a certain outgoing heat flux $q''(t)$ is imposed on the boundary at $x=W$. The governing energy conservation equation for the temperature distribution in the cell, $T_c(x,t)$ is

$$\frac{\partial^2 T_c}{\partial x^2} + \frac{Q'''}{k_c} = \frac{1}{\alpha_c}\frac{\partial T_c}{\partial t} \tag{8}$$

Boundary conditions associated with equation (8) are

$$\frac{\partial T_c}{\partial x} = 0 \qquad \text{at } x=0 \tag{9}$$

and

$$-k_c\frac{\partial T_c}{\partial x} = q''(t) \qquad \text{at } x=W \tag{10}$$

Due to the two non-homogeneities in the problem, the solution is split into two parts, each of which account for one of the non-homogeneities. The solution for the heat generation part is quite straightforward as follows:

$$T_{c1}(t) = \frac{Q'''}{\rho C_p} t \tag{11}$$

The method of undetermined parameters [32,33] is used for deriving the second part of the solution that accounts for the time-dependent heat flux. The solution is assumed to be a series sum of eigenfunctions of the corresponding homogeneous problem.

$$T_{c2}(x,t) = \sum_{n=0}^{\infty} C_n(t) Cos(\lambda_n x) \tag{12}$$

Where $\lambda_n = \frac{n\pi}{W}$ are the eigenvalues of the corresponding homogenous problem. The unknown coefficients *$C_n(t)$* in equation (12) are determined by differentiating equation (12) with respect to time, substituting in the governing energy equation and using the boundary conditions and the principle of orthogonality to simplify. This results in an ordinary differential equation for *$C_n(t)$*

$$C_n' + \alpha_c \lambda_n^2 C_n = \frac{\alpha_c}{N}\left(\frac{-q''(t)}{k_c}\right) Cosn\pi \tag{13}$$

for which, the solution, assuming zero temperature rise at t=0 is

$$C_n = -\frac{\alpha_c}{k_c W}\int_0^t q''(t)dt + \int_0^t -\frac{2\alpha_c}{k_c W} Cos(\lambda_n W) q''(t)\exp(-\alpha_c \lambda_n^2 (t-\tau))d\tau \tag{14}$$

where $N_n$ is the eigenvalue norm.

This completes the solution of the cell sub-problem shown in Figure 2(a), from where the interface temperature is found to be

$$T_{\text{int}\,erface}(t) = T_c(x=W,t) = -\frac{\alpha_c}{k_c W}\int_0^t q''(t)dt + \sum_{n=1}^{\infty} -\frac{2\alpha_c}{k_c W} Cos^2(\lambda_n W)\int_0^t q''(t)\exp(-\alpha_c \lambda_n^2 (t-\tau))d\tau + \frac{Q'''}{\rho C_p} t \tag{15}$$

Note that in this case, the internal heat generation rate $Q'''$ heats up the cell whereas the heat flux $q''(t)$ may cool the cell down. Therefore, for this sub-problem, the cell temperature may go up or down with time depending on the relative magnitudes of $Q'''$ and $q''(t)$.

### 5-2-3. Iterative process

The iterative procedure for solving the conjugate problem starts with guessing an initial cell-PCM interface temperature curve, $T_0(t)$. The PCM sub-problem is then solved using $T_0(t)$ as the boundary condition as discussed in section 2.2. The solution provides the cell-PCM interface heat flux, $q''(t)$ which can be used to solve the cell sub-problem. Solution to the cell sub-problem provides a new interface temperature $T_0(t)_{new}$, which is used to repeat the iterative procedure. The interface heat flux leaving the cell, $q''(t)$, may be large in the first few iterations due to the large temperature gradient between the cell and PCM caused by the initial interface temperature. This large outgoing heat flux may result in negative temperature particularly if the initial interface temperature is not accurate. To avoid such problems, the coupled interface temperature is blended with that from the previous iteration using a low value of the blending factor in order to prevent instability in the iterative process. Figure 3 shows a flowchart of the iterative method, including the blending process.

In summary, the iterative theoretical model presented in this section predicts temperature distribution in the cell and the surrounding PCM, taking into account various heat generation and heat transfer processes, including propagation of the phase change front. The next section presents a discussion of validation of and various results obtained based on this theoretical model.

## 5-3. Results and discussion

### 5-3-1. Validation and optimization of analytical model

Since the analytical solution approach is iterative in nature, it is important to track the predicted temperature distribution over multiple iterations. A realistic case is considered, wherein a 20 mm thick cell generating heat at 87000 W/m$^3$ corresponding to a discharge rate, also known as the C-rate of 5C [34] is being cooled by paraffin wax, a commonly used phase change material of thermal conductivity $k$=0.2 W/m.K and latent heat $L$=270.7 kJ/kg [25]. For reference, the C-rate of a Li-ion cell refers to the reciprocal of the time in hours needed for completely the discharging the cell. The higher the value of the C-rate, the more aggressive is the discharge process.

In these conditions, the computed temperature at the cell-PCM interface is plotted as a function of time for multiple number of iterations in Figure 4. The initial guess for the interface temperature as a function of time is also plotted. Figure 4 shows that the temperature distribution changes rapidly in the first few iterations, but eventually stabilizes as it converges. Beyond seven iterations, there is minimal change in the temperature distribution from one iteration to the next. This shows that for the conditions assumed here, around seven iterations are sufficient for obtaining the analytical solution. This is an important insight in optimizing the computation of the analytical model since each iteration requires additional computation time. Additional computations have been carried out with multiple other initial guesses to verify that the temperature field converges to the same value regardless of the initial guess. Note that these results are obtained with a blend factor $\gamma$=0.1. The convergence could be obtained faster with a large value of $\gamma$. However, in case the initially assumed temperature distribution deviates significantly from the correct temperature distribution, a large value of $\gamma$ may lead to instability. As a result, a conservative value of $\gamma$=0.1 is used throughout this work.

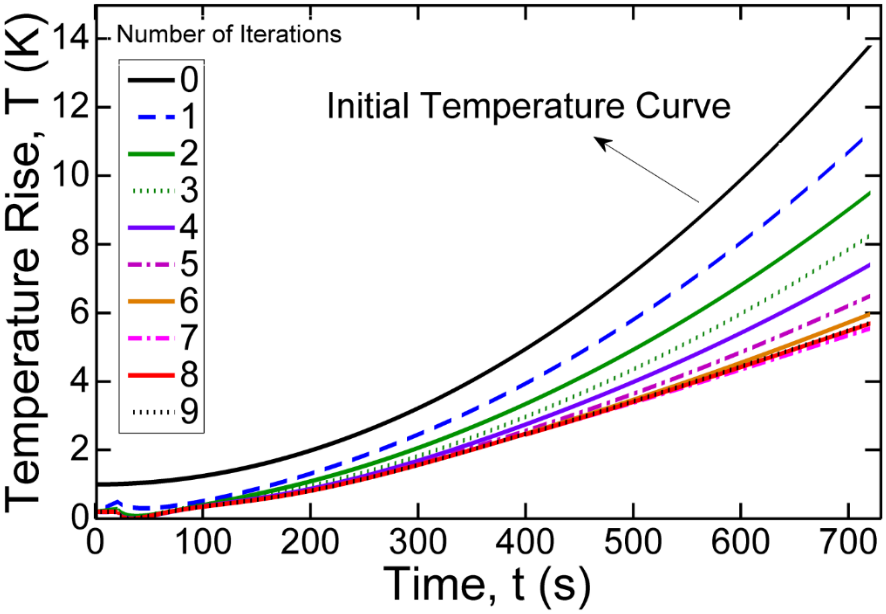

Figure 4. Cell-PCM interfacial temperature rise, $T_0(t)$ as a function of time for multiple number of iterations, including the initial temperature curve. Values for PCM thermal conductivity and latent heat are $k$=0.2 Wm$^{-1}$K$^{-1}$ and L=270.7 kJkg$^{-1}$ respectively. The cell generates heat at 87000 W/m$^3$, corresponding to 5C discharge rate. Plot indicates that the temperature distribution converges within around seven iterations.

Analytical solutions for the two sub-problems discussed in sections 2.1 and 2.2 are also validated by comparison of the predicted temperature distribution for specific cases with finite-element simulation results for a set of parameters representative of realistic conditions. In order to validate the PCM model, a one-dimensional transient finite-element simulation is carried out in ANSYS CFX. A phase change material of thermal conductivity $k$=0.2 W/m.K and latent heat $L$=270.7 kJ/kg is considered. A time-dependent temperature boundary condition $T_0(t) = 20 + \frac{t}{100}$ is imposed on the material at $x$=0 for 1000 seconds. To carry out the phase change simulation, same geometry as figure 2(b) is created in ANSYS CFX. A mesh sensitivity study shows that 1.5

million node is needed for the results be independent of mesh. PCM is defined as a homogenous binary mixture of liquid and solid where the liquid part has the specific reference enthalpy of 270.7 kJ/kg. Saturation properties for the binary mixture is defined as well based on the PCM properties. The analytical model is used for computing the melting front *y(t)* and compared against finite-element simulation results. As shown in Figure 5(a), the two are in good agreement with each other. While the analytical model can be computed quite rapidly, within 60 seconds, the transient finite-element simulation takes about 20 minutes, even when not accounting for the setup time needed for gridding prior to the finite element computations.

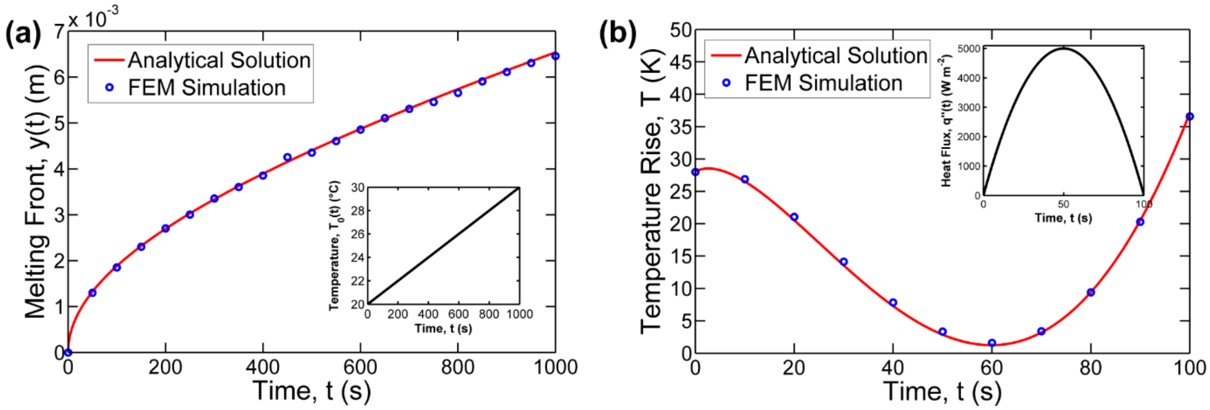

Figure 5. Comparison of the analytical solution (red curves) and a finite element simulation carried out in ANSYS-CFX (blue circles) for the two sub-problems: (a) PCM melting front, *y(t)* as a function of time for a time-dependent temperature boundary condition. (b) Cell core temperature rise as a function of time for a given heat flux $q''(t)$ on the $x=W$ boundary.

Similar to the PCM sub-problem, the cell sub-problem discussed in section 2.2 is also validated by comparison against finite-element simulations. For a cell of thermal conductivity $k$=0.2 Wm$^{-1}$K$^{-1}$ and generating 10$^{6}$ W/m$^{3}$ with a given heat flux $q''(t)$ on its boundary at $x$=$W$, the predicted interface temperature as a function of time and compared against finite element simulation results in Figure 5(b). The interfacial heat flux as a function of time, $q''(t)$ assumed for this comparison is also shown in Figure 5(b). In this case, the interfacial temperature initially decreases due to the increase in heat flux leaving the cell and insufficient generated heat reaching the boundary. As time progresses, however, more and more heat generated in the cell reaches the boundary, and also, heat flux imposed on the boundary decreases, resulting in an increase in the cell surface temperature. Throughout the entire period, the predicted interface temperature is in good agreement with finite-element simulation results. In this case, 500 eigenvalues are considered for the analytical solution represented by equation (15). It is verified that additional eigenvalues do not significantly change the predicted temperature distribution.

Comparison of the analytical models against finite-element simulations shown in Figure 5 provides a validation of these models. Phase change based thermal management of Li-ion cells in a variety of scenarios in analyzed next.

### 5-3-2. Effect of phase change material properties

Thermal properties of the phase change material are likely to be important for the design of phase change based thermal management because this process is driven primarily by heat absorption during phase change and because heat entering the phase change material must first conduct through the melted liquid before being absorbed in the phase change process. While phase change materials have reasonably high latent heat, the thermal conductivity is usually low, and multiple papers have attempted to improve thermal conductivity through various mechanisms such as insertion of metal foams, fillers, etc. [20-25]. The expected impact of these thermal property enhancements on cooling effectiveness is investigated here.

For a cell with a thermal conductivity of $k_c$=0.2 $Wm^{-1}K^{-1}$ – a realistic value based on past measurements [9] – undergoing 10C discharge, peak temperature rise in the cell that occurs at its core is plotted in Figure 6(a) as a function of time for multiple values of the phase change material thermal conductivity, assuming the latent heat to be 270.7 kJ/kg. Figure 6(b) shows the corresponding cell-PCM interface temperature rise as a function of time. These plots show that while improving PCM thermal conductivity has a significant impact on the cell surface temperature rise, there is only a minor change in cell core temperature rise. This happens because while a greater PCM thermal conductivity ensures heater heat transfer through the PCM, and therefore, reduced cell surface temperature, the core temperature remains relatively unaffected due to the slower rate of thermal conduction within the cell. The impact of improving PCM thermal conductivity – a heavily researched topic – on the core temperature of the cell saturates once the thermal conductivity reaches a threshold. Beyond that, there is minimal impact of further improving PCM thermal conductivity on the cell core temperature because the cell thermal conductivity is the rate-limiting property. This is a critical issue for safety of Li-ion cells and highlights a key limitation of external, phase change cooling of the cell.

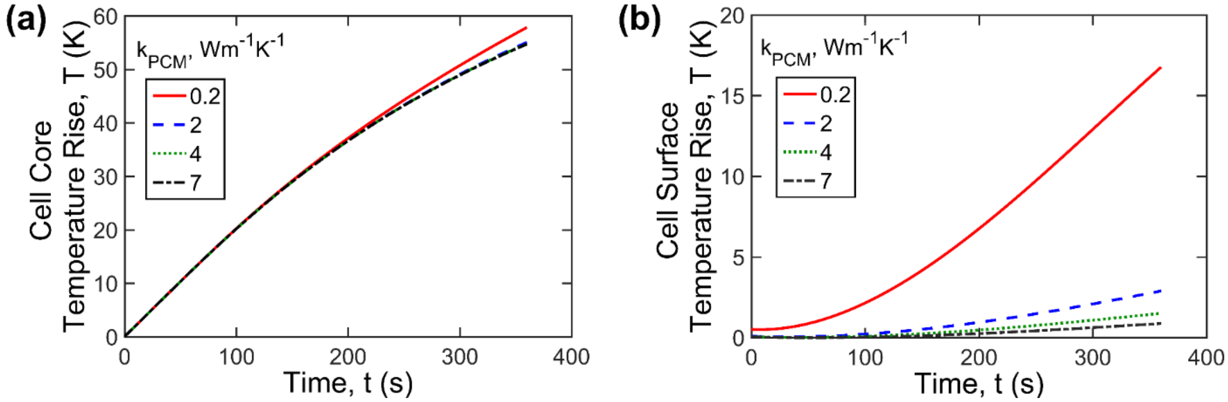

Figure 6. Effect of PCM thermal conductivity on (a) Cell peak temperature rise as a function of time; and (b) Cell surface temperature rise as a function of time. Results indicate that improving

PCM thermal conductivity significantly improves cell surface temperature but not the cell core temperature.

Figure 7 presents a similar investigation of the effect of latent heat of the phase change material. In this case, thermal conductivity is held constant at $k$=0.2 Wm$^{-1}$K$^{-1}$. Figures 7(a) and 7(b) plot the temperature rise at the cell core and surface respectively for multiple values of the latent heat at 6C discharge rate. Similar to thermal conductivity, a strong impact of latent heat on the cell surface temperature is seen. However, similar to Figure 6(a), the core temperature does not reduce significantly with increasing value of the latent heat, once again due to the throttling effect of the relatively poor thermal conductivity of the cell itself.

These results indicate that improving PCM thermal properties alone, as has been proposed in several recent papers [20-25], does not ensure effective cooling throughout the cell. Fundamentally, this occurs because of the low thermal conductivity of the Li-ion cell, which severely limits the rate of heat transfer from within the cell into the PCM, even if the PCM itself may have excellent thermal properties. Therefore, enhancing heat transfer within the cell and understanding the impact of improvements in cell thermal conductivity is equally important, and is investigated next.

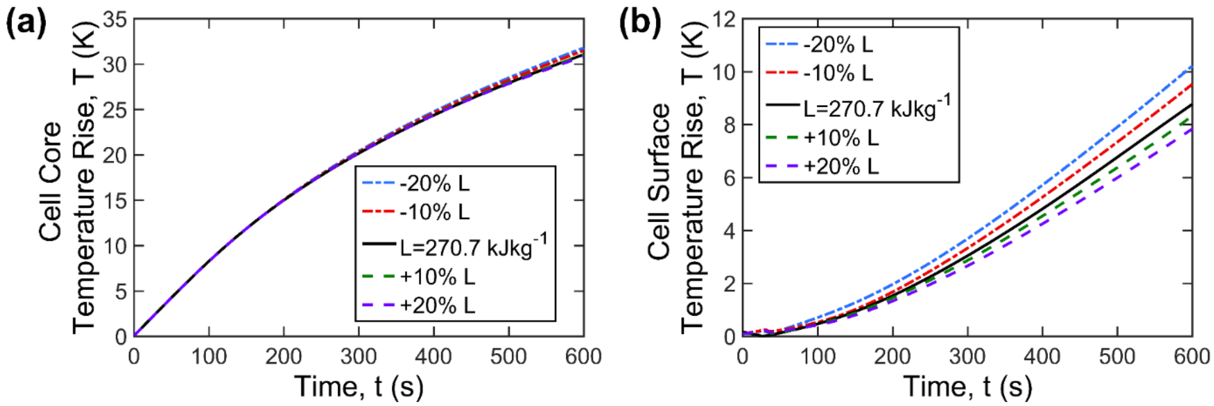

Figure 7. Effect of PCM latent heat on (a) Cell core temperature rise as a function of time; and (b) Cell surface temperature rise as a function of time. Results indicate that improving latent heat improves cell surface temperature but not the cell core temperature.

### 5-3-3. Effect of cell properties

Measurements reported in the past show that Li-ion cells have relatively poor thermal conductivity, around 0.1-1.0 $Wm^{-1}K^{-1}$ [3, 9, 35], due to which thermal conductivity may be a dominant parameter in determining the effectiveness of phase change thermal management. In order to investigate this, temperature distributions in the cell and phase change material are computed for a discharge rate of 6C. Figure 8(a) plots these temperature distributions at the end of the discharge process for different values of the cell thermal conductivity while holding all other parameters constant. A phase change material of thermal conductivity $k$=0.2 $Wm^{-1}K^{-1}$ and latent heat $L$=270.7 kJ/kg [25] is assumed. Figure 8(a) shows significant improvement in cell temperature distribution at higher values of cell thermal conductivity, including at the core of the cell. Up to 50% reduction in cell core temperature is seen for cell thermal conductivity of 2.0 $Wm^{-1}K^{-1}$ compared to the baseline value of 0.2 $Wm^{-1}K^{-1}$, unlike the case of improved PCM thermal conductivity, which reduces surface temperature but not the core temperature. In addition, Figure 8(a) also shows significant improvement in temperature uniformity across the cell, which is an important consideration in electrochemical performance of the cell.

The importance of cell thermal conductivity has been largely overlooked in past work on PCM thermal management, which has focused mostly on thermal properties of the PCM. Further, note that improving thermal conductivity of a Li-ion cell remains a key challenge due to the complicated, heterogeneous nature of the cell, with only limited work available, based on material and interfacial changes within the cell [36].

For the same conditions, Figure 8(b) plots the solid-liquid interface position *y(t),* measured from the cell-PCM interface as a function of time in the phase change material. This plot shows higher rate of phase change in the PCM with increasing cell thermal conductivity. This directly results from improved heat diffusion through the cell, leading to greater heat absorption by the PCM. Figure 8(b) further confirms that increasing cell thermal conductivity is critical for fully benefitting from phase change based thermal management.

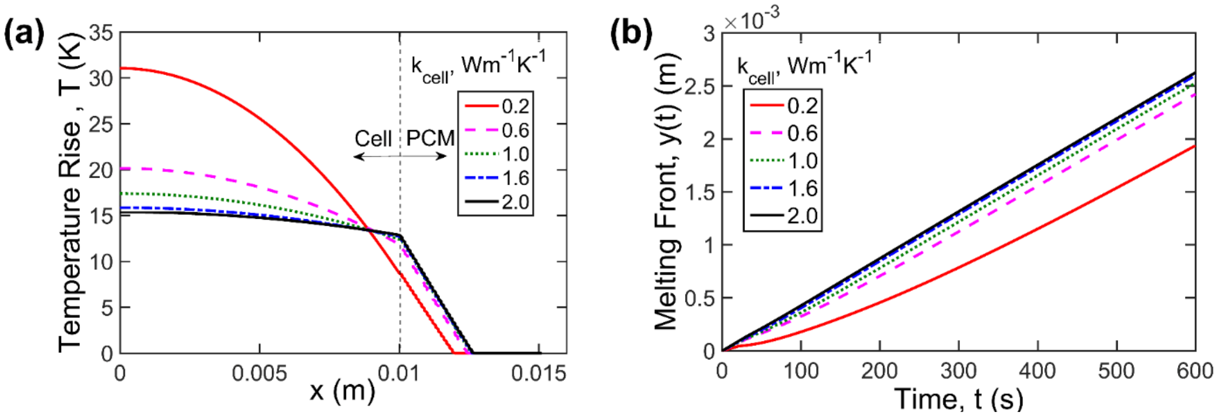

Figure 8. Effect of cell thermal conductivity on (a) Cell peak temperature rise; and (b) PCM melting front, *y(t)* as a function of time. Plots indicate significant improvement in cell core temperature and higher rate of phase change in the PCM with increasing cell thermal conductivity. PCM thermal conductivity and latent heat are taken to be $k$=0.2 Wm$^{-1}$K$^{-1}$ and $L$=270.7 kJkg$^{-1}$ respectively, corresponding to paraffin wax.

### 5-3-4. Trade-off between thermal management and energy storage density

Heat generation rate in a Li-ion cell can change significantly with time due to changes in the charge and discharge current. In general, the greater the discharge current, the higher is the heat generation rate. Any passive thermal management strategy, such as one based on phase change materials, must take these dynamics into account and be able to effectively cool the worst-case discharge rate expected during the duty cycle of the battery pack. As the discharge rate goes up, the volumetric heat generation rate also goes up, but the duration of heat generation reduces because the cell discharges faster [34]. In order to understand the effect of these parameters on thermal management, the peak temperature in the cell, which occurs at the cell core, is plotted in Figure 9 as a function of time for a number of discharge rates. For these simulations, a phase change material of thermal conductivity of 0.2 $Wm^{-1}K^{-1}$ and latent heat of 270.7 $kJkg^{-1}$ is assumed. Values for heat generation rate and thermal conductivity are taken from past measurements [9, 34]. Figure 9 shows that the effect of increased heat generation rate at larger C-rates dominates over the reduced time period, due to which the peak temperature is significantly greater at higher C-rates.

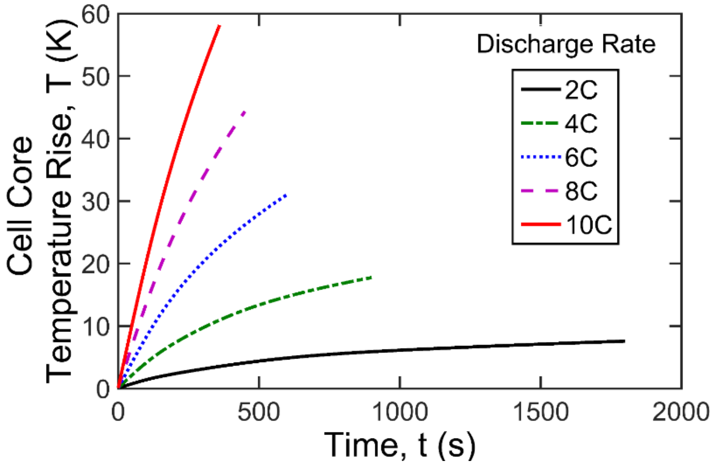

Figure 9. Effect of cell discharge rate on the peak temperature rise as a function of time. Phase change material of thermal conductivity of 0.2 $Wm^{-1}K^{-1}$ and latent heat of 270.7 kJ/kg is assumed. Heat generation values corresponding to different discharge rates are taken from past measurements [34].

To investigate this further, Figure 10 plots the maximum cell temperature, which occurs at the end of the discharge period as a function of C-rate. As expected, the peak temperature increases as discharge rates increases. Further, as the discharge rate goes up, the phase change front also increases, indicating the need for more and more phase change material between cells in order to sustain phase change cooling throughout the discharge process. Note that the phase change material in the battery pack is electrochemically passive, and therefore reduces energy storage density – a key performance parameter of the pack. To quantify this, Figure 10 also plots the energy storage density of the battery pack on a relative scale accounting for the presence of the passive PCM in the pack. Figure 10 shows that as the discharge rate goes up, the peak temperature rise goes up, and consequently, the energy storage density reduces due to inclusion of more and more PCM. This quantifies a fundamental, system-level trade-off in Li-ion battery pack design – the requirement of large discharge rate inherently reduces the energy storage density due to the need for greater thermal management. Many applications call for aggressive discharge rates, which Figure 10 shows will result in greater temperature rise and reduced energy storage density. Based on overall system requirements, a balance between these performance parameters must be achieved.

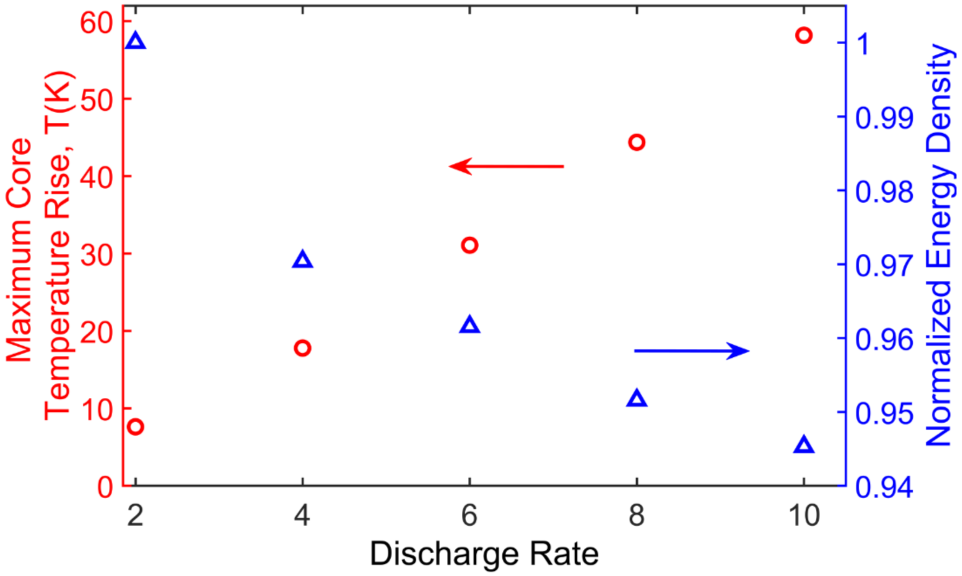

Figure 10. Plot of the maximum cell core temperature rise and relative energy storage density of the battery pack as a function of C-rate. Plot indicates that at larger discharge rates, there is greater temperature rise, and hence more PCM needed for thermal management, resulting in reduced energy storage density of the battery pack.

### 5-3-5. Phase change vs forced convection thermal management

Finally, the phase change based thermal management approach is compared with traditional, single phase convective cooling of the battery pack. For this comparison, the same cell as shown schematically in Figure 1(a), except with convective cooling with a heat transfer coefficient *h* instead of the phase change material. In this case, the transient temperature distribution in the cell can be easily derived to be [27]

$$T\left(x,t\right)=\sum_{n=1}^{\infty}\left[\frac{Cos\left(\lambda_n x\right)\exp(-\alpha\lambda_n^2 t)}{N(\lambda_n)}\int_{x'=0}^{W}-S(x')Cos\left(\lambda_n x'\right)dx'\right] \qquad (4)$$

where

$$S(x) = -\frac{Q'''}{2k}\left(x^2 - W^2\right) + \frac{Q'''W}{h} \tag{4}$$

For the case of a 20 mm cell undergoing 6C discharge, Figure 11 plots the peak temperature in the cell as a function of time for multiple values of the convective heat transfer coefficient $h$. For comparison, the peak temperature expected for phase change based cooling with a phase change material of $k$=0.2 $Wm^{-1}K^{-1}$ and $L$=270.7 kJ/kg is also plotted as a function of time. Figure 11 shows that convective cooling, even with fairly low heat transfer coefficient up to 50 $Wm^{-2}K^{-1}$ may be as effective as PCM-based thermal management assuming baseline PCM thermal conductivity. A higher convective heat transfer coefficient of 100 $Wm^{-2}K^{-1}$ compares well with the case of an improved PCM thermal conductivity of 7.0 $Wm^{-1}K^{-1}$ – a value that is at the higher end of the range reported in the literature [24]. This result is consistent with recent work where the performance of phase change cooling has been compared with forced convection cooling of Li-ion cells [37]. For comparison, Figure 11 also plots the expected thermal response in case of a PCM with a very high thermal conductivity of 15 $Wm^{-1}K^{-1}$, and shows that the impact of improving thermal conductivity saturates – the curves for 7 $Wm^{-1}K^{-1}$ and 15 $Wm^{-1}K^{-1}$ are nearly identical. In this range, improving PCM thermal conductivity does not offer improved performance compared to forced convective cooling.

This comparison demonstrates the limitations of PCM cooling in Li-ion cells because of the short time duration of heating. In many cases, convective cooling by itself may offer an attractive thermal management option. On the other hand, phase change thermal management is passive, easier to implement and does not require energy, whereas providing fluid flow and high convective heat transfer coefficient to the surface of each cell in a large battery pack complicates thermal management design, and may involve significant pressure drops, and therefore higher energy costs. Therefore, a holistic approach combining multiple thermal management may be more effective.

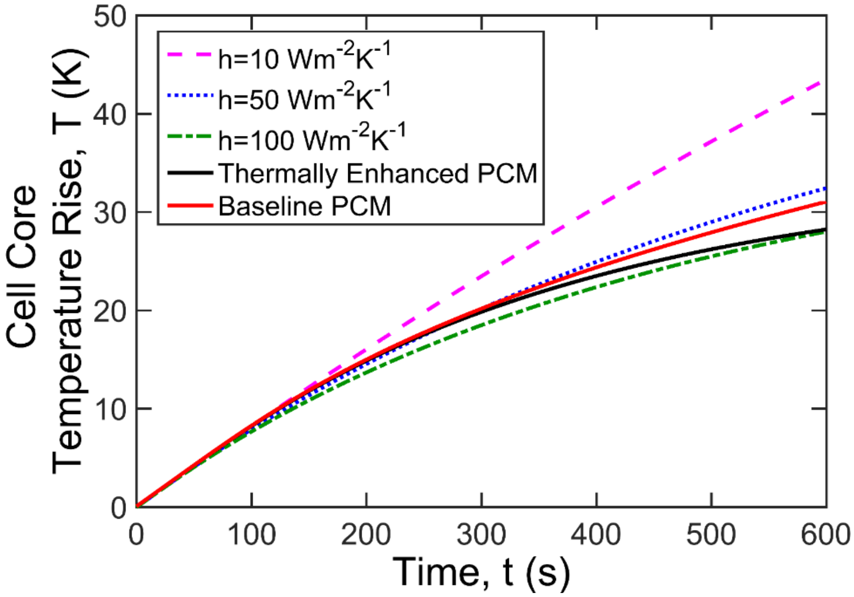

Figure 11. Comparison on phase change cooling with convective cooling. Plot of peak temperature rise in the cell as a function of time for multiple values of the convective heat transfer coefficient *h*. For comparison, plots for PCM cooling with baseline ($k$=0.2 Wm$^{-1}$K$^{-1}$) and thermally enhanced ($k$=7.0 Wm$^{-1}$K$^{-1}$) cases are also plotted.

## 5-4. Conclusions

Phase change cooling of Li-ion cells is a promising approach for thermal management of battery packs, particularly due to its passive nature and no power requirement. Modeling of phase change cooling, such as one presented in this work, involves several theoretical challenges. However, insights gained from such analysis can be critical for optimization of thermal management systems, particularly when applied together with experimental data. For example, multiple papers have investigated thermal conductivity improvement of the phase change material for battery cooling. However, this work shows that while such an approach has a significant impact on the melting rate and the cell surface temperature, adequate cooling of the core of the cell requires substantial improvement in thermal conductivity of the cell. While this is consistent with the basic principles of heat transfer, it has not been recognized adequately in past work. The present theoretical model quantifies this key challenge in PCM based thermal management.

Results also highlight and quantify the key system-level trade-off between discharge rate and energy storage density, which can prevent needless overdesign of thermal management. Another important insight from this work is the comparison between phase change cooling and convective cooling. It is expected that the theoretical model and key results presented in this work will contribute towards accurate design of practical thermal management systems for Li-ion battery packs, eventually leading to improvement in safety and performance of energy conversion and storage devices. The present theoretical approach ignores sensible heating of the PCM prior to phase change, which may occur if the melting temperature of the PCM is greater than ambient temperature. While this is unlikely to be a dominant effect due to the small value of Stefan number for most phase change materials, accounting for this may be an interesting direction for future work. Further, the model assumes perfect symmetry between cells in the battery pack, and needs to be extended to account for non-symmetric features in large battery packs. Further, integration of experiments with theoretical modeling is also an important direction for future work. Incorporation of the theoretical model presented here in practical Battery Management Systems (BMS) of large battery packs is also important. Finally, the impact of the phase change material in the battery pack on other battery functions, such as battery heating in a cold environment – relevant for automotive applications – is also important.

## 5-5. Nomenclature

| | |
|---|---|
| $C_p$ | specific heat capacity (Jkg$^{-1}$K$^{-1}$) |
| $f$ | non-dimensional temperature, $f=(T_0-T_m)/(T_m-T_{ref})$ |
| $h$ | convective heat transfer coefficient (Wm$^{-2}$K$^{-1}$) |
| $k$ | thermal conductivity (Wm$^{-1}$K$^{-1}$) |
| $L$ | latent heat of fusion (Jkg$^{-1}$) |
| $N$ | eigenvalue norm |
| $q''$ | heat flux (Wm$^{-2}$) |
| $Q'''$ | volumetric heat generation rate (Wm$^{-3}$) |
| $Ste$ | Stefan number, $Ste=Cp(T_m-T_{ref})/L$ |
| $T$ | temperature (K) |
| $t$ | time (s) |
| $T_m$ | phase change temperature (K) |
| $T_{ref}$ | reference temperature (K) |
| $W$ | cell half-thickness (m) |
| $x$ | length scale (m) |
| $y$ | location of phase change front (m) |
| $\alpha$ | thermal diffusivity (m$^2$s$^{-1}$) |
| $\lambda$ | eigenvalues $n\pi/W$ (m$^{-1}$) |
| $\rho$ | thermal diffusivity (m$^2$s$^{-1}$) |

## 5-6. References

[1] J.B. Goodenough, K.-S. Park, The Li-Ion Rechargeable Battery: A Perspective, Journal of the American Chemical Society. 135 (2013) 1167–1176.

[2] B. Scrosati, J. Garche, Lithium batteries: Status, prospects and future, Journal of Power Sources. 195 (2010) 2419–2430.

[3] K. Shah, V. Vishwakarma, A. Jain, Measurement of Multiscale Thermal Transport Phenomena in Li-Ion Cells: A Review, Journal of Electrochemical Energy Conversion and Storage. 13 (2016) 030801.

[4] T.M. Bandhauer, S. Garimella, T.F. Fuller, A Critical Review of Thermal Issues in Lithium-Ion Batteries, Journal of The Electrochemical Society. 158 (2011).

[5] C.F. Lopez, J.A. Jeevarajan, P.P. Mukherjee, Characterization of Lithium-Ion Battery Thermal Abuse Behavior Using Experimental and Computational Analysis, Journal of The Electrochemical Society. 162 (2015).

[6] K. Shah, D. Chalise, A. Jain, Experimental and theoretical analysis of a method to predict thermal runaway in Li-ion cells, Journal of Power Sources. 330 (2016) 167–174.

[7] M. Parhizi, M. Ahmed, A. Jain, Determination of the core temperature of a Li-ion cell during thermal runaway, Journal of Power Sources. 370 (2017) 27–35.

[8] R. Spotnitz, J. Franklin, Abuse behavior of high-power, lithium-ion cells, Journal of Power Sources. 113 (2003) 81–100.

[9] S. Drake, D. Wetz, J. Ostanek, S. Miller, J. Heinzel, A. Jain, Measurement of anisotropic thermophysical properties of cylindrical Li-ion cells, Journal of Power Sources. 252 (2014) 298–304.

[10] K. Shah, S. Drake, D. Wetz, J. Ostanek, S. Miller, J. Heinzel, et al., Modeling of steady-state convective cooling of cylindrical Li-ion cells, Journal of Power Sources. 258 (2014) 374–381.

[11] D. Chalise, K. Shah, R. Prasher, A. Jain, Conjugate Heat Transfer Analysis of Thermal Management of a Li-Ion Battery Pack, Journal of Electrochemical Energy Conversion and Storage. 15 (2017) 011008.

[12] N. Bigdeli, Optimal management of hybrid PV/fuel cell/battery power system: A comparison of optimal hybrid approaches, Renewable and Sustainable Energy Reviews. 42 (2015) 377–393.

[13] Y. Huo, Z. Rao, X. Liu, J. Zhao, Investigation of power battery thermal management by using mini-channel cold plate, Energy Conversion and Management. 89 (2015) 387–395.

[14] L. Jin, P. Lee, X. Kong, Y. Fan, S. Chou, Ultra-thin minichannel LCP for EV battery thermal management, Applied Energy. 113 (2014) 1786–1794.

[15] X. Xu, R. He, Research on the heat dissipation performance of battery pack based on forced air cooling, Journal of Power Sources. 240 (2013) 33–41.

[16] M.R. Giuliano, A.K. Prasad, S.G. Advani, Experimental study of an air-cooled thermal management system for high capacity lithium–titanate batteries, Journal of Power Sources. 216 (2012) 345–352.

[17] D. Anthony, D. Wong, D. Wetz, A. Jain, Improved Thermal Performance of a Li-Ion Cell through Heat Pipe Insertion, Journal of The Electrochemical Society. 164 (2017).

[18] Q. Wang, B. Jiang, Q. Xue, H. Sun, B. Li, H. Zou, et al., Experimental investigation on EV battery cooling and heating by heat pipes, Applied Thermal Engineering. 88 (2015) 54–60.

[19] L. Saw, Y. Ye, A. Tay, Feasibility study of Boron Nitride coating on Lithium-ion battery casing, Applied Thermal Engineering. 73 (2014) 154–161.

[20] G. Jiang, J. Huang, Y. Fu, M. Cao, M. Liu, Thermal optimization of composite phase change material/expanded graphite for Li-ion battery thermal management, Applied Thermal Engineering. 108 (2016) 1119–1125.

[21] F. Samimi, A. Babapoor, M. Azizi, G. Karimi, Thermal management analysis of a Li-ion battery cell using phase change material loaded with carbon fibers, Energy. 96 (2016) 355–371.

[22] S. Wilke, B. Schweitzer, S. Khateeb, S. Al-Hallaj, Preventing thermal runaway propagation in lithium ion battery packs using a phase change composite material: An experimental study, Journal of Power Sources. 340 (2017) 51–59.

[23] R. Zhao, J. Gu, J. Liu, Optimization of a phase change material based internal cooling system for cylindrical Li-ion battery pack and a hybrid cooling design, Energy. 135 (2017) 811–822.

[24] W. Li, Z. Qu, Y. He, Y. Tao, Experimental study of a passive thermal management system for high-powered lithium ion batteries using porous metal foam saturated with phase change materials, Journal of Power Sources. 255 (2014) 9–15. doi:10.1016/j.jpowsour.2014.01.006.

[25] L.H. Saw, Y. Ye, M.C. Yew, W.T. Chong, M.K. Yew, T.C. Ng, Computational fluid dynamics simulation on open cell aluminium foams for Li-ion battery cooling system, Applied Energy. 204 (2017) 1489–1499.

[26] N. Javani, I. Dincer, G. Naterer, B. Yilbas, Heat transfer and thermal management with PCMs in a Li-ion battery cell for electric vehicles, International Journal of Heat and Mass Transfer. 72 (2014) 690–703.

[27] D.W. Hahn, M.N. Özişik. Heat Conduction (2012).

[28] A.S. Dorfman, Conjugate problems in convective heat transfer, CRC Press, Boca Raton, (2010).

[29] K. Shah, A. Jain, An iterative, analytical method for solving conjugate heat transfer problems, International Journal of Heat and Mass Transfer. 90 (2015) 1232–1240.

[30] J. Caldwell, Y. Kwan, On the perturbation method for the Stefan problem with time-dependent boundary conditions, International Journal of Heat and Mass Transfer. 46 (2003) 1497–1501.

[31] N. Sadoun, E.-K. Si-Ahmed, P. Colinet, On the refined integral method for the one-phase Stefan problem with time-dependent boundary conditions, Applied Mathematical Modelling. 30 (2006) 531–544.

[32] G.E. Myers, Analytical methods in conduction heat transfer, AMCHT Publ., Madison, WI, (1998).

[33] D. Anthony, D. Sarkar, A. Jain, Non-invasive, transient determination of the core temperature of a heat-generating solid body, Scientific Reports. 6 (2016).

[34] S. Drake, M. Martin, D. Wetz, J. Ostanek, S. Miller, J. Heinzel, et al., Heat generation rate measurement in a Li-ion cell at large C-rates through temperature and heat flux measurements, Journal of Power Sources. 285 (2015) 266–273.

[35] D. Anthony, D. Wong, D. Wetz, A. Jain, Non-invasive measurement of internal temperature of a cylindrical Li-ion cell during high-rate discharge, International Journal of Heat and Mass Transfer. 111 (2017) 223–231.

[36] V. Vishwakarma, C. Waghela, Z. Wei, R. Prasher, S.C. Nagpure, J. Li, et al., Heat transfer enhancement in a lithium-ion cell through improved material-level thermal transport, Journal of Power Sources. 300 (2015) 123–131.

[37] Z. Ling, F. Wang, X. Fang, X. Gao, Z. Zhang, A hybrid thermal management system for lithium ion batteries combining phase change materials with forced-air cooling, Applied Energy. 148 (2015) 403–409.

# Chapter 6

# Determination of the core temperature of a Li-ion cell during thermal runaway

**Published as**: Parhizi, M., Ahmed, M. B., & Jain, A. (2017). Determination of the core temperature of a Li-ion cell during thermal runaway. *Journal of Power Sources*, *370*, 27-35.

## 6-1. Introduction

Li-ion cells offer an excellent mechanism for electrochemical energy storage and conversion, with superior energy storage and power density compared to predecessor technologies [1-4]. However, the performance of Li-ion cells is known to be highly sensitive to temperature [5, 6], and even modest rise in operating temperature results in severe safety and reliability concerns. Fundamentally, high temperature triggers multiple exothermic reactions and processes inside a Li-ion cell, such as degradation of separator, reaction between the anode active material and electrolyte, reaction between the positive active material and electrolyte and finally electrolyte decomposition [7-10]. As the cell temperature rises due to such processes, the rates of heat generation increase even more [11]. In addition, newer, more exothermic reactions are also triggered. This chain mechanism continues until the heat generation rate becomes unsustainably large, thereby pushing the cell into a catastrophic thermal runaway situation. Thermal runaway is a significant technological challenge that has been investigated in a large body of experimental and theoretical research [7, 8, 10-16].

A number of experimental techniques have been used for investigating the nature of thermal runaway in Li-ion cells [8, 10, 13]. Reactions and processes leading to thermal runaway are usually modeled based on Arrhenius kinetics. Reaction rate parameters for these processes have been experimentally determined [8, 17]. Heat generation rates have been measured in both nominal and runaway conditions using both calorimetric and non-calorimetric techniques [12, 18, 19]. At the cell level, thermal runaway has been induced through a variety of mechanisms including nail penetration, internal short circuit, high temperature oven tests, etc. [5, 6, 10, 13, 20]. In each case, the surface temperature of the cell has been measured and used as a metric to represent the thermal health of the cell. Surface temperature measurement has been carried out through both contact and non-contact techniques such as thermocouples and infrared thermography respectively [10, 13, 21-24]. Temperature thresholds in terms of the surface temperature for inducing a thermal runaway have been determined experimentally [10, 12, 13]. The fundamental processes that contribute towards thermal runaway, including temperature-dependent heat generation, thermal conduction and convection have been combined into a single non-dimensional number [11]. A threshold value for this number has been shown to exist, above which thermal runaway is imminent.

The risk of thermal runaway is usually managed by battery management approaches such as load reduction on the cell when its temperature exceeds a certain threshold. While this approach may keep the cell safe, it comes at the cost of performance. The effectiveness of this significant trade-off between safety and performance depends critically on accurate measurement of the cell temperature, which is a key indicator of the thermal health of the cell and a predictor of the onset of thermal runaway. Surface temperature measurement, while providing some indication of the thermal state of the cell, is not completely representative, since the internal temperature at the core of the cell may be much higher due to internal heat generation [18] and poor thermal conductivity [25] of the cell. The higher, internal temperature may drive thermal runaway even when the surface temperature is much lower. Information about the core temperature is therefore critical for fully understanding and alleviating thermal runaway. Any technique to manage thermal runaway based on surface temperature alone is likely to be in significant error, as the core temperature – and not the surface temperature – is an appropriate indicator of the thermal state of the cell.

Most past papers have only measured cell temperature on the outer surface [10, 12, 13] and not the core temperature, possibly due to the several challenges associated with core temperature measurement, such as the hermetically sealed nature of the cell and lack of physical access to the core. A limited number of techniques that have been evaluated for measuring the internal temperature of the cell include fiber Bragg gratings [26], temperature measurement through electrochemical parameter measurement [27] and even micro-thermocouples [28,29]. Limited work exists on internal temperature measurement using embedded thermocouples during short circuit and overcharge conditions [29], wherein a significant temperature difference between internal temperature and external surface temperature was reported. This work reported internal temperature of up to 195 °C for $LiCoO_2$ cells in mild abuse conditions [29], although temperature during a thermal runaway event that causes fire and explosion is expected to be much higher. Several of these techniques require physical insertion of a sensor into the cell, which often leads to cell failure and is unlikely to work well for widespread implementation. Others, such as electrochemical based temperature measurement only provide an average temperature of the cell, and not the peak temperature, which is more critical. In the recent past, a method for predicting the internal temperature of a cylindrical Li-ion cell based on measurement of the surface temperature has been developed [21, 22]. This method requires information about the heat generation rate and thermophysical properties of the cell, and has been experimentally demonstrated for nominal, non-runaway operating conditions. Given the technological importance of predicting, managing and preventing thermal runaway, it is of much interest to extend such methods for measurement of the internal temperature of the cell during extreme conditions encountered in thermal runaway. Any such effort will help understand the thermal state inside the cell during thermal runaway and will positively impact the fundamental understanding and practical management of thermal runaway in Li-ion cells.

This work presents an experimentally validated method for determining the core temperature of a cylindrical Li-ion during thermal runaway. This technique is based on measured surface temperature data as a function of time and chemical reaction kinetics during thermal runaway. These data are used in an analytical heat transfer model to determine the core temperature as a function of time. The core temperature determined in this manner is found to be in good agreement with experimental measurements on a thermal test cell undergoing a thermal process that mimics thermal runaway in real cells. The technique is used to determine the core temperature as a function of time for a number of surface temperature measurements reported in past papers. In each case, it is found that the core temperature reaches several hundred degrees Celsius higher than the surface temperature. This provides a critical, previously unavailable insight into the thermal state inside the cell, which is not possible through surface temperature measurement alone. The capability for determining the core temperature of the cell during thermal runaway, enabled by this work, may contribute towards an improved fundamental understanding of thermal runaway, as well as practical techniques for improved safety of Li-ion cells through effective management of thermal runaway risks.

## 6-2. Mathematical Modeling

Figure 1(a) shows a schematic of the geometry considered here, comprising a cylindrical lithium ion cell of radius $R$. Radial thermal conductivity and diffusivity of the cell are assumed to be $k_r$ and $\alpha$ respectively. Internal heat generation within the cell, $Q(T)$, which occurs due to various electrochemical processes, is a function of temperature. Surface temperature at the outer surface, $r=R$, is assumed to be known from experimental measurements, as reported in several past papers. The interest here is to develop a model to predict the evolution of the core temperature based on the measured surface temperature and the internal heat generation.

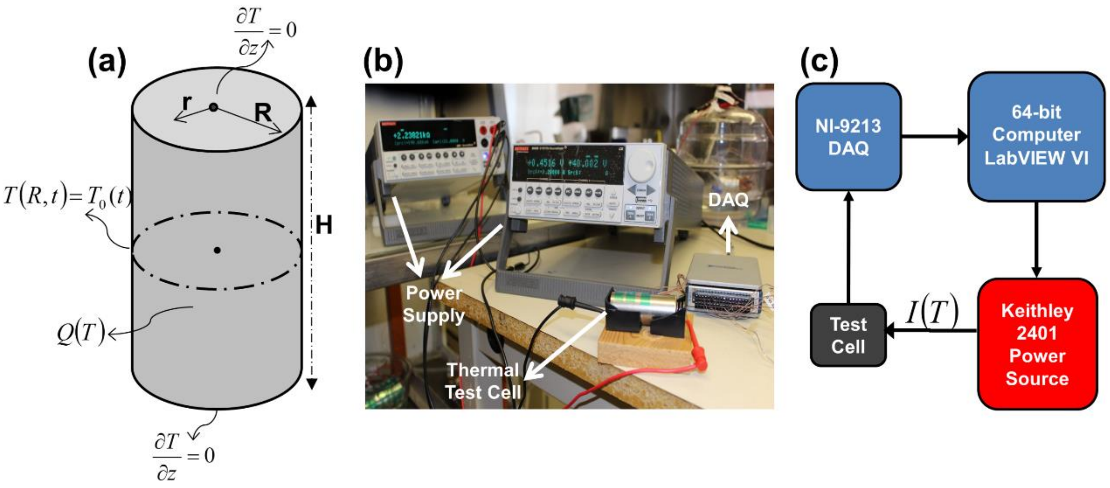

Figure 1. (a) Schematic of the problem, (b) Picture, and (c) Schematic of the experimental setup.

In the cylindrical coordinate system used here, it is possible to derive a governing partial differential equation for the temperature field *T(r,t)* by considering energy conservation of an infinitesimally small element [30,31]. By accounting for thermal conduction into and out of this element, as well as internal heat generation and energy storage, the energy equation, used commonly for heat transfer analysis, can be found to be

$$\left(\frac{\partial^2 T}{\partial r^2}+\frac{1}{r}\frac{\partial T}{\partial r}\right)+\frac{Q(T)}{k_r}=\frac{1}{\alpha}\frac{\partial T}{\partial t} \qquad (1)$$

Boundary conditions associated with equation (1) are

$$\frac{\partial T}{\partial r}=0 \qquad \text{at } r=0 \qquad (2)$$

and

$$T=T_0(t) \qquad \text{at } r=R \qquad (3)$$

Temperature rise at *t*=0 is assumed to be zero. Temperature-dependent heat generation in equation (1) and time-dependent surface temperature in equation (3) are the two non-homogeneities in this problem. In order to derive a solution, the problem is first divided into two sub-problems, $T_1(r,t)$ and $T_2(r,t)$ that account for each non-homogeneity separately. $T_1(r,t)$ represents the temperature rise due to internal heat generation alone, and $T_2(r,t)$ represents the temperature rise due to time-dependent surface temperature alone.

The solution for $T_1(r,t)$ depends on the nature of internal heat generation $Q(T)$. Heat generation during thermal runaway is usually modeled as an Arrhenius function

$$Q = Q_o \exp\left(\frac{-E_a}{R_u T}\right) \tag{4}$$

Where $Q_0$ is the pre-exponential constant, $E_a$ is the activation energy and $R_u$ is the universal gas constant.

Due to the exponential nature of temperature dependence of Q, the governing energy equation for $T(r,t)$ is highly nonlinear, and consequently very difficult to solve. Linearization through time-stepping is carried out in order to solve for $T_1(r,t)$. The time duration of interest is divided into a number of smaller time intervals, for which $T_1(r,t)$ is computed in a sequential fashion. Each time interval is chosen to be small enough, such that the change in heat generation due to increased temperature during the interval is reasonably small. This allows the $Q(T)$ term to be considered to be constant during each time interval. Based on linearization of the problem in this fashion, the temperature distribution $T_1(r,t)$ during each time interval can be computed using the method of separation of variables techniques. The solution for $T_1(r,t)$ is found to be

$$T_1(r,t) = s(r) + w(r,t) \tag{5}$$

where

$$s(r) = \frac{Q_{gen}}{4k}\left(R^2 - r^2\right) \tag{6}$$

and

$$w(r,t) = \sum_{n=1}^{\infty} A_n J_0(\lambda_n r)\exp\left(-\alpha\lambda_n^2 t\right) \tag{7}$$

where $A_n$ is given by

$$A_n = \frac{\int_0^R r\left(T_{initial}(r) - s(r)\right) J_0(\lambda_n r)\,dr}{\int_0^R r J_0(\lambda_n r)^2\,dr} \tag{8}$$

Where the eigenvalues $\lambda_n$ are given by the roots of $J_0$, the Bessel function of the first kind and of order zero.

Note that $Q_{gen}$ is the heat generation rate during the specific time interval, and $T_{initial}(r)$ is the temperature distribution in the cell at the start of the time interval, which must be determined by computing the temperature distribution during the immediately preceding time interval. Equations (5) through (8) provide an approach for handling the non-linearity in the equations for $T_1(r,t)$ and computing the temperature distribution in a recursive fashion.

This linearization approach introduces approximations in the temperature distribution because it assumes the heat generation rate to be uniform throughout the cell. Further, because the temperature distribution in the cell may be non-uniform due to the low thermal conductivity of the cell [25], it is important to determine the temperature at which to compute the heat generation rate for each time interval. These limitations of the linearization approach can be minimized by choosing the time intervals to be sufficiently short. During computation of $T_1(r,t)$.

Deriving an expression for $T_2(r,t)$ is relatively simpler, and is similar to a procedure outlined in a recent paper [21]. Using the method of undetermined parameters, $T_2(r,t)$ is found to be

$$T_2(r,t) = \sum_{n=1}^{\infty} B_n(t) J_0(\lambda_n r) \tag{9}$$

where $B_n(t)$ is given by

$$B_n(t) = \frac{\alpha \lambda_n R J_1(\lambda_n R)}{N_{r,n}} \int_0^t T_0(\tau) \exp\left[-\alpha \lambda_n^2 (t-\tau) d\tau\right] \tag{10}$$

and the radial norm $N_{r,n}$ is

$$N_{r,n} = \frac{R^2 J_1(\lambda_n R)^2}{2} \tag{11}$$

Equations (9) through (11) show that $T_2(r,t)$ can be determined by appropriately integrating the measured surface temperature $T_0(t)$.

Finally, by combining $T_1(r,t)$ and $T_2(r,t)$, the core temperature of the cell $T_{core}(t)$ can be computed as follows

$$T_{core}(t) = T_1(0,t) + T_2(0,t) \tag{12}$$

Note that determining the core temperature of the cell during thermal runaway using the method outlined above requires information about the temperature-dependent heat generation rates during runaway, as well as thermal properties of the cell. These parameters are generally available in several past papers. Heat generation rates are usually modeled using the Arrhenius equation and the various associated Arrhenius parameters have been determined and reported in past papers [7, 8, 10]. On the other hand, thermal properties of a Li-ion cell, including thermal conductivity and specific heat have also been measured [18] as well as estimated from theoretical models [19].

## 6-3. Experiments

Experiments are carried out to validate the analytical model for determining the core temperature of a cell as presented in section 2. Note that imposing a precise and well-controlled temperature-dependent heat generation rate in a Li-ion cell is not straight forward. Further, there is a lack of experimental methods to directly measure the core temperature, in part due to its hermetically sealed nature. As a result, these experiments are carried out on a thermal test cell that is carefully designed and fabricated in order to closely match the geometry and thermal transport properties of a 26650 Li-ion cell. Fabrication and measurements on such thermal test cells have been described in recent papers [11, 21, 22]. In short, the thermal test cell comprises a rolled, thin resistive 304 stainless steel foil placed inside a 26650 cell casing. Thermocouples are placed at different radii, including at the core and surface of the roll for temperature measurement. Heat is generated inside the cell by passing electrical current through the resistive metal foil. Temperature-dependence of heat generation rate is implemented by monitoring the cell temperature through embedded thermocouples and changing the heating current in order to implement any desired $Q(T)$ expression, as shown schematically in Figure 1(c).

### 6-3-1. Experimental Setup

Figure 1(b) shows a picture of the experimental setup, comprising the thermal test cell, T-type thermocouples, a NI-9213 data acquisition system (DAQ), Keithley 2401 power sources and LabView software running on a 64-bit computer. Figure 1(c) shows a schematic of the flow of information during the experiment.

Core temperature of the thermal test cell is measured in one second intervals by LabVIEW software through the NI-9213 DAQ. The heat generation rate to be imposed in the cell is determined using the measured temperature and the desired temperature dependence, $Q(T)$. The amount of current needed for the heat generation rate is determined based on the electrical resistance of the metal foil, which is then supplied to the thermal test cell by the Keithley 2401 power sources. Surface temperature of the thermal test cell is measured every one second. Experiments are repeated by changing the $Q(T)$ expression implemented in the heat generation feedback loop for multiple values of $Q_0$ and $E_a$.

In addition to experiments described above, analysis of experimental data on 18650 cells reported in three past papers is also carried out. Section 4 shows that specific heat of the 18650 cell is a critical parameter in these computations. As a result, experiments are carried out to independently measure the specific heat of an 18650 Li-ion cell.

To do so, a completely discharged 18650 Li-ion cell is heated up to 45°C inside a BOEKEL incubator. Surface temperature of the cell is measured using Omega T-type thermocouples connected to a NI-9213 data acquisition system (DAQ) and controlled by LabView software. Once the cell reaches a steady temperature, it is placed inside a lab-grade 350ml vacuum flask containing 150 grams of water at room temperature. It is ensured that the cell is completely submerged in water and the flask is sealed. Temperature of water is also monitored using a thermocouple. During the process, heat transfers from the cell to water due to temperature difference until they both reach the same temperature. Neglecting any minor heat losses from the flask to the ambient, a statement of energy conservation can be written as follows

$$m_c C_{p,c} \Delta T_c + m_w C_{p,w} \Delta T_w = 0 \tag{13}$$

Where $m$ is mass, $C_p$ is specific heat and $\Delta T$ is the total temperature change during the experiment. Subscripts $c$ and $w$ refer to the cell and water respectively. Since masses and temperatures are measured, therefore the specific heat of the cell can be determined from equation (13) based on the well-known specific heat of water.

## 6-4. Results and discussion

### 6-4-1. Numerical validation

The analytical model presented in section 2 is first validated against numerical simulations. Figure 2 shows a comparison between the core temperature rise as a function of time predicted by the analytical model and a finite-element numerical simulation carried out in ANSYS-CFX. The boundary temperature used in this comparison is obtained from one of the experimental data on a thermal test cell illustrated in section 3. The values for $Q_0$ and $E_a$ in the heat generation expression for this comparison are $5\times10^{22}$ Wm$^{-3}$ and $1.3\times10^{5}$ Jmol$^{-1}$ respectively. Figure 2 shows that the analytical model and finite-element simulations are in very good agreement throughout the entire time duration, with a worst-case deviation of only 3.1% between the two. This provides validation of the accuracy of the analytical model presented in section 2.

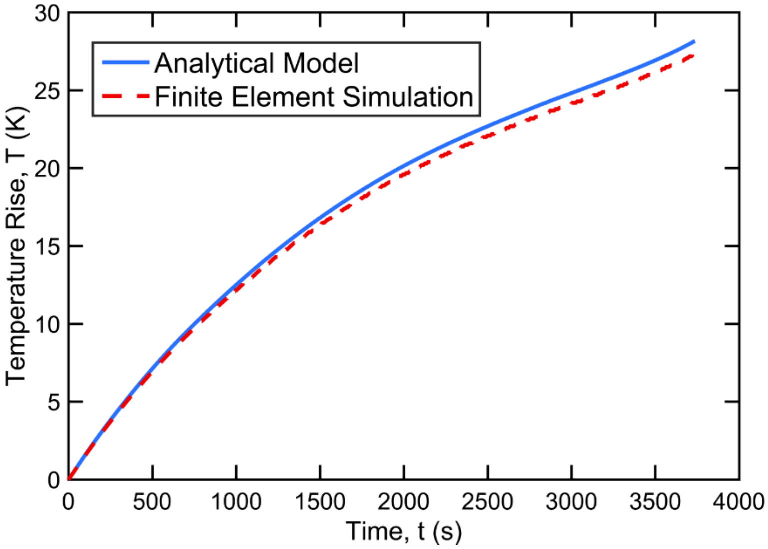

Figure 2. Core temperature rise of the thermal test cell as a function of time predicted by the analytical model (blue curve) and a finite-element numerical simulation carried out in ANSYS-CFX (red curve). Values for $Q_0$ and $E_a$ for this comparison are $5\times10^{22}$ $Wm^{-3}$ and $1.3\times10^{5}$ $Jmol^{-1}$ respectively.

6-4-2. Experimental validation

Further validation is carried out by comparison with experimental data on a thermal test cell with known heat generation rate $Q(T)$. Two sets of experiments are carried out. In the first set, the pre-exponential factor, $Q_0$ is kept constant at $10^{44}$ $Wm^{-3}$ while varying the activation energy $E_a$ for heat generation in the thermal test cell through temperature-dependent heating current implemented by the LabVIEW controller. Figure 3(a) compares the core temperature rise as a function of time measured through experiments with the one predicted by the analytical model for different values of activation energy. Experimental data and analytical model are in very good agreement. It is seen that as the activation energy increases while keeping $Q_0$ constant, there is reduction in temperature rise, and thermal runaway occurs much later in time. In each case, the experimental data are found to agree well with predictions from the analytical model. The worst-case deviation between the two is found to be less than 1%. In addition to validating the analytical model, these data also show that increase in the value of activation energy results in a decrease in the slope of temperature rise as a function of time, implying that as the activation energy increases, the temperature curve will eventually begin to reach a steady state and therefore not go in thermal runaway. Both experimental data and the analytical model from section 2 follow this trend.

In the second set of experiments, $Q_0$ is varied while holding $E_a$ constant at 246.9 kJmol$^{-1}$. Similar to the first set of experiments, there is very good agreement between experimental data and analytical model, as shown in Figure 3(b), with a worst-case deviation of 1.2%. These experiments demonstrate the accuracy of the theoretical model in section 2 for computing the core temperature of the cell undergoing temperature-dependent heat generation over a wide parameter space.

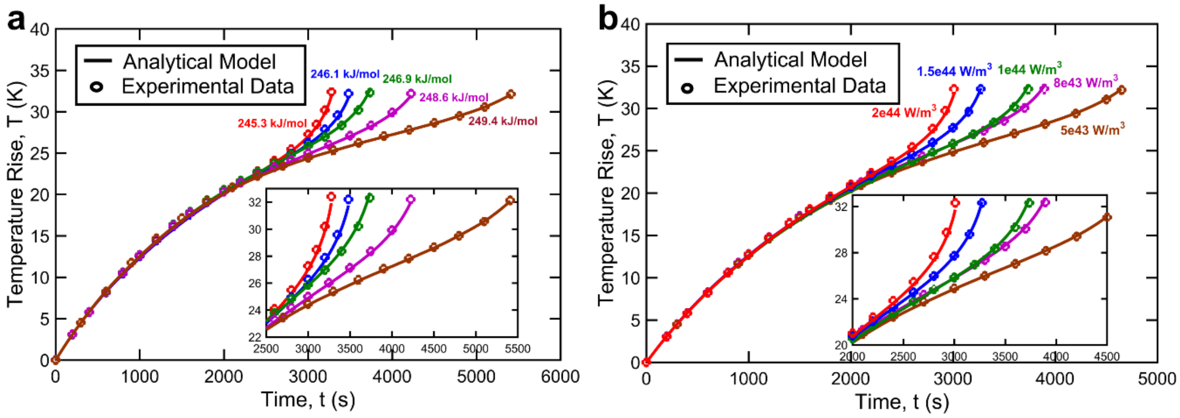

Figure 3. Experimental validation of the analytical model. Core temperature rise as a function of time (a) for different values of activation energy $E_a$, while the pre exponential factor $Q_0$ is kept constant at $10^{44}$ Wm$^{-3}$; (b) for different values of pre-exponential constant $Q_0$ while activation energy $E_a$ is kept constant at 246.9 kJmol$^{-1}$. Both experimental measurements and analytical

model are presented. Subplots show zoom-ins at the later stages of each experiment when the cell begins to enter thermal runaway.

### 6-4-3. Components of the core temperature

As outlined in section 2, the core temperature of the cell is computed as the sum of two different contributions, $T_{1,core}$ and $T_{2,core}$ that account for the effect of internal heat generation and outside surface temperature respectively. Under different experimental conditions, either of these two may dominate the overall core temperature. To illustrate this, Figures 4(a) and 4(b) plot the core temperature rise as a function of time, along with its two components $T_{1,core}$ and $T_{2,core}$ for two different scenarios.In the first case, the value of the activation energy is relatively small. In this case, as shown in Figure 4(a), the core temperature is dominated by contributions from the surface temperature component $T_{2,core}$ for the first 1500 seconds or so. Subsequently, however, as the temperature rises, internal heat generation becomes more and more important, and as shown in Figure 4(a), the contribution from $T_{1,core}$ begins to increase, and eventually dominate the core temperature computation, beyond 3500 seconds or so. In a different scenario, however, the core temperature could be dominated throughout by only one of the two components. This is illustrated in Figure 4(b), where the internal heat generation rate is so small that the surface temperature component $T_{2,core}$ dominates the overall core temperature throughout the duration. These insights into the dominance of one or the other component, or the switch from one to the other as time passes are critical in designing computational approaches for determining the core temperature. For example, knowing that one of the two components is not significant under certain conditions can be used to speed up core temperature computation by not computing that component at all.

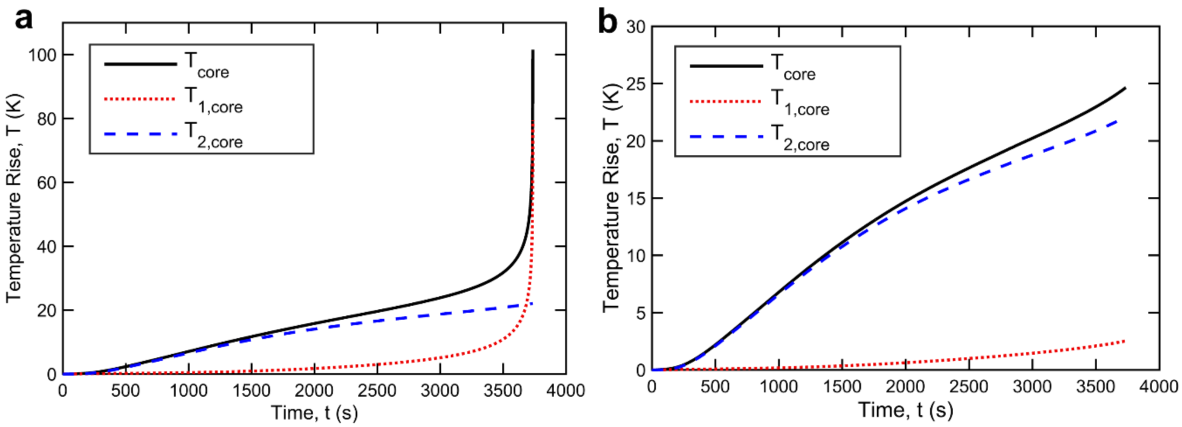

Figure 4. Plots of the core temperature rise as a function of time, along with its two components $T_{1,core}$ and $T_{2,core}$ for (a) $Q_0 = 5\times10^{22}$ Wm$^{-3}$ and $E_a = 1.1\times10^5$ Jmol$^{-1}$; (b) $Q_0 = 5\times10^{22}$ Wm$^{-3}$ and $E_a = 1.1\times10^6$ Jmol$^{-1}$.

### 6-4-4. Prediction of the core temperature for past papers

Several past papers have reported measurement of surface temperature of Li-ion cells during thermal runaway events caused by a variety of factors such as high ambient temperature during an oven test [10,12,13]. A key drawback of these papers is the lack of information on the true temperature at the core of the cell, which may be significantly different from the reported surface temperature data. The analytical model presented in section 2, and validated through comparison with experimental data in section 4.2 is used to determine the core temperature as a function of time and compare against surface temperature measurements reported by these papers. The primary interest here is to determine how much hotter the core is compared to the surface temperature during a thermal runaway event.In order to do so, it is first important to define the total heat generation during thermal runaway based on chemical reaction kinetics. Heat generation during thermal runaway has been well characterized in several past papers [8-10]. The total heat generation is the sum of heat generated due to multiple processes, including solid electrolyte interface (SEI) decomposition, negative-solvent reaction, positive-solvent reaction and electrolyte decomposition. Each of these reactions begins at a specific temperature. Table 1 summarizes the governing equations for heat generation for each of these processes, as well as the respective starting temperature. In these equations, $H$, $W$ and $R$ refer to reaction specific heat release, material content and reaction rate, respectively. Further, $m$, $E_a$, $A$, $c$ and $\alpha$ refer to order, activation energy, frequency factor and initial dimensionless content, respectively. Also, $t_{SEI}$ is the initial SEI thickness. Values for various kinetic and physical parameters in the equations in Table 1 have been taken from past papers [9, 10].

Total heat generation within the cell during thermal runaway is the sum of all the heat generations due to the specified reactions and is given by

$$Q_{gen} = Q_{sei} + Q_{ne} + Q_{pe} + Q_e \tag{14}$$

Core temperature of an 18650 cell undergoing thermal runaway as reported by Lopez, et al. [10] is computed and compared against the reported surface temperature data. In this work, a Lithium-cobalt-oxide 18650 cell was subjected to a conventional oven test at 155 °C and surface temperature measurement using a thermocouple was reported. In order to determine the core temperature under these conditions, the reported surface temperature measurement is extracted, and used as the boundary condition for the mathematical model in section 2.

Table 1: Governing equations and parameters for heat generation rates of various processes responsible for thermal runaway.

| Reaction | Heat Generation | Rate of Reaction | Starting Temperature |
|---|---|---|---|
| SEI Decomposition | $Q_{sei} = H_{sei} W_c R_{sei}$ | $R_{sei} = A_{sei} \exp\left(-\frac{E_{a,sei}}{R_u T}\right) c_{sei}^{m,sei}$<br>$\frac{dc_{sei}}{dt} = -R_{sei}$ | 90-120 °C |
| Negative-Solvent Reaction | $Q_{ne} = H_{ne} W_c R_{ne}$ | $R_{ne} = A_{ne}\left(-\frac{t_{sei}}{t_{sei,ref}}\right) \exp\left(-\frac{E_{a,ne}}{R_u T}\right) c_{ne}^{m,ne}$<br>$\frac{dc_{ne}}{dt} = -R_{ne}$ | 120 °C |
| Positive-Solvent Reaction | $Q_{pe} = H_{pe} W_p R_{pe}$ | $R_{pe} = A_{pe} \alpha^{m,pe} (1-\alpha)^{m,pe} \exp\left(-\frac{E_{a,pe}}{R_u T}\right)$<br>$\frac{d\alpha}{dt} = R_{pe}$ | 170 °C |
| Electrolyte Decomposition | $Q_e = H_e W_e R_e$ | $R_e = A_e \exp\left(-\frac{E_{a,e}}{R_u T}\right) c_e^{m,e}$<br>$\frac{dc_e}{dt} = -R_e$ | 200 °C |

Figure 5 shows a plot of the computed core temperature for another study by Golubkove, et al. [13]. In this work, an 18650 NMC ($Li\ (Ni_{0.45}\ Mn_{0.45}\ Co_{0.10})O_2$ layered oxide cathode) Li-ion cell fixed inside a heater sleeve was placed inside a heatable reactor. The cell was initially at 25 °C and heated through constant power Joule heating. Surface temperature of the cell, measured using thermocouples, is used to determine the core temperature using the analytical model in section 2. In the absence of significant internal heat generation for the first 4000 seconds, the core and surface temperatures remain very close to each other. In this study the temperature of the heater increases slowly which results in only a minor difference between the core and the surface temperature during the initial period. When the cell temperature becomes large enough, significant heat begins to be generated due to exothermic reactions, which results in sharp increase in the core temperature. The peak core temperature during thermal runaway is several hundred of degrees Celsius higher than the measured surface temperature. Once the external heating is stopped, both core and surface temperature begin to drop off, similar to the previous case.

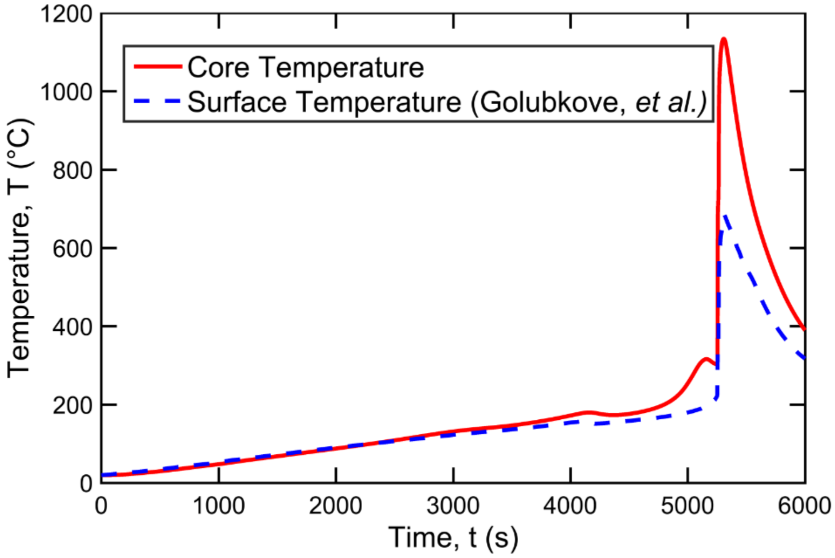

Figure 5. Plot of the computed core temperature compared to reported surface temperature [13] for a NMC 18650 cell undergoing an oven test.

Finally, the core temperature is also computed for thermal runaway of a $LiMn_2O_4$ Li-ion cell in an oven test [12]. In this case, the oven temperature is set to 240 °C throughout the experiment. The core temperature for this case, computed using the analytical model in section 2, as well as the reported surface temperature measurement [12] is plotted in Figure 6. Similar to the previous case, this plot shows a significant difference in the computed core temperature and measured surface temperature. This shows the importance of determining the core temperature during thermal runaway events instead of relying only on surface temperature measurements, which may significantly under-predict the thermal state of the cell. During thermal runaway, the cell may be much hotter than reported by an external thermocouple, and this must be accounted for in design and run-time management of a thermal runaway situation.

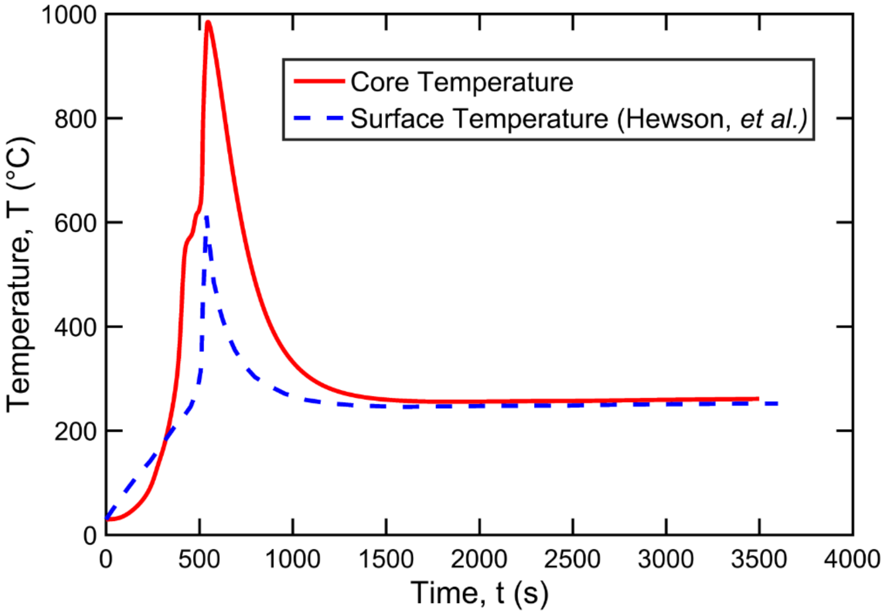

Figure 6. Plot of the computed core temperature compared to reported surface temperature measurement for an 18650 $LiMn_2O_4$ Li-ion cell undergoing an oven test [12].

As pointed out in section 2, the determination of the core temperature of the cell during thermal runaway requires information about heat generation parameters as well as thermal properties of the cell. Both of these data are easily available in past papers, where values of Arrhenius parameters of various processes during thermal runaway [7,8,10] as well as thermal properties of Li-ion cells [18,19] have been presented.

## 6-5. Conclusions

This work develops an analytical heat transfer model to determine the core temperature of a Li-ion cell undergoing thermal runaway based on surface temperature measurement. The technique is suitable for determining the core temperature as a function of time for a variety of experimental conditions where the surface temperature has been measured. Results show that the maximum core temperature during thermal runaway is several hundreds of degrees Celsius higher than the surface temperature. This demonstrates the critical importance of the core temperature of the cell during thermal runaway. The accuracy of the technique depends on chemical kinetics data during thermal runaway, as well as on thermophysical properties of the cell, particularly its specific heat. This work provides a new fundamental insight into the thermal behavior of Li-ion cells during thermal runaway, which is not possible through surface temperature measurement alone. It is expected that information about the core temperature of the cell during thermal runaway, determined by the technique described here may help improve the fundamental understanding of thermal runaway, as well as help design practical tools to predict the thermal state of the cell so that thermal runaway could be mitigated.

## 6-5. References

[1] V. Etacheri, R. Marom, R. Elazari, G. Salitra, D. Aurbach, Energy Environmental Sci. 4 (2011) 3243. (DOI: 10.1039/c1ee01598b).

[2] J.B. Goodenough, K.-S. Park, J. Am. Chem. Soc. 135 (2013) 1167. (DOI: 10.1021/ja3091438).

[3] B. Scrosati, J. Garche, J. Power Sources 195 (2010) 2419–2430. (DOI: 10.1016/j.jpowsour.2009.11.048).

[4] K. Shah, N. Balsara, S. Banerjee, M. Chintapalli, A.P. Cocco, W.K.S. Chiu, et al., J. Electrochem. Energy Conv. Storage 14 (2017) 020801. (DOI: 10.1115/1.4036456).

[5] K. Shah, V. Vishwakarma, A. Jain, J. Electrochem. Energy Conv. Storage 13 (2016) 030801. (DOI: 10.1115/1.4034413).

[6] T.M. Bandhauer, S. Garimella, T.F. Fuller, J. Electrochem. Soc. 158 (2011) R1. (DOI: 10.1149/1.3515880).

[7] A. Melcher, C. Ziebert, M. Rohde, H. Seifert, Energies 9 (2016) 292. (DOI: 10.3390/en9040292)

[8] R. Spotnitz, J. Franklin, J. Power Sources 113 (2003) 81–100. (DOI: 10.1016/s0378-7753(02)00488-3).

[9] G.-H. Kim, A. Pesaran, R. Spotnitz, J. Power Sources 170 (2007) 476–489. (DOI: 10.1016/j.jpowsour.2007.04.018).

[10] C.F. Lopez, J.A. Jeevarajan, P.P. Mukherjee, J. Electrochem. Soc. 162 (2015) A2163. (DOI: 10.1149/2.0751510jes).

[10] K. Shah, D. Chalise, A. Jain, J. Power Sources 330 (2016) 167–174. (DOI: 10.1016/j.jpowsour.2016.08.133).

[12] J. Hewson, R. Shurtz, Energy Storage Systems Safety & Reliability Workshop, Sante Fe, NM (2017).

[13] A.W. Golubkov, D. Fuchs, J. Wagner, H. Wiltsche, C. Stangl, G. Fauler, et al., RSC Adv. 4 (2014) 3633–3642. (DOI: 10.1039/c3ra45748f).

[14] H. Maleki, J. Electrochem. Soc. 146 (1999) 3224. (DOI: 10.1149/1.1392458).

[15] E. Roth, D. Doughty, J. Power Sources 128 (2004) 308–318. (DOI: 10.1016/j.jpowsour.2003.09.068).

[16] J. Dahn, E. Fuller, M. Obrovac, U. Vonsacken, Solid State Ionics 69 (1994) 265–270. (DOI: 10.1016/0167-2738(94)90415-4).

[17] D. Macneil, Z. Lu, Z. Chen, J. Dahn, J. Power Sources 108 (2002) 8–14. (DOI: 10.1016/s0378-7753(01)01013-8).

[18] S. Drake, M. Martin, D. Wetz, J. Ostanek, S. Miller, J. Heinzel, et al., J. Power Sources 285 (2015) 266–273. (DOI: 10.1016/j.jpowsour.2015.03.008).

[19] Y. Ye, L.H. Saw, Y. Shi, K. Somasundaram, A.A. Tay, Electrochimica Acta 134 (2014) 327–337. (DOI: 10.1016/j.electacta.2014.04.134).

[20] J. Jeevarajan, Safety of Commercial Lithium-Ion Cells and Batteries, In: Lithium-Ion Batteries, G. Pistoia (Ed.) (2014) 387–407. (DOI: 10.1016/b978-0-444-59513-3.00017-0).

[21] D. Anthony, D. Sarkar, A. Jain, Scientific Reports 6 (2016) 35886:1. (DOI: 10.1038/srep35886).

[22] D. Anthony, D. Wong, D. Wetz, A. Jain, Int. J. Heat Mass Transfer 111 (2017) 223–231. (DOI: 10.1016/j.ijheatmasstransfer.2017.03.095).

[23] Forgez, D.V. Do, G. Friedrich, M. Morcrette, C. Delacourt, J. Power Sources 195 (2010) 2961–2968. (DOI: 10.1016/j.jpowsour.2009.10.105).

[24] J.B. Robinson, J.A. Darr, D.S. Eastwood, G. Hinds, P.D. Lee, P.R. Shearing, et al., J. Power Sources 252 (2014) 51–57. (DOI: 10.1016/j.jpowsour.2013.11.059).

[25] S. Drake, D. Wetz, J. Ostanek, S. Miller, J. Heinzel, A. Jain, J. Power Sources 252 (2014) 298–304. (DOI: 10.1016/j.jpowsour.2013.11.107).

[26 ] S. Novais, M. Nascimento, L. Grande, M. Domingues, P. Antunes, N. Alberto, et al., Sensors 16 (2016) 1394. (DOI: 10.3390/s16091394).

[27] R. Srinivasan, B.G. Carkhuff, M.H. Butler, A.C. Baisden, Electrochimica Acta 56 (2011) 6198–6204. (DOI: 10.1016/j.electacta.2011.03.136).

[28] G. Zhang, L. Cao, S. Ge, C.-Y. Wang, C.E. Shaffer, C.D. Rahn, J. Electrochem. Soc. 161 (2014). (DOI: 10.1149/2.0051410jes).

[29] R.A. Leising, M.J. Palazzo, E.S. Takeuchi, K.J. Takeuchi, J. Electrochem. Soc. 148 (2001) A838-A844.

[30] Hahn, D.W., Özişik, M.N., 'Heat Conduction,' 3rd Ed., John Wiley & Sons, Hoboken, New Jersey, 2012.

[31] Incropera, F.P., DeWitt, D.P., Bergman, T.L., Levine, A.S., 'Introduction to Heat Transfer,' 5th Ed., John Wiley & Sons, 2006.

# Chapter 7

# Analytical Modeling of Solid Phase Diffusion in Single-Layer and Composite Electrodes under Time-Dependent Flux Boundary Condition

**Published as**: Parhizi, M., & Jain, A. (2020). Analytical Modeling of Solid Phase Diffusion in Single-Layer and Composite Electrodes Under Time-Dependent Flux Boundary Condition. *Journal of The Electrochemical Society*, *167*(6), 060528.

## 7-1. Introduction

Superior electrochemical characteristics of Li-ion cells compared to other secondary batteries have made them the preferred energy storage and conversion devices in a wide variety of applications[1-3]. Higher power and energy density, longer cycle life and lower self-discharge rate are among the key advantages of Li-ion cells over competing technologies[4-7]. A wide variety of mathematical models have been developed to predict and optimize electrochemical transport in a Li-ion cell under different operating conditions[8,9]. Mathematical models for Li-ion cells can broadly be divided into two categories – empirical and electrochemical models[10,11]. Empirical models employ data analysis techniques to predict the future state of a Li-ion cell based on past experimental data[12,13]. Compared to electrochemical models, empirical models are relatively faster and simpler, but cannot be used to determine finer details of electrochemical properties and cell characteristics. Alternatively, electrochemical models are more detailed, physics-based models that solve reaction kinetics, mass and charge transport equations[8,14,15]. Among the available physics-based models for Li-ion cells, Pseudo-2D model (P2D) and Single Particle Model (SPM) are the most popular ones[8]. P2D model solves for diffusion of Li-ions in the liquid electrolyte phase, as well as diffusion of Li-ions in solid particles and charge transport in both liquid and solid phases[8,10]. Diffusion of Li-ions in electrolyte and electronic conduction in both the liquid and solid phase are considered to occur in the linear dimension, *x,* while the diffusion of Li-ions in solid phase, assumed to be a spherical particle is considered to be a function of radial dimension, *r* within the solid particle, as well as *x*. Although P2D model is robust and accurate, the large number of equations needed to be solved significantly increases computational time[16]. Some work has been presented in simplification of computation associated with the P2D model[16,17]. In contrast, the SPM is a simplified, one-dimensional P2D model that describes only the solid phase diffusion of

Li-ions in porous electrodes and neglects spatial variations in the electrolyte concentration and the potentials[8,18,19]. SPM is simple and computationally fast but limited to thin electrodes and applications with low discharge rates where the gradient in concentration of Li-ions in the liquid phase can be neglected and the porous electrode can be assumed to be a single particle[16,20].

Mathematical models summarized above often result in a set of coupled equations that are often non-linear. As a result, exact solutions for these mathematical models exist only for a few limited cases. For example, diffusion equation for a solid solution cathodes initially at zero concentration has been solved using Laplace transformation approach[21]. Separation of Variables (SOV) technique has been used to solve a similar model for discharging of a Li-ion cell for different limiting cases[22]. Analytical solution for 1-D transient diffusion in a thin film, spherical electrode particle and composite electrode under constant galvanostatic discharge boundary condition and zero initial concentration has been developed using an extended separation of variables method[23,24]. Laplace transformation technique has been used to solve material balance equation in both solid and solution phases with non-zero initial concentration[25]. This model considers the migration term in solution phase diffusion with a constant transference number[25]. Integral transform method has been used to solve material balance equation for different cathode geometries under galvanostatic discharge boundary conditions[26]. A Finite Integral Transform (FIT) method has been used to find an exact solution for the diffusion of Li/Li+ into a spherical particle for arbitrary initial and boundary conditions[27]. The method of Pseudo-Steady-State (PSS) is used to ensure convergence in this work[27]. Green's function approach has been used to solve the material balance equation in solution phase of a thin film electrode under a constant galvanostatic discharge condition[28].

In addition to the limited cases where an exact solution is possible, approximate analytical solutions have also been developed in order to reduce the complexity and required computational time. An example is the Parabolic Profile approximation (PP) method, in which the concentration profile in a spherical electrode particle is assumed to be a second, fourth, or sixth order polynomial[29,30]. Other approximate analytical methods include residue grouping technique which is based on the transcendental transfer function approach[31], State Variable Model (SVM), which is a combination of analytical transfer functions and a numerical transfer matrix[31,32], Electrode Averaged Model (EAM)[33], Proper Orthogonal Decomposition (POD)[34], Extended Single Particle Model (ESPM)[35,36], etc.

While most of the past analytical models focus on constant galvanostatic discharge conditions, there is a relative lack of work on time-dependent flux boundary conditions. For example, the diffusion problem in composite electrode has been solved for a constant boundary condition[23]. However, in some cases, time-dependent boundary conditions are also important since the applied current density may be time-dependent. While several past studies presented approximate solutions to such problems[15,16,37,38], there is a relative lack of analytical solutions for this class of problems. The few analytical solutions has been presented for such problems are for the case of single-layer electrodes and not composite electrodes[27]. For instance, exact solutions for diffusion in a spherical single electrode particle has been presented using the finite integral transform method for time-dependent boundary conditions[27]. Green's function is a powerful tool for solving such problems. While the use of Green's functions in heat transfer problems is quite common[39,40], only limited work exists on the use of this tool for species diffusion problems in electrochemical systems[28].

This work presents an exact analytical solution for Li-ion diffusion in thin film and spherical electrodes, as well as composite two-layer electrodes with arbitrary initial conditions and time-dependent flux boundary condition using Green's function approach. The exact solution presented here is validated against both numerical simulations and previous studies. Concentration distribution for cases representative of realistic discharge conditions is predicted using the model. The mathematical tools developed in this work help understand species transport in a Li-ion cell, thereby contributing towards improved performance of electrochemical energy storage devices and systems.

## 7-2. Mathematical Modeling

### 7-2-1. Green's function solution

Greens' function is a powerful mathematical tool which can be used to solve linear partial differential equations with multiple non-homogeneities in the governing equation, boundary conditions and initial condition[39,40]. While the method of separation of variables is not applicable to problems with time-dependent non-homogeneities, Green's function approach can be used to solve a wide variety of such problems. Green's function approach has been used for a wide variety of thermal conduction problems[39,40]. Since thermal and species diffusion are governed by similar conservation equations, Green's function approach can also be used for solving species diffusion problems, such as those that appear in Li-ion cell electrodes.

The general form of the solution to any 1-D diffusion problem in non-dimensional form using Green's function approach is given by[39]:

$$c(x,t) = \int G(x,t|x',t')_{t'=0} F(x') x'^p dx' + \iint G(x,t|x',t')\, g(x',t') x'^p dx' dt' \qquad (1)$$

$$+ \sum_{i=1}^{N} \left\{ \int \left[ x'^p G(x,t|x',t') \right]_{x=x'} f_i(t') dt' \right\}$$

Where $x'^p$ is the Sturm–Liouville weight function, and $p$=0, 1 and 2 for slabs, cylinders and spheres respectively. Here, *F(x)* is the initial condition and *g* is the generation or consumption term. The summation is taken over all boundaries of the problem. *G* is the Green's function that must be determined.

The three terms on the right-hand side of equation (1) represent contributions of the initial concentration, generation or consumption, and boundary conditions respectively. In order to present the solution given by equation (1) for a specific problem, the Green's function, $G(x,t|x',t')$ needs to be determined first. This is usually done by solving the corresponding homogeneous version of the problem. For any homogeneous problem, the second and third term in equation (1) will be zero. Therefore, a comparison between the solution to the homogeneous problem and the first term in equation (1) provides the Green's function evaluated at $t' = 0$, $G(x,t|x',t')_{t'=0}$. The full Green's function, $G(x,t|x',t')$ is then determined by replacing *t* with $(t - t')$ in $G(x,t|x',t')_{t'=0}$.

Analytical solutions for transient diffusion under a time-dependent flux condition using Green's function approach are presented next. A number of progressively complicated cases are considered – a thin film electrode, a spherical particle electrode and composite electrodes, both Cartesian and spherical. Figures 1(a)-(d) show schematics of the thin film, spherical particle, two layer and spherical composite electrodes respectively. Specific details for these cases are discussed in sub-sections below.

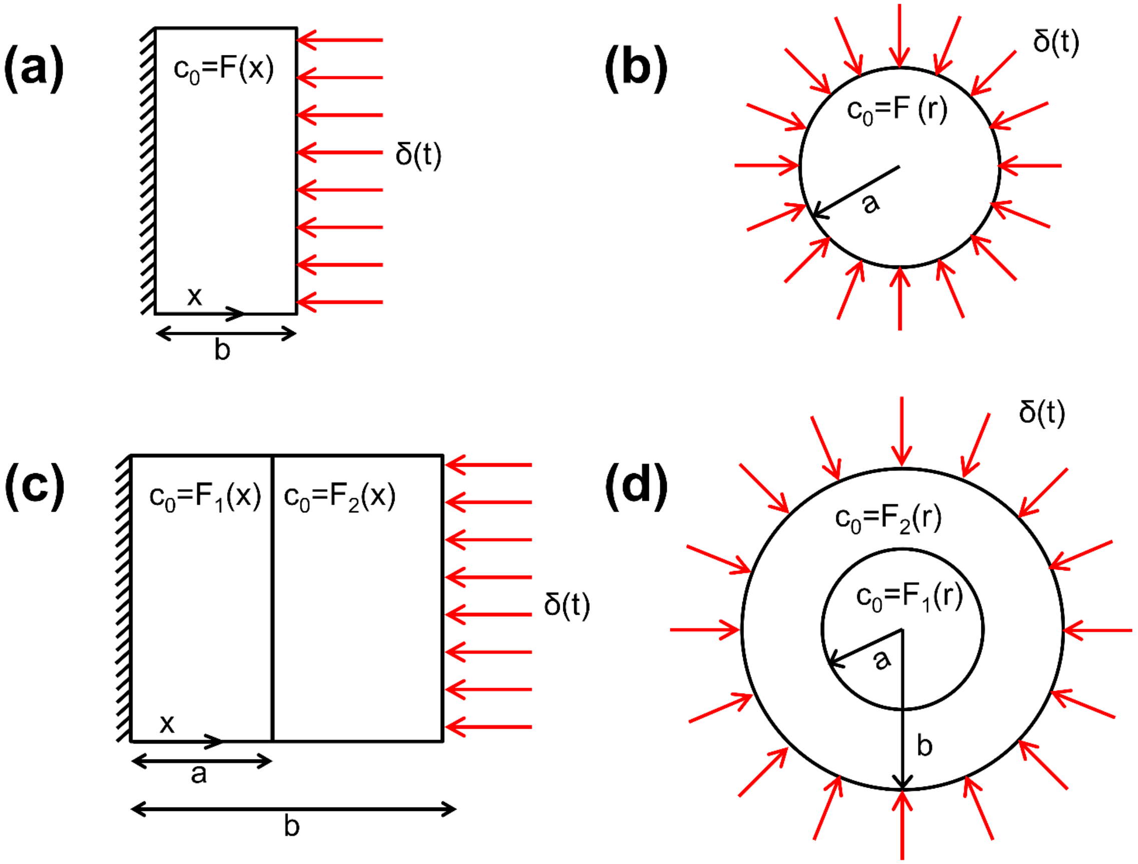

Figure 1. Schematic of the four electrode geometries considered in this work: (a) Thin film electrode; (b) Spherical electrode particle; (c) Composite slab electrode; (d) Composite spherical electrode.

### 7-2-2. Thin film electrode

Figure 1(a) shows a schematic of a one-dimensional thin film electrode initially at a non-uniform concentration of *F(x)* and operating under a time-dependent flux boundary condition. Referring to the non-dimensionalization scheme presented in the Nomenclature section, the governing equation for concentration distribution can be written in non-dimensional form as follows:

$$\frac{\partial^2 c}{\partial x^2} = \frac{\partial c}{\partial t} \tag{2}$$

Associated boundary conditions at the two ends are

$$\left(\frac{\partial c}{\partial x}\right)_{x=0} = 0 \qquad \text{at } x = 0 \tag{3}$$

$$\left(\frac{\partial c}{\partial x}\right)_{x=1} = \delta(t) \qquad \text{at } x = 1 \tag{4}$$

Equation (3) results from symmetry at *x*=0 and equation (4) represents the applied, time-dependent flux boundary condition at *x*=1, where *δ(t)* is the dimensionless current density.

where $\delta$ is the dimensionless, time-dependent current density defined in the nomenclature section.

The initial condition associated with this problems is:

$$c = F(x) \qquad \text{at } t = 0 \tag{5}$$

As outlined in the previous sub-section, the first step to construct the Green's function associated with this problem is to solve the corresponding homogeneous problem. The solution to the homogeneous problem can be determined using the Separation of Variables technique[39] as follows:

$$c(x,t) = \int_0^1 F(x')dx' + \int_0^1 \sum_{n=1}^{\infty} [2\cos(\lambda_n x)\cos(\lambda_n x')\exp(-\lambda_n^2 t)]F(x')dx' \tag{6}$$

where $\lambda_n = n\pi$ are the eigenvalues for $n$=1,2,3,…. A comparison between equations (1) and (6) indicates that the expression for Green's function calculated for $t' = 0$ can be written as follows:

$$G(x,t|x',t')_{t'=0} = 1 + 2\sum_{n=1}^{\infty} \cos(\lambda_n x)\cos(\lambda_n x')\exp(-\lambda_n^2 t) \tag{7}$$

Therefore, the general form of the Green's function is obtained by replacing $t$ with $t - t'$ in equation (7):

$$G(x,t|x',t') = 1 + 2\sum_{n=1}^{\infty} \cos(\lambda_n x)\cos(\lambda_n x')\exp(-\lambda_n^2 (t-t')) \tag{8}$$

Now that the Green's function is determined, a solution for the problem defined in equations (2)-(5) can be constructed. The solution can be written as:

$$c(x,t) = c_1(x,t) + c_2(x,t) + c_3(x,t) \tag{9}$$

where

$$c_1(x,t) = \int_{x'=0}^{1} F(x')dx' + \int_{x'=0}^{1} \sum_{n=1}^{\infty} [2\cos(\lambda_n x)\cos(\lambda_n x')\exp(-\lambda_n^2 t)]F(x')dx' \tag{10}$$

$$c_2(x,t) = 0 \tag{11}$$

$$c_3(x,t) = \int_{t'=0}^{t} \delta(t')dt' + 2\sum_{n=1}^{\infty} \cos(\lambda_n x)\cos(\lambda_n) \int_{t'=0}^{t} \exp(-\lambda_n^2(t-t'))\delta(t')dt' \tag{12}$$

Note that the solution accounts for the time-dependent flux boundary condition in the expression for $c_3(x,t)$, given by equation (12). Further, since there is no non-homogeneity in equation (2), the second term of the Green's function solution is zero.

As a special case, if the initial concentration is constant, $C_0$, the second term in equation (10) becomes zero, leading to further simplification.

### 7-2-3. Spherical electrode particle

Figure 1(b) shows a schematic of a one-dimensional spherical particle initially at a given concentration distribution *F(r)* and subject to time-dependent flux at its surface. The non-dimensional governing equation for concentration distribution and boundary conditions can be written in non-dimensional form as follows:

$$\frac{1}{r^2}\frac{\partial}{\partial r}\left(r^2\frac{\partial c}{\partial r}\right) = \frac{\partial c}{\partial t} \tag{13}$$

where the initial and boundary conditions are

$$c = F(r) \qquad \text{at } t = 0 \tag{14}$$

$$c \Longrightarrow finite \qquad \text{as } r \longrightarrow 0 \tag{15}$$

$$\left(\frac{\partial c}{\partial r}\right)_{r=1} = \delta(t) \qquad \text{at } r = 1 \tag{16}$$

Similar to the thin film electrode problem, the homogeneous problem must be solved first. In order to do so, a new variable *U* is defined as $U(r,t) = rc(r,t)$, which facilitates a solution of the homogeneous problem using separation of variables method. The concentration profile can be derived to be:

$$c(r,t) = 3\int_0^1 r'^2 F(r) dr' + \int_0^1 \sum_{n=1}^{\infty} [\frac{1}{N_n r r'} \sin(\lambda_n r) \sin(\lambda_n r') \exp{(-\lambda_n^2 t)} r'^2 F(r') dr' \tag{17}$$

where *N<sub>n</sub>* is the norm defined as $N_n = \frac{\lambda_n^2}{2(\lambda_n^2+1)}$, and the eigenvalues $\lambda_n$ are positive roots of the transcendental equation $\lambda_n \cot \lambda_n = 1$.

Thus, comparing equation (17) with equation (1) and taking *p*=2 for the case of a sphere, the Green's function calculated at $t' = 0$ can be determined as follows:

$$G(r,t|r',t')_{t'=0} = 3 + \sum_{n=1}^{\infty} \frac{1}{N_n r r'} \sin(\lambda_n r) \sin(\lambda_n r') \exp{(-\lambda_n^2 t)} \tag{18}$$

The complete form of Green's function can be obtained by obtained by replacing *t* with $(t - t')$ in equation (18).

$$G(r,t|r',t') = 3 + \sum_{n=1}^{\infty} \frac{1}{N_n r r'} \sin(\lambda_n r) \sin(\lambda_n r') \exp\left(-\lambda_n^2 (t-t')\right) \tag{19}$$

Thus, based on equation (1), the concentration profile for the original problem can be written as:

$$c(r,t) = c_1(r,t) + c_2(r,t) + c_3(r,t) \tag{20}$$

where

$$c_1(r,t) = 3\int_{r'=0}^{1} r'^2 F(r') dr' + \int_0^1 \sum_{n=1}^{\infty} [\frac{1}{N_n r r'} \sin(\lambda_n r) \sin(\lambda_n r') \exp\left(-\lambda_n^2 t\right)] r'^2 F(r') dr' \tag{21}$$

$$c_2(r,t) = 0 \tag{22}$$

$$c_3(r,t) = 3\int_{t'=0}^{t} \delta(t') dt' + \frac{1}{r}\sum_{n=1}^{\infty} \frac{1}{N_n} \sin(\lambda_n r) \sin(\lambda_n) \int_{t'=0}^{t} \exp\left(-\lambda_n^2 (t-t')\right) \delta(t') dt' \tag{23}$$

Similar to the previous problem, the third component of the solution contains various integrals of the time-dependent flux boundary condition. Note that $c_2(x,t)$ becomes zero since there is no non-homogeneity in equation (13).

### 7-2-4. Composite electrodes

This section presents solutions for composite electrodes under time-dependent flux boundary condition. Section 2.3.1 presents the solution for a two-layer composite electrode in a rectangular geometry while Section 2.3.2 presents the solution for a composite spherical electrode particle.

Green's function approach can be used to solve multilayer problems. While the general procedure is similar to single-layer problems discussed in sections 2.2 and 2.3, the derivation of the solution is somewhat more complicated. Green's function solution for an *M*-layer problem involving non-homogeneities in the governing equation and boundary conditions can be written as[39]:

$$\begin{aligned} c(x,t) = &\sum_{j=1}^{M} \int_{x'=x_j}^{x_{j+1}} G_{ij}(x,t|x',t')_{t'=0} F_j(x') x'^{p} dx' \\ &+ \int_{t'=0}^{t} \int_{x'=x_j}^{x_{j+1}} G_{ij}(x,t|x',t') g_j(x',t') x'^{p} dx' dt' \\ &+ \sum_{k=1}^{K} \left\{ \int_{t'=0}^{t} \left[ x'^{p} G_{ij}(x,t|x',t') \right]_{x=x'} f_{jk}(t') dt' \right\} \end{aligned} \tag{24}$$

where *i*=1,2,…,*M* and *p*=0, 1 and 2 for slabs, cylinders and spheres, respectively

The composite Green's function is defined as[39]:

$$G_{ij}(x,t|x',t')_{t'=0} = \sum_{n=1}^{\infty} \frac{1}{N_n} \Gamma(t) \psi_{in}(x) \psi_{jn}(x') \tag{25}$$

$$G_{ij}(x,t|x',t') = \sum_{n=1}^{\infty} \frac{1}{N_n} \Gamma(t-t') \psi_{in}(x) \psi_{jn}(x') \tag{26}$$

where $x'^p$ is the Sturm–Liouville weight function. $N_n$ is the norm, given by

$$N_n = \sum_{j=1}^{M} \int_{x'=x_j}^{x_{j+1}} x'^p \psi_{jn}^2(x')dx' \tag{27}$$

where $\Gamma(t)$ and $\psi(x)$ can be found by solving the corresponding homogeneous problem, as discussed next.

### 7-2-4-1. Two-layer composite electrode

Figure 1(c) shows a two-layer composite electrode with an initial concentration distribution given by $F_1(x)$ and $F_2(x)$ in the two layers, respectively. The two layers have diffusion coefficient of $D_1$ and $D_2$, respectively. The goal is to find the concentration profile in the two regions. The governing equation, initial and boundary conditions can be written in non-dimensional form as follows:

$$\frac{\partial^2 c_1}{\partial x^2} = \frac{1}{\alpha}\frac{\partial c_1}{\partial t} \qquad 0 < x < l \tag{28}$$

$$\frac{\partial^2 c_2}{\partial x^2} = \frac{\partial c_2}{\partial t} \qquad l < x < 1 \tag{29}$$

Subject to the following boundary conditions

$$\left(\frac{\partial c_1}{\partial x}\right)_{x=0} = 0 \qquad \text{at } x = 0 \tag{30}$$

$$c_1 = c_2 \qquad \text{at } x = l \tag{31}$$

$$\alpha\left(\frac{\partial c_1}{\partial x}\right)_{x=l} = \left(\frac{\partial c_2}{\partial x}\right)_{x=l} \qquad \text{at } x = l \tag{32}$$

$$\left(\frac{\partial c_2}{\partial x}\right)_{x=1} = \delta(t) \qquad \text{at } x = 1 \tag{33}$$

Equation (30) arises from symmetry at x=0. Equations (31) and (32) are interfacial conditions representing species continuity and conservation of flux, respectively. Equation (33) is the applied time-dependent boundary condition.

The initial condition is

$$c_1 = F_1(x) \qquad \text{at } t = 0 \tag{34}$$

$$c_2 = F_2(x) \qquad \text{at } t = 0 \tag{35}$$

where $F_1$ and $F_2$ are the non-dimensional initial conditions.

Note the presence of additional non-dimensional parameters in this problem due to the presence of two layers that, in general, may have different thicknesses and diffusion coefficients.

This problem is considerably more complicated than the ones discussed in previous two sub-sections. However, the same concept of developing a Green's function solution can be applied, starting with derivation of a solution of the corresponding homogeneous problem. Similar to the separation of variables method for single-layer problems, the solution can be written as

$$c_i(x,t) = \psi_i(x)\Gamma(t) \tag{36}$$

Where $i$=1, 2.

Substituting equation (36) back into the governing equations results in two separate differential equations which can be solved for time-dependent and space-dependent components of equation (36) as follows:

$$\Gamma_n(t) = \exp\left(-\lambda_n^2 t\right) \tag{37}$$

$$\psi_{1n}(x) = A_{1n}\sin\left(\frac{\lambda_n x}{\sqrt{\alpha}}\right) + B_{1n}\cos\left(\frac{\lambda_n x}{\sqrt{\alpha}}\right) \tag{38}$$

$$\psi_{2n}(x) = A_{2n}\sin(\lambda_n x) + B_{2n}\cos(\lambda_n x) \tag{39}$$

Note that the non-dimensional parameter $\alpha$ is absorbed in the solution of one of the layers. Applying boundary conditions results in a set of equations for the unknown coefficients $A_{in}$ and $B_{in}$ written in matrix form as follows:

$$\begin{bmatrix} 1 & 0 & 0 & 0 \\ 0 & \cos\frac{\lambda_n l}{\sqrt{\alpha}} & -\sin\lambda_n l & -\cos\lambda_n l \\ 0 & \sqrt{\alpha}\sin\frac{\lambda_n l}{\sqrt{\alpha}} & \cos\lambda_n l & -\sin\lambda_n l \\ 0 & 0 & \cos\lambda_n & -\sin\lambda_n \end{bmatrix} \begin{bmatrix} A_{1n} \\ B_{1n} \\ A_{2n} \\ B_{2n} \end{bmatrix} = \begin{bmatrix} 0 \\ 0 \\ 0 \\ 0 \end{bmatrix} \tag{40}$$

In order to determine the eigenvalues, $\lambda_n$, equations (40) may be required to result in a nontrivial solution. This implies that the determinant of the matrix in equation (40) must be equal to zero, thereby resulting in a transcendental equation for the eigenvalues as follows:

$$\tan(\lambda_n l - \lambda_n) - \sqrt{\alpha}\tan(\lambda_n) = 0 \tag{41}$$

Without loss of generality, any one of the non-vanishing coefficients in equation (44) may be set to unity. In this case, $B_{1n}$ is chosen to be equal to 1. Consequently, the coefficients, $A_{in}$ and $B_{in}$, are determined to be

$$A_{1n} = 0 \tag{42}$$

$$B_{1n} = 1 \tag{43}$$

$$A_{2n} = \cos\frac{\lambda_n l}{\sqrt{\alpha}}\sin\lambda_n l - \sqrt{\alpha}\sin\frac{\lambda_n l}{\sqrt{\alpha}}\cos\lambda_n l \tag{44}$$

$$B_{2n} = \cos\frac{\lambda_n l}{\sqrt{\alpha}}\cos\lambda_n l + \sqrt{\alpha}\sin\frac{\lambda_n l}{\sqrt{\alpha}}\sin\lambda_n l \tag{45}$$

With these values, all the information is available to construct Green's functions based on equations (25) and (26). The concentration profile in each layer is found to be

$$c_1(x,t)=\sum_{n=0}^{\infty}\int_{x'=0}^{x'=l}\frac{1}{N_n}\exp(-\lambda_n^2 t)\cos\left(\frac{\lambda_n x}{\sqrt{\alpha}}\right)\cos\left(\frac{\lambda_n x'}{\sqrt{\alpha}}\right)F_1(x')dx' \tag{46}$$

$$+\int_{x'=l}^{x'=1}\frac{1}{N_n}\exp(-\lambda_n^2 t)\cos\left(\frac{\lambda_n x}{\sqrt{\alpha}}\right)(A_{2n}\sin(\lambda_n x')+B_{2n}\cos(\lambda_n x'))F_2(x')dx'$$

$$+\int_{t'=0}^{t'=t}\frac{1}{N_n}\exp(-\lambda_n^2(t-t'))\cos\left(\frac{\lambda_n x}{\sqrt{\alpha}}\right)(A_{2n}\sin(\lambda_n)+B_{2n}\cos(\lambda_n))\delta(t')dt'$$

$$c_2(x,t)=\sum_{n=0}^{\infty}\int_{x'=0}^{x'=l}\frac{1}{N_n}\exp(-\lambda_n^2 t)\,(A_{2n}\sin(\lambda_n x)+B_{2n}\cos(\lambda_n x))\cos\left(\frac{\lambda_n x'}{\sqrt{\alpha}}\right)F_1(x')dx' \tag{47}$$

$$+\int_{x'=l}^{x'=1}\frac{1}{N_n}\exp(-\lambda_n^2 t)\,(A_{2n}\sin(\lambda_n x)+B_{2n}\cos(\lambda_n x))(A_{2n}\sin(\lambda_n x')$$

$$+B_{2n}\cos(\lambda_n x'))F_2(x')dx'$$

$$+\int_{t'=0}^{t'=t}\frac{1}{N_n}\exp(-\lambda_n^2(t-t'))\,(A_{2n}\sin(\lambda_n x)+B_{2n}\cos(\lambda_n x))(A_{2n}\sin(\lambda_n)$$

$$+B_{2n}\cos(\lambda_n))\delta(t')dt'$$

Where $A_{2n}$ and $B_{2n}$ are shown in equations (44) and (45) and $N_n$ is defined in equation (27).Note that the zeroth terms of equations (46) and (47) can be calculated by finding the limits of these equations as $\lambda \to 0$. In a special case of zero initial concentration in both layers and constant flux, the solution can be written as follows:

$$c_1(x,t)=\delta\cdot t+\sum_{n=1}^{\infty}\int_{t'=0}^{t'=t}\frac{1}{N_n}\exp(-\lambda_n^2(t-t'))\cos\left(\frac{\lambda_n x}{\sqrt{\alpha}}\right)(A_{2n}\sin(\lambda_n)+B_{2n}\cos(\lambda_n))\delta(t')dt' \tag{48}$$

$$c_2(x,t) = \delta \cdot t + \sum_{n=1}^{\infty} \int_{t'=0}^{t\prime=t} \frac{1}{N_n} \exp(-\lambda_n^2(t-t'))\,(A_{2n}\sin(\lambda_n x) + B_{2n}\cos(\lambda_n x))(A_{2n}\sin(\lambda_n) + B_{2n}\cos(\lambda_n))\delta(t')dt' \tag{49}$$

Diffusion in a two-layer spherical composite electrode is analyzed next.

### 7-2-4-2. Spherical composite electrode

Figure 1(d) presents a schematic of a composite spherical electrode. Similar to the previous sub-section, the initial concentration in the two layers is assumed to be $F_1(r)$ and $F_2(r)$, respectively. A time-varying, inward flux $\delta(t)$ is assumed at the outer surface. In this case, the governing equation, initial and boundary conditions can be written as follows:

$$\frac{1}{r^2}\frac{\partial}{\partial r}\left(r^2\frac{\partial c}{\partial r}\right) = \frac{1}{\alpha}\frac{\partial c_1}{\partial t} \qquad 0 < x < b \tag{50}$$

$$\frac{1}{r^2}\frac{\partial}{\partial r}\left(r^2\frac{\partial c}{\partial r}\right) = \frac{\partial c_2}{\partial t} \qquad b < x < 1 \tag{51}$$

Subject to the following boundary conditions

$$c \Longrightarrow finite \qquad \text{as } r \longrightarrow 0 \tag{52}$$

$$c_1 = c_2 \qquad \text{at } r = l \tag{53}$$

$$\alpha\left(\frac{\partial c_1}{\partial r}\right)_{r=b} = \left(\frac{\partial c_2}{\partial r}\right)_{r=b} \qquad \text{at } r = l \tag{54}$$

$$\left(\frac{\partial c_2}{\partial r}\right)_{r=1} = \delta(t) \qquad \text{at } r = 1 \tag{55}$$

and the initial conditions

$$c_1 = F_1(r) \qquad \text{at } t = 0 \tag{56}$$

$$c_2 = F_2(r) \qquad \text{at } t = 0 \tag{57}$$

Here, equations (53) an (54) represent species continuity and flux conservation, respectively, at the interface.

Similar to the single spherical particle problem, a new variable $U$ is defined as $U(r,t) = rc(r,t)$, to facilitate the derivation. After re-writing the governing equations and boundary conditions based on the new variable, $U$, and employing the separation of variables technique, the solution to the homogeneous problem can be written as:

$$c_i(x,t) = r\psi_i(r)\Gamma(t) \tag{58}$$

$$\Gamma_n(t) = \exp\left(-\lambda_n^2 t\right) \tag{59}$$

$$\psi_{1n}(r) = A_{1n}\sin\left(\frac{\lambda_n r}{\sqrt{\alpha}}\right) + B_{1n}\cos\left(\frac{\lambda_n r}{\sqrt{\alpha}}\right) \tag{60}$$

$$\psi_{2n}(r) = A_{2n}\sin(\lambda_n r) + B_{2n}\cos\lambda_n r \tag{61}$$

Substituting equations (60) and (61) back into the boundary conditions results in the following equations in matrix form

$$\begin{bmatrix} \sin\frac{\lambda_n l}{\sqrt{\alpha}} & 0 & -\sin\lambda_n l & -\cos\lambda_n l \\ 1 & 0 & 0 & 0 \\ \alpha\left(\frac{\lambda_n l}{\sqrt{\alpha}}\cos\frac{\lambda_n l}{\sqrt{\alpha}} - \sin\frac{\lambda_n l}{\sqrt{\alpha}}\right) & 0 & \sin\lambda_n l - \lambda_n l\cos\lambda_n l & \cos\lambda_n l + \lambda_n l\sin\lambda_n l \\ 0 & 0 & \lambda_n\cos\lambda_n - \sin\lambda_n & \lambda_n\sin\lambda_n + \cos\lambda_n \end{bmatrix} \begin{bmatrix} A_{1n} \\ B_{1n} \\ A_{2n} \\ B_{2n} \end{bmatrix} = \begin{bmatrix} 0 \\ 0 \\ 0 \\ 0 \end{bmatrix} \tag{62}$$

Similar to the previous section, one of the non-zero coefficients, $A_{1n}$ is set to a value of 1. Therefore, the coefficients, $A_{in}$ and $B_{in}$, are determined to be

$$A_{1n} = 1 \tag{63}$$

$$B_{1n} = 0 \tag{64}$$

$$A_{2n} = \sin\frac{\lambda_n l}{\sqrt{\alpha}}(\cos\lambda_n l + \lambda_n l\sin\lambda_n l) - \alpha\cos\lambda_n l\left(\sin\frac{\lambda_n l}{\sqrt{\alpha}} - \frac{\lambda_n l}{\sqrt{\alpha}}\cos\frac{\lambda_n l}{\sqrt{\alpha}}\right) \tag{65}$$

$$B_{2n} = \alpha\sin\lambda_n l\left(\sin\frac{\lambda_n l}{\sqrt{\alpha}} - \frac{\lambda_n l}{\sqrt{\alpha}}\cos\frac{\lambda_n l}{\sqrt{\alpha}}\right) - \sin\frac{\lambda_n l}{\sqrt{\alpha}}(\sin\lambda_n l - \lambda_n l\cos\lambda_n l) \tag{66}$$

Based on the requirement of non-trivial solution of equation (62), the eigenvalues, $\lambda_n$ are determined to be given by the roots of the following transcendental equation

$$\tan\frac{\lambda_n l}{\sqrt{\alpha}}\tan(\lambda_n l-\lambda_n)(\alpha-1-\lambda_n^2 l)+\tan\frac{\lambda_n l}{\sqrt{\alpha}}(\lambda_n l-\lambda_n+\alpha\lambda_n)-\alpha\frac{\lambda_n l}{\sqrt{\alpha}}\tan(\lambda_n l-\lambda_n) \\ -\alpha\frac{\lambda_n^2 l}{\sqrt{\alpha}}=0 \tag{67}$$

Based on these expressions for the coefficients, the concentration profile can be determined in both spherical regions from the following equations:

$$c_1(x,t)=\sum_{n=0}^{\infty}\int_{r=0}^{r'=l}\frac{r'1}{rN_n}\exp(-\lambda_n^2 t)\sin\left(\frac{\lambda_n r}{\sqrt{\alpha}}\right)\sin\left(\frac{\lambda_n r'}{\sqrt{\alpha}}\right)F_1(r')dx' \\ +\int_{r'=l}^{r'=1}\frac{r'}{rN_n}\exp(-\lambda_n^2 t)\sin\left(\frac{\lambda_n r}{\sqrt{\alpha}}\right)(A_{2n}\sin(\lambda_n r')+B_{2n}\cos(\lambda_n r'))F_2(r')dx' \\ +\int_{t'=0}^{t\prime=t}\frac{l}{rN_n}\exp(-\lambda_n^2(t-t'))\sin\left(\frac{\lambda_n r}{\sqrt{\alpha}}\right)(A_{2n}\sin(\lambda_n)+B_{2n}\cos(\lambda_n))\delta(t')dt' \tag{68}$$

$$c_2(x,t)=\sum_{n=0}^{\infty}\int_{r'=0}^{r'=l}\frac{r'}{rN_n}\exp(-\lambda_n^2 t)\,(A_{2n}\sin(\lambda_n r)+B_{2n}\cos(\lambda_n r))\sin\left(\frac{\lambda_n r'}{\sqrt{\alpha}}\right)F_1(r')dx' \\ +\int_{r'=l}^{r'=1}\frac{r'}{rN_n}\exp(-\lambda_n^2 t)\,(A_{2n}\sin(\lambda_n r)+B_{2n}\cos(\lambda_n r))(A_{2n}\sin(\lambda_n r') \\ +B_{2n}\cos(\lambda_n r'))F_2(r')dr' \\ +\int_{t'=0}^{t\prime=t}\frac{l}{rN_n}\exp(-\lambda_n^2(t-t'))\,(A_{2n}\sin(\lambda_n r)+B_{2n}\cos(\lambda_n r))(A_{2n}\sin(\lambda_n) \\ +B_{2n}\cos(\lambda_n))\delta(t')dt' \tag{69}$$

Note that the zeroth terms of equations (68) and (69) can be calculated by finding the limits of these equations as λ→0. Moreover, in order to calculate the concentration at $r$=0, one must calculate the limit when $r$→0. In a simple case of zero concentration in both layers and constant flux, the solution can be written as follows:

$$c_1(x,t) = 3\delta \cdot t + \sum_{n=0}^{\infty} \int_{t'=0}^{t\prime=t} \frac{l}{rN_n} \exp(-\lambda_n^2(t-t')) \sin\left(\frac{\lambda_n r}{\sqrt{\alpha}}\right) (A_{2n}\sin(\lambda_n) + B_{2n}\cos(\lambda_n))\delta(t')dt' \tag{70}$$

$$c_2(x,t) = 3\delta \cdot t + \sum_{n=0}^{\infty} \int_{t'=0}^{t\prime=t} \frac{l}{rN_n} \exp(-\lambda_n^2(t-t'))\,(A_{2n}\sin(\lambda_n r) + B_{2n}\cos(\lambda_n r))(A_{2n}\sin(\lambda_n) + B_{2n}\cos(\lambda_n))\delta(t')dt' \tag{71}$$

## 7-3. Results and Discussion

### 7-3-1. Model validation

Validation of the Green’s function based models presented in Section 2 is carried out by comparison with past studies and numerical computation. This comparison is discussed in sub-sections 3.1.1 and 3.1.2, respectively, below.

#### 7-3-1-1. Validation against past studies

Concentration profiles predicted by the Green’s function based models are compared against past studies by Subramanian & White[23] and Guo & White[37]. While Subramanian & White[23] used the method of separation of variables for composite electrodes under a constant galvanostatic boundary condition, Guo & White[37] used an approximate analytical solution for spherical electrode particle under both constant and a time-dependent flux boundary conditions. For comparison with Subramanian & White[23], the cases of constant galvanostatic discharge boundary condition for both thin film composite electrodes and composite spherical electrode particle are considered. The dimensionless current density, $\delta$, and ratio of diffusion coefficients, $\alpha$, are taken to be 1 and 0.25, respectively, consistent with Subramanian & White[23]. Thicknesses of both layers are considered to be equal. Figure 2(a) plots the concentration profile determined by the present model and previous work[23] for a composite slab. Similar comparison is presented in Figure 2(b) for a composite spherical electrode. In both cases, results show very good agreement between the present model and past studies across the entire electrode and at multiple times. In order to further validate the Green's function model, a study by Guo & White[37] is used for comparison. This paper presented an approximate analytical solution for solid-phase diffusion in a spherical particle under constant and time-dependent flux boundary condition. Values of various parameters are taken to be consistent with the previous work. Figure 3 presents a plot of concentration as a function of time at the surface of the electrode for a constant dimensionless current density of $\delta$=0.2. Very good agreement between the present work and past work is seen.

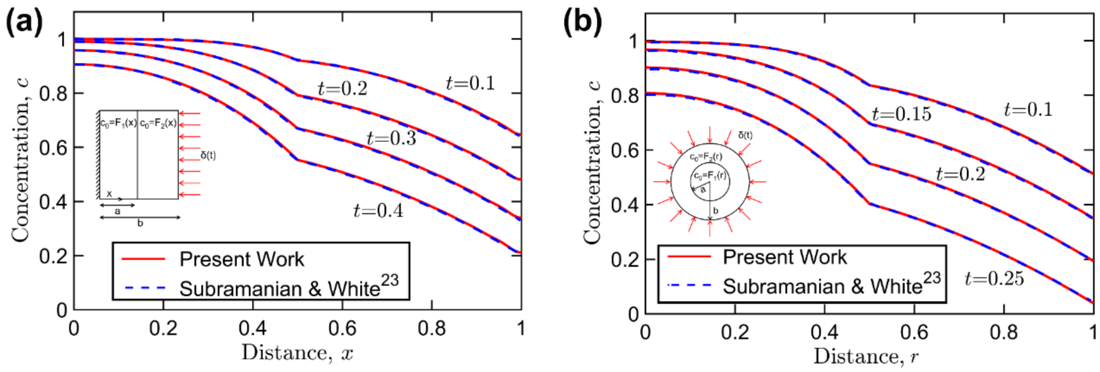

Figure 2. Validation against past study[23] for composite two-layer electrodes: Non-dimensional concentration as a function of non-dimensional distance, $x$ and $r$, at multiple times for (a) A

composite slab electrode, (b) A composite spherical electrode. Both cases are for discharge, with $\delta$=-1.

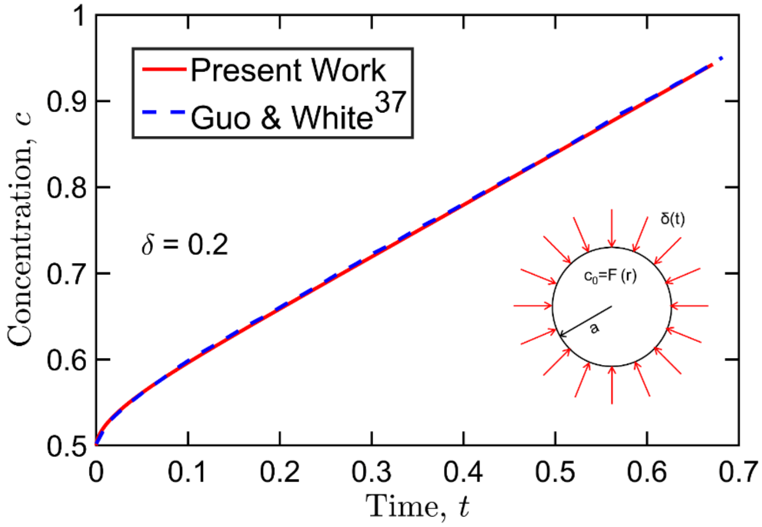

Figure 3. Validation against past study[37] for a spherical particle electrode: Non-dimensional concentration as a function of non-dimensional time at the particle's surface for a constant flux $\delta$=0.2.

### 7-3-1-2 Validation against numerical simulations

Further validation is carried out by comparison with a finite difference based calculation for solid-phase diffusion in thin film, spherical particle, composite slab and composite spherical electrodes. In order to do so, a finite difference method is used. The governing equations and boundary conditions are discretized using an implicit approach. 1000 and 2000 nodes are used for single layer and double layer electrodes, respectively. A time-step of 1 second is used for the numerical solution. Mesh and time-step sensitivity study is carried out in order to ensure that the results are independent of these variables. Figures (4)–(7) present comparisons between the Green's function solution and numerical solution.

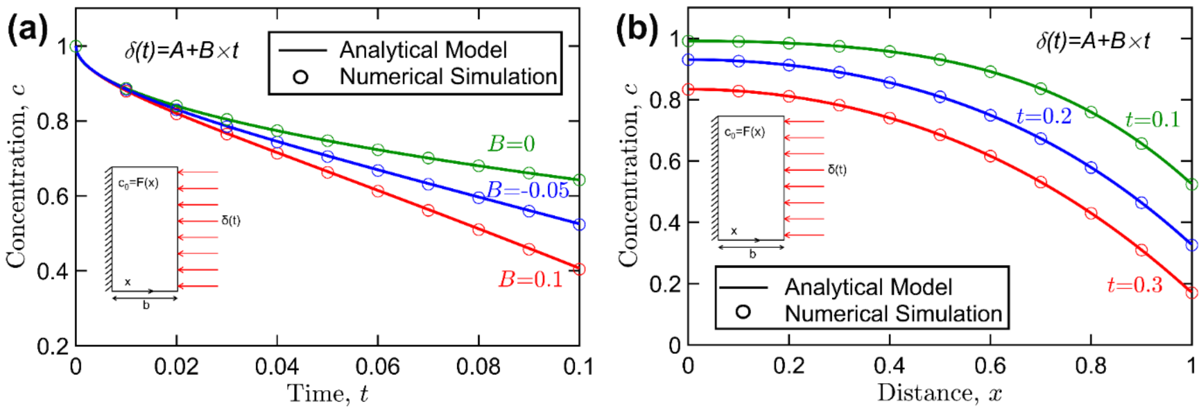

Figure 4. Validation against numerical model for a linear flux boundary condition, *δ(t)=A+B·t* in a thin film electrode: (a) Non-dimensional concentration as a function of non-dimensional time at the electrode's surface for *A*=-1 and multiple values of slope, *B*, (b) Non-dimensional concentration as function of non-dimensional distance, *x*, for *A*=-1 and *B*=-0.05 at multiple times.

Figure 4(a) plots concentration as a function of time for a linear time-dependent current density at the electrode's surface, $\delta(t)=A+B\cdot t$ for a thin film electrode for both analytical and numerical models. The concentration profile is plotted for a constant value of *A* and multiple values of slope, *B*. Very good agreement is seen for each case. Figure 4(b) plots the concentration as a function of distance, *x*, at multiple times for a linear current density, $\delta(t)=A+B\cdot t$, where A=-1 and B=-0.05. Note that the negative signs are due the discharge boundary condition.

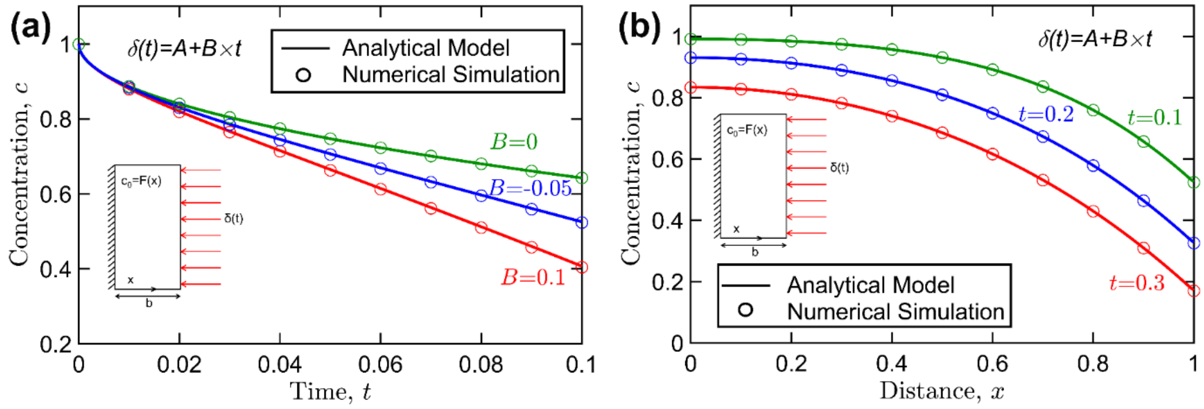

Figure 4. Validation against numerical model for a linear flux boundary condition, *δ(t)=A+B·t* in a thin film electrode: (a) Non-dimensional concentration as a function of non-dimensional time at the electrode's surface for *A*=-1 and multiple values of slope, *B*, (b) Non-dimensional concentration as function of non-dimensional distance, *x*, for *A*=-1 and *B*=-0.05 at multiple times.

Similarly, for the same linear boundary condition, Figures 5(a) and 5(b) plot the concentration as a function of time and distance for spherical electrode particle. Results show very good agreement between the two models.

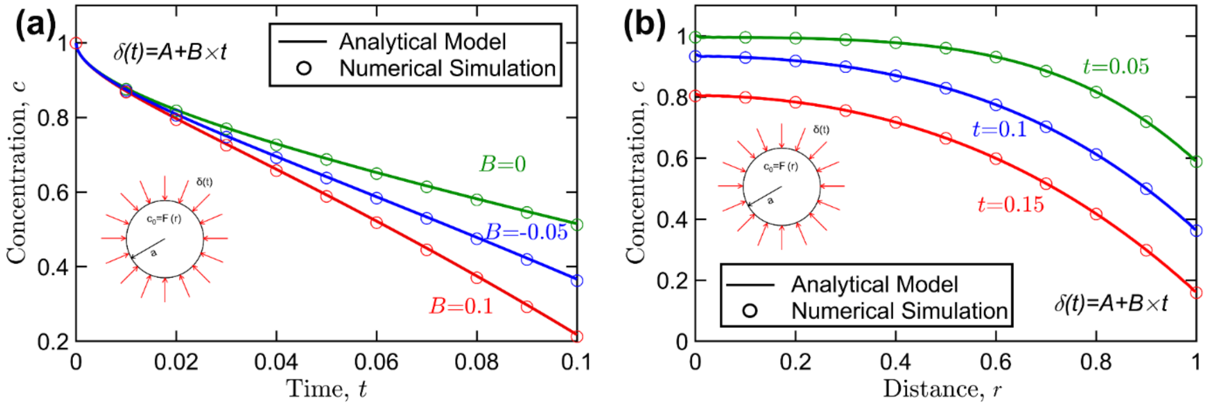

Figure 5. Validation against numerical model for a linear flux boundary condition, *δ*(*t*)=*A*+*B*·*t* in a spherical electrode particle: (a) Non-dimensional concentration as a function of non-dimensional time at the electrode's surface for *A*=-1 and multiple values of slope, *B*, (b) Non-

dimensional concentration as function of non-dimensional distance, *r*, for *A*=-1 and *B*=-0.05 at multiple times.

Similar plots are shown in Figures 6 and 7 for composite slab and spherical electrodes. The length of each layer in these composite electrodes are considered to be equal i.e. *l*=0.5 and the ration of diffusion coefficient, $\alpha$ is considered to be 0.25. A linear dimensionless current density, $\delta(t)= A+B\cdot t$, is used as the boundary condition for both geometries.

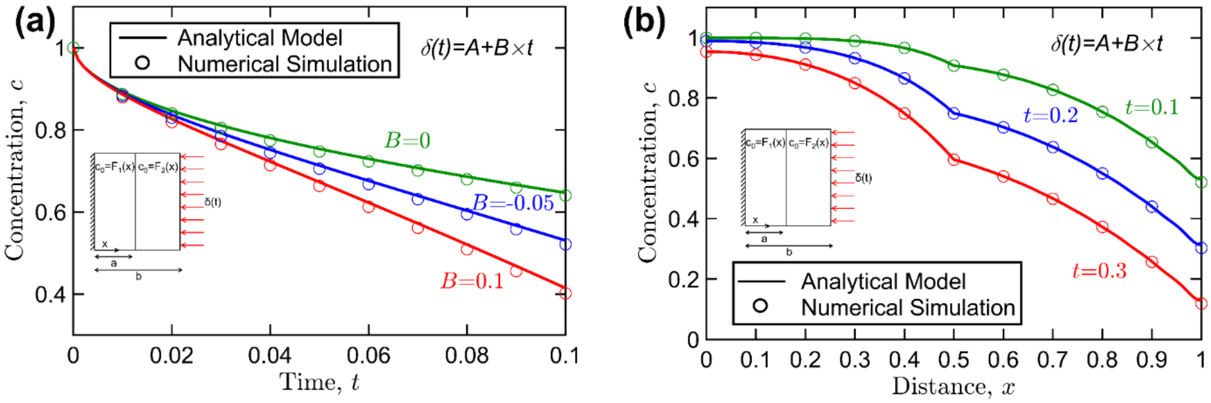

Figure 6. Validation against numerical model for a linear flux boundary condition, $\delta(t)=A+B\cdot t$ in a composite slab electrode: (a) Non-dimensional concentration as a function of non-dimensional time at the electrode's surface for *A*=-1 and multiple values of slope, *B*, (b) Non-dimensional concentration as function of non-dimensional distance, *x*, for *A*=-1 and *B*=-0.05 at multiple times.

Figure 6(a) plots the concentration as a function of time at the electrodes surface for different values of slope, *B* for a composite slab electrode for both numerical and analytical models. Figure 6(b) plots the concentration as a function of distance at multiple times for the same case. Similarly, Figures 7(a) and 7(b) plot concentration as a function of time at the electrode's surface and distance respectively for a composite spherical electrode for both numerical and analytical models. All plots show very good agreement between the analytical model and numerical simulation, thereby providing further validation in addition to the comparison with past studies.

### 7-3-2. Application of the model

Following validation, the Green's function based model is used for analyzing a number of realistic problems involving time-dependent current density functions. Specifically, two different types of time-dependent flux boundary conditions are considered – sinusoidal and step functions. The first category not only covers periodic functions but also any arbitrary function since any function can be written as a series summation of sinusoidal functions with different frequencies. Step functions can be used to address problems with sudden changes in C-rate during cyclic charge and discharge processes in Li-ion cells.

Figures 8(a) and 8(b) present plots for a non-dimensional time-dependent sinusoidal current density $\delta$=1+Sin($\omega t$) with two different frequencies. Figure 8(a) plots concentration as a function of time at the surface of a spherical particle for $\omega$=100, whereas Figure 8(b) presents a similar plot for $\omega$=1000. As expected, the concentration profile goes up and down with time at the expected frequency based on the value of $\omega$. Figures 8(a) and 8(b) also present the results from a previous study Guo & White[37] which used an approximate solution for diffusion in spherical electrode particle under time-dependent boundary conditions. As seen from the figures, there is very good agreement between the present work and past paper[37], with a worst-case deviation of 1.1% and 1% for data presented in Figures 8(a) and 8(b), respectively.

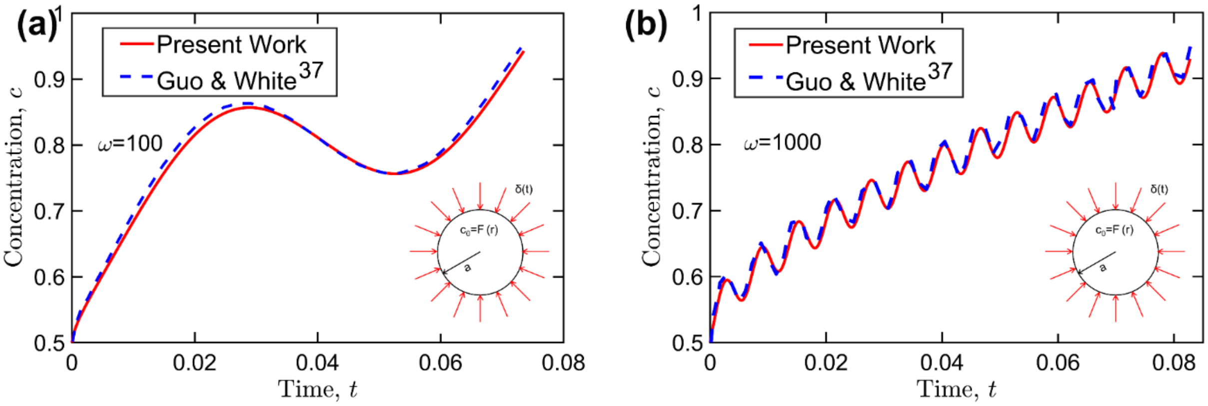

Figure 8. Non-dimensional concentration as a function of non-dimensional time at the surface of a spherical particle with sinusoidally varying flux, $\delta(t)=1+\sin(\omega t)$ for: (a) $\omega$=100; (b) $\omega$=1000. For comparison, plots from a past paper[37] are also shown.

Figures 9(a) and 9(b) present spatial distributions of concentration for the same boundary conditions as Figures 8(a) and 8(b), respectively. Figure 9(a) and 9(b) plot concentration as a function of distance, *r*, at multiple times for $\omega$=100 and $\omega$=1000, respectively. As expected, the concentration is highest at the surface of the electrode since the flux is coming in at this location. Figure 9(a) shows that concentration increases rapidly between *t*=0 and *t*=0.02, corresponding to the time during which flux is high. Following that, the concentration close to the surface actually reduces for *t*=0.04 and *t*=0.06, beyond which, there is a sharp increase. This is consistent with flux as a function of time, as well as the surface concentration plot as a function of time shown in Figure 8(a). The corresponding concentration distribution plots for $\omega$=1000 are, in comparison, monotonic, due to the larger frequency.

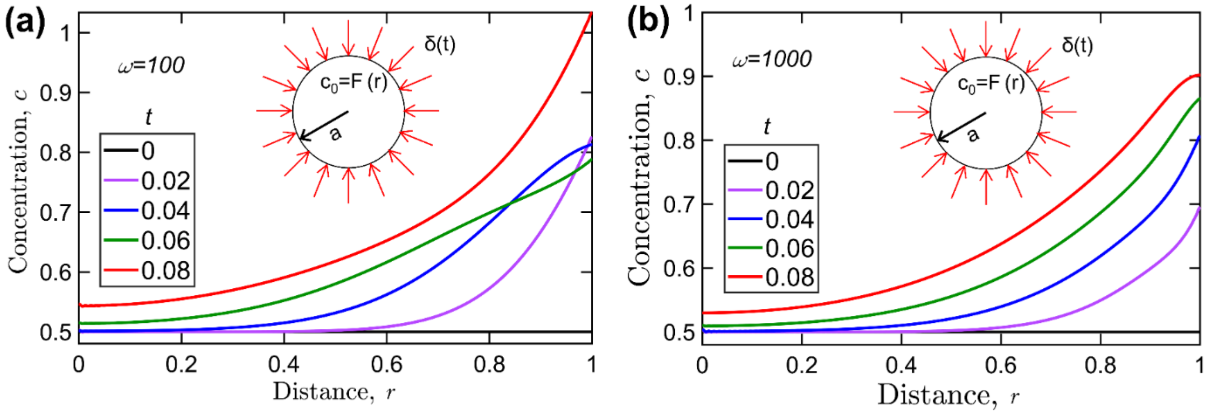

Figure 9. Non-dimensional concentration as a function of non-dimensional distance, $r$, at multiple times at the surface of a spherical particle with sinusoidally varying flux, *δ(t)=1+sin(ωt)* for: (a) *ω*=100; (b) *ω*=1000.

Figure 10 presents results for a discharge process with sinusoidal current density, $\delta(t) = A(1 + \sin \omega t)$ for multiple values of frequency, $\omega$. Surface concentration is plotted as a function of time for a thin film electrode and a spherical electrode particle in Figures 10(a) and 10(b), respectively. In both cases, the predicted concentration plot is consistent with the periodic nature of the forcing function. As expected, the concentration profile oscillates at the same frequency as the imposed current density, whereas the overall rate of reduction in the concentration is nearly the same for all cases.

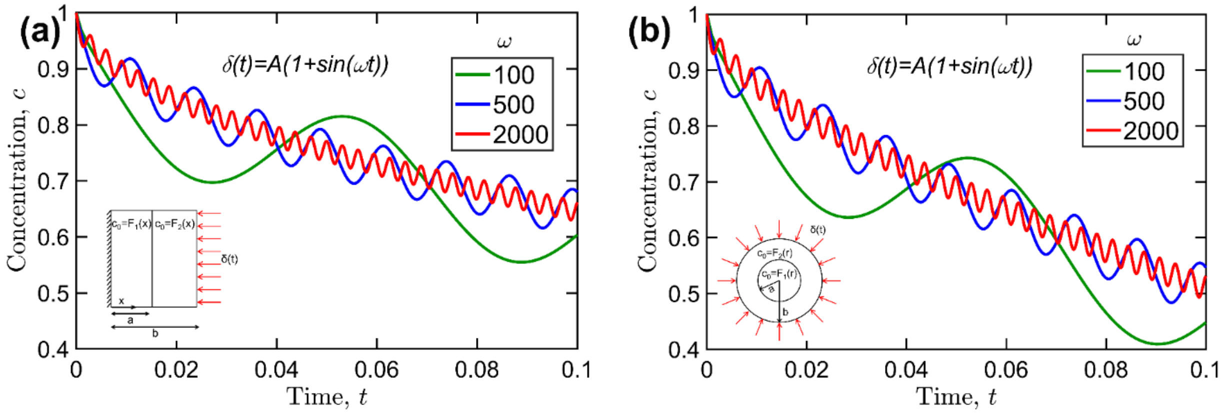

Figure 10. Practical application of the model in predicting concentration profile for periodic flux boundary condition, $\delta(t)= A(1+\sin(\omega t))$: Non-dimensional concentration as a function of non-dimensional time at the electrode's surface for $A$= -1 and multiple values of frequency, $\omega$, for (a) a composite slab electrode (b) a composite spherical electrode.

Figure 11 presents plots for a scenario where the current density changes with time as a step function. This may be relevant where the C-rate of the cell changes due to changes in the external circuit, such as when an electric vehicle suddenly brakes or accelerates. Another practical scenario of relevance may be the cyclic charge and discharge of a Li-ion cell where the current density switches directions between charge and discharge periods. Two specific cases are considered. In the first case, the current density changes from a negative value of $\delta$=-1 at $t$=0.025 to a positive value of $\delta$=0.5, and then becomes negative ($\delta$=-1.5) again at $t$=0.05. Figure 10(a) plots concentration as a function of time at the electrode's surface in a thin film electrode for this case. The current density is plotted as a function of time in the inset. Figure 10 shows that the concentration reduces during the discharge period, then increases rapidly during charge, and finally follows a downward trend again during the third phase of the process. The computational time associated with the calculations for Figure 10 is relatively small (less than 30s on a 3.30 GHz desktop computer with 8 GB RAM), since the eigenvalues depend only on the geometry and diffusivity, and need to be calculated only one time. Once the eigenvalues are calculated, they can be used to calculate the concentration profile under any types of boundary conditions. Therefore, the Green's function based model can be used for rapidly analyzing complicated, realistic charge/discharge scenarios. Figure 11(b) plots the concentration profile as a function of time for a spherical electrode particle with a step-change current density. In this case, the current density function is a three-step function with values of $\delta$=-0.5, -1 and -1.5, as shown in the inset of Figure 11(b). This scenario may occur in applications with sudden changes in discharge rate. Figure 11(b) shows, as expected, a gradual reduction in concentration due to the negative current density. As the discharge current density increases in magnitude, concentration reduces more and more rapidly, as expected.

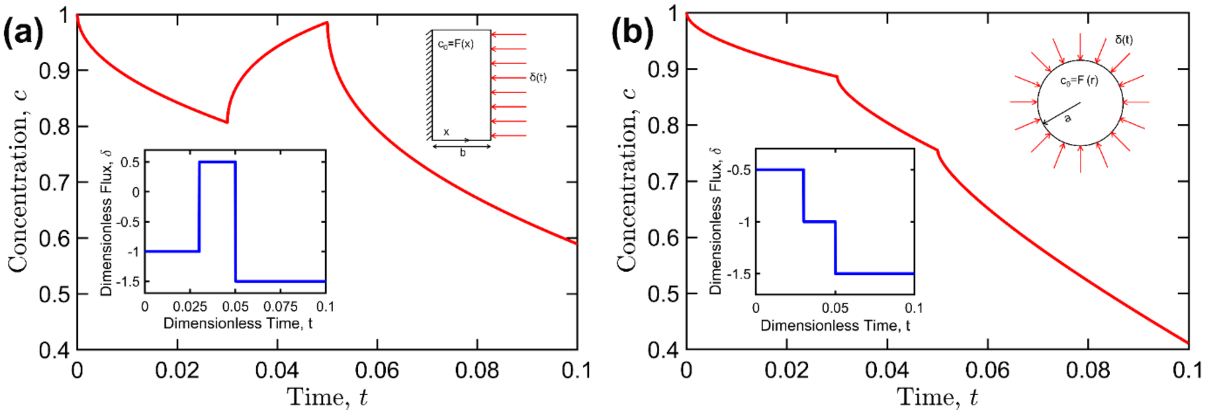

Figure 11. Practical application of the model in predicting concentration profile for step-change flux boundary conditionsNon-dimensional concentration as a function of non-dimensional time at the electrode's surface for (a) a charge-discharge process (b) a discharge process at different rates.

Figure 12 plots corresponding spatial concentration profiles at multiple times for the same parameters of step-function flux boundary condition as Figure 11. Figure 12(a) shows that the concentration reduces, then increases, and then reduces, consistent with the variation of the flux boundary condition over time. Concentration at *r*=1 is the highest at *t*=0.04, which is because *t*=0.04 lies in the region when the flux is positive. Concentration profiles in Figure 12(b) are similarly consistent with the corresponding variation of flux with time.

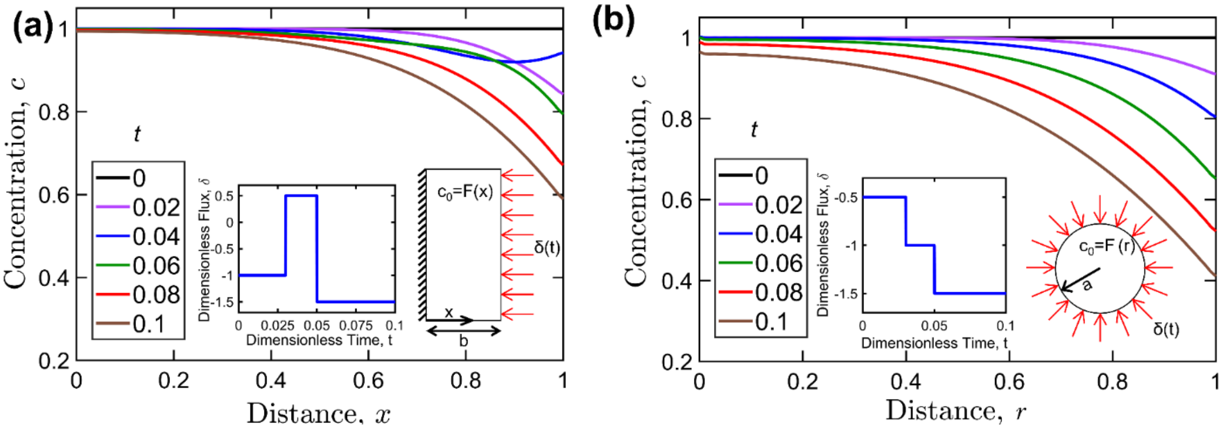

Figure 12. Practical application of the model in predicting concentration profile for step-change flux boundary conditions: Non-dimensional concentration as a function of non-dimensional distance, *x* and *r*, at multiple times at the electrode's surface for (a) a charge-discharge process (b) a discharge process at different rates.

## 7-4. Conclusions

In this work, an exact solution is developed for solid-phase diffusion under a time-dependent flux boundary condition using the Green's function approach, which has been used widely in the past for solving thermal conduction problems. The method is first applied to a thin film electrode and a spherical electrode particle. The method is then extended to determine the concentration profile in two-layer slab and spherical composite electrodes. The mathematical models agree well with previous studies for specific cases, as well as numerical simulations. The Green's function-based model presented here is able to accurately predict the transient behavior during solid phase diffusion process relevant to a Li-ion cell. The Laplace transform approach used in previous studies provides separate expressions for short time and long solutions. The short time solution derived using Laplace transform, which is very useful for some applications such as high rates and short times may be calculated faster than the Green's function solution presented here, since there is no separate expression for short time solution using this method. However, for complicated flux boundary conditions, inversion of the Laplace solution may be challenging, whereas the present approach offers a closed-form solution. The model presented here can be used to predict the concentration profile under realistic time-dependent boundary conditions that may appear in practical applications for electrochemical energy storage.

## 7-5. Nomenclature

| | |
|---|---|
| $a$ | Length of the inner layer from $x$=0 (m) |
| $b$ | Length of the outer layer from $x$=0 (m) |
| $c$ | non-dimensional concentration, $(C-C_0)/C_0$ |
| $C_0$ | initial concentration (mol $m^{-3}$) |
| $C$ | concentration (mol $m^{-3}$) |
| $D$ | diffusion coefficient ($m^2s^{-1}$) |
| $F(x)$ | non-dimensional initial concentration |
| $i$ | current (A) |
| $l$ | ratio of the inner layer to the outer layer of the electrodes, $l=a/b$ |
| $t$ | non-dimensional time, $t= D\tau/b^2$ |
| $x$ | non-dimensional lengthscale, $x=X/b$ |
| $X$ | lengthscale (m) |
| $R$ | radius (m) |
| $r$ | non-dimensional radius, $r=R/b$ |
| $\alpha$ | non-dimensional diffusion coefficient $\alpha=D_1/D_2$ |
| $\delta$ | non-dimensional current density, $\delta=ib/nFDC_0$ |
| $\varepsilon$ | frequency (1/s) |
| $\omega$ | non-dimensional frequency, $\omega = \varepsilon\, b^2/D$ |
| $\tau$ | time (s) |
| $\lambda$ | eigenvalues |

## 7-6. References

[1] B. Scrosati and J. Garche, *Journal of Power Sources*, **195**, 2419–2430 (2010).

[2] J. B. Goodenough and K.-S. Park, *ChemInform*, **44** (2013).

[3] K. Shah et al., *Journal of Electrochemical Energy Conversion and Storage*, **14** (2017).

[4] B. Dunn, H. Kamath, and J.-M. Tarascon, *Science*, **334**, 928–935 (2011).

[5] A. D. Pasquier, I. Plitz, S. Menocal, and G. Amatucci, *Journal of Power Sources*, **115**, 171–178 (2003).

[6] B. A. Johnson and R. E. White, *Journal of Power Sources*, **70**, 48–54 (1998).

[7] M. Parhizi, M. Ahmed, and A. Jain, *Journal of Power Sources*, **370**, 27–35 (2017).

[8] A. Jokar, B. Rajabloo, M. Désilets, and M. Lacroix, *Journal of Power Sources*, **327**, 44–55 (2016).

[9] R. Xiong, J. Cao, Q. Yu, H. He, and F. Sun, *IEEE Access*, **6**, 1832–1843 (2018).

[10] V. Ramadesigan et al., *Journal of The Electrochemical Society*, **159** (2012).

[11] A. Seaman, T.-S. Dao, and J. Mcphee, *Journal of Power Sources*, **256**, 410–423 (2014).

[12] J. Zhang and J. Lee, *Journal of Power Sources*, **196**, 6007–6014 (2011).

[13] T. Hansen and C.-J. Wang, *Journal of Power Sources*, **141**, 351–358 (2005).

[14] G. G. Botte, V. R. Subramanian, and R. E. White, *Electrochimica Acta*, **45**, 2595–2609 (2000).

[15] M. Doyle, *Journal of The Electrochemical Society*, **140**, 1526 (1993).

[16] V. Ramadesigan, V. Boovaragavan, J. C. Pirkle, and V. R. Subramanian, *Journal of The Electrochemical Society*, **157** (2010).

[17] V. R. Subramanian, V. Boovaragavan, V. Ramadesigan, and M. Arabandi, *Journal of The Electrochemical Society*, **156** (2009).

[18] G. Ning and B. N. Popov, *Journal of The Electrochemical Society*, **151** (2004).

[19] S. Santhanagopalan, Q. Guo, P. Ramadass, and R. E. White, Journal of Power Sources, 156, 620–628 (2006).

[20] S. K. Rahimian, S. Rayman, and R. E. White, *Journal of Power Sources*, **224**, 180–194 (2013).

[21] S. Atlung, *Journal of The Electrochemical Society*, **126**, 1311 (1979).

[22] M. Doyle, J. Newman, *Journal of* Applied Electrochemistry, 27, 846–856 (1997).

[23] V. R. Subramanian and R. E. White, *Journal of Power Sources*, **96**, 385–395 (2001).

[24] B. Suthar and V. R. Subramanian, *Journal of The Electrochemical Society*, **161** (2014).

[25] S. H. Ali, A. Hussin, and A. Arof, *Journal of Power Sources*, **112**, 435–442 (2002).

[226] M. R. Johan and A. K. Arof, *Ionics*, **10**, 405–414 (2004).

[27] S. Liu, *Solid State Ionics*, **177**, 53–58 (2006).

[28] M. R. Johan and A. K. Arof, *Journal of Power Sources*, **170**, 490–494 (2007).

[29] V. R. Subramanian, V. D. Diwakar, and D. Tapriyal, *Journal of The Electrochemical Society*, **152** (2005).

[30] V. R. Subramanian, J. A. Ritter, and R. E. White, *Journal of The Electrochemical Society*, **148** (2001).

[31] K. A. Smith, C. D. Rahn, and C.-Y. Wang, *Journal of Dynamic Systems, Measurement, and Control*, **130** (2008).

[32] K. A. Smith, C. D. Rahn, and C.-Y. Wang, *Energy Conversion and Management*, **48**, 2565–2578 (2007).

[33] D. D. Domenico, G. Fiengo, and A. Stefanopoulou, *2008 IEEE International Conference on Control Applications* (2008).

[34] L. Cai and R. E. White, *Journal of The Electrochemical Society*, **156** (2009).

[35] W. Luo, C. Lyu, L. Wang, and L. Zhang, *Microelectronics Reliability*, **53**, 797–804 (2013).

[36] W. Luo, C. Lyu, L. Wang, and L. Zhang, *Journal of Power Sources*, **241**, 295–310 (2013).

[37] M. Guo and R. E. White, *Journal of Power Sources*, **198**, 322–328 (2012).

[38] Q. Zhang and R. E. White, *Journal of Power Sources*, **165**, 880–886 (2007).

[39] D. W. Hahn, and M. N. Özişik, *John Wiley & Sons* (2012).

[40] K. D. Cole, J. V. Beck, A. Haji-Sheikh, & B. Litkouhi, *CRC Press* (2010).

# Chapter 8

# Analytical Model Based Prediction of State-of-Charge (SoC) of a Lithium-Ion Cell under Time-Varying Charge/Discharge Currents

**Accepted as**: Parhizi, M., & Jain, A. (2020). Analytical Model Based Prediction of State-of-Charge (SoC) of a Lithium-Ion Cell under Time-Varying Charge/Discharge Currents. *Journal of The Electrochemical Society*, 2020.

## 8-1. Introduction

Li-ion cells are an attractive candidate for electrochemical energy storage and conversion in electric vehicles (EVs) and power grids[1]. In such applications, managing the health and safety of Li-ion cells is very important, particularly for high power applications with significant demand variability. Battery Management Systems (BMS) using battery models of varying levels of complexity are commonly used to monitor and control the state of the cells, and to fulfill system design requirements[2-4]. The State of Charge (SoC) of a cell is one of the most important variables that needs to be estimated frequently by the BMS. SoC has been defined in several different ways, such as an indication of the fraction of energy left in the battery at a given time, or the ratio of the available capacity to the maximum capacity of the cell at a given time[2,5]. An accurate estimate of the SoC helps infer useful information about the vehicle range, remaining energy and health of the battery pack[5,6]. Unlike electric parameters such as voltage and current, SoC cannot be measured directly and other methods must be implemented to obtain an accurate estimate of SoC[7]. Due to the coupled and non-linear nature of the electrochemical phenomena that occurs in Li-ion cells, SoC estimation is always a challenging task[5]. While SoC estimation for constant current processes may be relatively easier, it is a much more complicated task under dynamic load conditions, as one would expect, for example, in an electric vehicle.

A variety of techniques have been proposed in the literature to evaluate SoC of Li-ion cells. State of charge estimation techniques can be broadly divided into the categories of non-model based techniques, data-driven (machine learning) approaches and model-based techniques[5,8,9]. One example of non-model based techniques is the open-circuit voltage (OCV) method that uses a look-up table based on a monotonic relationship between state of charge and open-circuit voltage[10]. This method is not suitable for SoC estimation in electric vehicles since an accurate real-time measurement of OCV is not straightforward[5,11]. Also, the flat nature of OCV behavior of certain cathode chemistries used in Li-ion batteries, such as Lithium Iron Phosphate makes it unsuitable to accurately estimate the SoC at all times. In the Ampere-hour integral method, also known as the Coulomb counting method, SoC is estimated by integrating the current over time[8,12]. This method can be fairly accurate as long as the initial SoC, cell maximum capacity and electric current are precisely known[5,13]. However, any inaccuracy in the initial SoC along with noise in the current measurements can significantly affect the accuracy of the SoC prediction.

Data-driven methods use large sets of experimental data obtained under different operating conditions to build a pattern and demonstrate a relationship – often non-linear – between different input and output variables[5,14]. Fuzzy logic[15], autoregressive moving average (ARMA)[16], artificial neural network (ANN)[17] and support vector machine (SVM)[18] are key data-driven methods[14]. Data-driven methods are often computationally expensive, and the accuracy depends strongly on the size and quality of the statistical population.

Model-based methods can be broadly divided into equivalent circuit models (ECMs) and electrochemical models. ECM uses a circuit network comprising of capacitors, resistors and other electrical circuit components to simulate battery behavior[5,19]. Compared to electrochemical models, ECMs are simpler and faster, but do not provide insights on electrochemical processes occurring inside the cell[2]. Estimation algorithms such as Kalman filter[20-23], extended Kalman filter[24], voltage inversion technique[25], sliding mode observer[26], and Luenberger observer[27] have been used with ECM techniques.

Electrochemical models, on the other hand, provide a robust and detailed solution by solving reaction kinetics, mass and charge transport equations under appropriate assumptions.

Pseudo-two dimensional model (P2D) proposed by Doyle et al.[28] has been used widely in modeling of Li-ion batteries and SoC estimation[29]. 1-D electrochemical model has been also used to predict the SoC of Li-ion cells[30-32]. Due to the coupled and non-linear nature of the partial differential equations (PDEs) that the P2D models solve, the equations usually need to be solved numerically, which is computationally expensive. Several researchers have proposed reduced-order models to simplify the computational complexity. Recently, a lumped electrochemical model for lithium-ion batteries called Tank-in-Series approach has been introduced, in which the governing equations of the P2D model are volume-averaged over each region of the cell[33]. One of the most commonly used simplifications is the single particle model (SPM)[34], in which each electrode is replaced by a representative single, spherical particle, and the concentration distribution in the particle due to the imposed current is solved analytically or numerically. Compared to P2D, this results in only one PDE for each electrode. The current density is assumed to fully contribute towards the pore wall flux that is uniformly distributed throughout the surface of the electrode[35,36]. Moreover, the concentration and potential gradient in the electrolyte is neglected. SPM is a valid approach only for low to moderate C-rate, where the concentration gradient in the electrolyte can be neglected[35,36]. At high current densities, the Li-ion concentration gradient and potential gradient in the electrolyte cannot be ignored and SPM results in inaccurate potential predictions[37]. A number of modifications of SPM have been proposed to overcome some of these limitations.For example extended SPM model has been proposed to account for energy balance[35] and the effect of electrolyte concentration and potential[8,38,39]. Moreover, state estimation techniques such as an extended Kalman filter (EKF)[40] and Luenberger observer[32] has been applied to traditional and extended SPM to estimate the SoC of a Lithium ion cell[40].

Regardless of the estimation technique, solving the concentration field in the spherical particle is a key step for SPM-based SoC estimation. Analytical solutions for the diffusion equation governing the concentration field are available only for galvanostatic (constant current) operating conditions where the applied current density is constant[36]. Even though step-wise changes in current can, in principle, be addressed by successively solving the concentration field in each galvanostatic time period, doing so is very difficult for rapidly changing current profiles encountered in vehicle drive cycles, or when the current changes smoothly over time, such as in alternating current (AC) systems. Previous studies have implemented a variety of numerical procedures and algorithms to predict the voltage and consequently SoC under dynamic discharge current conditions[3,4]. However, an analytical solution for determining the SoC during time-varying charge/discharge conditions is very desirable since it may offer the capability of rapid, in-line SoC estimation that integrates well with other BMS functions.

A Green's function based analytical solution for the concentration field in a single particle undergoing time-varying charge/discharge has recently been presented[41]. In the present work, this analytical model is used to determine the voltage profile of the cell and the SoC as a function of time under a general, time-dependent current profile. The approach presented in this study results in an analytical expression for the voltage and SoC that can be used for any arbitrary time-dependent current profile. The analytical solution presented in this study is validated against past numerical simulations and experimental data under different operating conditions. The model is then used to predict the voltage and SoC of a Li-ion cell operating under realistic conditions such as drive cycles with rapidly changing charge/discharge current, as well as stepwise or periodically varying charge/discharge. While recognizing that the model presented here is valid only under the assumptions associated with the use of SPM, it is expected that the present study may contribute towards improved SoC estimation in a wide variety of applications containing extremely low-memory computational platforms where numerical solutions are impractical.

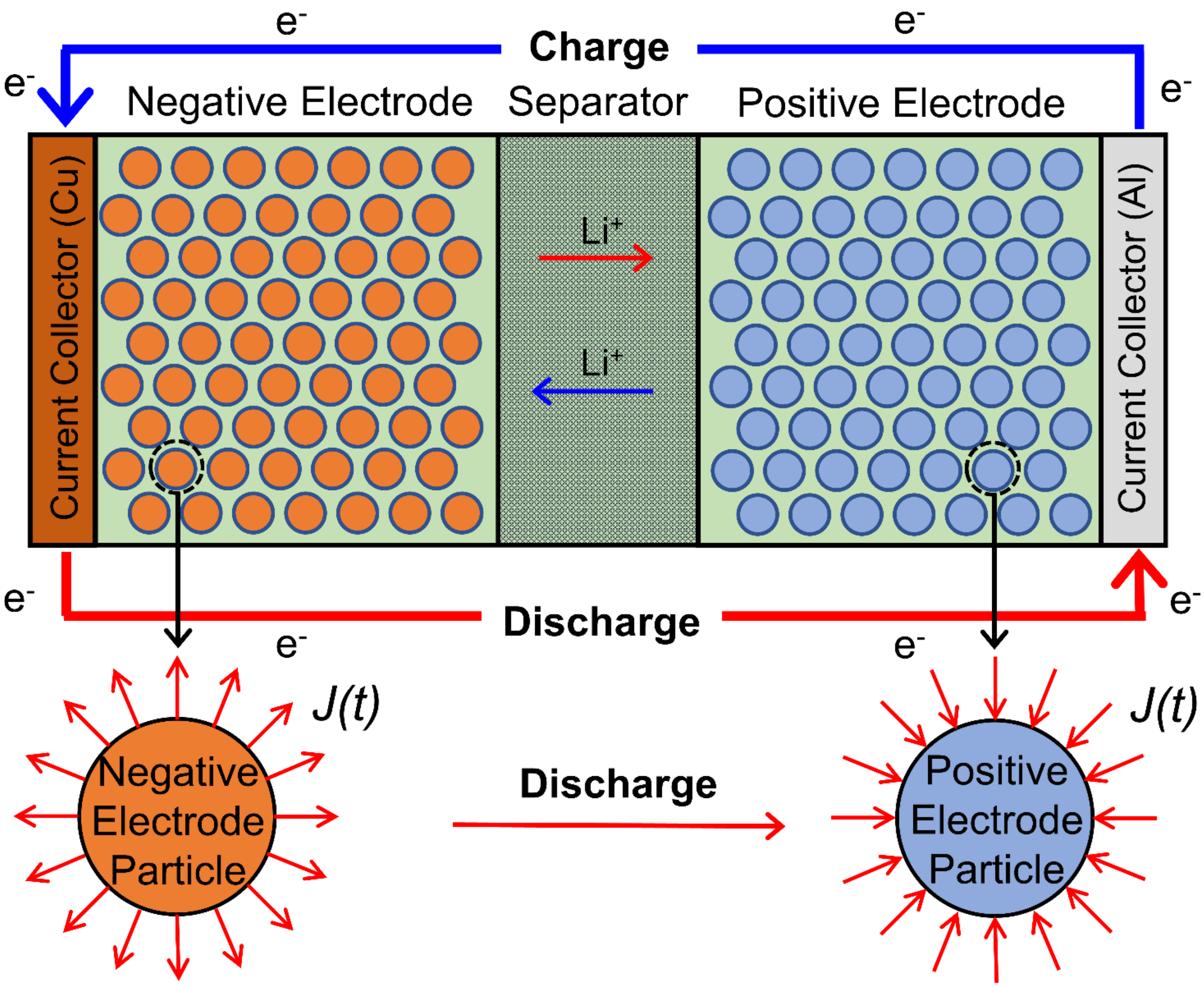

Figure 1. Schematic of a Li-ion cell comprising two electrodes, separator and current collectors. Two spherical particles representative of the two electrodes during discharge are also shown.

## 8-2. Mathematical Modeling

8-2-1. Solid phase diffusion

Single particle model (SPM) is used in the present study to predict the concentration profile in the electrodes. SPM neglects the concentration gradient in the solution phase and assumes the electrodes to comprise of spherical particles. Further, the assumption of a uniform current distribution results in identical conditions for each particle, so that a single spherical particle is representative of the entire electrode. It is important to note that these assumptions are valid for low current densities where the concentration gradient in the electrolyte can be neglected and the cell is dominated by the solid phase diffusion. Under these assumptions, the governing equation for concentration diffusion for the positive and negative electrodes can be written as[36]:

$$\frac{D_j}{r^2}\frac{\partial}{\partial r}\left(r^2\frac{\partial c_j}{\partial r}\right)=\frac{\partial c_j}{\partial t} \tag{1}$$

where the initial and boundary conditions are

$$c_j = c_{initial,j} \qquad \text{at } t = 0 \tag{2}$$

$$c_j \Rightarrow finite \qquad \text{as } r \longrightarrow 0 \tag{3}$$

$$D_j\left(\frac{\partial c_j}{\partial r}\right)_{r=R_j} = -J_j(t) \qquad \text{at } r = 1 \tag{4}$$

where the subscript *j*=*p*,*n* represents the positive and negative electrodes respectively. *D* is the solid phase diffusion coefficient and *J*(*t*) is the time-dependent molar flux at the surface of the particle. The molar flux for the cathode and anode can be written as[36]:

$$J_p(t) = \frac{I(t)R_p}{3\varepsilon_p V_p F} \tag{5}$$

$$J_n(t) = -\frac{I(t)R_n}{3\varepsilon_n V_n F} \tag{6}$$

Where *I(t)* is the current that is assumed to be time-dependent in this work, $R_j$ is the radius of the particle electrode $j$. $\varepsilon_j$ is the volume fraction of the active material in the electrode, $V_j$ is the total volume, and *F* is the Faraday's constant. Note that the sign of the current, *I,* is negative for discharge and positive for charge.

Equations (1)-(6) have been recently solved analytically using Green's function approach for the case of time-dependent current. A detailed description of the solution procedure for solid phase diffusion under time-dependent boundary conditions can be found in a recent publication[41], which results in the following equation for the concentration distribution in the electrode particle[41]:

$$\begin{aligned} c_j(r,t) = c_{initial,j} - \frac{3}{R_j}\int_{\tau=0}^{t} J_j(\tau)d\tau \\ - \sum_{n=1}^{\infty} \frac{R_j}{rN_{n,j}} \sin(\lambda_{n,j}r)\sin(\lambda_{n,j}R_j)\int_{\tau=0}^{t} J_j(\tau)\exp\left(-D_j\lambda_{n,j}^2(t-\tau)\right)d\tau \end{aligned} \tag{7}$$

where the eigenvalues, $\lambda_{n,j}$ are the positive roots of $R_j\lambda \quad \cot R_j\lambda \quad = 1$ and $N_{n,j}$ is the norm, defined as:

$$N_{n,j} = \frac{R_j\left(\lambda_{n,j}^2 + \frac{1}{R_j^2}\right) - \frac{1}{R_j}}{2\left(\lambda_{n,j}^2 + \frac{1}{R_j^2}\right)} \tag{8}$$

Specifically, concentration on the surface of the particle, which is important for calculating the potential can be determined by substituting $r=R_j$ in equation (7), resulting in:

$$\begin{aligned} c_{j,s}(t) &= c_j(R_j, t) \\ &= c_{initial,j} - \frac{3}{R_j}\int_{\tau=0}^{t} J_j(\tau)d\tau \\ &- \sum_{n=1}^{\infty}\frac{1}{N_{n,j}}\sin^2(\lambda_{n,j}R_j)\int_{\tau=0}^{t} J_j(\tau)\exp\left(-D_j\lambda_{n,j}^2(t-\tau)\right)d\tau \end{aligned} \tag{9}$$

8-2-2. Potential and state of charge (SoC)

Once the concentration profile is determined for an arbitrarily varying charge/discharge current, the cell voltage and SoC can be computed as functions of time using Butler-Volmer kinetics approach that has been widely used in past papers.

The state of charge of the electrode at any time can be written using the average concentration of the electrodes as follows:

$$SoC_j(t) = \frac{\bar{x}_{j,ave}(t) - x_{j,ave0\%,}}{x_{j,ave100\%} - x_{j,ave0\%,}} \tag{10}$$

Where $\bar{x}_{j,ave}(t)$ is the volume-averaged scaled concentration in electrode *j* at time *t* which can be obtained through integration as follows:

$$\bar{x}_{j,ave}(t) = \frac{3\int_{r=0}^{R_j} r^2 c_j(r,t)dr}{R_j^3 c_{j,max}} \tag{11}$$

By applying a total mass balance of Lithium in the full cell, the SoCs of the individual electrodes can easily be related to the overall capacity and correspondingly SoC of the cell. However, we only explore the variation of SoC of the negative electrode in this work to demonstrate the capability of this approach.

In order to calculate the electrode potential, the Butler-Volmer kinetics equation is used[36]:

$$J_j(t) = c_{j,max} k_j c_e^{0.5} x_{j,s}^{0.5} (1 - x_{j,s})^{0.5} \left[\exp\left(\frac{0.5F}{R_u T}\eta_j\right) - \exp\left(-\frac{0.5F}{R_u T}\eta_j\right)\right] \tag{12}$$

Where $x_{j,s} = \frac{c_{j,s}}{c_{j,max}}$ is the stoichiometry or scaled concentration at the surface of electrode $j$, $k$ is the reaction rate constant, $c_e$ is the electrolyte concentration, $R_u$ is the universal gas constant, $T$ is the surface temperature and $\eta_j$ is the overpotential that can be written as:

$$\eta_j = \varphi_{1,j} - \varphi_{2,j} - U_j \tag{13}$$

Where $U$ is the open circuit potential, which, in general, depends on the electrode material in the cell, and is obtained from the expressions presented in previous papers[36]. The solid phase and liquid phase potentials can be written as:

$$\varphi_{1,p} - \varphi_{1,n} = V_{cell} \tag{14}$$

$$\varphi_{2,p} - \varphi_{2,n} = IR_{cell} \tag{15}$$

Note that the potential difference in the solution phase is modeled as a resistor in this model. Equation (13)-(15) can be combined and substituted in equation (12). Finally, equation (12) can be inverted[36] to result in the following equation for the voltage of the cell as a function of time:

$$V_{cell}(t) = U_p - U_n + \frac{2R_uT}{F} ln\left[\frac{\sqrt{m_p^2+4}+m_p}{2}\right] + \frac{2R_uT}{F} ln\left[\frac{\sqrt{m_n^2+4}+m_n}{2}\right] + IR_{cell} \tag{16}$$

Where

$$m_p = \frac{I(t)}{Fk_pS_pc_{p,max}c_e^{0.5}(1-x_{p,s})^{0.5}x_{p,s}^{0.5}} \tag{17}$$

$$m_n = \frac{I(t)}{Fk_nS_nc_{n,max}c_e^{0.5}(1-x_{n,s})^{0.5}x_{n,s}^{0.5}} \tag{18}$$

and $S_j=3\varepsilon_j V_j/R_j$ is the total electroactive area of the electrodes.

Equation (16) provides an analytical expression for the cell voltage as a function of time during a charge/discharge process with time-varying current. Note that the concentration field in equation (16) comes from equation (9), which represents the Green's function solution for the concentration field under time-dependent flux. These equations make it possible to predict the cell voltage as a function of time for any arbitrary charge/discharge current profile, which could comprise both smooth and discontinuous variations of current with time. In addition, the time-dependence of current could be provided to the model either in the form of analytical equations, or discrete experimental data.

## 8-3. Results and Discussion

### 8-3-1. Model validation

The analytical model for predicting SoC and voltage curves for time-varying current presented in section 2 is validated by comparison against predictions based on numerical simulations as well as experimental data reported in the past. These results are discussed in sub-sections below.

#### 8-3-1-1. Validation against SPM numerical simulation

Voltage profile predicted by the analytical model is compared against numerical models for a special case of constant current as well as other time-dependent current profiles. For constant current, a previously reported SPM-based numerical computation tool for constant current charge/discharge (S. Kolluri & V. Subramanian, personal communication, May 17, 2020) is used for comparison. For time-dependent current, a finite-difference based code originally written for solving heat transfer problems is modified and used. In both cases, the governing equation and boundary conditions for solid phase diffusion in a spherical electrode particle (equations (1)-(4)) are discretized in time and space. The concentration at the surface of the electrodes is determined and used to calculate the cell voltage using equation (16).

For validation in constant current conditions, a $LiCoO_2$ cell is considered with nominal capacity of 1.78 A-hr. The cutoff voltage for charge and discharge are set to be 4.2 V and 2.8 V, respectively. Values of cell parameters used for comparison against the numerical simulation are taken from[28,42] and summarized in Table 1. Comparison is carried out for charge and discharge at four different C-rates, as shown in Figures 2(a) and 2(b), respectively. There is excellent agreement between the analytical model and numerical simulation at each C-rate for both charge and discharge. In each case, the curves for analytical model and numerical simulation are nearly indistinguishable from each other.

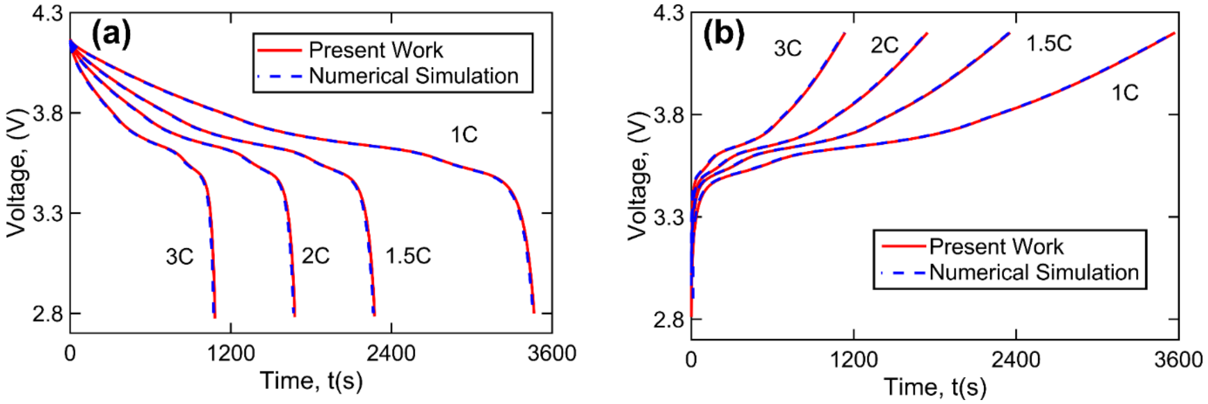

Figure 2. Validation of the analytical model against SPM-based numerical simulations for constant current processes: Voltage as a function of time for (a) discharge, and (b) charge for multiple C-rates.

Validation of the analytical model is then carried out for time-dependent currents. Two specific current profiles are used – the first one has two cycles of a discharge-rest-charge process, and the second one is a part of the US06 drive cycle commonly used for automotive benchmarking[43,44]. The US06 drive cycle features significant fluctuations in currents representative of realistic driving behavior. Figures 3(a) and 3(b) present comparison of the analytical model against numerical simulation for these two current profiles, respectively. In each case, the variation in current with time is also plotted for comparison. Plots show that the analytical model and the numerical simulation are in a very good agreement even for complicated time-dependent current profiles.

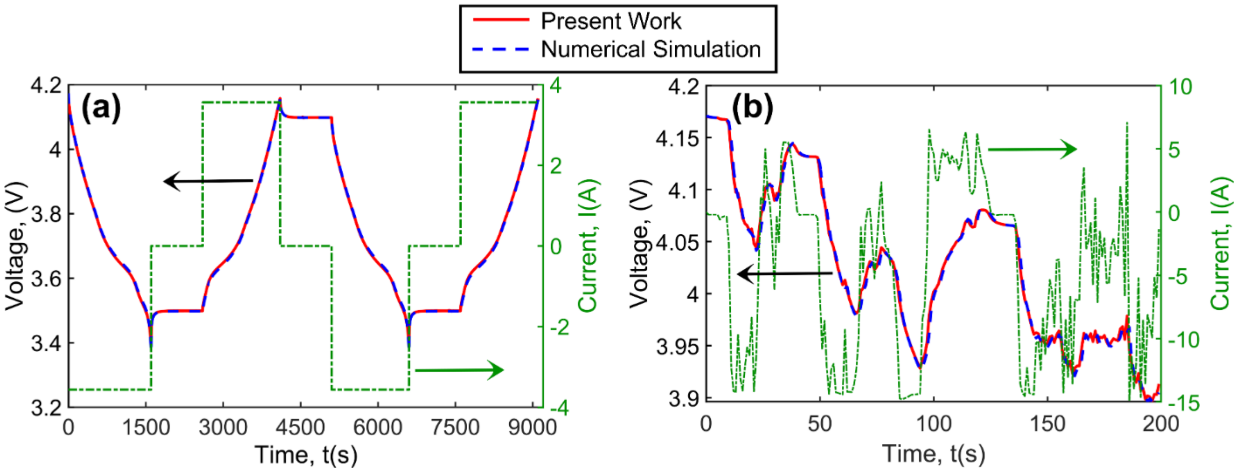

Figure 3. Validation of the analytical model against SPM-based numerical simulations for time-dependent current processes: Voltage as a function of time for (a) discharge-rest-discharge, and (b) dynamic current profile.

### 8-3-1-2. Validation against other models

This subsection presents a comparison of the model developed in this work with other past approaches for calculating the voltage curve. Two past models developed by Smith, et al.[31] and Cen & Kubiak[45] are considered here. Smith, et al.[31] presented a linear Kalman filter approach based on a reduced-order electrochemical model for voltage and SoC estimation. Cen & Kubiak[45], on the other hand, presented an adaptive observer based on a simplified single particle model (SPM) to predict the voltage and SoC of a Li-ion cell. The electrochemical parameters used for these comparison plots can be found in the corresponding papers[31,45]. Figure 4(a) plots voltage as a function of time obtained from the analytical model presented here and the past study by Smith, et al.[31]. The current profile used for this comparison is also shown on the right axis. Results show good agreement between the two models, with a worst-case disagreement of only around 0.4%. Note that the model presented by Smith, et al.[31] accounts for electrochemical dynamics of the electrolyte, while the present model considers the electrolyte dynamic as a fixed film resistance, which may explain the difference in the voltage peaks between the two models. Similarly, Figure 4(b) plots voltage as a function of time for the present analytical model and the past study by Cen & Kubiak[45] for a constant current-constant voltage (CC-CV) process, also shown in the Figure. There is a reasonable agreement between the two models. The slight disagreement between the two models is likely due to lack of clarity about some of the parameters used by Cen & Kubiak[45].

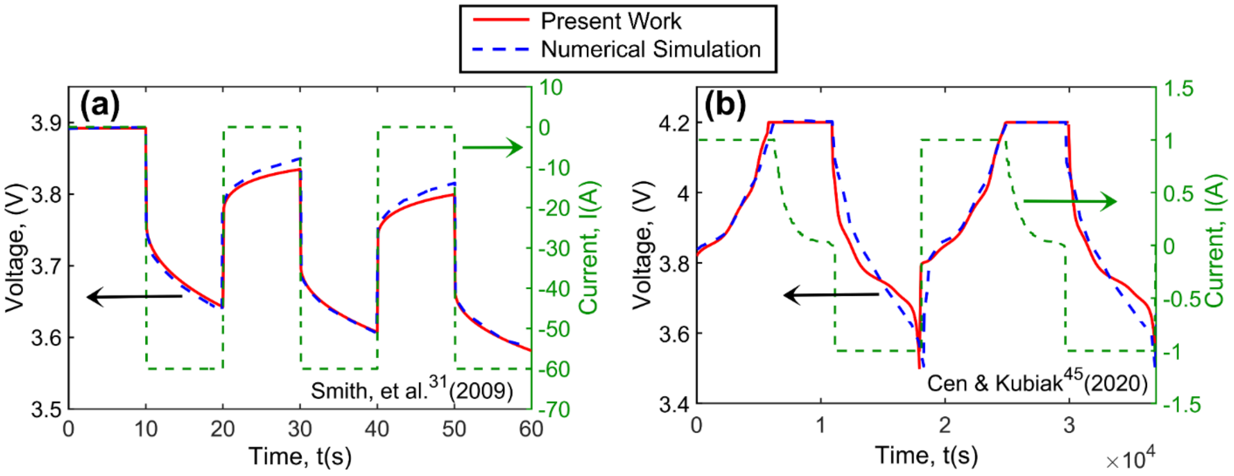

Figure 4. Validation of the analytical model against past numerical models for variable current processes: Voltage as a function of time for (a) discharge-charge process[31], and (b) discharge-rest-charge process[45]

### 8-3-1-3 Validation against past experimental data

Finally, validation of the analytical model is also carried out by comparison with previously reported experimental measurements by Guo, et al.[36] and Smith & Wang[32]. Guo, et al.[36] presented experimental measurement of voltage under a constant discharge rate of C/33 for a pouch cell with a nominal capacity of 1.656 A-hr. Smith and Wang[32], on the other hand, presented experimental data for a HPPC drive cycle profile for multiple values of initial state of charge. Both papers listed electrochemical properties of the cell used in experiments[32,36]. Using these cell parameters, the analytical model is used to compute the voltage curve for both experiments. Figures 5(a) presents a comparison between measurements and analytical model for constant current discharge measurements by Guo, et al. [36]. There is excellent agreement between the two throughout the entire measurement period. Figure 5(b) shows a similar comparison for a more complicated current profile used for voltage measurements by Smith and Wang[32] for two different values of the initial SoC. Figure 5(b) shows that the analytical model is able to successfully predict the voltage profile for the pulsed current profile.

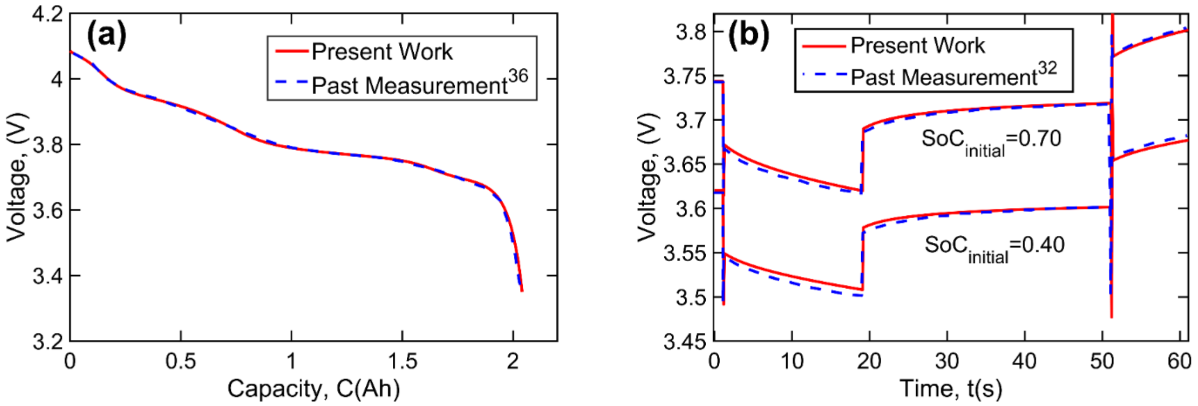

Figure 5. Validation of the analytical model against past experimental measurements: Voltage as a function of time for (a) constant current discharge[36], and (b) HPPC drive cycle[32]

Taken together, the comparison against numerical computation, other past models as well as experimental measurements in a variety of constant and time-varying current conditions provides very good validation of the analytical model presented in Section 2.

### 8-3-2. Applications of the model

In this section, the Green's function based analytical model is used to predict the voltage and SoC profiles of a cell in a number of operating conditions. Step-function and sinusoidal changes in current over time are considered. In addition, current profiles for two drive cycles – ECE-15 and US06 – that represent realistic driving conditions are analyzed. Cell parameters used in all the figures in this section are same as those used in Figures 2 and 3, and are summarized in Table 1.

Table 1. Electrochemical and physical properties used in this study.

| Properties | Anode | Cathode | Units |
|---|---|---|---|
| $R$ | $5\times10^{-6}$ | $5\times10^{-6}$ | m |
| $l$ | $4.000\times10^{-5}$ | $3.655\times10^{-5}$ | m |
| $D$ | $1.4\times10^{-14}$ | $2.0\times10^{-14}$ | $m^2\ s^{-1}$ |
| $c_{max}$ | 31080 | 51830 | $mol\ m^{-3}$ |
| $k$ | $0.6346667351\times10^{-9}$ | $0.6306608809\times10^{-9}$ | $m^{2.5}\ mol^{-0.5}\ s^{-1}$ |
| $S$ | 1.6206 | 1.2974 | $m^2$ |
| $x_{0\%}$ | 0.005139 | 0.947659 | ------- |

|  |  |  |  |
|---|---|---|---|
| $x_{100\%}$ | 0.790813 | 0.359749 | ------- |
| $T$ | 298 |  | K |
| $F$ | 96487 |  | C mol$^{-1}$ |
| $R_u$ | 8.314 |  | J mol$^{-1}$ K$^{-1}$ |
| $c_e$ | 1200 |  | mol m$^{-3}$ |
| $R_{cell}$ | 0.001 |  | Ω |
| $U_p$ | $-10.72\times x^4_{p,s}+23.88\times x^3_{p,s}-16.77\times x^2_{p,s}+2.595\times x_{p,s}+4.563$ |  | V |
| $U_n$ | $0.1493+0.8493\times \exp(-61.79\times x_{n,s})+.3824\times \exp(-665.8\times x_{n,s})-\exp(39.42\times x_{n,s}-41.92)-0.03131\times \mathrm{atan}(25.59\times x_{n,s}-4.099)-0.009434\times \mathrm{atan}(32.49\times x_{n,s}-15.74)$ |  | V |

8-3-2-1 Step-function current profile

Cell performance is analyzed under two different step-function current profiles – successive discharge at multiple C-rates (0.5C, 1.5C and 3C) and discharge-charge-discharge process. To illustrate the electrochemical phenomena that occurs inside the cell operating under step-function current profiles, surface concentrations on the positive and negative electrodes are computed using equation (9) and plotted as a function of time for the two current profiles in Figures 6(a) and 6(b), respectively. In both cases, the current profile is shown as an inset. As expected, during discharge, concentration on the surface of the negative electrode decreases while concentration on the surface of the positive electrode increases. Further, the rate of change of the concentration goes up as the discharge rate increases. Figure 6(b) presents a similar plot for a discharge-charge-discharge current profile, also shown as an inset. It is seen that concentration in the positive electrode increases for *t*<1500s while the cell discharges, then decreases for 1500s<*t*<3000s while the cell charges, and finally increases again for t>3000s while the cell discharges. Concentration on the surface of the negative electrode shows similar behavior that is consistent with the current profile. As expected, the slopes of the curves are larger for the second discharge than the first one due to the greater rate of the second discharge.

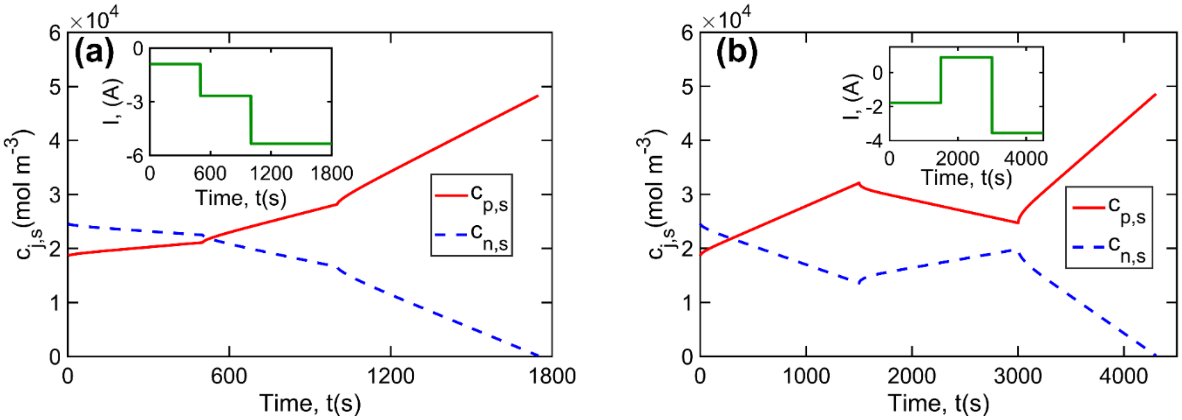

Figure 6. Application of the analytical model for a step-function current profile: Concentration as a function of time for (a) discharge at multiple C-rates, (b) discharge-charge-discharge process.

Based on the concentration fields computed by the Green's function approach, as illustrated in Figure 6, the voltage and SoC as functions of time are computed using equations (16) and (10), respectively. Figures 7(a) and 7(b) present voltage and average SoC at the negative electrode curves for the two current profiles discussed in Figure 6. It is seen from Figure 7(a) that the voltage decreases continuously due to the discharge process, and shows a change in the rate of reduction when the discharge rate changes from 0.5C to 1.5C, and then to 3C at 500s and 1000s, respectively. This is consistent with both the current profile as well as the concentration profile shown in Figure 6(a). The volume-averaged SoC of the negative electrode given by equation (10), also shown in Figure 6(a), is consistent with the current and voltage profiles. The SoC decreases throughout, as expected, and at the greatest rate for the highest C-rate, also as expected.

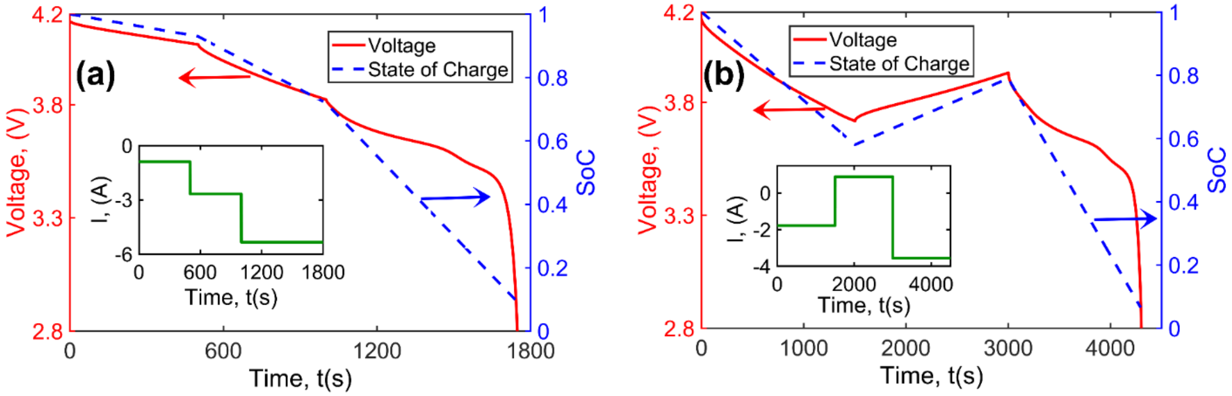

Figure 7. Application of the analytical model for a step-function current profile: Voltage and SOC as functions of time for (a) discharge at multiple C-rates, (b) discharge-charge-discharge process.

A similar plot for the discharge-charge-discharge profile is shown in Figure 7(b). In this case, as expected, both voltage and SoC decrease in the discharge period, increase in the charge period and finally decrease in the last period of discharge at a greater rate due to the greater C-rate.

These plots demonstrate the capability of the Green’s function based analytical model to predict the voltage and SoC variation in the cell over time due to current profiles comprising of step functions.

### 8-3-2-2 Sinusoidal current profile

The analytical model is used next to investigate the voltage/SoC behavior of a Li-ion cell operating under two sinusoidal current profiles, which may be the case for Electrochemical Impedance Spectroscopy (EIS), or for alternating current (AC) charging/discharging of the cell. Two different sinusoidal current profiles are considered. Figure 8 presents plots for voltage and SoC of a Li-ion cell under a sinusoidal discharge current profile of $I(t) = I_0(1 + sin\omega t)$, where $I_0$=-1.76 A corresponds to 1C discharge. This current profile is a combination of AC and DC that discharges the cell throughout the time period. This specific current profile is chosen in this study to demonstrate the applicability of this approach for complicated dynamic current profiles. Such profiles have been recently used for battery diagnostics[46]. Figures 8(a) and 8(b) plot cell voltage and SoC, respectively, as functions of time for three different values of frequency, $\omega$. The current profiles are also shown as an inset. While both voltage and SoC decrease over time, as expected, periodicity in the voltage and SoC is also seen, with the number of crests and troughs being consistent with the current profile for each frequency. At each crest, when the discharge current becomes zero for an instant, the voltage curve becomes flat momentarily. It is interesting that for each frequency considered here, the cell fully discharges at about the same time, which is because the integral of the current profile over the time period remains the same for all three frequencies considered here and the DC component of the current primarily causes the reduction in voltage and SoC. Figure 8(b) presents a plot of average SoC at the negative electrode as a function of time for different values of frequency. The sinusoidal footprint of the current profile is also easily seen in the SoC curve, where, similar to voltage, the SoC curve flattens momentarily when the current becomes zero.

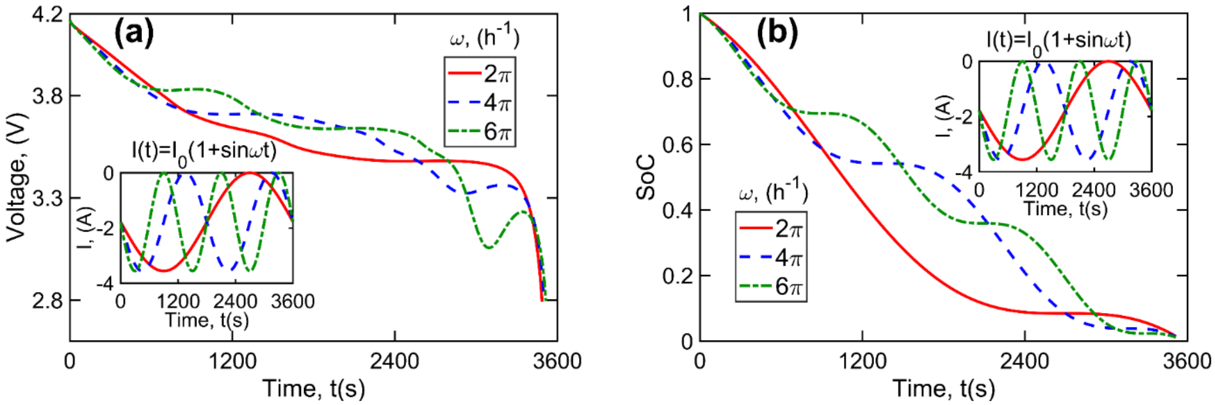

Figure 8. Application of the analytical model for a combination of AC-DC profile, $I(t)$=I$_0$(1+sin$\omega t$): (a) Voltage and (b) SOC as functions of time.

A second type of sinusoidal current profile $I(t) = I_0 sin\omega t$ is also considered. This profile is representative of AC charge/discharge, which is commonly used in EIS measurements for investigating the electrochemical processes that occur inside the cell. Based on this current profile, the cell is periodically subjected to both charge and discharge. Figures 9(a) and 9(b) plot voltage and SoC, respectively, as functions of time for this current profile with multiple values of frequency. The current profile is also shown as an inset. Unlike the previous case where the voltage and SoC gradually reduce over time due to the discharge-only nature of the process, in this case, both voltage and SoC oscillate harmonically due to the charge-discharge nature of the current profile. As the current frequency increases, the number of times that voltage and SoC plots oscillate also increases. EIS typically uses a very low current amplitude to probe only the linear response of the physical processes inside the cell, whereas a large amplitude of current used here causes a corresponding large amplitude of voltage and SoC.

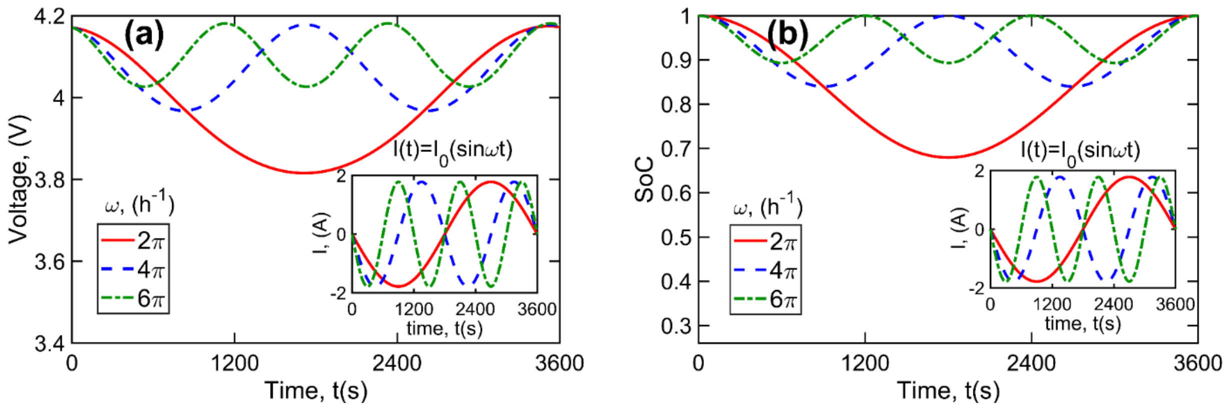

Figure 9. Application of the model for a harmonic current profile $I(t)=I_0(\sin\omega t)$: (a) Voltage and (b) SOC as functions of time.

### 8-3-2-3 ECE-15 and US06 current profiles

The current profiles considered so far are ideal ones, whereas current profiles may be a lot more complicated in realistic charge/discharge conditions, for example in automotive applications. The Green's function based analytical model presented in section 2 is next used to predict the behavior of a Li-ion cell operating under two dynamic load cycles – ECE-15 and US06. Both are representative of conditions that may be encountered in a realistic electric vehicle battery pack and are commonly used as benchmarks for studying battery performance. Figures 10(a) and 10(b) present voltage and SoC plots for an ECE-15[47] current profile, which is also plotted in both Figures for comparison. Both voltage and SoC plots closely follow the changes in the current profile. In general, the voltage and SoC curves are smoother than the current profile due to the diffusion time constants – it takes a finite time for voltage and SoC curves to respond to fluctuations in current. In some instances, such as around $t$=140 s, the voltage and SoC continue to drop even after the magnitude of the discharge current has passed its peak, which is likely because the cell is still being discharged even though the magnitude of the discharge current is reducing with time. Higher discharge current causes a larger voltage drop due to cell polarization. The voltage drop due to the cell polarization continues to decrease as the magnitude of the current decreases, leading to an increase in the voltage of the cell after 145s. It is interesting to see that whenever the current becomes zero, the voltage still changes a little while SoC becomes flat almost instantaneously which is expected as the cell reverts back to its open circuit potential.

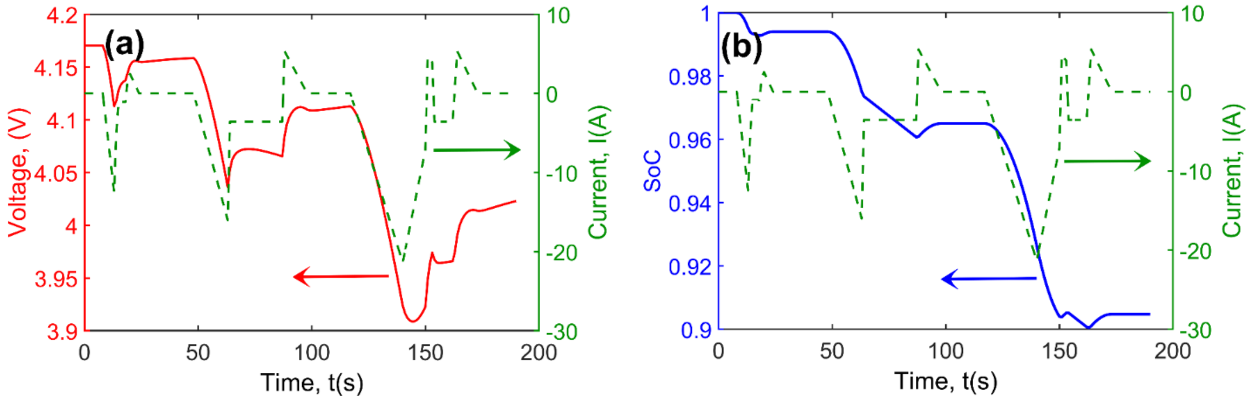

Figure 10. Cell response predicted by the analytical model for a realistic process based on ECE-15 drive cycle[47]: (a) Voltage and (b) SoC as functions of time

The second drive cycle is even more complicated, and illustrates the capability of the Green's function based analytical model to predict voltage and SoC for very complicated and dynamic drive profiles. The US06 drive cycle is commonly used to represent current profile for an electric vehicle battery pack for realistic driving conditions[43,44]. The drive profiles are scaled for an 1.78Ah cell, used in the analytical model. Figures 11(a) and 11(b) plot voltage and SoC, respectively, as functions of time for the US06 current profiles, also shown in these Figures. While the current profile is very dynamic and includes multiple, sharp changes, including between charge and discharge, Figures 11(a) and 11(b) demonstrate the capability of the analytical model to follow the current profile and predict the cell voltage and SoC as functions of time. The cell voltage and SoC are seen to follow the fluctuations in current, and generally decrease over time because the applied current is negative (discharge) for most of the duration. Note that, the concentration profile and consequently the voltage and SoC are determined analytically even for these very complicated profiles, which results in fast computation without the need for mesh generation.

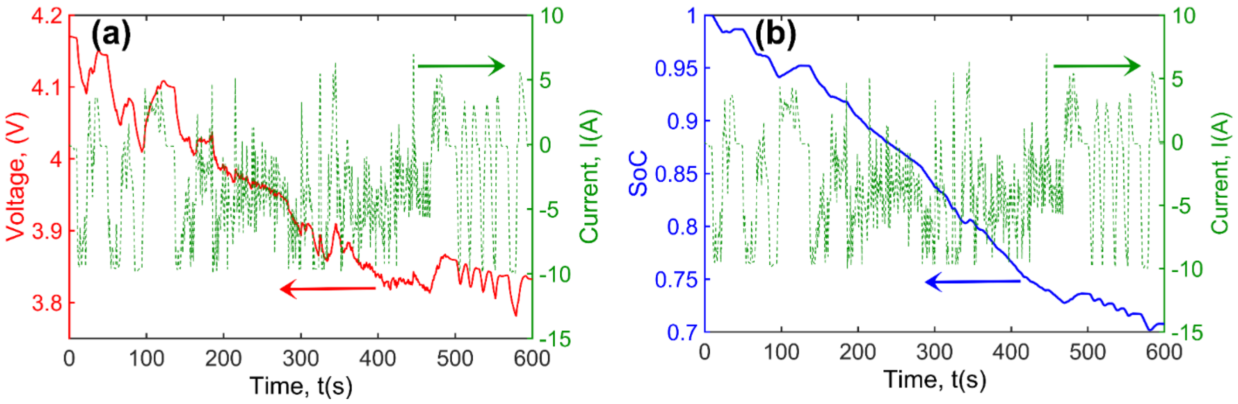

Figure 11. Cell response predicted by the analytical model for a realistic process based on US06 drive cycle: (a) Voltage and (b) SoC as functions of time.

## 8-4. Conclusions

The voltage and SoC computation presented here is carried out using a Green's function based exact analytical solution for the concentration profile in the electrodes for an arbitrary time-dependent current profile. This analytical approach agrees well with numerical simulations for a variety of conditions and may be easier to implement in practical battery management systems, especially with controllers containing limited memory. The individual electrode SoC can easily be related to the overall capacity/SoC of the cell. Even for very complicated current profiles, the analytical model is shown to be able to accurately predict the voltage and SoC changes in the cell over time. It should be noted that the model presented here is based on a single spherical particle model, and therefore is valid within the range of validity of the SPM model, i.e. low to moderate C-rates. Also note that the Green's function approach is inherently valid only for linear systems. Non-linearities such as concentration-dependent diffusivities, which may be significant for modeling of certain battery chemistries, sizes and form factors are not accounted for by the model. Finally, the model is isothermal, and does not account for the impact of temperature on diffusion or kinetic processes. Note that the analytical solution presented here can be used as a basis for state estimation algorithms such as Kalman filter approach for SoC estimation. Furthermore, the solution can also be coupled with the energy balance equation to account for thermal effects. This work is expected to contribute towards the improvement of battery management systems (BMS) for a variety of applications.

## 8-4. Nomenclature

| | |
|---|---|
| $c$ | concentration (mol $m^{-3}$) |
| $c_{initial}$ | initial concentration (mol $m^{-3}$) |
| $c_{max}$ | maximum concentration (mol $m^{-3}$) |
| $c_e$ | electrolyte concentration (mol $m^{-3}$) |
| $D$ | diffusion coefficient ($m^2s^{-1}$) |
| $F$ | Faraday constant (96485 C $mol^{-1}$) |
| $I$ | current (A) |

| | |
|---|---|
| $J$ | molar flux (mol $m^{-2}$ $s^{-1}$) |
| $k$ | reaction rate constant ($m^{2.5}$ $mol^{-0.5}$ $s^{-1}$) |
| $r$ | radial spatial coordinate (m) |
| $R$ | particle radius (m) |
| $R_u$ | universal gas constant (8.314 J $mol^{-1}$ $K^{-1}$) |
| $R_{cell}$ | cell resistance (Ω) |
| $S$ | total electroactive area ($m^2$) |
| $t$ | time (s) |
| $U$ | open circuit potential (V) |
| $V$ | total volume of the electrodes ($m^3$) |
| $x$ | state of charge |
| $\varepsilon$ | volume fraction of the active material in electrode |
| $\eta$ | overpotential (V) |
| $\lambda$ | eigenvalue ($m^{-1}$) |
| $\omega$ | frequency ($hr^{-1}$) |
| $\varphi$ | potential (V) |

## 8-5. References

[1] Rahimi-Eichi, H., Ojha, U., Baronti, F., & Chow, M. Y. (2013). Battery management system: An overview of its application in the smart grid and electric vehicles. *IEEE Industrial Electronics Magazine*, **7**(2), 4-16.

[2] Tanim, T. R., Rahn, C. D., & Wang, C. Y. (2015). State of charge estimation of a lithium ion cell based on a temperature dependent and electrolyte enhanced single particle model. *Energy*, **80**, 731-739.

[3] Xing, Y., Ma, E. W., Tsui, K. L., & Pecht, M. (2011). Battery management systems in electric and hybrid vehicles. *Energies*, **4**(11), 1840-1857.

[4] Lu, L., Han, X., Li, J., Hua, J., & Ouyang, M. (2013). A review on the key issues for lithium-ion battery management in electric vehicles. *Journal of Power Sources*, **226**, 272-288.

[5] Xiong, R., Cao, J., Yu, Q., He, H., & Sun, F. (2017). Critical review on the battery state of charge estimation methods for electric vehicles. *IEEE Access*, **6**, 1832-1843.

[6] Corno, M., Bhatt, N., Savaresi, S. M., & Verhaegen, M. (2014). Electrochemical model-based state of charge estimation for Li-ion cells. *IEEE Transactions on Control Systems Technology*, **23**(1), 117-127.

[7] Xiao, Y., Lin, C., & Fahimi, B. (2013, March). Online state of charge estimation in electrochemical batteries: Application of pattern recognition techniques. In *2013 Twenty-Eighth Annual IEEE Applied Power Electronics Conference and Exposition (APEC)* (pp. 2474-2478). IEEE

[8] Lin, C., Tang, A., & Xing, J. (2017). Evaluation of electrochemical models based battery state-of-charge estimation approaches for electric vehicles. *Applied Energy*, **207**, 394-404.

[9] Yang, F., Xing, Y., Wang, D., & Tsui, K. L. (2016). A comparative study of three model-based algorithms for estimating state-of-charge of lithium-ion batteries under a new combined dynamic loading profile. *Applied energy*, **164**, 387-399.

[10] Xing, Y., He, W., Pecht, M., & Tsui, K. L. (2014). State of charge estimation of lithium-ion batteries using the open-circuit voltage at various ambient temperatures. *Applied Energy*, **113**, 106-115.

[11] He, H., Xiong, R., & Guo, H. (2012). Online estimation of model parameters and state-of-charge of $LiFePO_4$ batteries in electric vehicles. *Applied Energy*, **89**(1), 413-420.

[12] Ng, K. S., Moo, C. S., Chen, Y. P., & Hsieh, Y. C. (2009). Enhanced coulomb counting method for estimating state-of-charge and state-of-health of lithium-ion batteries. *Applied Energy*, **86**(9), 1506-1511.

[13] Hu, X., Li, S., Peng, H., & Sun, F. (2012). Robustness analysis of State-of-Charge estimation methods for two types of Li-ion batteries. *Journal of Power Sources*, **217**, 209-219.

[14] Zhang, J., & Lee, J. (2011). A review on prognostics and health monitoring of Li-ion battery. *Journal of Power Sources*, **196**(15), 6007-6014.

[15] Salkind, A. J., Fennie, C., Singh, P., Atwater, T., & Reisner, D. E. (1999). Determination of state-of-charge and state-of-health of batteries by fuzzy logic methodology. *Journal of Power Sources*, **80**(1-2), 293-300.

[16] Kozlowski, J. D. (2003, March). Electrochemical cell prognostics using online impedance measurements and model-based data fusion techniques. In *2003 IEEE Aerospace Conference Proceedings (Cat. No. 03TH8652)* (Vol. 7, pp. 3257-3270). IEEE.

[17] Kang, L., Zhao, X., & Ma, J. (2014). A new neural network model for the state-of-charge estimation in the battery degradation process. *Applied Energy*, **121**, 20-27.

[18] Anton, J. C. A., Nieto, P. J. G., Viejo, C. B., & Vilán, J. A. V. (2013). Support vector machines used to estimate the battery state of charge. *IEEE Transactions on Power Electronics*, **28**(12), 5919-5926.

[19] Liaw, B. Y., Nagasubramanian, G., Jungst, R. G., & Doughty, D. H. (2004). Modeling of lithium ion cells—A simple equivalent-circuit model approach. *Solid State Ionics*, **175**(1-4), 835-839.

[20] Xiong, R., Sun, F., Chen, Z., & He, H. (2014). A data-driven multi-scale extended Kalman filtering based parameter and state estimation approach of lithium-ion polymer battery in electric vehicles. *Applied Energy*, **113**, 463-476.

[21] Plett, G. L. (2004). Extended Kalman filtering for battery management systems of LiPB-based HEV battery packs: Part 1. Background. *Journal of Power Sources*, **134***(2)*, 252–261.

[22] Plett, G. L. (2004). Extended Kalman filtering for battery management systems of LiPB-based HEV battery packs: Part 2. Modeling and identification. *Journal of Power Sources*, **134**(2), 262-276.

[23] Plett, G. L. (2004). Extended Kalman filtering for battery management systems of LiPB-based HEV battery packs: Part 3. State and parameter estimation. *Journal of Power Sources*, **134**(2), 277-292.

[24] Lee, J., Nam, O., & Cho, B. H. (2007). Li-ion battery SOC estimation method based on the reduced order extended Kalman filtering. *Journal of Power Sources*, **174**(1), 9-15.

[25] Verbrugge, M., & Tate, E. (2004). Adaptive state of charge algorithm for nickel metal hydride batteries including hysteresis phenomena. *Journal of Power Sources*, **126**(1-2), 236-249.

[26] Kim, I. S. (2006). The novel state of charge estimation method for lithium battery using sliding mode observer. *Journal of Power Sources*, **163**(1), 584-590.

[27] Hu, X., Sun, F., & Zou, Y. (2010). Estimation of state of charge of a lithium-ion battery pack for electric vehicles using an adaptive Luenberger observer. *Energies*, **3**(9), 1586-1603.

[28] Doyle, M., Fuller, T. F., & Newman, J. (1993). Modeling of galvanostatic charge and discharge of the lithium/polymer/insertion cell. *Journal of the Electrochemical society*, **140**(6), 1526.

[29] Han, X., Ouyang, M., Lu, L., & Li, J. (2015). Simplification of physics-based electrochemical model for lithium ion battery on electric vehicle. Part I: Diffusion simplification and single particle model. *Journal of Power Sources*, **278**, 802-813.

[30] Smith, K. A., Rahn, C. D., & Wang, C. Y. (2007). Control oriented 1D electrochemical model of lithium ion battery. *Energy Conversion and management*, **48**(9), 2565-2578.

[31] Smith, K. A., Rahn, C. D., & Wang, C. Y. (2009). Model-based electrochemical estimation and constraint management for pulse operation of lithium ion batteries. *IEEE Transactions on Control Systems Technology*, **18**(3), 654-663.

[32] Smith, K., & Wang, C. Y. (2006). Solid-state diffusion limitations on pulse operation of a lithium ion cell for hybrid electric vehicles. *Journal of Power Sources*, **161**(1), 628-639.

[33] Subramaniam, A., Kolluri, S., Parke, C. D., Pathak, M., Santhanagopalan, S., & Subramanian, V.R. (2020). Properly Lumped Lithium-ion Battery Models: A Tanks-in-Series Approach. *Journal of The Electrochemical Society*, **167**(1), 013534.

[34] Jokar, A., Rajabloo, B., Désilets, M., & Lacroix, M. (2016). Review of simplified Pseudo-two-Dimensional models of lithium-ion batteries. *Journal of Power Sources*, **327**, 44-55.

[35] Doyle, M., & Newman, J. (1997). Analysis of capacity–rate data for lithium batteries using simplified models of the discharge process. *Journal of Applied Electrochemistry*, **27**(7), 846-856.

[36] Guo, M., Sikha, G., & White, R. E. (2011). Single-particle model for a lithium-ion cell: Thermal behavior. *Journal of The Electrochemical Society*, **158**(2), A122-A132.

[37] Han, X., Ouyang, M., Lu, L., & Li, J. (2015). Simplification of physics-based electrochemical model for lithium ion battery on electric vehicle. Part I: Diffusion simplification and single particle model. *Journal of Power Sources*, **278**, 802-813.

[38] Tanim, T. R., Rahn, C. D., & Wang, C. Y. (2014, June). A reduced order electrolyte enhanced single particle lithium ion cell model for hybrid vehicle applications. In: *2014 American Control Conference* (pp. 141-146). IEEE.

[39] Luo, W., Lyu, C., Wang, L., & Zhang, L. (2013). A new extension of physics-based single particle model for higher charge–discharge rates. *Journal of Power Sources*, **241**, 295-310.

[40] Santhanagopalan, S., & White, R. E. (2006). Online estimation of the state of charge of a lithium ion cell. *Journal of Power Sources*, **161**(2), 1346-1355.

[41] Parhizi, M., & Jain, A. (2020). Analytical Modeling of Solid Phase Diffusion in Single-Layer and Composite Electrodes Under Time-Dependent Flux Boundary Condition. *Journal of The Electrochemical Society*, **167**(6), 060528.

[42] Ramadass, P., Haran, B., Gomadam, P. M., White, R., & Popov, B. N. (2004). Development of first principles capacity fade model for Li-ion cells. *Journal of the Electrochemical Society*, **151**(2), A196.

[43] Keil, P., Englberger, M., & Jossen, A. (2015). Hybrid energy storage systems for electric vehicles: An experimental analysis of performance improvements at subzero temperatures. *IEEE Transactions on Vehicular Technology*, **65**(3), 998-1006.

[44] Zhang, G., Ge, S., Yang, X. G., Leng, Y., Marple, D., & Wang, C. Y. (2017). Rapid restoration of electric vehicle battery performance while driving at cold temperatures. *Journal of Power Sources*, **371**, 35-40.

[45] Cen, Z., & Kubiak, P. (2020). Lithium-ion battery SOC/SOH adaptive estimation via simplified single particle model. *International Journal of Energy Research*, available at doi.org/10.1002/er.5374

[46] Teo, L., Pathak, M., Kolluri, S., Dawson-Elli, N., Schwartz, D. T., & Subramanian, V. R. An Analysis of Transient Impedance-like Diagnostic Signals in Batteries, ECS Meeting Abstract Volume MA2018-02, 2018, available at https://iopscience.iop.org/article/10.1149/MA2018-02/25/872, last accessed 07/09/2020.

[47] Sarıkurt, T., Ceylan, M., & Balikçi, A. (2014, June). An analytical battery state of health estimation method. In *2014 IEEE 23rd International Symposium on Industrial Electronics (ISIE)* (pp. 1605-1609). IEEE.

# Chapter 9

# Analytical Modeling of Solution Phase Diffusion in Porous Composite Electrodes under Time-Dependent Flux Boundary Conditions using Green's Function Method

**Accepted as**: Parhizi, M., & Jain, A. (2020). Analytical Modeling of Solution Phase Diffusion in Porous Composite Electrodes under Time-Dependent Flux Boundary Conditions using Green's Function Method. *Ionics*, 2020.

## 9-1. Introduction

Li-ion batteries are among the most popular rechargeable batteries for a wide variety of applications due to their promising electrochemical characteristics [1-3]. Favorable characteristics of Li-cells include high energy density, high power density, low self-discharge rate, stability and long cycle life [4-6]. The operation of Li-ion cells involves coupled thermal and electrochemical processes such as kinetic reactions, mass, charge and thermal transport phenomena [7,8]. Mathematical modeling of Li-ion cells is therefore, necessary to fully understand the underlying processes towards design and optimization of electrochemical energy conversion and storage systems [9,10].

Extensive research has been reported towards development of theoretical models to predict electrochemical and thermal transport in Li-ion cells subject to different operating conditions [11,12]. These electrochemical models solve the underlying charge, mass and thermal transport equations, as well as reaction kinetics [11-14]. Two most extensively-used electrochemical models are the Pseudo-2D model (P2D) and Single Particle Model (SPM) [11]. P2D model was constructed based on the porous electrode theory introduced by Newman [15] and the concentrated solution theory [16]. It solves the species and charge transport in both solution and solid phases [11,17]. P2D model is generally coupled and non-linear, resulting in a large number of equations and significant computational time. Thus, Single Particle Model (SPM) was developed to reduce the complexity associated with P2D model. In SPM, concentration gradients in the solution phase are neglected, leading to dominance of solid phase diffusion in the porous electrode, which can be represented by a single, one-dimensional particle [8,18,19]. At low discharge rates and for thin electrodes this may be a reasonable assumption [20-21]. However, at larger discharge rates or for thick electrodes for example energy cells, when concentration gradient in the solution phase cannot be neglected, the governing equations become coupled and simplification is needed in order to derive an analytical solution. Towards this, Doyle et al. [22] assumed a specific form for the reaction rate distribution in the porous electrode, leading to uncoupling of the governing equations. Based on this approach, analytical solutions have been derived using the Separation of Variables (SOV) method for three limiting cases – solid phase, solution phase and Ohmically-dominated cell [22]. The governing equations in the solid phase were defined based on Fick's law and the material balance in the solution phase was defined using the concentrated solution theory [22].

A variety of approximate analytical methods have been developed, including the Parabolic Profile (PP) method [23,24], State Variable Model (SVM) [25,26], Extended Single Particle Model (ESPM) [27-28], Proper Orthogonal Decomposition (POD) [29] and Electrode Averaged Model (EAM) [30]. Due to the coupled and non-linear nature of the underlying equations, exact solutions are available only for a limited number of problems. For example, an extended SOV technique has been used to predict concentration profile in both solid and liquid phase diffusion problems in composite electrodes under constant galvanostatic discharge boundary condition and zero initial concentration [31]. An exact solution has been presented for solid phase diffusion in a spherical particle under time-dependent flux boundary condition using Finite Integral Transform technique [32]. Material balance equations in thin film, cylindrical and spherical electrodes under galvanostatic boundary condition have been solved using integral transform method [33]. Exact solution for both solid and solution phase diffusion with non-zero initial condition has been developed using Laplace transformation technique [34]. Green's function approach has been used to solve the solution phase diffusion in composite electrode for a constant boundary condition [35].

The diffusion problem in Li-ion cells is inherently multi-layer in nature, involving diffusion through the electrodes as well as the separator. A number of papers have presented analysis of multilayer diffusion problems through a variety of theoretical methods, such as eigenvalue methods [36,37], Laplace transforms [38] and variable substitution followed by use of Vodicka-type orthogonality [39]. Time-dependent boundary conditions have been accounted for using Duhamel theorem [40] as well as Laplace transforms [41]. For eigenvalue-driven approaches, computation of eigenvalues is often challenging for a multilayer geometry [36].

While these methods have been discussed for a variety of applications such as heterogeneous porous media [38], geology [42,43], biotransport [37], semiconductor devices [44], etc., there is a relative lack of similar work on multilayer diffusion in Li-ion cells. Specifically, most of the past work in this field assumes constant boundary conditions and constant generation/consumption rate, while time-dependent boundary conditions may be important for practical applications, where the applied charging or discharging current changes with time. This could occur, for example, in an electric vehicle battery pack where the discharge rate changes with time due to changes in the driving load. In some cases, the cell may even switch between charge and discharge. Only a few analytical and approximate solutions have been presented to address such problems with time-dependent boundary conditions. For example, finite integral transform method has been used to develop an exact solution for solid-phase diffusion in a single spherical porous electrode operation under arbitrary initial and boundary conditions [32]. Green’s function approach has been used to solve the solid phase diffusion in single layer and composite electrodes [45]. Approximate solutions have been presented for solid phase diffusion limitation single layer electrode under time-dependent boundary conditions [28].

In light of the relative lack of analytical solutions for problems with time-dependent boundary conditions, time-dependent generation/consumption rate and an arbitrary space-dependent initial concentration, mathematical modeling of such problems may be of much interest. A feasible approach for providing solutions to such problems is the use of Green's function technique. Green's functions have been used commonly for heat transfer problems with complicated geometry and boundary/initial conditions [46,47], including the use of techniques such as method of fundamental solutions [42] and singular boundary method [43]. Green's function has been used for solving multilayer problems in biotransport [48] and multilayer materials [49]. However, only limited use of Green's function approach exists for addressing species transport problems in electrochemical systems [35,36].

This work presents an analytical solution for Li-ion diffusion in a composite porous electrode operating under time-dependent flux boundary condition and arbitrary initial conditions using Green's function approach. Solid-phase diffusion limitation is neglected and the solution phase diffusion limitation is dominant, which is one of the limiting cases of Li-ion cell operation [22]. While the reaction term in the species conservation equation is, in general, a function of both and time, under solution-phase diffusion limitation, this term has been treated to be a constant [22]. The present work generalizes this by considering a time-dependent function, which may occur when the external current changes with time, for example during cyclic charge/discharge of the battery pack of an electric vehicle. Also note that the governing equations in this study are presented for a single insertion electrode but the results can be easily generalized to two insertion electrodes. The analytical model presented in this work provides a useful mathematical tool to understand transport phenomena in a composite porous Li-ion cell, which may improve the analysis and design of electrochemical energy storage and conversion devices.

## 9-2. Mathematical Modeling

### 9-2-1. Green's function approach for composite electrodes

Heat and mass transport are often governed by similar diffusion equations. If the non-homogeneities in these equations are arbitrary functions of time, the commonly-used SOV method may not be applicable. On the other hand, Green's function approach continues to be a powerful mathematical tool for solving a wide range of linear partial differential equations with arbitrary time-dependent non-homogeneities in the governing equation and boundary conditions [46,47]. Green's function method can be used to address species diffusion problems in single or multi-layers bodies.

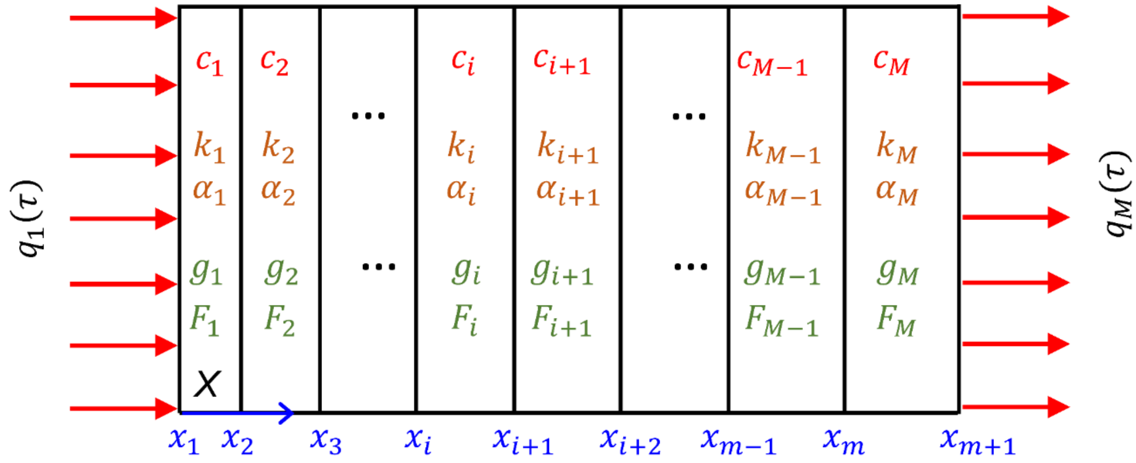

Figure 1. Schematic of a *M*-layer composite electrode.

Consider diffusion in a *M*-layer composite body shown in Figure 1. In general, each layer may have different properties and species consumption/generation due to reaction. In addition, two time-dependent flux boundary conditions are considered at the two ends. The governing conservation equation can be written in non-dimensional form as:

$$\alpha_i \frac{1}{x^p}\frac{\partial}{\partial x}\left(x^p \frac{\partial c_i}{\partial x}\right) + \frac{\alpha_i}{k_i} g_i(x,t) = \frac{\partial c_i}{\partial t} \qquad x_i < x < x_{i+1} \qquad (1)$$

subject to the following general boundary and initial conditions:

$$-k_1 \left(\frac{\partial c_1}{\partial x}\right)_{x=x_1} = q_1(\tau) \qquad \text{at } x = x_1 \qquad (2)$$

$$c_i|_{x=x_{i+1}} = c_{i+1}|_{x=x_{i+1}} \qquad \text{at interfaces } i = 1,2,\dots,M-1 \qquad (3)$$

$$k_i \left(\frac{\partial c_i}{\partial x}\right)_{x=x_{i+1}} = k_{i+1} \left(\frac{\partial c_{i+1}}{\partial x}\right)_{x=x_{i+1}} \qquad \text{at interfaces } i = 1,2,\dots,M-1 \qquad (4)$$

$$-k_M \left(\frac{\partial c_M}{\partial x}\right)_{x=x_{M+1}} = q_M(\tau) \qquad \text{at } x = x_{M+1} \qquad (5)$$

$$c_i = f_i(x) \qquad \text{at } t = 0 \qquad (6)$$

Where $x'^p$ is the Sturm–Liouville weight function, and *p*=0, 1 and 2 for slabs, cylinders and spheres respectively. α and *k* are constants and can be determined based on a specific problem. Here, equations (3) and (4) represent continuity of species and flux balance at the interfaces, whereas equations (2) and (5) represent a balance between diffusion and mass flux at the two ends. *f(x)* is the initial condition, *g* is the generation or consumption term and *q(τ)* is the non-homogeneous boundary condition.

The solution to this multi-layer diffusion problem using Green’s function approach is given by [48]:

$$c_i(x,t) = \sum_{j=1}^{M} \left\{ \int_{x'=x_j}^{x_{j+1}} G_{ij}(x,t|x',t')_{t'=0} f_j(x') x'^p dx' + \int_{t=0}^{t} \int_{x'=x_j}^{x_{j+1}} G_{ij}(x,t|x',t') \frac{\alpha_j}{k_j} g_j(x',t') x'^p dx' dt' \right\} + \sum_{m=1,M} \frac{\alpha_m}{k_m} \int_{t'=0}^{t} \left[ x'^p G_{im}(x,t|x',t') \right]_{x=x_{b,m}} q_m(t') dt' \tag{7}$$

Where the summation in the third term is taken over all layers with an external boundary. $x_{b,m}$ refers to the location of the external boundary for the $m^{th}$ layer (referring to Figure 1, $x_{b,1}=x_1$ and $x_{b,M}=x_{M+1}$).

The first term in equation (7) accounts for the initial condition, while the second and third terms represent contributions of non-homogeneities in the governing equation and boundary conditions, respectively. The solution represented by equation (7) is particularly powerful in its ability to account for the effect of arbitrary space-dependent initial condition, time- and space-dependent generation/consumption and time-dependent boundary conditions.

A key step in deriving the Green's function-based solution for the specific problem under consideration is to determine the Green's function, $G(X,\tau|X',\tau')$ that appears in equation (7). To do so, the corresponding homogeneous version of the problem must be solved first. For a homogeneous problem, the only non-zero term in equation (7) is the first term which represents the contribution of the initial concentration. Thus, a comparison between the first term in equation (7) and the solution to the homogeneous problem results in the evaluation of the Green's function at $t' = 0$, $G(x,t|x',t')_{t'=0}$. In order to determine the complete Green's function at any time, *t*, i.e. $G(x,t|x',t')$, *t* must be replaced with $(t-t')$ in $G(x,t|x',t')_{t'=0}$.

The next sections present the problem statement and derivation of the solution for liquid phase diffusion in a porous Li-ion cell sandwich under an arbitrary time-dependent flux using Green's function method.

### 9-2-2. Governing equations and boundary conditions

Figure 2 shows a schematic of a Li-ion cell sandwich comprising a porous electrode, separator and Li-ion foil electrode. The separator and porous electrode, referred to with subscripts 1 and 2, respectively, are initially at a non-uniform concentration of $F_1(x)$ and $F_2(x)$. The cell sandwich operates under a time-dependent discharge boundary condition, $q(\tau)$ at $X$=0. Doyle and Newman presented governing equations for composite Li-ion cell sandwich under a uniform current distribution [22]. Note that, the reaction rate distribution in the electrode is, in general, a function of both location and time, $J(x,t)$.

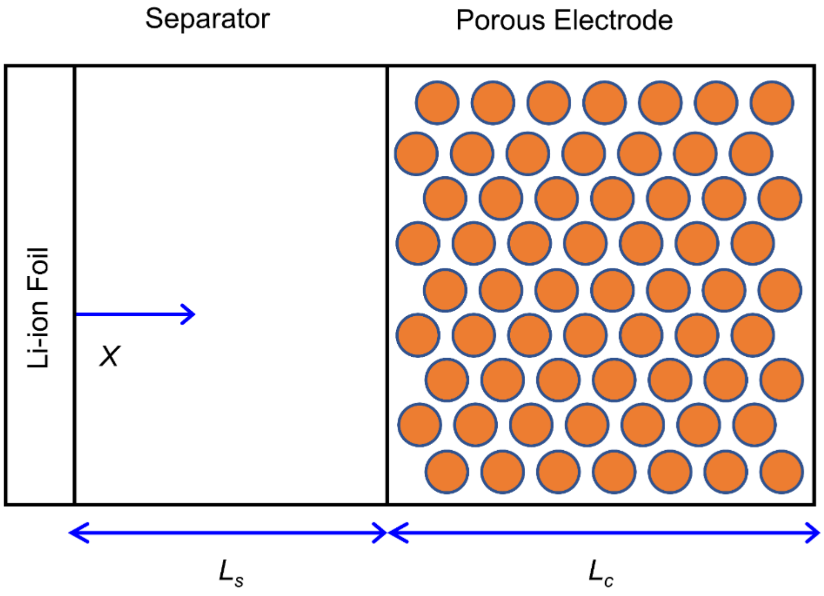

Figure 2. Schematic of the composite porous electrode consisting of Li-ion foil, separator and positive porous electrode.

However, under the solution-phase diffusion limitation, the spatial distribution of the reaction term can be neglected [22]. When the external current on the cell is a function of time, as may be the case during cyclic charge and discharge of a Li-ion cell in an electric vehicle, the reaction term is, in general, a function of time. Neglecting solid-phase diffusion limitation, conservation equations for the separator and porous electrodes for this case can be written as:

$$D\frac{\partial^2 C_1}{\partial X^2} = \frac{\partial C_1}{\partial \tau} \qquad 0 < X < L_s \tag{8}$$

$$D\varepsilon^{3/2}\frac{\partial^2 C_2}{\partial X^2} + aj_n(\tau)(1 - t^+) = \varepsilon\frac{\partial C_2}{\partial \tau} \qquad L_s < X < L_s + L_C \tag{9}$$

Subject to the following boundary conditions:

$$\left(\frac{\partial C_1}{\partial X}\right)_{X=0} = q(\tau) = -\frac{I(\tau)(1 - t^+)}{FD} \qquad \text{at } X = 0 \tag{10}$$

$$C_1 = C_2 \qquad \text{at } X = L_s \tag{11}$$

$$\left(\frac{\partial C_1}{\partial X}\right)_{X=L_s} = \varepsilon^{3/2}\left(\frac{\partial C_2}{\partial X}\right)_{X=L_s} \qquad \text{at } X = L_s \tag{12}$$

$$\left(\frac{\partial C_2}{\partial X}\right)_{X=L_s+L_C} = 0 \qquad \text{at } X = L_s + L_C \tag{13}$$

and initial conditions are:

$$C_1 = F_1(X) \qquad \text{at } \tau = 0 \qquad (14)$$

$$C_2 = F_2(X) \qquad \text{at } \tau = 0 \qquad (15)$$

Where $D$, $\varepsilon$ and $a$ refer to diffusion coefficient of the electrolyte, porosity of the electrode and specific interfacial area, respectively. $I$, $j_n$, $t^+$ and F refer to current density, pore wall flux, transference number, and Faraday constant respectively. $L_s$ and $L_C$ are the separator and porous electrode lengths, respectively. Note that equations (8) and (9) describe diffusion in the separator and material balance in the solution phase of the porous electrode, respectively. Equation (10) describes the time-dependent flux boundary condition. Equations (11) and (12) ensure the continuity of concentration and flux at the separator-electrode interface. Equation (13) ensures that no ions diffuse through the back of the electrode, and finally equations (14) and (15) represent the initial condition.

The current distribution is assumed to be time-dependent and uniform throughout the electrode. While in general, the reaction rate distribution might be quite complicated and non-uniform [22], it has been shown that if the kinetic resistance dominates Ohmic resistance, the reaction rate distribution can be considered as its average value throughout the electrode [15].

Note that, in case of uniform initial concentration, the two non-homogeneities driving this problem during discharge are concentration flux into the separator (equation (10)) and species consumption due to Lithium intercalation in the cathode. The interplay between the two processes over time determines how the concentration field changes with time.

For a uniform current distribution, $j_n$ can be written as its average value everywhere in the porous electrode [22] as follows:

$$j_n(\tau) = \frac{-I(\tau)}{aFL_c} \qquad (16)$$

Using the non-dimensionalization scheme presented in the nomenclature section, and after some mathematical simplification, the non-dimensional form of the governing equations for the separator and electrode can be written as:

$$\frac{\partial^2 c_1}{\partial x^2} = \frac{\partial c_1}{\partial t} \qquad 0 < x < 1 \qquad (17)$$

$$\varepsilon^{1/2}\frac{\partial^2 c_2}{\partial x^2} + \frac{\varepsilon^{1/2}}{\varepsilon^{3/2}}J(t) = \frac{\partial c_2}{\partial t} \qquad 1 < x < 1 + r \qquad (18)$$

Subject to the following boundary conditions:

$$\left(\frac{\partial c_1}{\partial x}\right)_{x=0} = J(t)r \qquad \text{at } x = 0 \qquad (19)$$

$$c_1 = c_2 \qquad \text{at } x = 1 \qquad (20)$$

$$\left(\frac{\partial c_1}{\partial x}\right)_{x=1} = \varepsilon^{3/2}\left(\frac{\partial c_2}{\partial x}\right)_{x=1} \qquad \text{at } x = 1 \qquad (21)$$

$$\left(\frac{\partial c_2}{\partial x}\right)_{x=1+r} = 0 \qquad \text{at } x = 1 + r \qquad (22)$$

The initial conditions for the separator and electrode are:

$$c_1 = f_1(x) \qquad \text{at } t = 0 \tag{23}$$

$$c_2 = f_2(x) \qquad \text{at } t = 0 \tag{24}$$

Comparison between equations (17)-(24) specific to this problem, and the general problem statement for Green's function solution given by equations (1)-(6) indicates that, in this case, $M$=2, $\alpha_1$=1, $k_1$=1, $\alpha_2$=$\varepsilon^{1/2}$, and $k_2$= $\varepsilon^{3/2}$. Note that $J$ in equation (19) has a negative sign in its expression shown in nomenclature section. This negative sign indicates species flux into the separator during discharge, when the electrode considered here is the cathode.

9-2-3. Solution procedure

In order to solve equations (17)-(24), the Green's function associated with this problem must be determined first. The general form of the Green's function for multi-layer geometries can be written as follows [22]:

$$G_{ij}(x,t|x',t')_{t'=0} = \sum_{n=1}^{\infty} \frac{1}{N_n} \frac{k_j}{\alpha_j} \Gamma(t) \psi_{in}(x) \psi_{jn}(x') \tag{25}$$

$$G_{ij}(x,t|x',t') = \sum_{n=1}^{\infty} \frac{1}{N_n} \frac{k_j}{\alpha_j} \Gamma(t-t') \psi_{in}(x) \psi_{jn}(x') \tag{26}$$

where $x'^{p}$ is the Sturm–Liouville weight function, and $N_n$ is the norm, given by

$$N_n = \sum_{j=1}^{M} \frac{k_j}{\alpha_j} \int_{x'=x_j}^{x_{j+1}} x'^p \psi_{jn}^2(x') dx' \tag{27}$$

In order to construct the Green's function associated with this problem, *Γ(t)* and *ψ(x)* are determined by solving the corresponding homogeneous problem. Note that the term *J(t)* in the governing equation, equation (18) and the boundary condition, equation (19) becomes zero in the corresponding homogeneous problem. The SOV technique can be used to solve the homogeneous problem, based on which, the concentration profile in the separator and electrode for the homogeneous problem can be written as follows:

$$c_{h,i}(x,t) = \sum_{n=0}^{\infty} \psi_{in}(x)\Gamma_n(t) \tag{28}$$

Where *i*=1, 2.

Equation (28) is then substituted back into the governing equations, which results in two separate differential equations in space and time. The solutions for time-dependent and space-dependent components of equation (28) can be written as:

$$\Gamma_n(t) = \exp\left(-\lambda_n^2 t\right) \tag{29}$$

$$\psi_{1n}(x) = A_{1n} \sin\left(\frac{\lambda_n x}{\sqrt{\alpha_1}}\right) + B_{1n} \cos\left(\frac{\lambda_n x}{\sqrt{\alpha_1}}\right) \tag{30}$$

$$\psi_{2n}(x) = A_{2n} \sin\left(\frac{\lambda_n x}{\sqrt{\alpha_2}}\right) + B_{2n} \cos\left(\frac{\lambda_n x}{\sqrt{\alpha_2}}\right) \tag{31}$$

Note that $\alpha_1$ and $\alpha_2$ are already defined in the previous section. Using boundary conditions, a set of equations can be written in a matrix form for the unknown coefficients $A_{in}$ and $B_{in}$ as follows:

$$\begin{bmatrix} 1 & 0 & 0 & 0 \\ 0 & \cos\frac{\lambda_n}{\sqrt{\alpha_1}} & -\sin\frac{\lambda_n}{\sqrt{\alpha_2}} & -\cos\frac{\lambda_n}{\sqrt{\alpha_2}} \\ 0 & K\sin\frac{\lambda_n}{\sqrt{\alpha_1}} & \cos\frac{\lambda_n}{\sqrt{\alpha_2}} & -\sin\frac{\lambda_n}{\sqrt{\alpha_2}} \\ 0 & 0 & \cos\frac{\lambda_n(1+r)}{\sqrt{\alpha_2}} & -\sin\frac{\lambda_n(1+r)}{\sqrt{\alpha_2}} \end{bmatrix} \begin{bmatrix} A_{1n} \\ B_{1n} \\ A_{2n} \\ B_{2n} \end{bmatrix} = \begin{bmatrix} 0 \\ 0 \\ 0 \\ 0 \end{bmatrix} \tag{32}$$

Where $K = \frac{k_1}{k_2}\sqrt{\frac{\alpha_2}{\alpha_1}} = \varepsilon^{-5/4}$. In order to determine the eigenvalues, $\lambda_n$, the determinant of the matrix in equation (32) must be equal to zero, in order to result in a nontrivial solution. This requirement results in a transcendental equation for the eigenvalues as follows:

$$\tan\left(\frac{\lambda_n r}{\sqrt{\alpha_2}}\right) + K\tan(\frac{\lambda_n}{\sqrt{\alpha_1}}) = 0 \tag{33}$$

Without loss of generality, any one of the non-vanishing coefficients in equation (44) may be set to unity. In this case, $B_{1n}$ is chosen to be equal to 1. Consequently, the coefficients, $A_{in}$ and $B_{in}$, are determined to be

$$A_{1n} = 0 \tag{34}$$

$$B_{1n} = 1 \tag{35}$$

$$A_{2n} = \cos\frac{\lambda_n}{\sqrt{\alpha_1}}\sin\frac{\lambda_n}{\sqrt{\alpha_2}} - K\sin\frac{\lambda_n}{\sqrt{\alpha_1}}\cos\frac{\lambda_n}{\sqrt{\alpha_2}} \tag{36}$$

$$B_{2n} = \cos\frac{\lambda_n}{\sqrt{\alpha_1}}\cos\frac{\lambda_n}{\sqrt{\alpha_2}} + K\sin\frac{\lambda_n}{\sqrt{\alpha_1}}\sin\frac{\lambda_n}{\sqrt{\alpha_2}} \tag{37}$$

This completes the derivation of the solution. Using equations (25) and (26), the concentration profile in the separator and electrode layers can be written as:

$$\begin{aligned}
c_1(x,t) = \sum_{n=0}^{\infty}\Bigg(&\int_{x'=0}^{x'=1}\frac{1}{N_n}\exp(-\lambda_n^2 t)\cos\left(\frac{\lambda_n x}{\sqrt{\alpha_1}}\right)\cos\left(\frac{\lambda_n x'}{\sqrt{\alpha_1}}\right)f_1(x')dx' \\
&+\int_{x'=1}^{x'=1+r}\frac{1}{N_n}\exp(-\lambda_n^2 t)\cos\left(\frac{\lambda_n x}{\sqrt{\alpha_1}}\right)\left(A_{2n}\sin\left(\frac{\lambda_n x'}{\sqrt{\alpha_2}}\right)\right. \\
&\left.+B_{2n}\cos\left(\frac{\lambda_n x'}{\sqrt{\alpha_2}}\right)\right)f_2(x')dx' \\
&+\frac{\alpha_2}{k_2}\int_{\tau=0}^{\tau}\int_{X'=1}^{1+r}\frac{1}{N_n}\exp(-\lambda_n^2(t-t'))\cos\left(\frac{\lambda_n x}{\sqrt{\alpha_1}}\right)\left(A_{2n}\sin\left(\frac{\lambda_n x'}{\sqrt{\alpha_2}}\right)\right. \\
&\left.+B_{2n}\cos\left(\frac{\lambda_n x'}{\sqrt{\alpha_2}}\right)\right)J(t')x'^p\,dx'\,d\tau' \\
&+\frac{\alpha_2}{k_2}\int_{t'=0}^{t'=t}\frac{1}{N_n}\exp(-\lambda_n^2(t-t'))\cos\left(\frac{\lambda_n x}{\sqrt{\alpha_1}}\right)\left(A_{2n}\sin\left(\frac{\lambda_n(1+r)}{\sqrt{\alpha_2}}\right)\right. \\
&\left.+B_{2n}\cos\left(\frac{\lambda_n(1+r)}{\sqrt{\alpha_2}}\right)\right)(-rJ(t'))dt'\Bigg)
\end{aligned} \tag{38}$$

$$
\begin{aligned}
c_2(x,t) = \sum_{n=0}^{\infty} \int_{x'=0}^{x'=1} \frac{1}{N_n} \exp(-\lambda_n^2 t) \left(A_{2n} \sin\left(\frac{\lambda_n x}{\sqrt{\alpha_2}}\right) + B_{2n} \cos\left(\frac{\lambda_n x}{\sqrt{\alpha_2}}\right)\right) \cos\left(\frac{\lambda_n x'}{\sqrt{\alpha_1}}\right) f_1(x') dx' \qquad (39) \\
+ \int_{x'=1}^{x'=1+r} \frac{1}{N_n} \exp(-\lambda_n^2 t) \left(A_{2n} \sin\left(\frac{\lambda_n x}{\sqrt{\alpha_2}}\right) + B_{2n} \cos\left(\frac{\lambda_n x}{\sqrt{\alpha_2}}\right)\right) \left(A_{2n} \sin\left(\frac{\lambda_n x'}{\sqrt{\alpha_2}}\right)\right. \\
\left. + B_{2n} \cos\left(\frac{\lambda_n x'}{\sqrt{\alpha_2}}\right)\right) F_2(x') dx' \\
+ \frac{\alpha_2}{k_2} \int_{\tau=0}^{\tau} \int_{X'=1}^{1+r} \frac{1}{N_n} \exp(-\lambda_n^2 (t-t')) \left(A_{2n} \sin\left(\frac{\lambda_n x}{\sqrt{\alpha_2}}\right)\right. \\
\left. + B_{2n} \cos\left(\frac{\lambda_n x}{\sqrt{\alpha_2}}\right)\right) \left(A_{2n} \sin\left(\frac{\lambda_n x'}{\sqrt{\alpha_2}}\right) + B_{2n} \cos\left(\frac{\lambda_n x'}{\sqrt{\alpha_2}}\right)\right) J(t') x'^{p} dx' d\tau' \\
+ \frac{\alpha_2}{k_2} \int_{t'=0}^{t'=t} \frac{1}{N_n} \exp(-\lambda_n^2 (t-t')) \left(A_{2n} \sin\left(\frac{\lambda_n x}{\sqrt{\alpha_2}}\right)\right. \\
\left. + B_{2n} \cos\left(\frac{\lambda_n x}{\sqrt{\alpha_2}}\right)\right) \left(A_{2n} \sin\left(\frac{\lambda_n (1+r)}{\sqrt{\alpha_2}}\right) + B_{2n} \cos\left(\frac{\lambda_n (1+r)}{\sqrt{\alpha_2}}\right)\right) (-r J(t')) dt'
\end{aligned}
$$

Where $A_{2n}$ and $B_{2n}$ are defined in equations (36) and (37) and $N_n$ is defined in equation (27). Note that the zeroth terms of equations (38) and (39), as well as the norm for the zeroth term must be determined by calculating the limits of these equations as $\lambda \to 0$. Further, note that if initial concentrations $f_1$ and $f_2$ are zero, there is some simplification in equations (38) and (39).

Next, the validation of the model and its applications in a variety of realistic scenarios will be discussed. All plots in the next section are generated for a cathode.

## 9-3. Results and Discussion

### 9-3-1. Model validation

Analytical model derived in the previous section is validated against past work and numerical simulations. To the best of our knowledge, no literature is available for solution-phase diffusion under time-dependent flux boundary condition. Therefore, comparison with past studies has been carried out for a special case of galvanostatic boundary condition where the applied current density is constant.

Table 1. Electrochemical and physical properties used in this study.

| Properties | Values | Units |
|---|---|---|
| $D$ | $2.6\times10^{-10}$ | $m^2s^{-1}$ |
| $F$ | 96,487 | C $mol^{-1}$ |
| $t^+$ | 0.2 | - |
| $\varepsilon$ | 0.35 | - |
| $L_s$ | $25\times10^{-6}$ | m |
| $L_c$ | $125\times10^{-6}$ | m |
| $C_0$ | 1000 | mol $m^{-3}$ |

|  |  |  |
|---|---|---|
| $r$ | 5 | ----- |

Green's function-based model presented in this study is compared against a past work by Subramanian, et al. [50], where an approximate method was used to solve the solution phase diffusion in the porous electrode without solving for concentration in the separator [50]. Note that their method was limited to galvanostatic boundary conditions where the current density is constant. Thus, comparison of the present model against this previous study is carried out for a special case of constant current density. For comparison, a composite electrode comprising a porous cathode, separator and Li-ion foil similar to Figure 1 operating under a galvanostatic discharge boundary condition is considered.

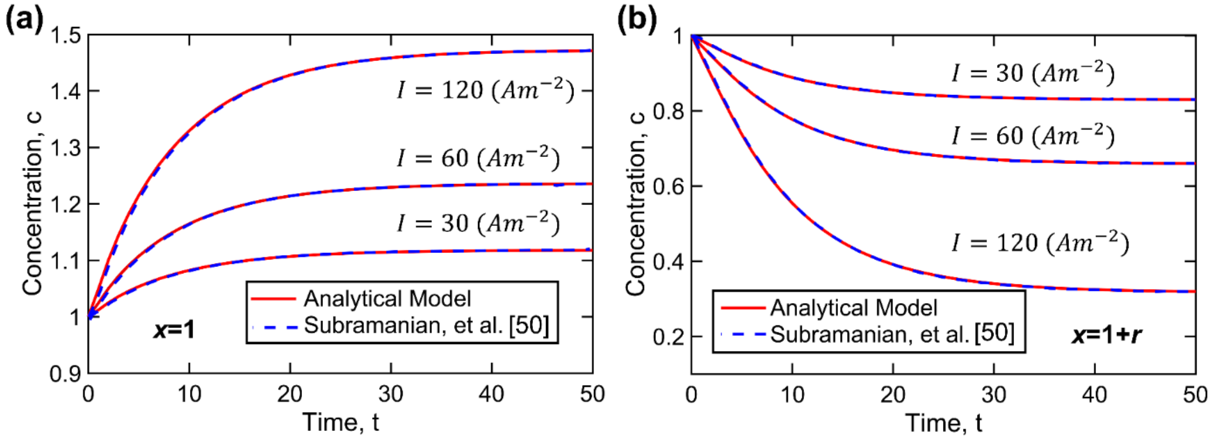

Figure 3. Validation against previous study [50] for a special case of constant current density: (a) dimensionless concentration at the electrode/separator interface ($x$=1) as a function of dimensionless time for different rates of discharge; (b) dimensionless concentration at the current collector ($x$=1+$r$) as a function of dimensionless time for different rates of discharge.

The parameters used for comparison are listed in Table 1, consistent with Subramanian, et al. [50]. Figure 3(a) plots the non-dimensional concentration as a function of non-dimensional time at the electrode/separator interface, $x$=1, for multiple values of current density for both the present model and previous work [50]. Figure 3(b) presents a similar plot at the current collector, $x$=1+$r$ for both models. Results show excellent agreement between the Green's function solution and past work. These Figures show, as expected, that concentration at the separator-electrode interface increases with time, while concentration at the end of the electrode decreases with time. This is consistent with species consumption occurring throughout the electrode and species flux into the electrode only from the separator side. The rate of change of concentration increases with increasing current, and a steady-state concentration is reached in each case. As expected, the larger the current, the greater/lower is the concentration at $x$=1 and $x$=1+$r$, respectively.

To further validate the analytical model presented here, a numerical simulation of solution-phase diffusion limitation in the composite porous electrode is carried out. The numerical method solves equations (17)-(24) using an implicit finite difference method in MATLAB. The numerical computation uses a fully implicit approach to discretize the governing equations and boundary conditions in both separator and porous electrode, resulting in $m$+1 number of equations where $m$ is the number of nodes. Each equation contains three unknowns including the concentration of the $i^{th}$ point and its two neighbors for the next time, $n$+1. Initial, boundary and interface conditions on the other hand provide the known values for these equations. Spatial discretization is carried out in a way that ensures that a node is always present at the intersection between layers. Interface conditions are defined to ensure the continuity of concentration and flux at the separator/electrode interface. The resultant equations in the matrix form are solved using tri-diagonal matrix algorithm (TDMA) instead of direct inversion to reduce the computational time. 2000 nodes are found to sufficiently ensure mesh-independent of computed results. Figure 4(a) compares the non-dimensional concentration as a function of non-dimensional time at the current collector, $x$=1+$r$, determined from the Green's function approach with numerical simulations. This comparison is carried out for multiple values of $B$ for a linear time-dependent current density, $I(t) = I_0(1 + B \cdot t)$ where $I_0$=60 Am$^{-2}$. The plot shows very good agreement between the Green's function-based model and numerical solution for each case. Figure 4(a) shows that as the current density increases over time due to the slope $B$, the concentration at the back of the electrode, $x$=1+$r$, decreases faster, which consistent with results from Subramanian, et al. [50]. The rate of reduction in concentration is greater for higher values of $B$, as expected. Figure 4(b) plots the non-dimensional concentration as a function of non-dimensional distance, $x$, at multiple times for the same current density profile as Figure 4(a) and $B$=1/30. Similar to Figure 4(a), results show good agreement between the present analytical model and numerical simulations. The concentration behavior agrees well with results presented in a study by Subramanian & White [31] in which an exact solution for solution phase diffusion in composite electrodes under galvanostatic boundary conditions was derived. Results from the present work and [31] both show that as the passes, concentration increases in the separator due to the incoming flux from negative electrode, while the concentration deceases at the back of the electrode due to consumption of Li-ions.

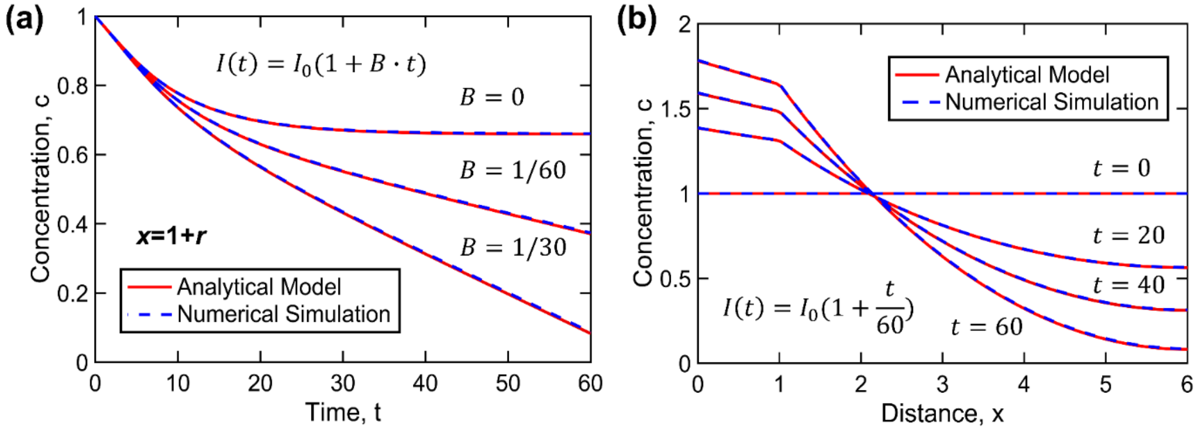

Figure 4. Validation against numerical simulation for a linear current density $I(t) = I_0(1 + B \cdot t)$ where $I_0$=60 Am$^{-2}$ (a) dimensionless concentration at the current collector ($x$=1+$r$) as a function of dimensionless time for different values of slopes, $B$, (b) dimensionless concentration as a function of dimensionless distance at multiple times for $B$=1/60.

### 9-3-2. Application of the model

In this section, the Green's function solution is used to address a number of practical problems in which time-dependent boundary conditions may occur. Among different possible types of time-dependent functions, sinusoidal and step functions may be particularly relevant to battery operation. Sinusoidal functions are important since any reasonably well-behaved time-varying function may be expressed in the form of a Fourier series comprising sinusoidal functions. Another important type of boundary conditions relevant to operation of Li-ion cells are step functions, since sudden changes in charge/discharge rate may be encountered in realistic settings. Therefore, this section focuses specifically on problems with sinusoidal and step function boundary conditions.

First, discharge process for a porous cathode is considered, with a time-dependent sinusoidal current density, $I(t) = I_0(1 + \sin(2\pi\omega t)$ where $I_0$=60 Am$^{-2}$. Two different frequencies $\omega$=1/60 & $\omega$=1/30 are considered. All other problem parameters are similar to previous figures and summarized in Table 1. Figure 5(a) plots non-dimensional concentration as a function of time at three different locations – $x$=0, 1 and 1+$r$ – for the two frequencies. Results show a periodic behavior for concentration consistent with the sinusoidal current density. Figure 5(b) presents a plot of non-dimensional concentration as a function of non-dimensional distance at multiple times for $I_0$=60 Am$^{-2}$ and $\omega$=1/30. Figure 5(b) shows an interesting behavior with intersections at multiple points and a non-monotonic nature. The concentration in the separator region is maximum at $t$=40, minimum at $t$=60 and in between at $t$= 20. This behavior reverses in the region close to the back of the electrode, $x$=1+$r$. This can be explained with the help of Figure 5(a). For instance, in Figure 5(a), at t=60, due to the periodic nature of the current density, the concentration at the back of the electrode is at its maximum whereas the concentration at $x$=0 and 1 are at their minimum. These Figures show that the model is successfully able to capture the concertation profiles under a sinusoidal time-dependent current density.

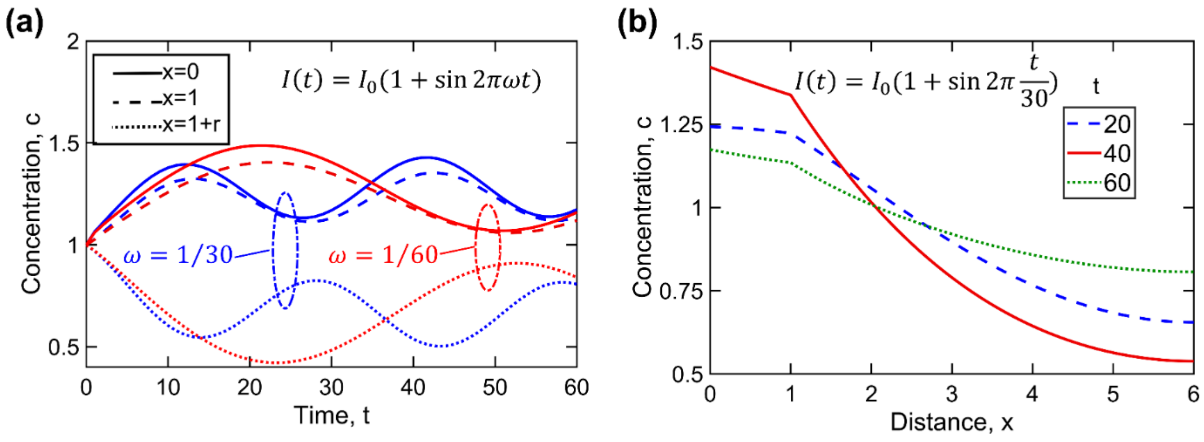

Figure 5. Application of the model for a periodic current density $I(t) = I_0(1 + \sin 2\pi\omega t)$ where $I_0$=60 Am$^{-2}$ (a) dimensionless concentration at multiple location as a function of dimensionless time for $\omega$=1/30 and 1/60, (b) dimensionless concentration as a function of dimensionless distance at multiple times for $\omega$=1/30.

In order to more comprehensively capture the concertation profile throughout the composite electrode at different times, Figure 6 shows a colorplot of concentration as a function of time and space, with the same current density profile as Figure 4, and $\omega$=1/15. It is seen that four maxima/minima occur up to $t$=60, which is consistent with the frequency of the sinusoidal current density.

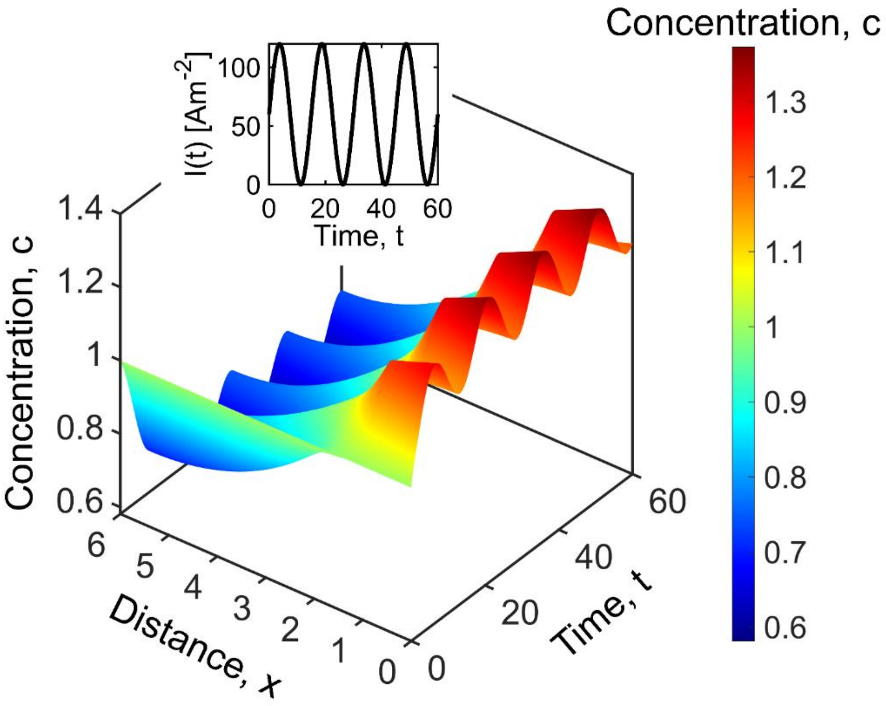

Figure 6. Application of the model for a periodic current density $I(t) = I_0(1 + \sin 2\pi\omega t)$ where $I_0$=60 Am$^{-2}$ and $\omega$ =1/15: Three dimensional plot of concentration as functions of space and time.

Figures 7 and 8 present plots for applications where the current density profile can be represented by step functions. This scenario may occur, for example, in the battery pack of an electric vehicle, where the discharge rate may suddenly change due to changes in the external load. Further, in several commonly used charge/discharge protocols, Li-cells may be cyclically charged and discharged at different rates, so that the current density may change its magnitude and/or direction over time. Two specific cases are presented in Figures 7 and 8.

Figure 7 presents concentration plots for a step-function boundary condition, with changes only in the magnitude of current, and not the direction. In this case, the current density function is a three-step discharge process at multiple discharge rate of 60, 120 and 180 $Am^{-2}$ corresponding to C-rates of 1, 2 and 3, respectively. Figure 7(a) plots non-dimensional concentration as a function of non-dimensional time at three different locations, whereas Figure 7(b) presents the plot of non-dimensional concentration as a function of non-dimensional distance at multiple times. It is seen from Figure 7(a) that the concentration at the back of the electrode decreases gradually and the rate of this reduction increases with increasing magnitude of current density. On the other hand, concentration in the separator increases with time. This is due to concentration flux into the separator during the discharge process, and simultaneous depletion of species in the electrode due to reaction. As expected from the current density profile, Figure 7(b) shows that concentration at the back of the electrode is lowest at the highest discharge rate and the concentration in the separator is highest at the highest discharge rate.

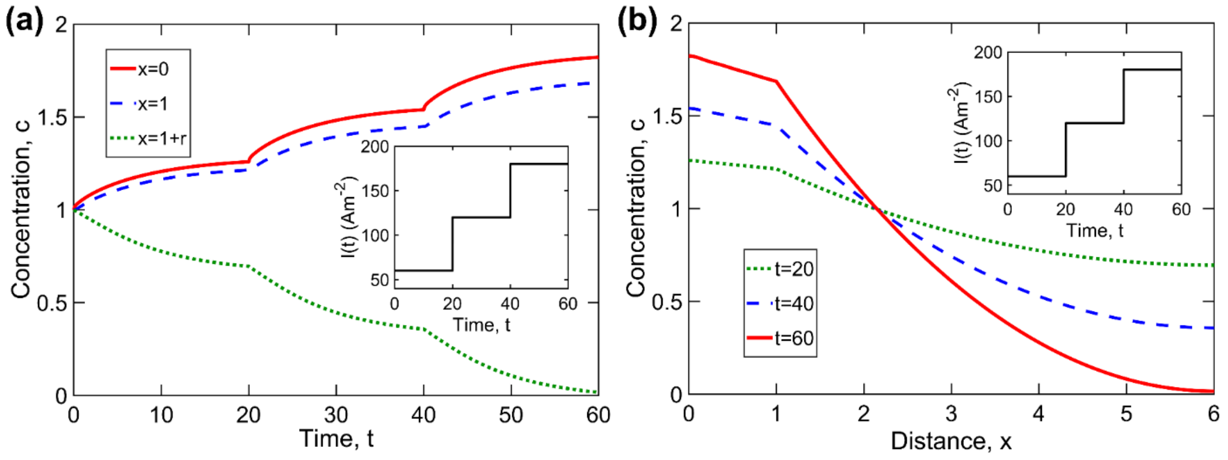

Figure 7. Application of the model for a step function discharge current density (a) dimensionless concentration as a function of dimensionless time at multiple locations, *x*=0, 1 and 1+*r* (b) dimensionless concentration as a function of dimensionless distance at multiple times, *t*=20, 40 and 60.

Figure 8 considers a somewhat more complicated scenario, in which the current density starts with a constant discharge rate of 60 Am$^{-2}$, switches directions to a 40 Am$^{-2}$ charge at *t*=20, and finally changes back to 120 Am$^{-2}$ discharge at *t*=40. Figure 8(a) plots the computed non-dimensional concentration for this case as a function of non-dimensional time at three different locations, *x*=0, 1 and 1+*r*. For reference, the current density profile as a function of time is also plotted in the inset. It is seen that concentration at the back of the electrode decreases in the beginning for *t*<20 (discharge), and increases as the current density switches directions in the 20<*t*<40 period (Charge). Finally, the concentration at *x*=1+*r* decreases again for *t*>40 (discharge), consistent with the current density profile. Concentration profiles at the other two locations, *x*=0 and *x*=1 exhibit the opposite trend, which is consistent with concentration flux dominating over species consumption due to intercalation in the electrode. Figure 6(b) presents a plot of dimensionless concentration throughout the composite electrode at multiple times. Concentration profiles are plotted at *t*=20, 40 and 60. Results in this plot are consistent with Figure 6(a). The maximum concentration in the electrode occurs at *t*=40, consistent with the inset plot of current density.

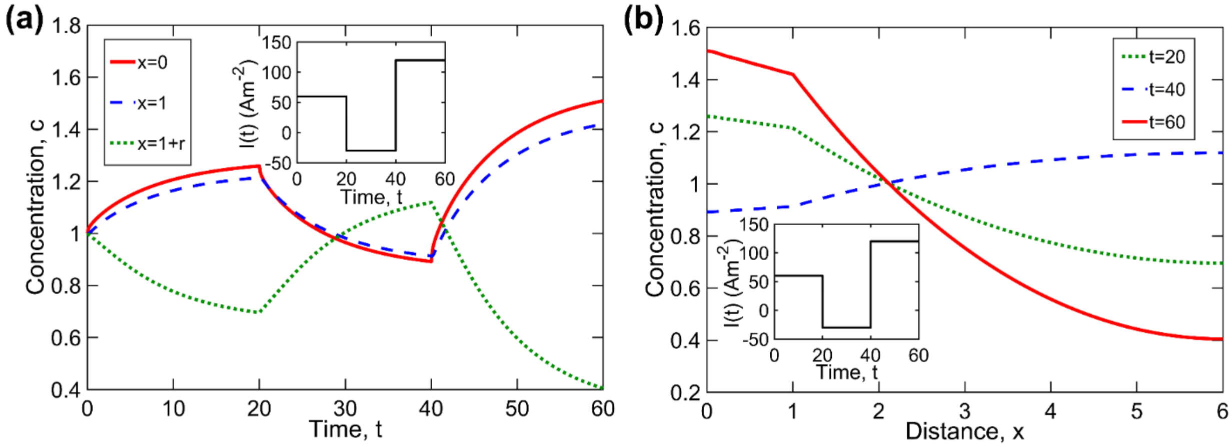

Figure 8. Application of the model for a cyclic step function current density (a) dimensionless concentration as a function of dimensionless time at multiple locations, *x*=0, 1 and 1+*r* (b) dimensionless concentration as a function of dimensionless distance at multiple times, *t*=20, 40 and 60.

Note that all results presented here are computed with only five eigenvalues. This helps significantly reduce the computational time, particularly when the operating condition is a complicated function of time. The use of more than five eigenvalues is found to result in no significant change in the computed concentration distribution. It is important to note that eigenvalues for this problem depend only on *r* and $\varepsilon$ and therefore, once the values of these parameters is known, the eigenvalues can be calculated once and be used for any arbitrary boundary condition. Table 2 presents the first five eigenvalues for $\varepsilon=0.35$ and multiple values of *r*.

Table 2. Values of eigenvalues for $\varepsilon=0.35$ for multiple values of $r$

| $r$ | $\lambda_1$ | $\lambda_2$ | $\lambda_3$ | $\lambda_4$ | $\lambda_5$ |
|---|---|---|---|---|---|
| 4 | 0 | 0.408935 | 0.943229 | 1.513226 | 2.085300 |
| 5 | 0 | 0.341385 | 0.766828 | 1.223153 | 1.686654 |
| 6 | 0 | 0.294434 | 0.647903 | 1.02749 | 1.414978 |
| 8 | 0 | 0.232656 | 0.497336 | 0.780636 | 1.071196 |
| 10 | 0 | 0.193285 | 0.405536 | 0.631237 | 0.863146 |

## 9-4. Conclusions

In this work, the Green's function approach is used to derive an analytical solution for solution-phase limitation diffusion in composite electrodes under a wide variety of time-dependent flux boundary conditions. The method is applied to a composite electrode consisting of Li-ion foil, separator and porous electrode similar to the composite Li-ion cell sandwich proposed by Doyle and Newman [22]. Concentration profiles in the separator and porous electrode are determined as functions of space and time. The mathematical model is validated against previous studies for the special case of galvanostatic boundary conditions. Furthermore, Green's function-based model is validated by comparison with numerical simulations for time-dependent boundary conditions. The mathematical model presented in this study can be used to accurately predict the transient behavior of solution-phase limitation diffusion. The model is used to predict the concentration profile for a number of realistic time-dependent current densities such as sinusoidal and step functions that may be encountered in energy conversion and storage applications. The computational time associated with the present model is lower than numerical simulations due to the low number of eigenvalues required for convergence. This work contributes towards the theoretical understanding of species diffusion in Li-ion cells, and provides tools that may be helpful for designing, predicting and improving the performance of electrochemical devices.

## 9-5. Nomenclature

| | |
|---|---|
| $a$ | specific interfacial area ($m^{-1}$) |
| $c$ | non-dimensional concentration, $c=C/C_0$ |
| $C_0$ | reference concentration (mol $m^{-3}$) |
| $C$ | concentration (mol $m^{-3}$) |
| $D$ | diffusion coefficient of electrolyte in the solution ($m^2s^{-1}$) |
| $f(x)$ | non-dimensional initial concentration, $f(x)=F(x)/C_0$ |
| $F(x)$ | initial concentration (mol $m^{-3}$) |
| $F$ | Faraday’s constant (C $mol^{-1}$) |
| $g$ | non-dimensional generation or consumption |
| $G$ | Green’s function |
| $I$ | current density ($A/m^2$) |
| $j_n$ | pore wall flux, $j_n=-I/aFL_c$ (mol $m^{-2}$ $s^{-1}$) |
| $J$ | non-dimensional pore wall flux, $J=-I(1-t^+)L_s^2/FDL_cC_0$ |
| $k$ | non-dimensional constant |
| $L_s$ | length of the separator (m) |

| | |
|---|---|
| $L_c$ | length of the porous electrode (m) |
| $r$ | ratio of electrode length to separator length, $r=L_c/L_s$ |
| $t$ | non-dimensional time, $t= D\tau/L_s^2$ |
| $t^+$ | transference number |
| $x$ | non-dimensional lengthscale, $x=X/L_s$ |
| $X$ | lengthscale (m) |
| $\alpha$ | non-dimensional constant |
| $\varepsilon$ | porosity |
| $\omega$ | non-dimensional frequency |
| $\tau$ | time (s) |
| $\lambda$ | eigenvalues |

Subscripts

| | |
|---|---|
| $c$ | cathode |
| $h$ | homogeneous problem |
| $s$ | separator |

## 9-6. REFERENCES

[1] J.B. Goodenough, K.-S. Park, ChemInform Abstract: The Li-Ion Rechargeable Battery: A Perspective, ChemInform. 44 (2013). doi:10.1002/chin.201320273.

[2] B. Scrosati, J. Garche, Lithium batteries: Status, prospects and future, Journal of Power Sources. 195 (2010) 2419–2430. doi:10.1016/j.jpowsour.2009.11.048.

[3] B. Dunn, H. Kamath, J.-M. Tarascon, Electrical Energy Storage for the Grid: A Battery of Choices, Science. 334 (2011) 928–935. doi:10.1126/science.1212741.

[4] A.D. Pasquier, I. Plitz, S. Menocal, G. Amatucci, A comparative study of Li-ion battery, supercapacitor and nonaqueous asymmetric hybrid devices for automotive applications, Journal of Power Sources. 115 (2003) 171–178. doi:10.1016/s0378-7753(02)00718-8.

[5] B.A. Johnson, R.E. White, Characterization of commercially available lithium-ion batteries, Journal of Power Sources. 70 (1998) 48–54. doi:10.1016/s0378-7753(97)02659-1.

[6] M. Parhizi, M. Ahmed, A. Jain, Determination of the core temperature of a Li-ion cell during thermal runaway, Journal of Power Sources. 370 (2017) 27–35. doi:10.1016/j.jpowsour.2017.09.086.

[7] K. Shah, N. Balsara, S. Banerjee, M. Chintapalli, A.P. Cocco, W.K.S. Chiu, et al., State of the Art and Future Research Needs for Multiscale Analysis of Li-Ion Cells, Journal of Electrochemical Energy Conversion and Storage. 14 (2017). doi:10.1115/1.4036456.

[8] B. Diouf, R. Pode, Potential of lithium-ion batteries in renewable energy, Renewable Energy. 76 (2015) 375–380. doi:10.1016/j.renene.2014.11.058.

[9] J. Zhang, J. Lee, A review on prognostics and health monitoring of Li-ion battery, Journal of Power Sources. 196 (2011) 6007–6014. doi:10.1016/j.jpowsour.2011.03.101.

[10] M.L. Sushko, K.M. Rosso, J.-G.(J. Zhang, J. Liu, Multiscale Simulations of Li Ion Conductivity in Solid Electrolyte, The Journal of Physical Chemistry Letters. 2 (2011) 2352–2356. doi:10.1021/jz201032w.

[11] A. Jokar, B. Rajabloo, M. Désilets, M. Lacroix, Review of simplified Pseudo-two-Dimensional models of lithium-ion batteries, Journal of Power Sources. 327 (2016) 44–55. doi:10.1016/j.jpowsour.2016.07.036.

[12] R. Xiong, J. Cao, Q. Yu, H. He, F. Sun, Critical Review on the Battery State of Charge Estimation Methods for Electric Vehicles, IEEE Access. 6 (2018) 1832–1843. doi:10.1109/access.2017.2780258.

[13] G.G. Botte, V.R. Subramanian, R.E. White, Mathematical modeling of secondary lithium batteries, Electrochimica Acta. 45 (2000) 2595–2609. doi:10.1016/s0013-4686(00)00340-6.

[14] M. Doyle, Modeling of Galvanostatic Charge and Discharge of the Lithium/Polymer/Insertion Cell, Journal of The Electrochemical Society. 140 (1993) 1526. doi:10.1149/1.2221597.

[15] J. Newman, K.E. Thomas-Alyea. Electrochemical systems. John Wiley & Sons, 2012.

[16] T. F. Fuller, J. A. Newman, Concentrated solution theory model of transport in solid–polymer–electrolyte fuel cells. Electrochem. Soc. Proc. (1989). Ser, 89-14.

[17] V. Ramadesigan, P.W.C. Northrop, S. De, S. Santhanagopalan, R.D. Braatz, V.R. Subramanian, Modeling and Simulation of Lithium-Ion Batteries from a Systems Engineering Perspective, Journal of The Electrochemical Society. 159 (2012). doi:10.1149/2.018203jes.

[18] G. Ning, B.N. Popov, Cycle Life Modeling of Lithium-Ion Batteries, Journal of The Electrochemical Society. 151 (2004). doi:10.1149/1.1787631.

[19] S. Santhanagopalan, Q. Guo, P. Ramadass, R.E. White, Review of models for predicting the cycling performance of lithium ion batteries, Journal of Power Sources. 156 (2006) 620–628. doi:10.1016/j.jpowsour.2005.05.070.

[20] V. Ramadesigan, V. Boovaragavan, V.R. Subramanian, Efficient Reformulation of Solid-Phase Diffusion in Physics-Based Lithium-ion Battery Models, ECS Transactions. (2009). doi:10.1149/1.3115314.

[21] S.K. Rahimian, S. Rayman, R.E. White, Extension of physics-based single particle model for higher charge–discharge rates, Journal of Power Sources. 224 (2013) 180–194. doi:10.1016/j.jpowsour.2012.09.084.

[22] M. Doyle, J. Newman, Analysis of capacity–rate data for lithium batteries using simplified models of the discharge process, Journal of Applied Electrochemistry 27, 846–856 (1997). https://doi.org/10.1023/A:1018481030499

[23] K.A. Smith, C.D. Rahn, C.-Y. Wang, Model Order Reduction of 1D Diffusion Systems Via Residue Grouping, Journal of Dynamic Systems, Measurement, and Control. 130 (2008). doi:10.1115/1.2807068.

[24] V.R. Subramanian, J.A. Ritter, R.E. White, Approximate Solutions for Galvanostatic Discharge of Spherical Particles I. Constant Diffusion Coefficient, Journal of The Electrochemical Society. 148 (2001). doi:10.1149/1.1409397.

[25] D.D. Domenico, G. Fiengo, A. Stefanopoulou, Lithium-ion battery state of charge estimation with a Kalman Filter based on a electrochemical model, 2008 IEEE International Conference on Control Applications. (2008). doi:10.1109/cca.2008.4629639.

[26] K.A. Smith, C.D. Rahn, C.-Y. Wang, Control oriented 1D electrochemical model of lithium ion battery, Energy Conversion and Management. 48 (2007) 2565–2578. doi:10.1016/j.enconman.2007.03.015.

[27] W. Luo, C. Lyu, L. Wang, L. Zhang, A new extension of physics-based single particle model for higher charge–discharge rates, Journal of Power Sources. 241 (2013) 295–310. doi:10.1016/j.jpowsour.2013.04.129.

[28] M. Guo, R.E. White, An approximate solution for solid-phase diffusion in a spherical particle in physics-based Li-ion cell models, Journal of Power Sources. 198 (2012) 322–328. doi:10.1016/j.jpowsour.2011.08.096.

[29] W. Luo, C. Lyu, L. Wang, L. Zhang, An approximate solution for electrolyte concentration distribution in physics-based lithium-ion cell models, Microelectronics Reliability. 53 (2013) 797–804. doi:10.1016/j.microrel.2012.11.002.

[30] L. Cai, R.E. White, Reduction of Model Order Based on Proper Orthogonal Decomposition for Lithium-Ion Battery Simulations, Journal of The Electrochemical Society. 156 (2009). doi:10.1149/1.3049347.

[31] V.R. Subramanian, R.E. White, New separation of variables method for composite electrodes with galvanostatic boundary conditions, Journal of Power Sources. 96 (2001) 385–395. doi:10.1016/s0378-7753(00)00656-x.

[32] S. Liu, An analytical solution to Li/Li insertion into a porous electrode, Solid State Ionics. 177 (2006) 53–58. doi:10.1016/j.ssi.2005.09.053.

[33] M.R. Johan, A.K. Arof, Analytical solution to the material balance equation by integral transform for different cathode geometries, Ionics. 10 (2004) 405–414. doi:10.1007/bf02378001.

[34] S.H. Ali, A. Hussin, A. Arof, Short- and long-time solutions for material balance equation in lithium-ion batteries by Laplace transform, Journal of Power Sources. 112 (2002) 435–442. doi:10.1016/s0378-7753(02)00420-2.

[35] M.R. Johan, A.K. Arof, Modeling of electrochemical intercalation of lithium into a LiMn2O4 electrode using Green function, Journal of Power Sources. 170 (2007) 490–494. doi:10.1016/j.jpowsour.2007.03.069.

[36] P. Johnston, Diffusion in composite media: solution with simple eigenvalues and eigenfunctions, Math. Comput. Modeling. 15 (1991) 115-123. doi: 10.1016/0895-7177(91)90096-P

[37] R.I. Hickson, S.I. Barry, G.N. Mercer, Critical times in multilayer diffusion. Part 1: Exact solutions, International Journal of Heat and Mass Transfer. 52 (2009) 5776-5783. doi:10.1016/j.ijheatmasstransfer.2009.08.013

[38] E.J. Carr, I.W. Turner, A semi-analytical solution for multilayer diffusion in a composite medium consisting of a large number of layers, Appl. Math. Modeling. 40 (2016) 7034-7050.

[39] G.P. Mulholland, M.H. Cobble, Diffusion through composite media, International Journal of Heat and Mass Transfer. 15 (1972) 147-160. doi: 10.1016/0017-9310(72)90172-X

[40] J.S. Pérez Guerrero, E.M. Pontedeiro, M.Th. van Genuchten, T.H. Skaggs, Analytical solutions of the one-dimensional advection–dispersion solute transport equation subject to time-dependent boundary conditions, Chem. Eng. J. 221 (2013) 487-491. doi: 10.1016/j.cej.2013.01.095

[41] M.R. Rodrigo, A.L. Worthy, Solution of multilayer diffusion problems via the Laplace transform, J. Math. Analy. Appl. 444 (2016) 475-502.

[43] J. Lin, C.S. Chen, C.-S. Liu, J. Lu, ‘Fast simulation of multi-dimensional wave problems by the sparse scheme of the method of fundamental solutions,’ Computers and Mathematics with Applications. 72 (2016) 555-567.

[44] J. Lin, C. Zhang, L. Sun, J. Lu, ‘Simulation of seismic wave scattering by embedded cavities in an elastic half-plane using the novel singular boundary method,’ Advances in Applied Mathematics and Mechanics. 10 (2018) 322-342.

[45] L. Choobineh, A. Jain, An explicit analytical model for rapid computation of temperature field in a three-dimensional integrated circuit (3D IC), Int. J. Therm. Sci. 87 (2015) 103-109. doi: 10.1016/j.ijthermalsci.2014.08.012.

[46] M. Parhizi, A. Jain, Analytical Modeling of Solid Phase Diffusion in Single-Layer and Composite Electrodes Under Time-Dependent Flux Boundary Condition, Journal of The Electrochemical Society. 167 (2020) 060528. doi:10.1149/1945-7111/ab847c.

[47] D. W. Hahn and M. N. Özişik, Heat Conduction (Wiley, New York) (2012). doi:10.1002/9781118411285.

[48] K. Cole, J. Beck, A. Haji-Sheikh, B. Litkouhi, Heat Conduction Using Greens Functions, (2010). doi:10.1201/9781439895214.

[49] S. Yang, Z. Meng, G. Peng, Y. Gong, The solutions of Green's function of diffusion equation for three-layered matched medium in the steady state, Proc. 4th Int. Conf. Photonics & Imaging in Biology and Medicine 604706 (2006). doi: 10.1117/12.709787

[50] K.N. Kulkarni, L.R. Ram-Mohan, M.A. Dayananda, Matrix Green's function analysis of multicomponent diffusion in multilayered assemblies, J. Appl. Phys. 102 (2007) 064908. doi: 10.1063/1.2779235

[51] V.R. Subramanian, D. Tapriyal, R.E. White, A Boundary Condition for Porous Electrodes, Electrochemical and Solid-State Letters. 7 (2004). doi:10.1149/1.1773751.

# Chapter 10

# Conclusion and Future Direction

## 10-1. Conclusion

In chapter 2, a solution for the phase change heat transfer problem with time-dependent heat flux boundary condition using the perturbation method is presented. The solution is shown to converge at large times, where solutions from past papers are known to diverge. This represents a significant improvement in our theoretical understanding of phase change heat transfer. The theoretical results presented here may be relevant to multiple engineering applications such as cooling of Li-ion cells. Results derived here are used to understand the effect of linear and periodic heat flux boundary conditions, which may arise in such applications. These results can be easily extended to cylindrical and spherical coordinate systems.

Chapter 3 shows that while improving thermal conductivity is helpful for increasing the rate of energy stored, it is not similarly helpful for improving the energy storage density, which may be an important performance parameter in several applications. Using well-establised theoretical models, the present work helps fully understand the impact of previously reported thermal conductivity enhancement on performance of phase change energy storage systems. Based on the theoretical model, the performance of various PCMs can be compared with each other, and the optimal PCM can be chosen, depending of the relative importance of rate of energy stored and energy storage density, as well the geometry of energy storage system.

Chapter 4 presents a theoretical solution for heat transfer problems involving phase change in which a pre-melted or pre-solidified region exists initially. Results derived here, based on an iterative approach, highlight the nature of heat transfer in a problem that can be used to model a number of engineering problems. While presented here for the specific case of melting, the solidification problem can also be addressed based on these results. Other complexities, such as convection in the liquid phase may also be accounted for, provided the underlying analytical solutions for the liquid phase are available. This work improves our fundamental understanding of phase change heat transfer, and facilitates analysis of heat transfer in applications related to energy conversion and thermal management.

Chapter 5 develops a theoretical model for phase change cooling of Li-ion battery packs. Results highlight and quantify the key system-level trade-off between discharge rate and energy storage density, which can prevent needless overdesign of thermal management. Another important insight from this work is the comparison between phase change cooling and convective cooling. It is expected that the theoretical model and key results presented in this work will contribute towards accurate design of practical thermal management systems for Li-ion battery packs, eventually leading to improvement in safety and performance of energy conversion and storage devices.

Chapter 6 develops an analytical heat transfer model to determine the core temperature of a Li-ion cell undergoing thermal runaway based on surface temperature measurement. The technique is suitable for determining the core temperature as a function of time for a variety of experimental conditions where the surface temperature has been measured. Results show that the maximum core temperature during thermal runaway is several hundreds of degrees Celsius higher than the surface temperature. This demonstrates the critical importance of the core temperature of the cell during thermal runaway. The accuracy of the technique depends on chemical kinetics data during thermal runaway, as well as on thermophysical properties of the cell, particularly its specific heat. This work provides a new fundamental insight into the thermal behavior of Li-ion cells during thermal runaway, which is not possible through surface temperature measurement alone. It is expected that information about the core temperature of the cell during thermal runaway, determined by the technique described here may help improve the fundamental understanding of thermal runaway, as well as help design practical tools to predict the thermal state of the cell so that thermal runaway could be mitigated.

In chapter 7, an exact solution is developed for solid-phase diffusion under a time-dependent flux boundary condition using the Green's function approach, which has been used widely in the past for solving thermal conduction problems. The method is first applied to a thin film electrode and a spherical electrode particle. The method is then extended to determine the concertation profile in two-layer slab and spherical composite electrodes. The mathematical models agree well with previous studies for specific cases, as well as numerical simulations. The Green's function-based model presented here is able to accurately predict the transient behavior during solid phase diffusion process relevant to a Li-ion cell. The Laplace transform approach used in previous studies provides separate expressions for short time and long solutions. The short time solution derived using Laplace transform, which is very useful for some applications such as high rates and short times may be calculated faster than the Green's function solution presented here, since there is no separate expression for short time solution using this method. However, for complicated flux boundary conditions, inversion of the Laplace solution may be challenging, whereas the present approach offers a closed-form solution. The model presented here can be used to predict the concentration profile under realistic time-dependent boundary conditions that may appear in practical applications for electrochemical energy storage.

The voltage and SoC computation presented in chapter 8 is carried out using a Green's function based exact analytical solution for the concentration profile in the electrodes for an arbitrary time-dependent current profile. This analytical approach agrees well with numerical simulations for a variety of conditions and may be easier to implement in practical battery management systems, especially with controllers containing limited memory. The individual electrode SoC can easily be related to the overall capacity/SoC of the cell. Even for very complicated current profiles, the analytical model is shown to be able to accurately predict the voltage and SoC changes in the cell over time. It should be noted that the model presented here is based on a single spherical particle model, and therefore is valid within the range of validity of the SPM model, i.e. low to moderate C-rates. Also note that the Green's function approach is inherently valid only for linear systems. Non-linearities such as concentration-dependent diffusivities, which may be significant for modeling of certain battery chemistries, sizes and form factors are not accounted for by the model. Finally, the model is isothermal, and does not account for the impact of temperature on diffusion or kinetic processes. Note that the analytical solution presented here can be used as a basis for state estimation algorithms such as Kalman filter approach for SoC estimation. Furthermore, the solution can also be coupled with the energy balance equation to account for thermal effects. This work is expected to contribute towards the improvement of battery management systems (BMS) for a variety of applications.

In chapter 9, the Green's function approach is used to derive an analytical solution for solution-phase limitation diffusion in composite electrodes under a wide variety of time-dependent flux boundary conditions. The method is applied to a composite electrode consisting of Li-ion foil, separator and porous electrode similar to the composite Li-ion cell sandwich proposed by Doyle and Newman [22]. Concentration profiles in the separator and porous electrode are determined as functions of space and time. The mathematical model is validated against previous studies for the special case of galvanostatic boundary conditions. Furthermore, Green's function-based model is validated by comparison with numerical simulations for time-dependent boundary conditions. The mathematical model presented in this study can be used to accurately predict the transient behavior of solution-phase limitation diffusion. The model is used to predict the concentration profile for a number of realistic time-dependent current densities such as sinusoidal and step functions that may be encountered in energy conversion and storage applications.  The computational time associated with the present model is lower than numerical simulations due to the low number of eigenvalues required for convergence. This work contributes towards the theoretical understanding of species diffusion in Li-ion cells, and provides tools that may be helpful for designing, predicting and improving the performance of electrochemical devices.

## 10-2. Future direction

Mathematical modeling presented in this dissertation might be extended to investigate multiple engineering problems. For example, theoretical modeling of phase change heat transfer can might be extended and coupled with flow in porous media for local thermal equilibrium and non-local thermal equilibrium conditions.

Electrochemical models presented in this dissertation can be extended to account for energy equations and result in a coupled thermal-electrochemical model. Further, the SPM-based analytical solution for solid phase diffusion under time-dependent flux boundary conditions may be used for cell parameter estimation. Also, analytical solution presented here may be used as a basis for state estimation algorithms such as Kalman filter approach for SoC estimation.

# BIOGRAPHICAL INFORMATION

Mohammad Parhizi received his Bachelor of Science degree in Mechanical Engineering from Guilan University, Iran. He started his Master of Science in Mechanical Engineering in Fall 2013 and received his degree in May 2015 from the University of Texas at Arlington. He started his Ph.D. in Mechanical Engineering at the same university in Spring 2017. His research area includes heat transfer, phase change, energy storage and Li-ion batteries. He worked as an Intern at Underwriters Laboratories in Summer 2019. He plans to continue his research as a postdoctoral fellow in near future.

Email: Parhizi.m@gmail.com